

**Crystal Engineering through Particle Size and Shape  
Monitoring, Modeling, and Control**

by

Daniel Bruce Patience

A dissertation submitted in partial fulfillment  
of the requirements for the degree of

DOCTOR OF PHILOSOPHY

(Chemical Engineering)

at the

UNIVERSITY OF WISCONSIN-MADISON

2002

© Copyright by Daniel Bruce Patience 2002  
All Rights Reserved

To Mum and Dad



# Acknowledgments

The University of Wisconsin (UW) Madison has been good to me. There are so many people to thank that made what the unique graduate school experience is supposed to be. I will always have fond memories, I miss the place already. I hope I do not leave anyone out. Definitely, I cannot thank enough my advisor Jim Rawlings. He has taught me the true meaning of patience as he has waited for me to grasp concepts, the true meaning of divide and conquer as we tackled problems, and he raises the bar high. His ability to understand and solve problems and concisely summarize the solution to them is amazing. I am fortunate to have had the experience and learned as much as I could.

I would like to thank my Ph.D. oral exam committee: Professors N. L. Abbott, D. J. Klingenberg, and W. H. Ray in Chemical Engineering, and R. W. Hartel in Food Science. I appreciate their time spent being on my oral defense committee. I would also like thank other Chemical Engineering faculty at UW that have contributed to my work. Professors J. A. Dumesic for being on my preliminary oral exam committee, J. Yin for being on my prepreliminary oral exam committee, T. F. Kuech for help with SEM, and M. D. Graham for help with the ChE 470 laboratory. They have all helped with insightful advice that helped to keep me thinking: What is new about what I am doing?.

For the nuts and bolts of my work I would like to thank many other faculty over the world. Professor John D. Sherwood in the Chemistry Department at the University of Strathclyde in Glasgow, Scotland. You were instrumental in pointing me in the right direction in manipulating sodium chlorate habit in a batch system. I am grateful to Professor Jim Kuelbs in the Department of Mathematics here at UW for teaching me the basics of stochastic processes. I am grateful to Dr. Philip C. Dell'Orco at GlaxoSmithKline in Philadelphia for donating an interesting pharmaceutical to study. Thanks Phil for introducing me to some of the basics in the pharmaceutical industry. I am really looking forward to working in the pharmaceutical industry and I hope we cross paths many times in the future. Thanks also to Dr. Terry Redman at Lasentec for allowing me to use the process vision measurement probe. Thanks to my undergraduate teachers, Drs. R. M. Allen, W. B. Earl, P. J. Jordan, and J. Abrahamson at the University of Canterbury in New Zealand for encouraging me to pursue graduate school. Todd Ninman deserves special mention, thanks for all your help with computing support when I rebuilt the laboratory. Dan P. Miller, besides the antics of unforgettable late nights on State Street, thanks for your help and positive encouragement with job hunting, and showing me the ropes with some of the high-tech laboratory equipment in the department.

The Rawlings research group. I have never worked with such an interesting close-

knit bunch of colorful characters and legends. First, the old original Rawlings group: Rock Matthews, I appreciate all your help, you were my biggest advocate for getting me into the group. For that and your wonderful thesis which provided a good starting point for many of my thoughts and questions, I do not know how to repay you. John Campbell, you taught me many knicks and knacks about our computing facilities when I first came here. It felt like someone was looking out for me, thank you for teaching me teamwork. Peter and Rolf Findeisen, I remember you as hard workers and provided a great role model for me when I first arrived, thank you. Rahul Bindlish, we could discuss cricket for hours and make all the lunch bets in the world on whether India or New Zealand had the better cricket team. Deep down, as we both know in cricket a lot depends on the day. Your personal advice to me is summarized as: it's just not cricket. It took me a while to see that. Chris Rao, thank you for all your encouragement to take classes, to publish, and raise the bar high. Scott Middlebrooks, thank you for teaching me some of the LabVIEW programming tips, and providing me with some of the best entertainment this department has ever seen. The latter Rawlings group members: Jenny Wang, I appreciated your kind nature and friendly smile as I saw you each day studiously working in the office, thanks for showing me the ropes in the ChE 470 laboratory. Matt Tenny, thank you for your programming tips, suggestions and opinions as I toiled through my work, you were a great help in the final year. Brian Odelson, thank you for setting up our computers and bringing us into the 21<sup>st</sup> century. Gabriele Pannocchia, thank you for all the help with LaTeX, you were a great substitute for John Eaton. Eric Haseltine, thank you for picking up the project on stochastic modeling, that really helped to get me back into the laboratory. I wish Aswin Venkat the best of luck with his studies, and I wish we got to spend more time discussing cricket. I cannot forget John Eaton for administrating our computers, providing us with Octave, and showing me all the good things Linux has to offer. I can never stop learning from you. Mary Diaz, thank you for administrating the group, you spoiled us too much with your cookies and candy. You keep the group functioning and kept Brian and I in line, I am going to miss you, your personality, and talents.

Being in the group does not come without making lifelong friends. Chris, thanks for listening and thanks for the fun times spent on campus that defined student life in USA for me. I miss drinking beer with you. Rahul, thanks for listening and giving sound academic and career advice. Scott, thanks for listening, introducing me to Rocky's and teaching me how to appreciate some simple things in life. Gabriele, in the short time we have, I really enjoyed yours and Rita's company. I seem to remember winning darts over you by 200 points. It is nice to know another crazy U2 fan in person. I cannot wait to see your country. Brian, thanks for listening, teaching me how to drive on the right hand side of the road. You kept my final year of research alive by showing there is always another way to find something interesting to do when we poke our heads in Hawaii T1.

I am fortunate to have had a great roommate, Julio Rique. Julio's advice and patience taught me another meaning of friendship. I will never forget that apartment and the times we had there. My family deserves mention, my brothers Robert, Stephen, James,

and my parents all gave me up as I left for USA. I miss you all a lot, who knows where we end up. Finally, I must thank the love of my life. Nicole Diliberti, you have supported me so much this last year, I will return the support when you graduate. I am so lucky to have met someone like you.

DANIEL BRUCE PATIENCE

*University of Wisconsin–Madison  
June 2002*



# Crystal Engineering through Particle Size and Shape Monitoring, Modeling, and Control

Daniel Bruce Patience

Under the supervision of Professor James B. Rawlings  
At the University of Wisconsin–Madison

This study presents efforts to develop and assemble tools required for crystal engineering: reliable modeling frameworks, sound particle size and shape measurement technology, nucleation and growth kinetic determination from data, optimal operations policies given the identified models, prediction of final product size, shape and purity at all levels of the process design. Kinetic models are developed that describe the complicated behavior in three systems: (1) an industrial pharmaceutical crystallization (2) para-xylene crystallization in a scraped-surface crystallizer (3) sodium chlorate crystallization.

For the industrial pharmaceutical batch crystallization, we develop a model that describes size-spreading in crystal size densities. On-line measurements of solution concentration, slurry transmittance, crystal mean size and crystal size density standard deviation are used to identify the parameters in a seeded crystallization with no secondary nucleation. The industrial pharmaceutical crystallization exhibits apparent growth-rate dispersion. Unlike previous models used to describe apparent growth-rate dispersion, the developed growth-dependent dispersion model accurately describes crystal size density size-spreading and with an appended dissolution model allows prediction of four experimental measurements. The kinetic model for the industrial pharmaceutical crystallization is used to design an experiment that grows seeds of a desired polymorph to a specified final size, subject to operating constraints. The profiles are implemented for model validation purposes and found to agree reasonably well with model predictions for concentration and crystal size responses. The experimental designs allow the removal of the post-crystallization processing steps, sieving and milling. The successful demonstration of open-loop crystal size control is the first demonstration of a model-based approach for controlling crystal size of an industrial pharmaceutical. This model development study shows that without the newly developed appended dissolution model, the model parameters cannot be uniquely identified for all four experimental on-line measurements.

For the para-xylene batch crystallization, we develop a model that describes high growth rates undetectable with current measurement technology. On-line measurements

of solution temperature and slurry transmittance are used to identify the parameters in an unseeded scraped-surface crystallization. The standard, population based kinetic model is used to identify nucleation and growth parameters for the para-xylene crystallization experiments and shows the system is a high-growth system. We reduce the model and identify nucleation parameters. The data from the experiments are uninformative, however, and alternative designs are developed to uniquely identify the parameters in the newly developed high-growth model. Previous models developed for high-growth systems can only describe steady-state continuous systems. The model in this study is further developed for batch and transient continuous systems.

For the sodium chlorate semi-batch crystallization, we present a model to describe crystal habit as a function of the loading of the habit modifier. On-line measurements of crystal shape are used to monitor crystal habit. An on-line video microscope particle size and shape sensor is installed that provides measurements of particle aspect ratio, particle area to bounding boxed area ratio and maximum particle diameter. We show how standard image analysis packages can be augmented with user-defined algorithms to accurately detect crystal habit changes. We show this sensor is capable of maintaining a desired habit of sodium chlorate crystals in the face of unmeasured impurity disturbances. The chapter shows a successful, new and unique demonstration of on-line crystal habit monitoring and control.

# Contents

<b>Acknowledgments</b>	<b>iii</b>
<b>Abstract</b>	<b>vii</b>
<b>List of Tables</b>	<b>xiii</b>
<b>List of Figures</b>	<b>xv</b>
<b>Chapter 1 Introduction</b>	<b>1</b>
1.1 Dissertation overview . . . . .	3
<b>Chapter 2 Review of Previous Work</b>	<b>5</b>
2.1 Characterization of Crystals . . . . .	5
2.2 Modeling Crystallization Processes . . . . .	7
2.3 Parameter Estimation . . . . .	11
2.4 Monitoring Particle Size Densities . . . . .	12
2.4.1 Forward Laser Light Scattering . . . . .	14
2.4.2 Photon Migration and Acoustic Spectroscopy . . . . .	15
2.4.3 Backward Laser Light Scattering and the Focussed Beam Reflected Measurement (FBRM) . . . . .	16
2.4.4 Turbidity Measurements . . . . .	17
2.4.5 Photomicroscopy, Particle Vision Measurement (PVM), and Image Analysis . . . . .	18
2.4.6 Attenuated Total Reflection Fourier Transform Infra-Red (ATR FTIR) Spectroscopy for Measuring Meta-Stable Zone Widths and Crystalline Properties . . . . .	19
2.5 Control of Crystallizers . . . . .	20
2.5.1 Control of Continuous Crystallizers . . . . .	20
2.5.2 Control of Batch Crystallizers . . . . .	22
2.6 Future Outlook . . . . .	26
<b>Chapter 3 Experimental Apparatus</b>	<b>27</b>
3.1 Introduction . . . . .	27
3.2 Crystallizer Apparatus . . . . .	28

3.2.1	Laboratory . . . . .	28
3.2.2	Pilot Plant . . . . .	29
3.3	Chemical Systems . . . . .	30
3.3.1	Industrial Pharmaceutical . . . . .	30
3.3.2	Para-xylene . . . . .	31
3.3.3	Sodium Chlorate . . . . .	32
3.4	State Measurements . . . . .	32
3.4.1	Temperature . . . . .	32
3.4.2	Concentration . . . . .	32
3.4.3	Transmittance . . . . .	35
3.4.4	Crystal Size, Standard Deviation and Shape . . . . .	35
3.5	Data Acquisition and Control . . . . .	38
3.5.1	PC . . . . .	41
3.5.2	Signal Conditioning System . . . . .	42
3.6	Operating Procedures . . . . .	42
<b>Chapter 4 Model Summary and Solution</b>		<b>47</b>
4.1	The Population, Mass, and Energy Balance Equations . . . . .	48
4.1.1	Seed Size Density . . . . .	49
4.2	Model Solution . . . . .	50
4.2.1	Method of Weighted Residuals . . . . .	50
4.2.2	Orthogonal Collocation . . . . .	52
<b>Chapter 5 Information-Rich Systems: Industrial Pharmaceutical</b>		<b>59</b>
5.1	Introduction . . . . .	60
5.2	Experimental Apparatus . . . . .	63
5.3	Crystal Size Densities from Process Vision Measurement . . . . .	65
5.4	Initial Estimation of Kinetic Parameters . . . . .	72
5.5	Alternative Model: Growth-dependent Dispersion and Dissolution . . . . .	81
5.5.1	Size-Dependent Growth Model Fit . . . . .	85
5.6	Best Operating Policies . . . . .	88
5.7	Conclusions . . . . .	90
<b>Chapter 6 Information-Poor Systems: Industrial Polymer Precursor</b>		<b>95</b>
6.1	Introduction . . . . .	96
6.2	Initial Estimation of Kinetic Parameters . . . . .	98
6.3	Model Reduction: High Growth Rate Limit . . . . .	101
6.4	High Growth Limits for MSMPR Crystallizers . . . . .	105
6.5	Analysis of Confidence Regions for the Reduced Model . . . . .	108
6.6	Experimental Design . . . . .	111
6.7	Conclusions . . . . .	114

<b>Chapter 7 Particle Shape-Monitoring and Control in Crystallization Processes</b>	<b>115</b>
7.1 Introduction . . . . .	116
7.2 Chemical System and Experimental Apparatus . . . . .	117
7.3 Results and Discussion . . . . .	121
7.3.1 Raw Measurement and Standard Image Analysis . . . . .	121
7.3.2 Refined Image Analysis . . . . .	123
7.3.3 Feedback Control . . . . .	126
7.4 Conclusions . . . . .	130
<b>Chapter 8 Conclusions</b>	<b>137</b>
8.1 Experimental Design for Systems with Growth-Dependent Dispersion . . . . .	138
8.2 High-Growth Systems . . . . .	138
8.3 Monitoring and Controlling Crystal Habit . . . . .	138
8.4 Future Work . . . . .	139
<b>Notation</b>	<b>141</b>
<b>Appendix A Model-Predictive Control of Crystallizer Temperature</b>	<b>147</b>
<b>Appendix B Physical Properties</b>	<b>153</b>
B.1 Physical Parameters of the Pharmaceutical System . . . . .	153
B.2 Physical Parameters of the Para-xylene System . . . . .	153
B.3 Physical Parameters of the Sodium Chlorate System . . . . .	157
<b>Appendix C Model Formulation</b>	<b>159</b>
C.1 Population Balance . . . . .	159
C.1.1 Population Balance with Diffusion . . . . .	163
C.1.2 Population Balance for Particles with Discrete Sizes . . . . .	168
C.2 Continuous Phase Mass Balance . . . . .	170
C.3 Energy Balance . . . . .	171
<b>Appendix D Stochastic Modeling of Chemical Kinetics and Crystallization Processes</b>	<b>175</b>
D.1 Model Formulation . . . . .	175
D.2 Model Solution . . . . .	183
<b>Bibliography</b>	<b>189</b>
<b>Vita</b>	<b>201</b>



# List of Tables

2.1	Models for nucleation and growth. Supersaturation, $S = (C - C_s)/C_s$ . Unless specified, the models are given in Randolph and Larson [106]. . . . .	9
3.1	Serial port parameters for densitometer through COM 0 port. . . . .	33
4.1	Kinetic parameters for Equations 4.24, 4.26, 4.27 and 4.28 the constant dispersion model with no secondary nucleation or fines dissolution. . . . .	52
4.2	Kinetic parameters for Equations 4.24 and 4.33, the size-dependent growth model with no secondary nucleation or fines dissolution. . . . .	57
5.1	Parameter estimates and approximate 95% confidence intervals from concentration, transmittance, mean crystal length, and standard deviation measured for runs 13-16. . . . .	81
5.2	Parameter estimates and approximate 95% confidence intervals from concentration, transmittance, mean crystal length, and standard deviation measured for run 16. . . . .	82
5.3	Size-dependent growth rate model parameter estimates and approximate 95% confidence intervals from concentration, transmittance, mean crystal length, and CSD standard deviation measured for run 16. . . . .	88
6.1	Parameter estimates and approximate 95% confidence intervals resulting from the temperature and transmittance measurements for runs 14 and 15. . . . .	101
6.2	Parameter estimates and approximate 95% confidence intervals resulting from the temperature and transmittance measurements for runs 14 and 15 and the simultaneous fit of the simulated data and run 15 using the reduced model. Confidence regions are summarized in Figures 6.8 and 6.13. . . . .	108
7.1	Definitions and values of boxed area, aspect ratio and roundness measurements for a square and equilateral triangle. . . . .	123
B.1	Physical properties of the pharmaceutical-IPA-water system. . . . .	154
B.2	Physical properties of para-xylene used in Equation B.3. . . . .	157
B.3	Sodium chlorate solubility in water, Mullin [80]. . . . .	158
B.4	Segregation coefficients for sodium dithionite in sodium chlorate-water system, Ristić et al. [114]. . . . .	158

D.1 Solutions to the forward equation (Equation D.16) of some common pure birth processes [47]. . . . .	181
---	-----

# List of Figures

2.1	Truncated cube with 100, 110, 111 and $\bar{1}\bar{1}\bar{1}$ faces. . . . .	6
2.2	Erosion of a cube (i) to an octahedron (v). . . . .	6
2.3	Parallelepiped of length $l$ , width $w$ , and depth $d$ . . . . .	11
2.4	<i>In-situ</i> focussed beam reflected measurement (FBRM) probe for monitoring particle chord lengths in a crystallizer (top). Scanned chords as measured by the FRBM probe (bottom). Source: <a href="http://www.lasentec.com">www.lasentec.com</a> . . . . .	16
2.5	<i>In-situ</i> transmittance probe. . . . .	17
2.6	Principle of attenuated total reflection Fourier transform infra-red (ATR FTIR) spectroscopy. . . . .	20
2.7	Temperature profiles for a batch cooling crystallizer. Cooling policies include natural and linear cooling and cooling to maximize final-time seed size [110].	24
2.8	Supersaturation profiles for a batch cooling crystallizer corresponding to the temperature profiles in Figure 2.7 [110]. . . . .	24
3.1	Crystallizer vessel, headplate, impeller, and draft tube [68]. . . . .	28
3.2	Pilot plant para-xylene crystallization process. . . . .	29
3.3	Xylene mixture. . . . .	31
3.4	Densitometer calibration data collected from six reference solutions of known concentration. . . . .	34
3.5	Densitometer calibration data collected from three reference solutions of known concentration. . . . .	34
3.6	Colorimeter, transmittance probe, and glass sleeve [68]. . . . .	36
3.7	Glass flowcell for photo-microscopy. Circular to rectangular to circular duct. Not drawn to scale. All dimensions in mm. 1. Slurry enters cell. 2. The flow stops and crystals settle. 3. The flow is re-started and the slurry leaves the cell. . . . .	36
3.8	Standard reference material NIST1017b in the flowcell in Figure 3.7 once particles settle (left). Results from digital image analysis (right). . . . .	38
3.9	Cumulative particle size distribution for the standard reference material NIST1017b in Figure 3.8 after 5, 10, 50 and 125 images are collected compared with NIST's measurement. . . . .	39

3.10 Cumulative particle size distribution for the standard reference material NIST1018b after 5, 10, 50 and 100 images are collected compared with NIST's measurement. . . . .	39
3.11 Cumulative particle size distribution for the standard reference material NIST1004a after 5, 10, 25, 40, 50 and 100 images are collected compared with NIST's measurement. . . . .	40
3.12 Standard reference materials NIST1018b and NIST1004a. . . . .	40
3.13 Cumulative particle size distribution for a mix of standard reference materials NIST1018b and NIST1004a in Figure 3.12 after 20, 40, 50, 60, 80 and 100 images are collected. . . . .	41
3.14 Laboratory heating and cooling system for the crystallizer jacket water. . . . .	42
 4.1 Concentration, transmittance, length, and standard deviation as a function of time for the model described by Equations 4.24, 4.26, 4.27 and 4.28 with the parameters given in Table 4.1. . . . .	53
4.2 Concentration, transmittance, length, standard deviation, and particle size density as a function of time for the model described by Equations 4.24 and 4.33 with the parameters given in Table 4.2. . . . .	56
 5.1 Temperature profiles for runs 13–16. . . . .	64
5.2 Thresholding effects on particle size and count of a PVM image of the industrial pharmaceutical. . . . .	66
5.3 Process vision measurement (PVM) images and photo-microscope images of the industrial pharmaceutical at equilibrium. (i) PVM image before manual digitizing. (ii) PVM after manual digitizing resulting in five plengths. (iii) Photo-microscope image before manual digitizing. (iv) Photo-microscope image after manual digitizing. . . . .	67
5.4 The $x, y, z$ dimensions of a needle as a function of its spherical coordinates in which $0 \leq \theta \leq \pi$ and $0 \leq \phi \leq 2\pi$ . . . . .	67
5.5 (i) The projected lengths in two dimensions of a randomly-oriented needle of unit length as seen from the $z$ -direction given by the coordinate system in Figure 5.4. (ii) The single particle PVMPPD, $q(p, L)$ , for a needle seen in the $z$ -direction. (iii) The projected lengths in two dimensions of a randomly-oriented needle of unit length as seen from the $x$ -direction given by the coordinate system in Figure 5.4. (iv) The single particle PVMPPD, $q(p, L)$ , for a needle seen in the $z$ -direction. . . . .	69
5.6 (i) Particle size density of crystals in Figure 5.3 (iii). (ii) PVMPPD of particle population of crystals in Figure 5.3 (i). (iii) PVMPPD of particle population based on lengths from Figure 5.6 (i) seen from the $z$ -direction. (iv) PVMPPD of particle population based on lengths from Figure 5.6 (i) seen from the $x$ -direction. . . . .	70

5.7	Recovery of the CSD from PVM data. . . . .	71
5.8	Mean size as a function of number of crystals in PVM images. . . . .	72
5.9	Growth of pharmaceutical seed crystals for run 13. . . . .	73
5.10	Growth of pharmaceutical seed crystals for run 14. . . . .	74
5.11	Growth of pharmaceutical seed crystals for run 15. . . . .	74
5.12	Growth of pharmaceutical seed crystals for run 16. . . . .	75
5.13	Concentration, transmittance and model fit for runs 13 and 14. . . . .	77
5.14	Mean length and standard deviation and model fit for runs 13 and 14. . . . .	78
5.15	Concentration, transmittance and model fit for runs 15 and 16. . . . .	79
5.16	Mean length and standard deviation and model fit for runs 15 and 16. . . . .	80
5.17	Concentration, transmittance and model fits for run 16. . . . .	83
5.18	Mean length and standard deviation and model fits for run 16. . . . .	84
5.19	Concentration, transmittance data, and size-dependent growth rate model fits. . . . .	86
5.20	Mean length, CSD standard deviation, and size-dependent growth rate model fits. . . . .	87
5.21	Supersaturation, temperature, mean length and CSD coefficient of variation for pharmaceutical crystallization. The profiles are for minimizing batch time with a final mean size constraint of $110 \mu\text{m}$ and a final mean supersaturation constraint zero, without constraints on the cooling rate and supersaturation constrained to be positive. . . . .	89
5.22	Supersaturation, temperature, mean length and CSD coefficient of variation for pharmaceutical crystallization. The profiles are for minimizing batch time with a final mean size constraint of $110 \mu\text{m}$ and a final mean supersaturation constraint zero, with constraints on the cooling rate and supersaturation constrained between zero and 0.1. The two constrained profiles are compared with the unconstrained cooling rate case for a $\Delta t$ of 1 min. . . . .	91
5.23	Concentration and temperature experimental data for temperature rate constrained and supersaturation constrained experiments with model predictions. . . . .	92
5.24	Mean length and standard deviation experimental data for temperature rate constrained and supersaturation constrained experiments with model predictions. . . . .	93
6.1	The Amoco para-xylene crystallization process. . . . .	97
6.2	Comparison between the experimental gas chromatography (GC) measurements (symbols) and the equilibrium concentration (solid line) for three different runs. The solubility is calculated from Equation B.3 and the physical properties of para-xylene in Table B.2. . . . .	98
6.3	Typical collected temperature data from the pilot-plant scraped-surface crystallizer in Figure 3.2, run 15. Cooling rate = $0.2 \text{ }^{\circ}\text{F} \cdot \text{min}^{-1}$ . . . . .	100
6.4	Temperature profile at T1 and full model fit for runs 14 and 15. . . . .	102
6.5	Transmittance profile and full model fit for runs 14 and 15. . . . .	103

6.6	Temperature profile at T1 and reduced model fit for runs 14 and 15. . . . .	106
6.7	Transmittance profile and reduced model fit for runs 14 and 15. . . . .	107
6.8	Parameter approximate 95% inference regions for runs 14 and 15 data using the reduced model. . . . .	109
6.9	Objective function ( $\Phi_{be}$ ) contours and a portion of the 95% inference regions for runs 14 and 15 data. . . . .	110
6.10	Supersaturation profiles at the wall predicted using the reduced model for runs 14 and 15. . . . .	111
6.11	Temperature profile at T1 and reduced model fit for run 15 and simulated data. . . . .	112
6.12	Transmittance profile and reduced model fit for run 15 and simulated data. . . . .	113
6.13	Objective function ( $\Phi_{be}$ ) contours and the 95% inference region for run 15 and simulated data. . . . .	113
7.1	The habit of sodium chlorate ( $\text{NaClO}_3$ ). (Top left) Typical cubic structure. (Top right) Growth towards a tetrahedral structure in the presence of sodium dithionite ( $\text{Na}_2\text{S}_2\text{O}_6$ ), $\bar{1}\bar{1}\bar{1}$ faces begin to dominate the structure. (Bottom) Experimental apparatus. . . . .	119
7.2	Nucleation and growth of sodium chlorate at $23.5^\circ\text{C}$ . Impurity injected at 30 min and contaminated solution flush started at 80 min. . . . .	121
7.3	Nucleation and growth of sodium chlorate as seen by process vision measurement (PVM). Impurity is injected after 20 min. . . . .	122
7.4	Raw data boxed area as a function of time. Impurity injected at 30 min, contaminated solution flush started at 80 min and stopped at 144 min. A second dosage of impurity is injected at 144 min. . . . .	124
7.5	Raw data aspect ratio as a function of time. Impurity injected at 30 min, contaminated solution flush started at 80 min and stopped at 144 min. A second dosage of impurity is injected at 144 min. . . . .	125
7.6	Raw data roundness as a function of time. Impurity injected at 30 min, contaminated solution flush started at 80 min and stopped at 144 min. A second dosage of impurity is injected at 144 min. . . . .	126
7.7	Raw data maximum crystal length, $l$ as a function of time. Impurity injected at 30 min, contaminated solution flush started at 80 min and stopped at 144 min. A second dosage of impurity is injected at 144 min. . . . .	127
7.8	Possible sodium chlorate views in two dimensions when the crystal rests either on the 100 face (square) or $\bar{1}\bar{1}\bar{1}$ face (triangle). . . . .	127
7.9	Boxed area as a function of $w/l$ for a sodium chlorate crystal resting on its 100 and $\bar{1}\bar{1}\bar{1}$ faces. $w$ is the length across the 100 face from the top of one $\bar{1}\bar{1}\bar{1}$ face to the diametrically opposite $\bar{1}\bar{1}\bar{1}$ face. $l$ is the length across the 100 face perpendicular to the $w$ length. . . . .	128

7.10 Aspect ratio as a function of $w/l$ for a sodium chlorate crystal resting on its 100 and $\bar{1}\bar{1}\bar{1}$ faces. $w$ is the length across the 100 face from the top of one $\bar{1}\bar{1}\bar{1}$ face to the diametrically opposite $\bar{1}\bar{1}\bar{1}$ face. $l$ is the length across the 100 face perpendicular to the $w$ length. . . . .	129
7.11 The ratio of the total surface area of all four $\bar{1}\bar{1}\bar{1}$ faces to the total surface area of the whole sodium chlorate crystal as a function of $w/l$ . . . . .	130
7.12 Likelihood regions in which Image Pro Plus will detect a square and equilateral triangle using boxed area and aspect ratio. The ellipse for detecting a square is based on squares 1-7, 9-10 at two sizes. The ellipse for detecting a triangle is based on triangles 11-14 at two sizes. . . . .	131
7.13 Raw data in boxed area - aspect ratio plane with regions indicating where an object is a square or triangle. . . . .	132
7.14 Boxed area as a function of time. Impurity injected at 30 min, contaminated solution flush started at 80 min and stopped at 144 min. A second dosage of impurity is injected at 144 min. . . . .	132
7.15 Aspect ratio as a function of time. Impurity injected at 30 min, contaminated solution flush started at 80 min and stopped at 144 min. A second dosage of impurity is injected at 144 min. . . . .	133
7.16 Roundness as a function of time. Impurity injected at 30 min, contaminated solution flush started at 80 min and stopped at 144 min. A second dosage of impurity is injected at 144 min. . . . .	134
7.17 Maximum crystal diameter, $l$ as a function of time. Impurity injected at 30 min, contaminated solution flush started at 80 min and stopped at 144 min. A second dosage of impurity is injected at 144 min. . . . .	135
7.18 Boxed area as a function of time for a replicated experiment of the experiment in Figure 7.14. . . . .	135
7.19 Feedback control of particle shape based on on-line measurements of shape. After 60 minutes, an impurity-free solution of sodium chlorate is fed to the reactor and a solids-free solution removed at equal rates for the remainder of the experiment. . . . .	136
A.1 Response of the crystallizer to a $10^\circ\text{C}$ step change in the inlet jacket temperature with a fit of a first order with dead-time model. The fit of the model $dT_{\text{crystallizer}}/dt = -(1/\tau)T_{\text{crystallizer}}(t) + (K/\tau)T_{\text{inlet}}^{\text{set}}(t - \alpha)$ where $\alpha = 2.17$ min, $\tau = 15.95$ min and $K=0.90^\circ\text{C}/^\circ\text{C}$ is also shown. . . . .	148
A.2 Moving horizon reference trajectory. . . . .	150
A.3 Performance of cascaded horizon tracking-PID controller, $Q=0.5$ , $S=5$ . . . . .	152
A.4 Typical temperature profile for pharmaceutical crystallization. . . . .	152
B.1 Equilibrium concentration fits using Equation B.1 for the data of 12-20-00 and using Equation B.2 for all the data. . . . .	154

B.2	Photomicrograph of pharmaceutical seed crystals. . . . .	155
B.3	Particle size density (measured using image analysis) of pharmaceutical seeds in Figure B.2. . . . .	156
B.4	Length to width ratio as a function of time for pharmaceutical crystallization.	156
C.1	Possible changes in the size of a cluster of $n$ units [57]. . . . .	164
C.2	Szilard model of nucleation in which a cluster of size $n$ can only grow as a result of a unit attachment or detachment [57]. . . . .	166
C.3	Region of length $\Delta L$ fixed in particle size space through which particles grow and diffuse into and out of. . . . .	168
C.4	Region of length $\Delta L$ fixed in particle size space through which particles of discrete sizes $\{\Delta, 2\Delta, \dots, L - \Delta, L, L + \Delta, \dots\}$ grow into and out of. . . . .	169
D.1	Transition diagram of birth and death process . . . . .	179
D.2	Transition diagram of the crystal growth process in a mixed-suspension mixed- product removal (MSMPR) [50] reactor. . . . .	180
D.3	Transition diagram of the crystal growth process in a batch crystallizer with no dissolution [47] . . . . .	181
D.4	Transition diagram of the agglomeration process. Arrows are drawn consid- ering only the first 3 states. . . . .	182
D.5	Crystal size density given by Equation D.25 for 1000 particles at the start of the simulation. $N_o = 1000$ , $v_o = 1$ and after 500 agglomeration events start- ing with 1000 particles. The analytical solution is given by Equation D.26. $N_o = 1000$ , $v_o = 1$ , $\beta_0 = 0.01$ . . . . .	186

## Chapter 1

# Introduction

*I've entertained the thought...*

— Rao, C. V.

As my crystallization forefathers, Witkowski [146], Miller [75], and Matthews [68] ingeminate, crystallization occurs everywhere and has been utilized for thousands of years. In chemical engineering, crystallization finds applications in the petrochemical industry for separation and purification. In the specialty chemicals industry, crystallization is utilized in the manufacture of polymers, high-valued chemicals and household products. In recent years, crystallization finds applications in new areas in chemical engineering, for example, in understanding surfactant behavior [1]. In the pharmaceutical industry, protein crystallization is required for drug design [144]. Some pharmaceuticals are crystallized for bioavailability and stability reasons during preparation of drug delivery devices. Applications of crystallization are found in the microelectronics industry for silicon production and chemical vapor deposition for manufacture of semiconductors [74]. Crystallization also finds applications in the food industry for stability and texture issues [87, 38].

Traditionally, industrial practice of crystal engineering can be characterized as empirical. Typical empirical approaches include factorial design and trial and error methods which investigate the effects of a wide range of process variables on a desired crystal product characteristic such as yield or crystal size. The non model-based approach is almost invalid during scale-up and unreliable during subsequent operations of a crystallization process. The resulting final product's crystal size and shape distribution cannot be reliably reproduced. Furthermore, small disturbances such as feed impurities and vessel mixing, can lead to large changes in the final product properties. The problems are compounded when researchers and operators do not use the latest in crystallization measurement technologies.

These problems in the current industrial practice of crystal engineering especially arise in the manufacture of complex organic pharmaceutical molecules. The processing problems that arise with these new and unusual pharmaceuticals often cannot be solved with these non-model based approaches that have been developed with established products.

If manufacturers wish to capitalize on their large investment in new product discovery research, then manufacturers must also generate product and process understanding as quickly as possible.

To improve process understanding, crystallization systems are modeled using a population balance approach. The population balance is a conservation equation describing the time evolution of the crystal size density (CSD) through the state space and other internal characteristic variables that describe the crystal's properties. Coupled with the population balance are the mass and energy balances and kinetic expressions that describe nucleation and growth.

Before estimating the kinetic parameters in the population balance model, we require measurements of the solution and slurry properties, such as the solution concentration and the CSD. The CSD itself is difficult to measure. Sensors that provide information about the solid phase usually provide a measurement related to a property of the CSD. Transmittance probes measure the ratio of transmitted to incident light through a dilute slurry providing a measurement of the second moment of the CSD. Photomicroscopy provides a measurement of the CSD mean, variance and crystal habit.

Given the identified model and parameters, experimental design objectives that minimize the extent of nucleation or maximize the seed size to improve the post-crystallization steps have been determined for industrially relevant chemicals. Experimental policies have been implemented for industrially relevant chemicals. Experimental designs have also been determined and implemented to further improve the confidence of the estimated parameters. However, implementation of these policies are typically open-loop and require minimal deviation from the designed trajectory. Implementation of closed-loop control would help ensure achievement of the final process objective. Closed-loop control is rarely implemented in crystallization because of the difficulties in identifying the sources of disturbances mentioned above. The unpredictable number of polymorphs that exist for newly discovered pharmaceuticals pose another disturbance source. On-line sensors that detect polymorph or habit changes are qualitative measurements, and so cannot provide detailed information for closed-loop control. However, on-line sensors such as video microscopy and process vision measurement probes are providing some insight into crystal size and habit phenomena as a function of operating conditions. The standard population balance models are limited to describing the time-averaged behavior of crystallization, and these new video microscopy sensors can measure the fluctuations and stochastic behavior of the crystallizer, previously unobserved and unmodeled. The rapidly improving sensor technology is motivating the need for new microscopic stochastic crystallization models that describe the observed macroscopic behavior. Once these sensors and models reach industrial and academic acceptance, closed-loop control applications will be a more common occurrence in research and industrial application.

The goal of this study is to monitor, model, and control the crystallization of three systems: an industrially relevant pharmaceutical, para-xylene, and sodium chlorate. The study uses three sensors: densitometry, colorimetry and video microscopy to monitor crys-

tallization kinetics. We have different goals for the three systems. After model identification and parameter estimation, we design experiments for a pharmaceutical crystallization to produce a crystal of a desired size. After model identification and parameter estimation for para-xylene, we design experiments to obtain data that improve the confidence in the estimated parameters. The goal of the sodium chlorate crystallization study is to design a monitoring procedure to convert habit modification viewed with video microscopy into a quantitative signal adequate for control purposes.

## 1.1 Dissertation overview

The remainder of this dissertation is organized as follows. Chapter 2 reviews the literature in the crystal engineering field, with emphasis on modeling, monitoring and control. Most of the standard models are listed, the latest crystal size and shape monitoring tools for these applications are described, and some control studies are described for batch and continuous crystallization.

Chapter 3 outlines the experimental apparatus and procedures used to produce the data in latter chapters. Chapter 4 summarizes the model used to describe crystallization kinetics and the two techniques, method of moments and orthogonal collocation, used for solving these models. Models that describe apparent growth-rate dispersion, seen as crystal size density size spreading, are also given.

Chapter 5 is a study of information-rich systems. Information-rich systems are ones in which the tools and techniques outlined in Chapters 2, 3, and 4 are successfully implemented and provide an insightful description of the system. Chapter 5 studies crystallization of an industrially relevant pharmaceutical with apparent growth-rate dispersion. First, we discuss the problem of the existence of more than one model that describes apparent growth-rate dispersion and the assumptions used in each model. Using the latest in sensor technology through photomicroscopy, process vision measurement, and image analysis, and some of the traditional measurements, densitometry and transmittance for concentration and turbidity, we are able to quantify growth-rate dispersion by using a general population balance model to describe the phenomenon. We estimate the parameters in the identified model and design experiments that remove post-crystallization processing steps.

In contrast, Chapter 6 discusses information-poor systems. When limited to the measurements: on-line temperature and transmittance data, off-line concentration data, and one operating condition, we then show the amount of useful information in these data. We use the standard population balance model and show how it can be reduced for high-growth systems. We find the experiments are uninformative for uniquely identifying the parameters in the reduced model. We design informative experiments by operating the crystallization process at different levels of supersaturation. As far as the author knows, the discussion of the reduced model for high-growth systems is the first development of a general model for transient systems.

In Chapter 7, we extract information from existing crystal size and shape sensor

technology. We install a flow loop that collects and returns slurry samples from the crystallizer. We create a classification algorithm that uses existing measurements available with most photomicroscopy and image analysis units. The refined algorithm is used to detect the presence of sodium chlorate cubes and tetrahedra in a semi-batch crystallization. Based on the percentage of one habit compared to the other, we demonstrate successful on-line control of habit. As far as the author knows, these results are the first demonstration of real-time monitoring and control of crystal habit.

Chapter 8 summarizes the modeling, monitoring, and control results of this study and suggests future work.

## Chapter 2

# Review of Previous Work

*It's a slippery-a-slopea.*

— Pannocchia G.

## 2.1 Characterization of Crystals

The geometry of a particular crystal is characterized by its size and habit. The size of a crystal is meaningless if the habit is not defined first. The *Miller indices* describe the orientation of an individual face of a crystal. The crystal habit is described by the number of faces and the set of Miller indices for all the faces of the crystal. The procedure for determining the Miller indices is outlined in any materials or crystallography text [80]. Consider some simple examples of Miller indices applicable to the symmetric sodium chlorate system shown in Figure 2.1. In three dimensions and Cartesian coordinates, a face that only intersects with the  $x$  axis and is parallel to the  $y$  and  $z$  axes is called a 100 face. A plane that intersects both the  $x$  and  $y$  axes at  $45^\circ$  is a 110 face and a plane that intersects the positive  $x$ ,  $y$  and  $z$  axes equidistant from the origin is called a 111 face. Other permutations of the set  $\{1, \bar{1}, 0\}$  in triplets are analogous to 100, 110 and 111. The bar on  $\bar{1}$  indicates intersection with the negative axes. The characteristic size  $L$  of a crystal is usually defined by the maximum distance between two points along or parallel to the major axis of the crystal. The volume shape factor  $k_v$  converts  $L^3$  to the crystal volume and is a function of the ratios of the two other lengths in the orthogonal direction. For simple shapes, such as a sphere, cube, and tetrahedron, the volumetric shape factors are  $\pi/6$ , 1, and 0.5, respectively.

Care must be taken with the terms *form*, *habit*, *morphology* and *shape* when describing crystals. *Shape* is a general term used to describe the overall appearance of a two or three dimensional object. According to Philips [92], before defining habit, form must be defined. The definition of *form* is *the assemblage of faces necessitated by the symmetry when one face is given*. For example, consider the cube (hexahedron) in Figure 2.2i. A cube consists of six faces (all the same size and shape) and eight corners. By cutting away at the original corners of the cube, we are left with the truncated cube in Figure 2.2ii in

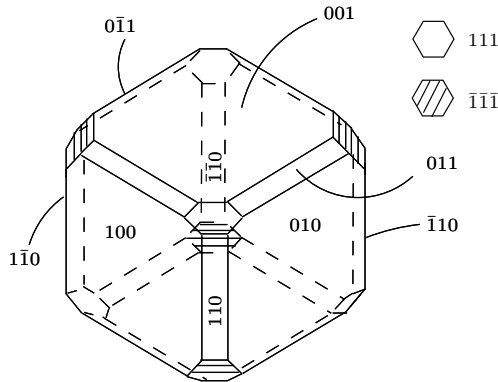


Figure 2.1: Truncated cube with 100, 110, 111 and  $\bar{1}\bar{1}\bar{1}$  faces.

which the corners are replaced by triangular faces, and the cube faces are octagonal. The object in Figure 2.2ii is said to have 14 faces of 2 *forms*. Further cutting results in the original cube faces becoming squares again, seen in Figure 2.2iii, again 14 faces of 2 *forms*, however, different forms from Figure 2.2ii. Further cutting again results in the corners becoming hexagonal, Figure 2.2iv. Ultimately, the final development in Figure 2.2v is the octahedron. The *habit* of a crystal is then defined as *the general aspect conferred by the relative development of the different forms*. The habit of a crystal is usually influenced by the solvent used, the temperature, and the presence of impurities.

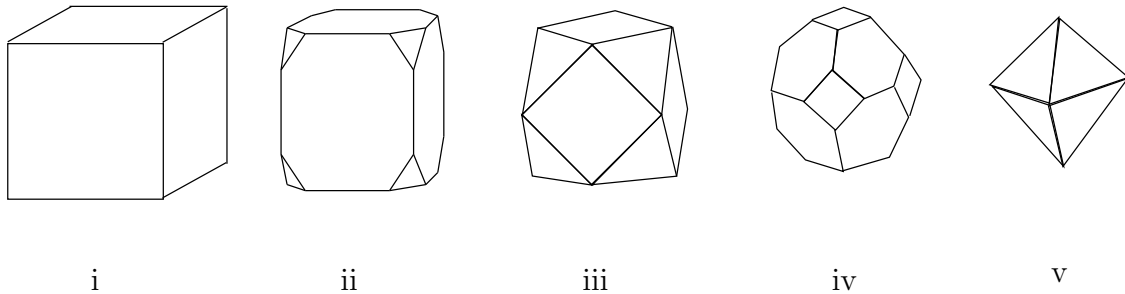


Figure 2.2: Erosion of a cube (i) to an octahedron (v).

A *unit cell* is the smallest region that completely describes the pattern of the three dimensional crystal lattice and the *morphology* of a crystal refers to a particular molecular structure in the unit cell. Often times, but not always, two crystals with different morphologies result in crystals with different habits. For example, carbon and graphite have different morphologies and habits. Crystals with different habits do not necessarily have different morphologies. Sodium chlorate is an example of a system that exhibits different habits with the same morphology, seen in Figure 7.1 in Chapter 7. Mullin [80] provides a list of other systems which exhibit multiple habits with identical morphologies and their respective habit modifiers.

The variable of interest to describe crystallization systems is usually a crystal char-

acteristic length,  $L$ .  $L$  is usually defined as the largest dimension of a crystal, the equivalent diameter of a sphere that has the same volume as the particle or a characteristic dimension chosen to suit the sensor technology. Sometimes the *chord length*, defined in two dimensions as *the set of points connecting two fixed points on the boundary of the object* is used to describe the size of a particle. The *Martin diameter*, defined as *a chord that bisects the object* and the *Feret diameter*, defined as *a chord whose two fixed points on the object perimeter have parallel tangent lines to the object* are some commonly used chords to measure length. In the case of agglomeration, it is practical to consider the particle volume as the variable of interest because during some simple agglomeration processes, volume is conserved and not length.

The particle size density (PSD)  $f(\mathbf{z}, t)$  is defined as

$$f(\mathbf{z}, t) \equiv \lim_{\Delta \mathbf{z} \rightarrow 0} \frac{\Delta F(\mathbf{z}, t)}{\Delta \mathbf{z}} \quad (2.1)$$

where  $F(\mathbf{z}, t)$  is the cumulative distribution (fraction of particles size less than  $\mathbf{z}$ ). Assuming a shape factor  $k_v$  that converts  $L^3$  (where  $L$  is a characteristic length of a particle) to the volume of the particle reduces the internal coordinate vector  $\mathbf{z}$  to one dimension. The particle is then described by one characteristic dimension. Besides particles that are regular polyhedrons, a finite number of more than one internal coordinate is all that is needed (without a shape factor) to describe the size and habit of a particle. However, in practice, shape factors are usually assumed for simplicity.

## 2.2 Modeling Crystallization Processes

The classical framework for modeling crystallization processes consists of coupled population, mass, and energy balances. Descriptions of phenomena such as nucleation, growth, agglomeration, and breakage are well-established. Randolph and Larson [105], Hulbert and Katz [51], and Ramkrishna and Borwanker [102, 103] have extensively studied the analysis and treatment of the population balance equation (PBE) to these crystal formation mechanisms. Hulbert and Katz [51] develop the population balance to include an arbitrary number of characteristic variables and used the method of moments to solve the PBE for a variety of applications such as modeling systems with one or two length dimensions with nucleation and growth occurring, and modeling agglomerating systems. Smit et al. [123] use the method of moments to solve the PBE for a variety of agglomeration mechanisms. More details on the development of the PBE are in Appendix C. Many population modeling issues remain open, however, including accurate modeling of nucleation events governed by Brownian dynamics and modeling apparent growth-rate dispersion phenomena.

Equation 2.2 is the general equation that describes the behavior of a population of crystals in a batch, semi-batch or continuous crystallizer with nucleation, growth, agglom-

eration and breakage processes.

$$V \left( \frac{\partial f(L, t)}{\partial t} + (\nabla \cdot Gf(L, t)) - (B - D) \right) = - \left[ \frac{w_{\text{eff}}}{\rho_{\text{eff}}} f(L, t) - \frac{w_{\text{feed}}}{\rho_{\text{feed}}} f_f(L, t) \right] - f(L, t) \frac{dV}{dt} \quad (2.2)$$

$G$  is the growth rate,  $B$  is a birth function that can describe nucleation or agglomeration,  $D$  is a death function that can describe dissolution or breakage,  $V$  is the system volume and  $w/\rho$  is the stream volumetric flowrate. Equations 2.3 and 2.4 are the macroscopic mass and energy balance equations that describe batch, semi-batch or continuous processes, given by Bird et al. [14]<sup>1</sup>

$$\frac{dm_{\text{tot}}}{dt} = \rho_1 \langle \bar{v}_1 \rangle S_1 - \rho_2 \langle \bar{v}_2 \rangle S_2 - R \quad (2.3)$$

$$\frac{d}{dt} (U_{\text{tot}} + K_{\text{tot}} + \Phi_{\text{tot}}) = -\Delta \left[ \left( \hat{U} + \frac{1}{2} \frac{\langle \bar{v}^3 \rangle}{\langle \bar{v} \rangle} + \hat{\Phi} + p \hat{V} \right) w \right] + Q - W \quad (2.4)$$

Table 2.1 lists constitutive relations for nucleation and growth for describing a large class of various nucleation and growth mechanisms.

Segregated feed models (SFM) are used when the system is not well-mixed and when Equation 2.2 no longer applies to the whole system. SFMs consist of at least two well-mixed compartments in which each compartment describes the phenomena occurring in the respective zone of the reactor. Nucleation, for example, may rapidly occur at the inlet where a feed stream enters the vessel, and the subsequent nuclei grow slowly in the bulk. A two-compartment model would then consist of a feed compartment and a bulk compartment. Crystals, mass and energy are exchanged between the two compartments according to the time constants characteristic for micromixing and mesomixing in the reactor. Population, mass, and energy balances are applied to the individual compartments accounting for the different levels of supersaturation in the zones of the reactor. Zauner and Jones [149] successfully apply a SFM to a semi-batch precipitation process in a continuous reactor with two inlet streams and one outlet stream. SFMs can also be applied to static crystallizers for models for crystallization on a stationary surface, Ossipov [84] and for models for crystallization on a moving surface, Smith [126].

In most modeling studies, it is assumed that the habit of the crystals remains constant i.e. spherical, cubic, parallelepiped. Neglecting breakage, crystal habit is determined by the relative growth rates of the individual faces of a crystal. The slower the growth rate of a face, the larger the face size on the crystal. Given enough time, every crystal should grow into its equilibrium shape, which is one that minimizes the total surface free energy per unit volume. Most often, however, the shape remains in a non-equilibrium shape.

Wulff's theorem is used for predicting the equilibrium shape of a crystal. The theorem states there is a point, called the *Wulff point*, such that the distance,  $l$  from a surface area tangent plane with direction,  $\mathbf{n}$  to the Wulff point, is proportional to the surface free

---

<sup>1</sup>Note the change in sign for the work term.

Event	Expression	Comment
Homogeneous Nucleation	$B = C_1 \exp \left[ \frac{-16\pi\sigma^3\nu^2}{3k^3T^3(\ln S)^2} \right]$	
Heterogeneous Nucleation	$B = C_1 \exp \left[ \frac{-16\pi\sigma^3\nu^2b}{3k^3T^3(\ln S)^2} \right]$	The extra parameter $b$ corrects for nucleation on foreign surfaces
Secondary Nucleation	$B = k_b S^b$	
Secondary Nucleation	$B = k_b e^{-(\Delta E/kT)} S^b$	Temperature-dependent $k_b$
Secondary Nucleation	$B = k_b S^b, \quad S > S_m$	Nucleation occurs when $S$ is larger than a metastable limit
Secondary Nucleation	$B = k_b S^b N^l \mu_3^j$ $B = k_b S^b N^l \mu_2^j$	Includes crystal-agitation and crystal-crystal effects
Size-dependent Nucleation	$B = k_b S^b \mu_3 (L_{min})^j$	Matthews and Rawlings [70]
Growth	$G = k_g S^g$	
Growth	$G = k_g e^{-(\Delta E/kT)} S^g$	Temperature-dependent $k_g$
Size-dependent Growth	$G = G(1 + \gamma_1 L)^{\gamma_2}$	
BCF Model of Growth	$G = \frac{k'_g}{k_{bcf}} S^2 \tanh \left( \frac{k_{bcf}}{S} \right)$	Burton et al. [18] Includes effects of steps and surface defects

Table 2.1: Models for nucleation and growth. Supersaturation,  $S = (C - C_s)/C_s$ . Unless specified, the models are given in Randolph and Larson [106].

energy,  $\gamma(\mathbf{n})$  of that tangent plane. From Wulff's theorem, the following relationship can be derived and used for predicting crystal shapes based on the relative facet growth rates,  $v(\mathbf{n}_i)$

$$\frac{v(\mathbf{n}_1)}{l_1} = \frac{v(\mathbf{n}_2)}{l_2} = \dots = \frac{v(\mathbf{n}_i)}{l_i} \quad (2.5)$$

There are two common models for relating facet growth rates,  $v(\mathbf{n}_i)$ , with the internal crystal structure: the Bravis-Friedel, Donnay-Harker (BFDH) model and the Hartman-Perdock approach. The BFDH model predicts facet growth rates from knowledge of the arrangement and geometry of the molecules in the lattice. The BFDH model states that the slowest growing facets are the ones with the highest molecular density on the surface of the respective face and the largest molecular spacing between adjacent layers of molecules. The Hartman-Perdock model predicts that the growth rate of a face is proportional to the interaction energy between the molecules on the surface and all the molecules in the bulk of the crystal. In their review, Winn and Doherty [145] outline Wulff's theorem, the BFDH and Hartman-Perdock models in detail. The authors show that the predictions of crystal habit using the BFDH and Hartman-Perdock models closely predict the habits of crystals grown from vapor. However, the models poorly predict habit of crystals grown from solution. Winn and Doherty [145] state that in the solution phase, external forces to the crystal structure cause the departure from model predictions, whereas external forces in the vapor phase are not significant.

Matthews and Rawlings [70] model crystal habit with two length coordinates. The authors assume the crystal is a parallelepiped (Figure 2.3) with a width-to-depth ratio equal to one. The habit dynamics can then be modeled as changes in the length-to-width ratio,  $l_w$ . Given a seed with initial width,  $L(0)$ , a dynamic model of  $l_w$  for an individual crystal is given

$$l_w(t) = \frac{l_w(0)L(0) + l_w(\infty)\Delta L(t)}{L(0) + \Delta L(t)} \quad (2.6)$$

in which  $l_w(0)$  is the initial length-to-width ratio determined from image analysis,  $\Delta L(t)$  is the integral of the growth from  $t = 0$  to  $t$ , and  $l_w(\infty)$  is the asymptotic length-to-width ratio as  $\Delta L$  goes to infinity.  $l_w(\infty)$  is an estimate of the ratio of the growth rates along the length and width dimensions. The parameter  $L(0)$  is integrated out of equation 2.6 assuming the seed distribution is linear, resulting in a relationship for the dynamic average length-to-width ratio. The habit dynamics are applied to the seeds and the nuclei are assumed to have the habit dictated by  $l_w(\infty)$ . The length-to-width ratio prediction is then incorporated into the volume and area shape factors,  $k_v(t) = l_w(t)d_w$  and  $k_a(t) = 2(l_w(t)d_w + d_w + l_w(t))$ , respectively, in the PBE, mass, and energy balances. The parameter  $l_w(\infty)$  is estimated from the data. The model predicted a  $l_w(\infty)$  ratio of 11.2 for an industrial photochemical that grows from crystals with  $l_w$  of 2 to 4, to needles with  $l_w$  of 6 to 14. The model predictions were found to agree with off-line photo-microscope images of the slurry.

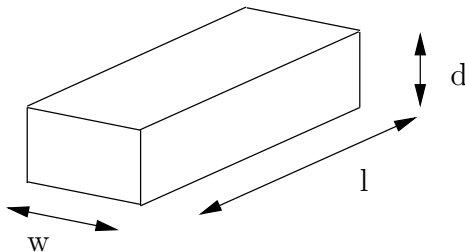


Figure 2.3: Parallelepiped of length  $l$ , width  $w$ , and depth  $d$ .

## 2.3 Parameter Estimation

Estimates of kinetic parameters are required for several reasons: to obtain process insight in terms of which rates are limiting, to design experiments to discriminate between candidate models, to design controllers to maximize product quality or minimize operating costs. In all cases, the experimental data should provide sufficient information about the system under investigation. Model identification is considered reasonably complete when the parameter uncertainty and the model reliability are assessed. A wide variety of experimental techniques have been used for crystallization parameter estimation. Two types of experimental data are generally required. One type of information considers the solution phase (temperature, concentration data), the other considers the solid phase (transmittance data) [134]. Matthews and Rawlings [70], Miller and Rawlings [76], and Witkowski et al. [147] apply a non-linear program (NLP) with a maximum likelihood objective function to deduce the nucleation rate and growth rate kinetic parameters (Table 2.1) simultaneously for a photochemical-heptane system, a  $\text{KNO}_3\text{-H}_2\text{O}$  system, and a naphthalene-toluene system, respectively. The authors use on-line concentration and slurry transmittance as the two measurements. A method for assessing the confidence regions of the parameter estimates is also presented by the authors. Matthews and Rawlings [70] show it is difficult to attain sufficient data to accurately identify the process dynamics affecting the PSD. The authors use a single internal coordinate PBE and a seven parameter model that describes both size and habit with measurements of solution concentration, temperature and slurry transmittance. The parameters could not be uniquely identified with strict convergence tolerance for the estimation scheme. Monnier et al. [77] studied the crystallization kinetics of adipic acid in water. They used the calorimetric method as an indirect method to measure the supersaturation providing information about the solution phase and used off-line image analysis to give information about the solid phase. Qiu and Rasmuson [99] estimated the kinetics of succinic acid crystallization in aqueous solution. Concentration and final product size distribution are the two measurements used to estimate the parameters.

In a nonlinear parameter scheme, the following assumptions are considered for modeling the prediction errors:

- The prediction errors are Normally distributed with zero mean and covariance matrix  $\mathbf{V}$ .

- Prediction errors corresponding to different sample times are uncorrelated.
- Prediction errors corresponding to the  $m$  different measurement types are uncorrelated.
- The prediction errors are homoscedastic (error variance is independent of the magnitude of the measured variable).

Under these assumptions, it is shown by Bard [6] that the maximum likelihood method is equivalent to the minimization of

$$\Phi_{be} = \sum_{k=1}^m (n_k + 1) \ln \left( \sum_{i=1}^{n_k} e_{ik}^2(\theta) \right) \quad (2.7)$$

where  $n_k$  is the number of measurements of the  $k^{th}$  type and  $e_{ik}$  is the prediction error of the  $i^{th}$  measurement of the  $k^{th}$  type. Given the optimal model parameters,  $\hat{\theta}$ , the maximum-density estimate of the prediction variance for the  $k^{th}$  measurement type,  $\hat{\sigma}_k^2$ , is

$$\hat{\sigma}_k^2 = \frac{\sum_{i=1}^{n_k} e_{ik}^2(\hat{\theta})}{n_k + 1} \quad (2.8)$$

An approximation of the spread of the posterior density may be obtained by assuming that the model can be represented as linear in the parameters in the vicinity of the modal estimates. Linearization allows the determination of the Hessian,  $\mathbf{H}_{\theta\theta}$ , which describes the curvature of the distribution about the mode.

The confidence intervals for the model parameters may be determined according to

$$\theta_i \approx \hat{\theta}_i \pm \sqrt{\chi_p^2(\alpha) \mathbf{H}_{\theta\theta}^{-1}(\mathbf{i}, \mathbf{i})} \quad (2.9)$$

where  $\mathbf{H}_{\theta\theta}^{-1}(\mathbf{i}, \mathbf{i})$  is  $i, i$  element of  $H_{\theta\theta}^{-1}$ . The linear 95% confidence intervals are calculated according to Equation 2.9 with  $\alpha$  equal to 0.025. More detailed presentations of Bayesian inference of parameters from data are given by Stewart et al. [129, 130] and Box and Tiao [16].

## 2.4 Monitoring Particle Size Densities

Unlike the temperature measurement, there is no simple technique for measuring the PSD in which one can place a probe into a crystallizer and obtain a measure of the PSD. PSD measurements can be classified as either *off-line*, *on-line* or *in-line*. Off-line sensors remove samples from the process and are not returned to the process. Sieving is the classical off-line measurement that provides precise measurements of the PSD, but is too slow and of no use in kinetic studies and feedback control.

On-line sensors continuously remove a sample from the process and return the sample to the process once it is analyzed. Forward light scattering is an on-line measurement that

measures the scattered energy pattern of light through a dilute slurry of particles on an array of concentric annular photo-diodes or an array of wedge photo-diodes. Forward light scattering usually requires on-line slurry dilution, which is expensive if the operator wishes to return the sample [52] to the process. Photon migration and acoustic spectroscopy are on-line measurements that examine the phase shift and amplitude modulation of sinusoidally modulated light or sound as it passes through the crystal slurry. In the studies by Miller [75] for forward light scattering, Sevick-Muraca et al. [120] for photon migration and Mougin et al. [79] for acoustic spectroscopy, all authors estimate the PSD by applying a quadrature rule to evaluate the integral that predicts the PSD's influence on the sensor's signal. The resulting matrix equation is inverted to estimate the PSD, but due to its ill-conditioning, it cannot be solved using simple least squares. Instead, by assuming information about the shape of the actual PSD, some information about the PSD can be recovered. Sun and Sevick-Muraca [131] develop new inversion algorithms for particle sizing measurements, but the techniques are limited to some simple shaped unimodal and bimodal densities.

In-line (or *in-situ*) sensors are placed directly into the crystallizer and are the preferred measurement in modern crystallization studies. Lasentec's ([www.lasentec.com](http://www.lasentec.com)) focussed beam reflected measurement (FBRM) and particle vision measurement (PVM) probes currently are the most commonly used probes in monitoring PSDs [17]. In particular, the FBRM probe is a precise measurement and useful for monitoring batch to batch variations of nucleation and growth rates [7]. In the pharmaceutical industry, the Sympatec, or laser diffraction of suspended particles in dry air is the approved instrument for assessing product quality of pharmaceuticals. The protocol and Sympatec instrument is a time-consuming technique. However, Wood-Kaczmar [148] compares FBRM measurements with the Sympatec laser diffraction measurements of pharmaceutical products so FBRM users in manufacturing can quickly assess whether a product will be the approved product.

Turbidity probes are an inexpensive option for in-line monitoring of crystallization kinetics, in particular, nucleation kinetics. The technique compares the amount of transmitted light through a dilute slurry to the incident light and provides an estimate of the second moment of the PSD for dilute slurries. Cournil and coworkers [44] show that the probe is suitable for accurately and precisely measuring nucleation induction times that are comparable to those predicted by FBRM.

An electrical sensor for PSD measurement, such as the Coulter counter, detects a change in electrical conductivity as a particle passes through an orifice of a particular dimension. When a particle passes through the orifice, it displaces a certain amount of electrolyte, which changes the electrical conductivity between two electrodes on opposite sides of the orifice. The magnitude and duration of the impulse can be related to the size of the particle. However, electrical sensors are limited to electrolyte systems.

### 2.4.1 Forward Laser Light Scattering

The forward light scattering sensor measures the energy pattern of scattered light through a slurry. The energy pattern of scattered light at a circular detector of inner radius,  $r_i$ , is the integral of energies scattered by individual particles of diameter  $L$  at the detector,  $e(L, r_i)$ , times the PSD  $f(L)$

$$e_t(r_i) = \int_0^\infty e(L, r_i) f(L) dL \quad (2.10)$$

$e(L, r_i)$  is a known function that depends on the size of the particle, the inner and outer radii of the sensor, the focal length of the lens and optical properties of the laser and the diode. Applying a quadrature rule to evaluate the integral in equation 2.10 gives a matrix equation for  $f(L)$  at the  $p$  quadrature points,

$$e_t(r_i) = \sum_{j=1}^p w_j e(L_j, r_i) f(L_j) \quad i = 1, \dots, n \quad (2.11)$$

in which  $n$  is the number of photo-diodes,  $L_j$  are the quadrature points and  $w_j$  are the quadrature weights. The PSD,  $f(L)$ , can be solved by inversion,  $\mathbf{f} = (\mathbf{E}^T \mathbf{E})^{-1} \mathbf{E}^T \mathbf{e}_t$ . However, the inverse operator is ill-conditioned and extremely different PSDs can give similar scattering patterns, so small errors in  $e_t(r_i)$  can produce large errors in the inferred PSD.

Rawlings et al. [111] use a technique to find the inferred PSD from the scattering pattern by posing the problem as a quadratic program (QP)

$$\begin{aligned} \min \quad & \mathbf{c}^T \mathbf{f} + \frac{1}{2} \mathbf{f}^T (\mathbf{B}^T + \mathbf{B}) \mathbf{f} \\ \text{subject to : } & m_j \geq 0, \quad j = 1, 2, \dots, p \end{aligned} \quad (\text{QP1})$$

in which  $\mathbf{B} = \mathbf{E}^T \mathbf{E} + \gamma \mathbf{H}$  ( $E_{ij} = w_j e(L_j, r_i) f(L_j)$ ),  $\mathbf{c} = -2\mathbf{E}^T \mathbf{e}_t$  ( $e_{ti} = e_t(r_i)$ ),  $\mathbf{H}$  is a regularization matrix and  $\gamma$  is a penalty weight. Different regularization methods can be chosen for  $\mathbf{H}$ , such as the zeroth-, first-, and second-order regularizations. The second-order regularization form provides a smoothing constraint and is given as

$$\sum_{j=3}^N (f_j - 2f_{j-1} + f_{j-2}) \quad (2.12)$$

The penalty weight,  $\gamma$  must be chosen large enough to provide a smooth solution and avoid the instabilities in the ill-conditioning (due to the residual errors or noise) of the inversion, though not large enough to cause a bias and incorrect inference of the PSD. Smoothing alone does not guarantee stable non-negative solutions for the PSD and the non-negativity constraint requiring  $m_j \geq 0$  in QP1 ensures a stable solution.

Heffels et al. [40] detect particle habit information present in the diffraction pattern from forward light scattering. Spheres produce symmetry in the intensity of the diffraction

pattern with the azimuthal angle, though other habits produce intensity variations with the azimuthal angle. On-line habit change can be detected for simple habits such as squares and ellipsoids, however, the technique is limited because the size of the particles must be known to obtain the respective habit information from the scattering pattern. The number density of particles cannot be inferred from the pattern.

In recent years, the error in the signal  $e(L, r_i)$  has been improved by increasing the number of detection array elements in a forward light scattering instrument [41]. Light scattering instruments provide either a shape or size signal. For the technique to stay as an accepted measurement in the crystallization field, laser light scattering instruments will need to provide both size and shape information simultaneously.

For dense slurries, Heffels et al. [43] place the detector array perpendicular to the light source to measure back-scattered light. Like forward light scattering, an intensity pattern is measured as a function of the angle or radius on a detector array. The authors use a charged coupled device (CCD) camera. CCD cameras are replacing photo-diodes as detector arrays. Typical CCD cameras can capture a light pattern on an array of  $512 \times 512$  pixels with 256 grayness levels. The widths of intensity peaks on a scattering pattern are affected by the particle size and the height of the intensity is related to the particle concentration. Heffels et al. [42] calibrate a backward light scattering sensor to monitor the habit of glass beads in a slurry. The technique is limited to having *a priori* knowledge of the particle sizes so the apparatus can be calibrated to measure habit.

#### 2.4.2 Photon Migration and Acoustic Spectroscopy

Sevick-Muraca et al. [120] study photon migration in concentrated slurries where multiple light scattering occurs so the sensor is not limited to dilute slurries. Photon migration monitors the time-dependent propagation characteristics of multiply scattered light rather than the amount of light detected. The technique involves passing light whose intensity is sinusoidally modulated through the slurry and monitoring the phase shift and amplitude modulation relative to the incident light. The phase shift and amplitude modulation are used to calculate the dispersion (or *fluence*) of photons through the media. By solving a diffusion equation an optical diffusion coefficient is then determined which is related to an isotropic scattering coefficient,  $(1 - g)\mu_s$ . The PSD and particle volume fraction,  $\phi$  is then found by inverting

$$(1 - g)\mu_s(\lambda) = \int_0^\infty 3Q_{\text{scat}}(L, n, \lambda)[1 - g(L, n, \lambda)]\phi \frac{f(L)dL}{L} \quad (2.13)$$

in which  $g$  is the mean cosine of the scattering angle from a single particle, and  $Q_{\text{scat}}$  is the scattering efficiency. The inversion technique is similar to QP1 presented by Rawlings et al. [111]. The technique produces excellent results that agree with light scattering measurements of the same diluted solution, but the functional form of the PSD is assumed by the authors. Similarly, acoustic spectroscopy measures the amplitude and phase shift of acoustic waves through a sample relative to the incident wave for various frequencies. The use of

acoustic spectroscopy for on-line PSD monitoring utilizes theory similar to the theory for inferring a PSD and volume fraction from photon migration measurements [46]. Recently, Sun and Sevick-Muraca [131] approximate the inferred PSD in QP1 with B-splines and obtain accurate unimodal and bimodal PSDs of titanium dioxide suspensions that agree with off-line measurements.

#### 2.4.3 Backward Laser Light Scattering and the Focussed Beam Reflected Measurement (FBRM)

Backward light scattering offers some attractive advantages over forward light scattering. Back scattering makes it possible to investigate higher particle concentrations and can be designed as an *in-situ* probe. Heffels et al. [43] state, however, that backward light scattering has difficulty detecting transparent crystals. Faceted particles strongly influence the backscatter pulse duration that is a measure for particle chord length. Figure 2.4 shows the principle behind backward light scattering for monitoring particle chord lengths with the FBRM probe. The theory for inferring the PSD from a particle chord length density (CLD) is the same as forward light scattering, described by equation 2.11. The ill-conditioned inversion problem and technique previously discussed for inferring PSD from forward light scattering patterns are the same for backward light scattering.

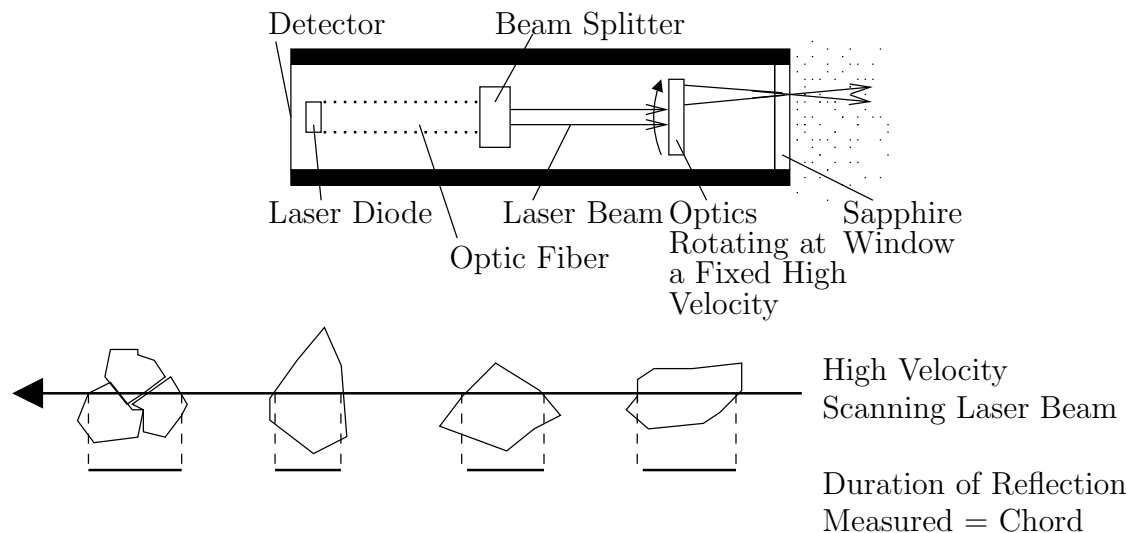


Figure 2.4: *In-situ* focussed beam reflected measurement (FBRM) probe for monitoring particle chord lengths in a crystallizer (top). Scanned chords as measured by the FBRM probe (bottom). Source: [www.lasentec.com](http://www.lasentec.com).

The FBRM probe measures the pulse duration of a peak of back-scattered light from a particle and correlates that with length knowing the speed at which the light source is rotating. A disadvantage of the FBRM probe is the effect of particle opacity. Identically sized particles of different opacities will back-scatter light for different durations for a light

beam that traverses an identical chord across both particles [119]. Ruf et al. [119] apply QP1 to estimate the PSD from a CLD and show that the CLD cannot be inverted into a PSD unless information about the particle shape is known.

Monnier et al. [77] use the FBRM probe and calorimetry to estimate crystallization kinetic parameters in a batch crystallizer and image analysis to verify the final product PSDs. The authors did not use an algorithm similar to QP1 or that of Ruf et al. [119] and claimed the FBRM probe underestimates large particles and overestimates small particles compared to image analysis measurements. The incorrect prediction of size can be attributed to biased sampling by the FBRM probe. To verify the technique with image analysis, 500–1000 particles are required to provide a PSD, and this was achieved by randomly moving an automated bench with the final product PSD after crystallization under the microscope.

#### 2.4.4 Turbidity Measurements

Turbidity measurements monitor the extinction of light through a sample. Extinction can be observed by measuring the observed intensity of light ( $I$ ) through a sample and comparing it with the intensity of the incident light ( $I_0$ ) beam, shown in Figure 2.5. The incident light

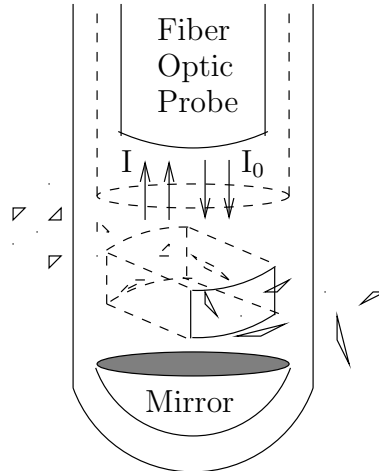


Figure 2.5: *In-situ* transmittance probe.

is projected perpendicular through the sample and the light is scattered by the particles. The measurement requires that only single light scattering occurs. Multiple light scattering occurs when the incident light reflects off more than one particle in the sample. For single light scattering, the Beer-Lambert law relates the ratio of the incident and transmitted light intensities to the PSD by

$$\frac{I}{I_0} = \exp \left( -l \int_0^{\infty} Q(L) f(L, t) A_p(L) dL \right) \quad (2.14)$$

in which the integral term is the slurry turbidity,  $\tau$ ,  $l$  is the light transmission path length,  $f(L, t)$  is the PSD in characteristic length  $L$  at time  $t$ ,  $A_p(L)$  is the projected surface area of a particle of size  $L$ , and  $Q(L)$  is the light extinction efficiency factor. The extinction efficiency factor describes the amount of light that is diffracted due to interference with a particle. For particles that are large compared to the wavelength of the incident light, the efficiency factor is equal to 2, meaning that a large particle removes from the light exactly twice the amount of light it can intercept. This is known as Fraunhofer diffraction provided that the light is scattered in the forward direction. van de Hulst [137] presents a theorem that states the expectation of the projected area of a randomly oriented convex particle is one fourth its surface area. Given that the surface area of a crystal may be written as proportional to the square of its characteristic dimension  $A_p(L) = k_a L^2$ , then the second moment of the PSD can be related to the ratio of the light intensities by

$$\frac{I}{I_0} = \exp\left(-\frac{k_a l}{2} \int_0^\infty L^2 f(L, t) dL\right) \quad (2.15)$$

The measurement is limited to dilute slurries in which single light scattering occurs, with convex particles and does not provide information about crystal habit [137]. However, due to its simplicity, transmittance is still a commonly used measurement for monitoring crystallization. In particular, the technique is sensitive and useful for monitoring nucleation induction times and determining meta-stable zone widths [125].

#### 2.4.5 Photomicroscopy, Particle Vision Measurement (PVM), and Image Analysis

Photomicroscopy views crystals on-line and PVM probes view crystals in-line. Image analysis requires quality images from photomicroscopes and PVM probes that are representative of the PSD. A description of the microscope, digital camera and image analyzing software used in this work are listed in Chapter 3 and more details about image analysis routines for binarizing an image are given by Pons and Vivier [96]. PVM instruments are *in-situ* video microscopes with an internal strobing light source. Instrument diagrams are available at Lasentec's website, [www.lasentec.com](http://www.lasentec.com). Image analysis is a technique that requires no assumptions about particle habit and does not require inversion of a measurement to obtain a PSD. Image analysis is a direct observation technique, however, it is a two dimensional measurement and care must be taken if one is to infer particle habit. Lasentec provides image analysis software for PVM images. The results of image analysis of PVM images are available in Lasentec's PVM brochure, ([www.lasentec.com](http://www.lasentec.com)). Photomicroscope images are similar to PVM images if the sample is not well-prepared for viewing. Typical images from photomicroscopes and PVM can be seen in Chapters 3, 5 and 7. Many particles are not viewed clearly and some blurry objects are incorrectly digitized. Care must be taken with sample preparation for quality image capture for both the PVM probe and photomicroscopes.

Plummer and Kausch [93] crystallize polyoxymethylene under a microscope and capture real-time PSD growth data with image analysis and obtain excellent agreement with differential scanning calorimetry kinetic data. However, the crystallization was carried out on a static hot-stage. Care must be taken with images from in-line techniques. Many sources of error exist: particles may be touching each other or the boundary of view. Microscope lenses can only focus on specified particle size ranges, so some particles will be out of focus potentially resulting in erroneous digitizing by image analysis algorithms. The sampling technique to get the slurry to the field of view may also cause sampling bias.

Sometimes, limited information about crystal habit is obtained from the 2 dimensional projection of the crystal. Bernard-Michel et al. [11] calculate Fourier descriptors of polygons with 3 to 20 edges. Once an image is binarized, each object contour is traced. A polygon consists of a finite number of vertices, with angular directions and arc lengths. The Fourier descriptors are a function of the angular directions and arc lengths. Bernard-Michel et al. [11] calculate the Fourier descriptors for KCl crystals and automatically classify them into groups of circles, squares, rectangles and irregular habits. With these advantages, simple algorithms and readily available hardware, image analysis is clearly the technique of choice for monitoring and controlling particle size and habit in crystallization processes.

Bharati and MacGregor [12] use principal component analysis to extract information such as the frequency of occurrence of specific features in the process or product space from images in real time. A digital image array  $\mathbf{X}$ , or data from a binarized digital array describing characteristics of objects on the array as a function of the number, location and arrangements of pixels can be decomposed into a series of principal components consisting of score matrices  $\mathbf{T}_a$  and loading vectors  $\mathbf{p}_a$  and a residual matrix,  $\mathbf{E}$

$$\mathbf{X} = \sum_{a=1}^r \mathbf{T}_a \mathbf{p}_a + \mathbf{E} \quad (2.16)$$

The principal components are ordered so that the first component describes the greatest amount of variance in  $\mathbf{X}$ , the second the next greatest variance and so on. Pixels in the image  $\mathbf{X}$  are enumerated and significant features are proportional to these enumerated pixel densities.

#### 2.4.6 Attenuated Total Reflection Fourier Transform Infra-Red (ATR FTIR) Spectroscopy for Measuring Meta-Stable Zone Widths and Crystalline Properties

ATR FTIR spectroscopy is a popular technique for *in-situ* monitoring of solute concentration [64, 136, 36]. ATR probes measure the interaction of an evanescent field in a solution phase in contact with an optically denser medium, the crystal. The IR light is propagated into the solution phase due to internal reflection in the solid phase, see Figure 2.6. The interaction of the light with the solution phase can be calibrated with solutions of known concentration. The key advantage of this approach is that the signal is not influenced by the

presence of solids and requires no external sampling devices. Lewiner et al. [64] show that the ATR FTIR probe is capable of detecting the meta-stable zone width. A meta-stable solution is one in which the solution is saturated so there is a driving force for growth, but no driving force for nucleation. The meta-stable zone width is measured by monitoring the concentration as a solution is slowly cooled below the saturation temperature. The probe precisely detects a decrease in concentration as nuclei form soon as the solution is cooled beyond the meta-stable zone. Lewiner et al. [64] also show that ATR FTIR probes can detect polymorphic transitions. ATR FTIR is ranked closely with FBRM and transmittance as being a precise sensor for detecting nucleation induction times.

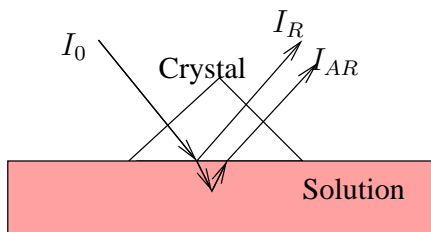


Figure 2.6: Principle of attenuated total reflection Fourier transform infra-red (ATR FTIR) spectroscopy.

## 2.5 Control of Crystallizers

### 2.5.1 Control of Continuous Crystallizers

A review of control of solution crystallization processes by Rawlings et al. [110] discusses the research areas still open in crystallizer control. Continuous crystallizers were created to produce large tonnage products such as fertilizers and foods. To manufacture a product of constant quality it is expected that the crystallizer is operated at steady state. Sometimes, this steady state is unstable and using non model-based feedback control schemes, small disturbances can cause sustained oscillations in the crystal size or product weight percent or other properties. Stability issues due to disturbances and model uncertainties, and multi-variable control are the active areas in research of continuous crystallizers.

Control of unstable oscillatory continuous crystallization processes has been an active area of research over the past two decades. Randolph et al. [104] implemented proportional control of inferred nuclei density by manipulating the particle fines removal rate and determined a satisfactory tuning gain from simulations. A bound for stability on the gain was derived by applying the Routh stability criterion to the characteristic equation for the set of the first three linearized moment equations of the PBE [8]. The best gain for steady-state control was determined from simulations, and is not based directly on an explicit plant model. Redman et al. [112] implement a cascaded PI control scheme on the supersaturation by manipulating the co-saturated feed temperature setpoint while maintaining the crystal-

lizer temperature. The authors assume that the desired PSD properties are the ones at the steady-state operating conditions of a continuous crystallizer and successfully regulate the supersaturation and reject supersaturation disturbances in the feed flow. However, the tuning parameters were not model based and were determined by trial and error. Control of the supersaturation affects the properties of the product PSD and unless the control scheme is model based (i.e. optimal control or MPC), desired properties of the PSD cannot be achieved through control of supersaturation alone.

Eek et al. [24] implemented an optimal state feedback controller based on a quadratic control objective and compare the control strategy with simple proportional feedback control. Simple proportional control was found to be effective at stabilizing a continuous crystallizer by manipulating the fines removal rate. The optimal state feedback control strategy based on the linearized PBE, mass and energy balance process models takes into account dynamic changes in the whole PSD and greatly improves rejection of disturbances by manipulating either the product or fines removal rates. The latter manipulated variable has the advantage that the mass production rate and the slurry void fraction are not affected. The combined estimation and control strategy requires a substantial investment in time to develop models for the process and sensors.

Another control technique for continuous crystallizers is the nonlinear state feedback controller of the general form

$$u = p(\tilde{x}) + Q(\tilde{x})v \quad (2.17)$$

and has been applied by Chiu and Christofides [20] to the PBE reduced to a set of ODEs by the method of weighted residuals. The variables  $p(\tilde{x})$  and  $Q(\tilde{x})$  are functions of the state and  $v$  is the desired reference trajectory. The controller guarantees local exponential stability.

$H_\infty$ -control has been applied to continuous crystallizers by Vollmer and Raisch [142]. The  $H_\infty$ -control performance problem is

$$\|\epsilon w\|_\infty < 1 \quad (2.18)$$

in which  $\epsilon$  is the sensitivity function and  $w$  is a frequency dependent input weight. The controller design by Vollmer and Raisch [141] is based on the linearized PBE model and the resulting infinite dimensional controller transfer function is approximated by an 8th order finite dimensional transfer function. Vollmer and Raisch [141] designed a robust controller that rejects disturbances at low frequencies and is robust to model uncertainties at high frequencies. This work stresses the current state in the field of control of continuous crystallizers. All designed controllers should be subjected to a robustness analysis in which the effect of parameter uncertainty and disturbances on the controller performance and stability are evaluated.

### 2.5.2 Control of Batch Crystallizers

Batch crystallizers are often used in industry for processing small scale quantities or high value specialty chemicals. Batch crystallization has the advantage of being flexible at handling variable volume quantities and is usually simple to operate. During batch cooling crystallization, nucleation and growth processes compete to deplete the solute concentration, so the optimal cooling profile must be one that optimizes the resource (solute) among the population (new crystals and seeds). If a natural exponential cooling rate is used, then the initial high cooling rate of this profile usually produces a large number of nuclei that cannot grow to the desired size because the supersaturation is depleted, making filtration of the product difficult<sup>2</sup>. Mullin and Nývlt [81] derive a theoretical cooling curve for a given crystallization time assuming the nucleation rate is negligible and the growth rate is constant. The resulting profile increases the mean crystal size. Jones and Mullin [54] calculate a cooling profile that maintains supersaturation so that constant nucleation occurs and produces a PSD with a larger mean size and smaller variance than the PSD from natural cooling.

Ajinkya and Ray [3] highlight the need to define the *best* temperature profile that produces a product of the desired quality. The authors suggest a cooling profile that maximizes the average particle size at the end of the batch time and use a model that incorporates nucleation and growth kinetics. Morari [78] determines the analytical solution to the model of Ajinkya and Ray [3] assuming no nucleation so the number of crystals in the final product is equal to the number of seeds initially introduced to the crystallizer.

Jones [53] uses optimal control theory to calculate optimal cooling curves for a seeded batch cooling crystallizer. The predicted optimal cooling policy shows a significant difference from natural, linear or constant nucleation rate cooling profiles. The supersaturation (nucleation rate) is initially decreased then increased passing through a maximum towards the end of the run, before finally being reduced. As the supersaturation increases at the end of the run, high rates of nucleation and growth results, then the supersaturation is decreased to prevent the large numbers of new nuclei to grow significantly. In this way, the amount of solute deposited on the seed crystals is maximized and the extent of nucleation is suppressed. The results were experimentally supported with potassium sulfate solutions. The optimal control policy designed by Jones [53] is only applicable to closed systems of ODEs without constraints. The model used by Jones [53] results from applying the method of moments to the PBE. The optimal control policy is limited to closed systems of ODEs so is applicable to non-continuous systems or systems without fines destruction. The moment equations are not closed for fines destruction or size-dependent growth that is not a linear function in size and so the optimal control policy has limitations. Miller and Rawlings [76] show that the open loop optimal control problem can be stated as an NLP problem. The crystallizer temperature is considered as the manipulated variable and is parameterized as

---

<sup>2</sup>If growth is a higher order than nucleation, large nucleation rates do not occur. For example, the KNO<sub>3</sub>-H<sub>2</sub>O system [75].

piecewise linear over time. Linear constraints are imposed on the temperature variables and nonlinear constraints on the state variables, as well as a final time yield constraint that is imposed to ensure obtaining a minimum yield. The state constraints are imposed by defining a new state variable that is the integral of the squares of the path constraint violations, then the path constraints are satisfied if the terminal value of newly defined state variable is zero. The optimal control problem can then be stated as follows:

$$\begin{aligned}
 & \min_{\{\mathbf{T}\}} && \Phi(\mathbf{T}, \mathbf{x}(t_f); \theta) \\
 & \text{subject to :} && \text{Crystallizer Model} \\
 & && \mathbf{b}_l \leq \mathbf{AT} \leq \mathbf{b}_u \\
 & && \mathbf{h}(\mathbf{x}(t_i)) = \mathbf{0} \quad i = 1, \dots, m \\
 & && \mathbf{g}(\mathbf{x}(t_i)) \geq \mathbf{0} \quad i = 1, \dots, m
 \end{aligned} \tag{NLP1}$$

in which  $t_i$  is one of  $m$  points in time over the run,  $\mathbf{A}$  is a constant matrix with  $n$  columns, and  $\mathbf{T}$  is a vector of temperature values at  $n$  points in time between  $t = 0$  and  $t = t_f$ . The solution to NLP1 compared to natural and linear cooling profiles is shown in Figures 2.7 and 2.8. The temperature profile is initially flat and supersaturation low so growth is favored over nucleation. The seed crystals grow and the total mass of product approaches the required final time mass constraint and the extent of nucleation is minimized. The temperature is decreased (supersaturation increased) near the end to generate nuclei and grow to meet the final time mass constraint.

Matthews and Rawlings [70] apply NLP1 and design an optimal open loop temperature schedule that improves the filtration of final time slurries. The profile minimizes the mass of nucleated crystal relative to seed crystal mass, and was experimentally verified using constant pressure filtration giving a filter cake resistance 25% lower than the best identification experiment. Chung et al. [21] add the seed PSD width and mean as extra decision variables to NLP1 and investigate the effects on the weight mean size, coefficient of variation and mass of nucleated crystal relative to seed crystal mass of the final product. Minimizing the coefficient of variation was found to have adverse effects on the weight mean size and mass of nucleated crystals to mass of seed crystals, because minimizing the coefficient of variation was found to favor nucleation over growth. The results show that the mass of nucleated crystals to the mass of seed crystals is minimized by maximizing the seed mass and minimizing the seed mean size and the width of the seed density. Increasing the seed mass and decreasing the seed mean size increases the seed surface area for growth, thus favoring growth over nucleation. These results are experimentally verified by Bohlin and Rasmussen [15].

The connection between model uncertainty and the optimal open loop cooling profiles is examined by Matthews et al. [69] and Ma et al. [65]. One approach to examine the relationship between the nominal optimal cooling profile and the parameter uncertainty is to find the worst case optimal profile as a function of the parameter uncertainty.

$$\delta \mathbf{u} = N(\theta) - N(\theta^*) \approx \mathbf{L}(\theta - \theta^*) = \mathbf{L}\delta\theta \tag{2.19}$$

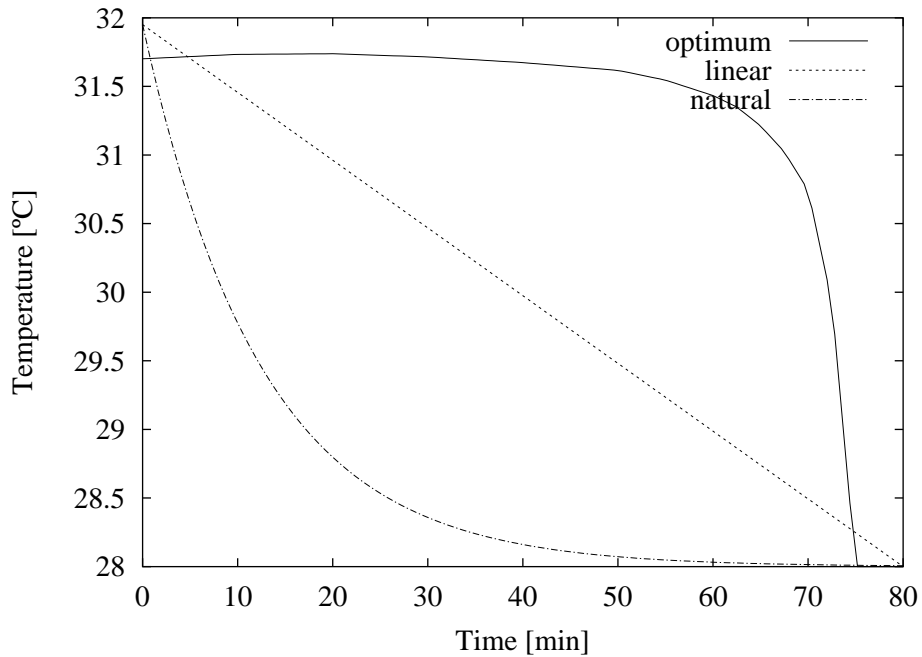


Figure 2.7: Temperature profiles for a batch cooling crystallizer. Cooling policies include natural and linear cooling and cooling to maximize final-time seed size [110].

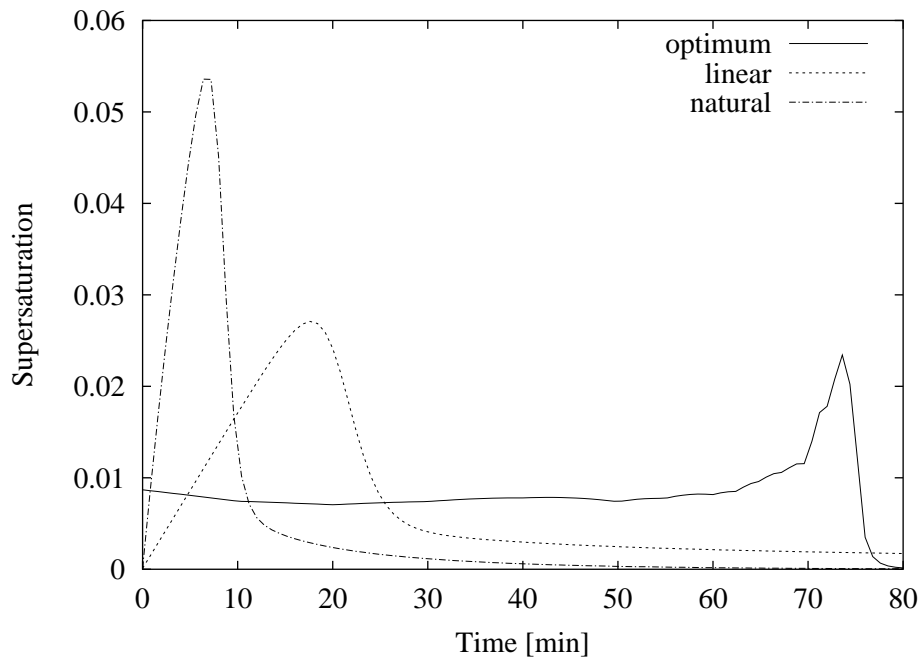


Figure 2.8: Supersaturation profiles for a batch cooling crystallizer corresponding to the temperature profiles in Figure 2.7 [110].

in which  $N$  is a nonlinear operator and  $\mathbf{u}$  is the optimal profile vector of manipulated variables as a function of the parameter vector  $\theta$ .  $\mathbf{L}$  is the first order approximation of  $N$  where the  $ij^{th}$  elements of  $\mathbf{L}$  are the derivatives of the  $i^{th}$  input with respect to the  $j^{th}$  parameter.

$$\delta\theta = \theta^* \pm \left( \frac{\chi_{N_p}^2(\alpha)}{\delta\theta_{\text{worst}}^T \delta \mathbf{V}_\theta^{-1} \delta\theta_{\text{worst}}} \right)^{1/2} \delta\theta_{\text{worst}} \quad (2.20)$$

Matthews et al. [69] find the sensitivity analysis for a  $\text{KNO}_3\text{-H}_2\text{O}$  system suggests that for tight confidence intervals, the parameter uncertainty does not influence the optimal control policy. However, the parameter uncertainty for an industrial photochemical-heptane system in which the nucleation and growth orders were found to be close in value influenced the optimal profile. A deviation in which the difference between the nucleation and growth orders is opposite in sign to the nominal difference produces an optimal profile that is a departure from the nominal profile. Also, the final time values for  $m_n/m_s$  for a four and five parameter model is found to be dissimilar and castes doubt on the estimation technique to accurately determine the kinetic parameters for this industrial system. The problem can be attributed to an incorrect model, though the sensor measurements (transmittance and concentration) are more likely to blame because they only provide information regarding the second and third moments of the PSD. Ma et al. [65] examine the robustness of the optimal control trajectory and the predicted performance to model uncertainty and control implementation uncertainty. Their simulations agree with experimental studies by Miller and Rawlings [76] and Bohlin and Rasmussen [15], showing that the nucleated mass to seed mass ratio is most sensitive to  $0.1^\circ\text{C}$  variations in the crystallizer temperature.

Rohani et al. [116] develop a PI feedback control scheme for control of the PSD during batch crystallization of a potash alum-water system based on an indirect measurement of the fines PSD and manipulating a fines dissolution flowrate. Although the control scheme is not optimal, the method was considered adequate provided the fines dissolution flowrate is high. Low fines dissolution flowrates cause regions of high supersaturation where the solution is returned to the crystallizer. Regions of high supersaturation causes excessive nucleation and produces a large amount of undesirable fines in the PSD. Rohani et al. [116] considered the method easy to implement due to low computational costs, but computational capabilities are rapidly improving today and so more advanced model based control algorithms can be implemented.

Farrell and Tsai [26] define a single-input-single-output model relating solubility (hence solution temperature) to the weight mean size based on the chord length FBRM sensor. They use a batch generic model control (GMC) algorithm so that the process output approaches its desired value of  $y^*$  along a reference trajectory  $r^*$ . The reference trajectory is designed for a slightly over-damped second order response that avoids overshoot resulting in crystal dissolution, though still contains integral action for offset free control. The controller is applied to batch crystallization of potassium sulfate and is successful at achieving the desired weight mean crystal size. However, the authors naively claim that

rigorous modeling of the process and sensor with regard to the PBE is not a prerequisite for model based control. More than one property of the product PSD must be controlled to begin to address the common problems in industrial crystallization.

## 2.6 Future Outlook

Many problems still exist in industrial crystallization, in particular with application to the pharmaceutical industry. Techniques for using X-ray diffraction to identify on-line the presence of the desired polymorphic structure in a crystallization process are currently under investigation by Roberts [124] and coworkers. Techniques for using Raman spectroscopy are being developed by Mettler Co. for monitoring on-line solution structure prior to nucleation. Lasentec's PVM probe is in its infancy and most PVM images are out-of-focus and contain unclassifiable particles. However, X-ray diffraction, Raman spectroscopy and the PVM probe generate a wealth of data, which are mostly unused today. The field of crystallization now needs to develop techniques for reducing the size of these data sets into predominantly informative data. The field also needs to develop new models to accurately and precisely describe the phenomena these probes are now detecting. For example, nucleation behavior that is governed by Brownian dynamics, apparent growth rate dispersion, and the non-equilibrium habit of crystals.

## Chapter 3

# Experimental Apparatus

*Time to go out in a blaze of sour grapes!*

— Odelson, B. J.

This chapter describes the experimental apparatus used for the pharmaceutical crystallization and sodium chlorate crystallizations, and the pilot plant apparatus used for scraped-surface crystallization of para-xylene. The pharmaceutical, para-xylene and sodium chlorate chemical systems are briefly described. A description on the monitoring and control hardware is also given. Finally an outline of the operating procedure for the pharmaceutical and sodium chlorate crystallization experiments is described.

### 3.1 Introduction

The crystallization apparatus used in this study is similar to the apparatus used by Witkowski [146], Miller [75] and Matthews [68]. Witkowski [146] first used the apparatus with concentration and crystal slurry light scattering characteristics to identify naphthalene crystallization kinetics in toluene. Miller [75] later used the apparatus to identify potassium nitrate crystallization kinetics in water. Finally, Matthews [68] used the apparatus to identify the crystallization kinetics of an industrially relevant photochemical in heptane. One common goal of all these studies was to determine the extent particulate system modeling techniques may be used to describe the behavior of these systems and optimize their performance within physical constraints.

In this study, the monitoring, modeling and control aspects of the crystallization apparatus are all improved. A new data acquisition and particle size and shape sensor is installed that provides real-time measurements of individual characteristic lengths. New models are developed to describe high crystal growth-rate behavior and growth-rate dispersion that is not observed in previous studies. Model-predictive control is used for precise temperature control of the apparatus and replaces the quadratic dynamic matrix controller (QDMC), developed by García and Morshedi [28] that is used in the previous studies.

## 3.2 Crystallizer Apparatus

### 3.2.1 Laboratory

The sodium chlorate and pharmaceutical crystallization experiments are carried out in a 3 L, flat bottomed, jacketed, glass vessel (Applikon), see Figure 3.1. In the sodium chlorate crystallization experiments, the volume is 2.2 L. In the pharmaceutical crystallization experiments, the volume is 2.25 L. During the experiments, the vessel is insulated with foam to prevent any heat losses to the environment or any temperature disturbances to the crystallizer.

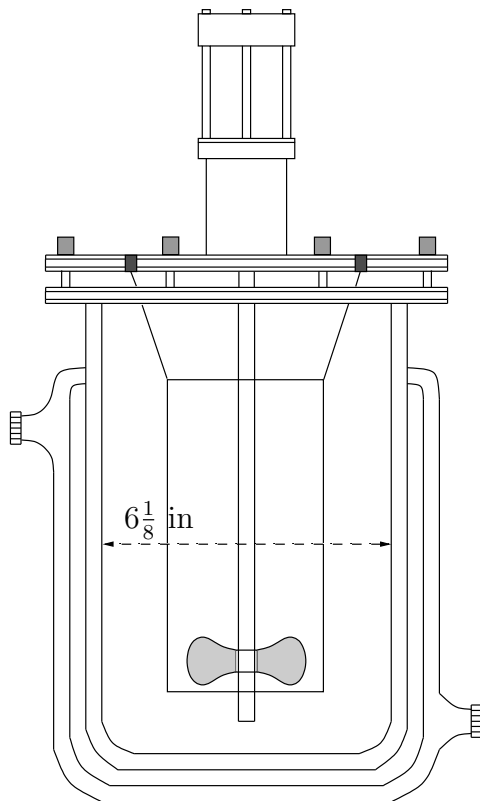


Figure 3.1: Crystallizer vessel, headplate, impeller, and draft tube [68].

A stainless steel headplate which supports the drive unit, coupling and sealed impeller shaft sits on the top of the crystallizer. The headplate is then fixed to the vessel and forms a seal with the vessel lip preventing any evaporation from the system. The headplate has six 18 mm sample port holes which are closed with screw caps. The headplate also has four 8 mm and three 6 mm sealable holes. The transmittance probe is fixed into one of the 18 mm sample port holes. Slurry samples are manually withdrawn and seed crystals and impurity loadings are manually injected via a pipette through the 18 mm sample port holes. The densitometer exit and return streams, and crystallizer temperature probe pass

through the 6 mm ports. The headplate supports a 5 in. diameter stainless steel draft tube which improves mixing within the vessel.

A marine type propeller is supported on the impeller shaft. The propeller is fixed so that the process fluid is driven down the inside of the draft tube and the process fluid then passes up the walls of the vessel. A removable DC current impeller motor drives the coupling that is connected to the impeller shaft through the headplate. The motor is controlled by an external controller (Applikon, ADI 1012) that can control speeds from 0 to 1250 RPM. The impeller speeds for these experiments are 400 RPM.

### 3.2.2 Pilot Plant

The para-xylene experiments are carried out in a pilot plant, 10 gal., nickel-chromium, scraped-surface crystallizer (SSC) shown in Figure 3.2. The SSC has a width to height ratio of 0.25. Scraper blades are mounted on a central shaft and are pressed against the crystallizer's wall. The shaft rotates at a constant speed of 12 RPM.

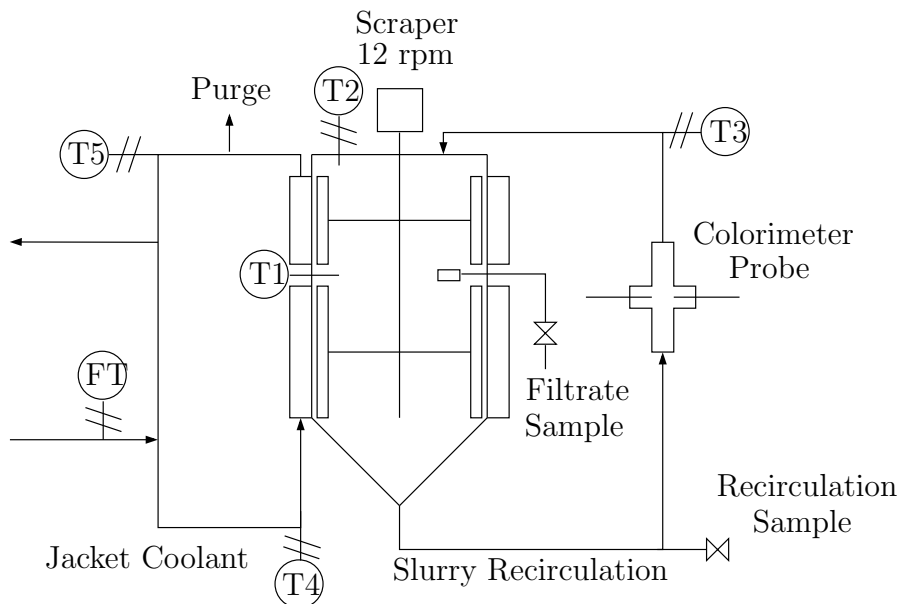


Figure 3.2: Pilot plant para-xylene crystallization process.

An alcohol-water coolant mixture passes through the jacket of the crystallizer and has a freezing point below 193 K. A spiral partition wall is inserted in the jacket in order to keep a large flowing speed through the jacket for better heat transfer. Fresh coolant is mixed with part of the outlet jacket stream before returning to the jacket of the crystallizer. Excess coolant is purged from the jacket circuit at the outlet of the jacket. The fresh coolant flow rate coming from the coolant supply is measured and controlled by a Prowirl 70 vortex flow meter and microprocessor. The crystallizer and piping are thermally insulated. A transmittance measurement is provided by an *in-situ* colorimeter probe (Brinkman) that

is mounted in the slurry recirculation loop. The incident light from the transmitting light fiber on one side of the tube is projected perpendicular through the flowing slurry. The receiving light fiber (opposite the incident light beam) takes the transmitted light beam and sends it to the colorimeter. The distance the light beam travels through the slurry is 2 mm. Temperature measurement is provided by *in-situ* resistance temperature detectors (RTD) installed in the middle (T1) and top (T2) of the crystallizer, the slurry recirculation loop (T3), the inlet (T4) and outlet (T5) jacket temperatures.

The fresh coolant is injected into the jacket circuit at an absolute temperature of approximately 193 K. The absolute temperature of the coolant exit stream is approximately 201 K. The middle temperature, T1, inside the crystallizer is controlled by a cascade controller. The master controller uses T1 as a measurement and changes the set point for the inlet coolant temperature to the slave controller. The slave controller uses the inlet jacket temperature as a measurement and manipulates the fresh coolant flowrate coming from a chiller to the jacket circuit.

For safety reasons and to avoid any oxidation of the xylene mixture, an inert nitrogen gas blanket is provided inside the crystallizer and the feed tank. The para-xylene concentrations are measured using gas chromatography (GC). The samples are drawn off through a sampling tube extending through the wall of the crystallizer. A micro-metallic filter is welded to the tube on the inner side of the crystallizer to avoid intake of the solid crystals with mother liquor. A hand pump is attached to the other side where the samples are collected. Samples are taken at the start and at different times during the experiments.

All the experiments are done in batch mode in which 38.6 kg of the xylene mixture is introduced to the crystallizer at the beginning of the crystallization run. The crystallizer is cooled down to 3 K above the saturation temperature and cooled at a rate of  $0.11 \text{ K} \cdot \text{min}^{-1}$  ( $0.2 \text{ }^{\circ}\text{F} \cdot \text{min}^{-1}$ ). All the temperatures and the transmittance measurements are recorded and sent to a main computer with a sampling time of 10 sec.

### 3.3 Chemical Systems

Three chemical systems are used in this study: an industrial pharmaceutical, para-xylene and sodium chlorate. For proprietary reasons, the chemical formula and molecular structure of the pharmaceutical are not given and is referred to as an *industrial pharmaceutical*.

#### 3.3.1 Industrial Pharmaceutical

The pharmaceutical in iso-propyl alcohol (IPA) and water (93/7 vol.%) system used in this study is a bench-scale version of a crystallization performed at GlaxoSmithKline in its R&D facilities in King of Prussia, Pennsylvania. The system is chosen because it has economic relevance to the pharmaceutical industry. Improvements in crystallization with the pharmaceutical has direct influence on the processing stages at the manufacturing facilities. Some previously known features this chemical system possesses are as follows:

- The system is polymorphic.
- The particular polymorph in this study exhibits a parallelepiped habit.
- Solubility as a function of temperature data for this polymorph are available and are given in Appendix B.
- The system does not exhibit secondary nucleation in the metastable zone,  $S$  (super-saturation)  $\leq 0.2$  for the temperature range between 20°C to 75°C.

After post-crystallization steps, the protocol for the pharmaceutical requires a size range of crystals between 20-200  $\mu\text{m}$ . Crystals outside of the size range of 20-200  $\mu\text{m}$  do not have the required stability or bioavailability.

### 3.3.2 Para-xylene

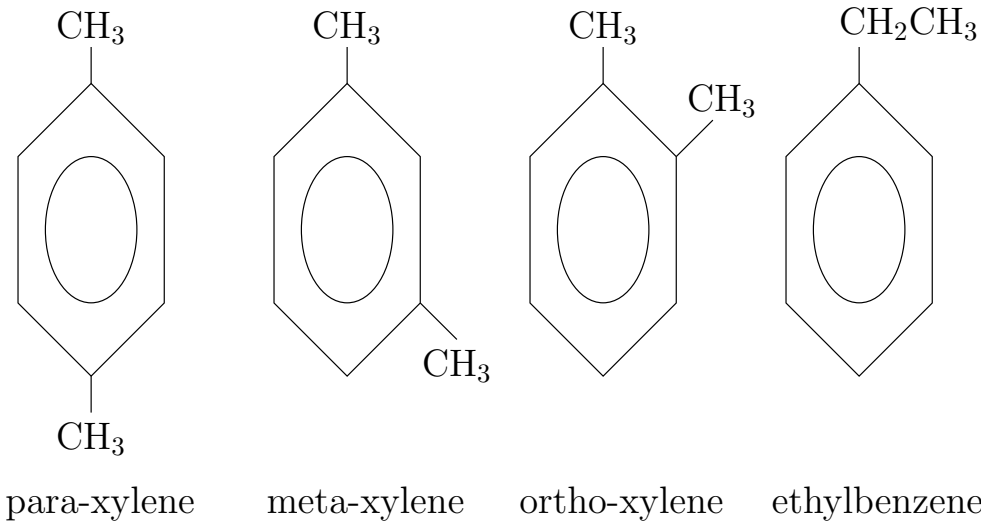


Figure 3.3: Xylene mixture.

The para-xylene crystallization experiments are carried out using a feed stock that has an approximate composition of 25 wt% para-xylene, 45 wt% meta-xylene, 18 wt% ortho-xylene, 8 wt% ethylbenzene and 4 wt% other hydrocarbons. The chemical structures are shown in Figure 3.3. This feed stock has a saturation temperature of approximately 238 K (the temperature at which the crystals are first formed). Toluene concentration is kept at less than 0.7 wt% for final product purity requirements [22]. Molecular sieves are used to reduce the water content in the feed stock to less than 200 ppm. Some previously known features this chemical system possesses are as follows:

- For the temperature ranges 230-240 K, it can be assumed that the xylene mixture behaves as an ideal solution and the crystallized phase is pure para-xylene.
- The solubility of para-xylene is known and given by Equation B.3 in Appendix B.

### 3.3.3 Sodium Chlorate

The semi-batch crystallization of sodium chlorate ( $\text{NaClO}_3$ ) in water system is a proto-typical system for demonstrating on-line shape measurement and control. Sodium dithionite ( $\text{Na}_2\text{S}_2\text{O}_6$ ) is a habit modifier for sodium chlorate crystallization. In pure solution, sodium chlorate crystallizes with a cubic habit and in the presence of 50 ppm sodium dithionite, sodium chlorate crystallizes with a tetrahedral habit. During semi-batch crystallization, sodium dithionite habit modifier-free sodium chlorate solution is feed to the bench-scale reactor and a solids-free solution is removed at equal rates and a low flowrate sodium dithionite stream is fed to the crystallizer. Both the habit modifier and pure sodium chlorate streams act as manipulated variables or disturbances in a proto-typical shape control problem. Some previously known features this chemical system possesses are as follows:

- Sodium chlorate has two predominant habits: cubic when grown in pure solutions and tetrahedral when grown in solutions with at least 50 ppm sodium dithionite.
- Segregation coefficients for  $\text{Na}_2\text{S}_2\text{O}_6$  impurity incorporation and  $\text{NaClO}_3$  solubility IN  $\text{H}_2\text{O}$  data are known and given in Appendix B.

## 3.4 State Measurements

For batch cooling crystallization, the states of interest are the solution temperature and concentration, slurry transmittance and the particle size density (PSD). The solution temperature and concentration provide information about the solution phase and the slurry transmittance and PSD provide information about the dispersed solid phase. Unfortunately, in this study, we cannot measure the PSD explicitly, instead we can only measure some of the PSD properties. Such properties include the mean crystal size and the PSD standard deviation, provided via video microscopy and image analysis. The second moment of the PSD is provided via transmittance.

### 3.4.1 Temperature

Temperature readings for the sodium chlorate and pharmaceutical crystallization experiments are provided via resistance temperature detectors (RTD). Temperatures for the slurry temperature, inlet and outlet jacket temperatures, and densitometer return stream are recorded every second by the data acquisition system.

### 3.4.2 Concentration

Concentration readings for the pharmaceutical crystallization experiments are provided via densitometry. Although *in-situ* ATR FTIR probes are well-used for in-line concentration measurements (see Chapter 2, Section 2.4.6), on-line densitometry is a valid technique

Baud rate	1200
Parity	Even
Data bits	7
Stop bits	2
Bytes read	75
Time limit	1 min

Table 3.1: Serial port parameters for densitometer through COM 0 port.

for measuring solution concentration. In densitometry, solution density is correlated with solutions of known concentration.

In this study, concentration is measured using a u-tube densitometer (Anton Paar, Model DPR 412 YE). The densitometer consists of a 2 mm flow through tube with a platinum 100 RTD temperature measurement in the sample cell and a serial interface (Anton Paar, model DPR-S). The serial interface connects directly to the RS232 serial COM 0 port of the PC. The serial port parameters are given in Table 3.1.

The solids-free stream is removed from the crystallizer through a  $0.5 \mu\text{m}$  filter tube and passes to the densitometer u-tube via a peristaltic pump (Masterflex, Model 7523-00). The 8 mm ID filter tube is inserted through a sample port in the headplate of the crystallizer and the filter is placed next to the impeller to prevent encrustation of solids on the filter. The high fluid velocity near the impeller and low flowrate through the densitometer flow lines ensure no solids deposit on the face of the filter as the solids-free solution is removed from the crystallizer. The flow lines to and from the crystallizer are wrapped in heat tape (Thermolyne) and kept at  $65^\circ\text{C}$  to prevent crystallization in the flow lines. A Haake water bath provides water to the sample cell heat exchanger maintaining the temperature of the cell near to the crystallizer temperature.

The solution density is correlated with the period of oscillation of the u-tube as the solution passes through the cell at  $30 \text{ mL}\cdot\text{min}^{-1}$ . The serial interface records a T-value and a cell temperature. Examples of T-values as a function of cell temperature for solutions of known concentration are given in Figures 3.4 and 3.5. Once a T-value and cell temperature are recorded, a linear interpolation routine is applied to find the solution concentration. First, for the given temperature, a T-value is determined by linear interpolation for each concentration line. Given the actual T-value, a concentration value is linearly interpolated for the interpolated T-values.

T-values and cell temperatures are recorded every 10-20 sec. The densitometer can accurately measure the solution concentration to within  $\pm 5 \times 10^{-4} \text{ g}\cdot\text{g}^{-1}$ . The densitometer T-values drift and calibrations must be done regularly.

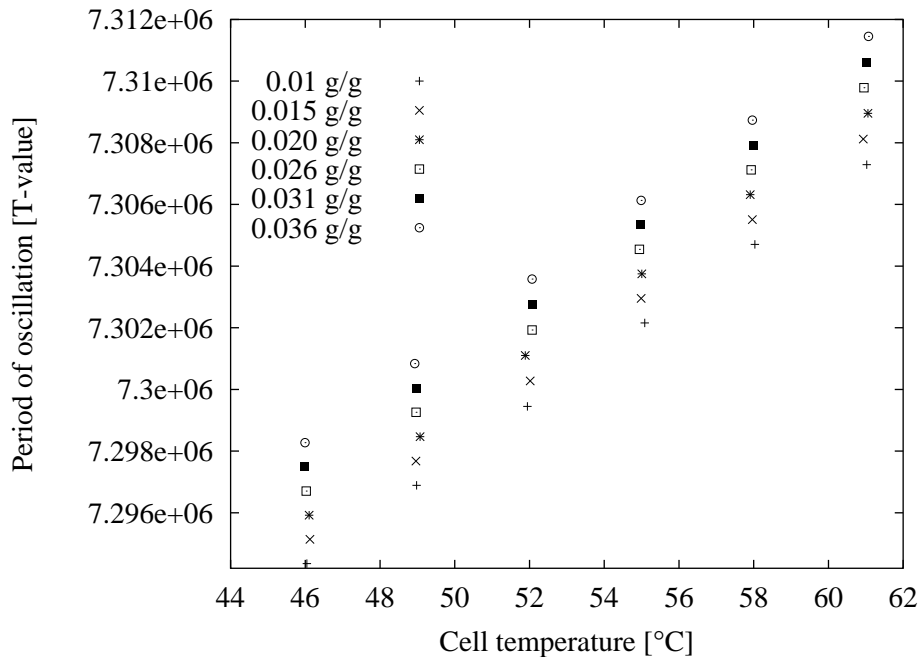


Figure 3.4: Densitometer calibration data collected from six reference solutions of known concentration.

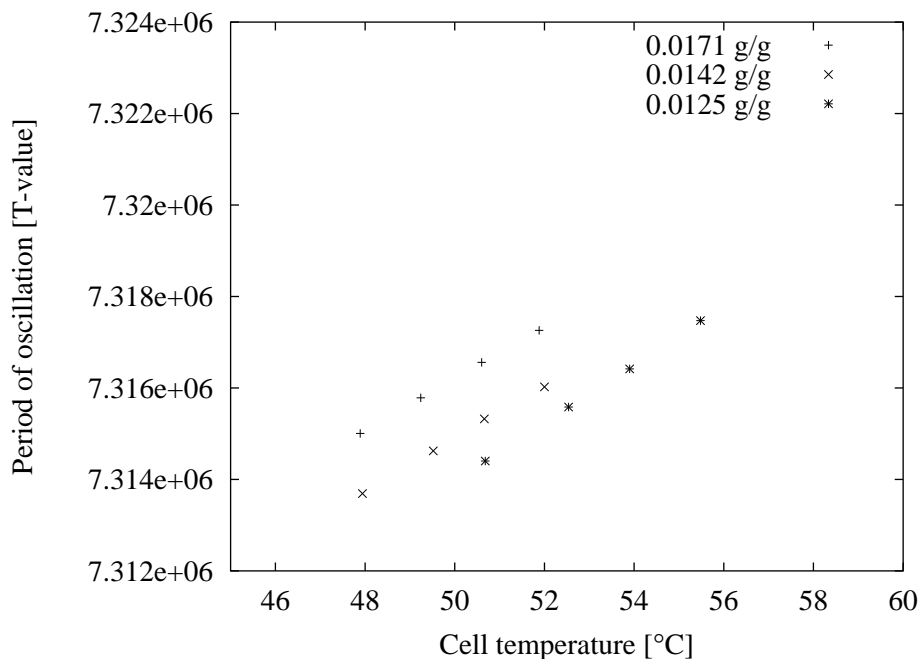


Figure 3.5: Densitometer calibration data collected from three reference solutions of known concentration.

### 3.4.3 Transmittance

The relationship between the PSD and transmittance is given by Equation 2.15 in Section 2.4.4. The measurement is restricted to dilute slurries. According to van de Hulst [137], dilute slurries are ones in which the optical depth (given by the product of the beam length and the integral term in Equation 2.14), is less than 0.1. When correcting for double scattering, the optical depth for which Equation 2.15 is still valid is 0.3. Using Equation 2.14, transmittance readings as low as 90% may be used for inferring the second moment of the PSD for single scattering and transmittance readings as low as 74% for double scattering. In the para-xylene study we have few transmittance readings because data is collected every 10 sec and the system has a large growth rate. We find it is beneficial to use as many data points as possible and use transmittance readings as low as 74 % in parameter estimation. For the pharmaceutical crystallization, we use transmittance readings as low as 80 %.

Figure 3.6 shows the colorimeter and transmittance probe. The colorimeter uses an *in-situ* probe that is inserted through an 18 mm port in the headplate of the crystallizer. The probe consists of a 30 in. bundle of optic fibers that runs from the colorimeter to the probe tip. One half of the fibers transmits light and the other half receives light. The probe tip is inserted into a glass sleeve. At the end of the enclosed probe tip, the glass sleeve has a 1 mm gap and silver mirror. The glass sleeve is held onto the end of the colorimeter probe by rubber fastenings attached to glass hooks. The colorimeter probe is completely enclosed so it does not come into contact with the process fluid. The slurry passes through the gap. Transmitted light passes through the slurry and is reflected back by the mirror. The effective path length is 2 mm.

The colorimeter has an analog output that sends a 0 to 10 V signal to a 5B31 isolated analog input module (National Instruments) on the 5B series backplane. Data points are recorded every second.

### 3.4.4 Crystal Size, Standard Deviation and Shape

A stream from the crystallizer is pumped continuously from the crystallizer, passes through the glass flowcell shown in Figure 3.7 at  $50 \text{ mL}\cdot\text{min}^{-1}$  and then returns to the crystallizer. The total volume of the loop is approximately 20 mL. The flow is automatically stopped by sending a 0 V signal to the pump via a 5B39 isolated analog output module (National Instruments) on the 5B series backplane. An image of the settled crystals in the flow cell is automatically captured 10 sec after the flow is stopped. After image capture, the flow is restarted by sending a 2 V signal to the pump and the slurry returns to the reactor.

The timing between stopping the flow, image capture and re-starting the flow is provided via dynamic data exchange (DDE) between the imaging software, Image Pro Plus macro language (Media Cybernetics) and the main data acquisition software written in LabVIEW (National Instruments). The Image Pro Plus macro language sends a flag to LabVIEW (via Excel) 10 sec before image capture and analysis. LabVIEW receives the flag and sends a 0 V signal to stop flow. Once the image is captured and analyzed,

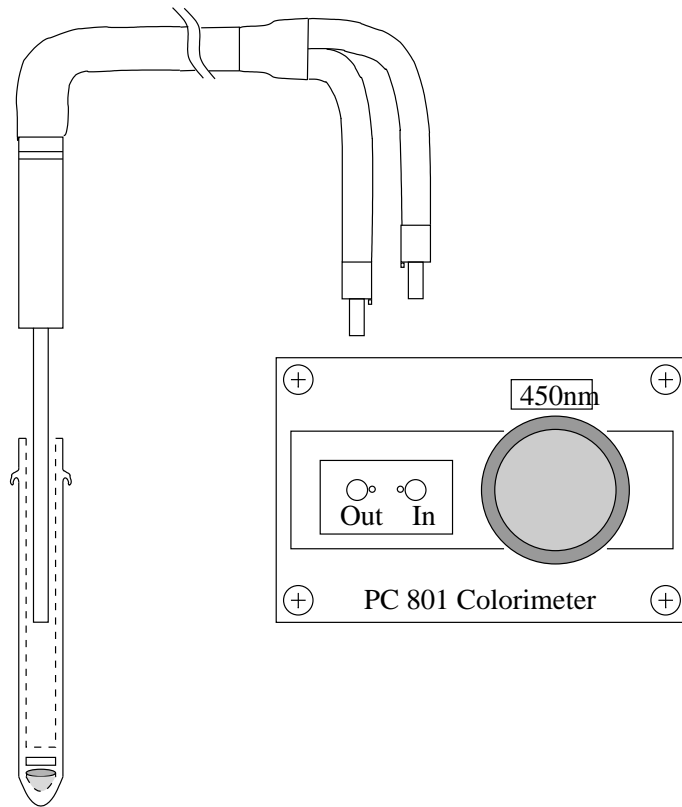


Figure 3.6: Colorimeter, transmittance probe, and glass sleeve [68].

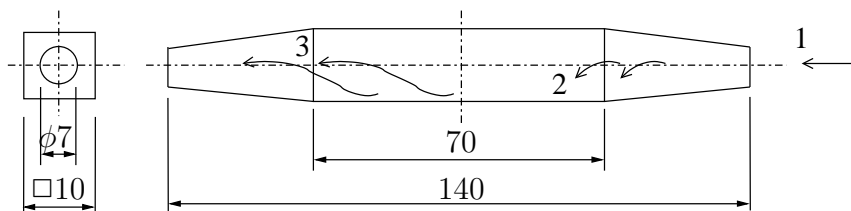


Figure 3.7: Glass flowcell for photo-microscopy. Circular to rectangular to circular duct. Not drawn to scale. All dimensions in mm. 1. Slurry enters cell. 2. The flow stops and crystals settle. 3. The flow is re-started and the slurry leaves the cell.

Image Pro Plus sends another flag to LabVIEW and the flow is restarted. The complete process, particles settling, image capture and image analysis takes 20-30 sec depending on the number of objects in the image. Image capture and analysis can be repeated as often as every 20-30 sec or any other time greater than 30 s specified by the operator.

An Olympus BX60 microscope with 4X magnification, a Hitachi HV-C20 charged coupled device (CCD) camera with 2X magnification (combined 8X magnification) and a PC with frame grabber are used to capture color images of  $585 \times 700$  pixels with 256 grayness levels. Each pixel is represented by a color in the Red, Blue, and Green (RGB) color model. The RGB color model is the standard way to mathematically represent color. A color is expressed in terms that define the amount of red, green and blue. Pure red is expressed as 255/000/000, in which 255 is the highest level of red light possible, untainted by any green or blue light. For the sodium chlorate system, a RGB threshold of 000/084/002 is applied. The RGB threshold is then converted to a 0 to 255 gray scale threshold. The color image is then converted to a gray scale image. Each pixel in the image is converted to one of two colors, black and white, depending on whether the pixel is darker or lighter than the threshold. Black represents objects in the image and white represents the background.

Objects that are in contact with the border are eliminated and objects that have holes are filled. Two clustered objects are automatically separated if their intersection can be identified by two concave points. If the resulting split results in convex objects, then the split is considered, otherwise the object remains un-split. The particles are then sized according to a pixel calibration with a stage micrometer. The minimum object diameter is defined as the minimum chord length that connects two points on the object boundary passes through the objects centroid. Similarly, the maximum object diameter. The average object diameter, defined as the mean of 180 chords, at angles of  $2^\circ$ , passing through the object's centroid. Object shape is measured using a variety of measurements. The aspect ratio used in this study is defined as the ratio of the maximum and minimum object diameters. The object boxed area is defined as the ratio of the projected area of the object to the minimum area of a bounding box around the object. The object roundness, that describes how close the object resembles a circle is defined as the ratio of the square of the object perimeter to  $4\pi$  times the object's projected area. A square has a roundness of approximately 1.27 and an equilateral triangle has a value of approximately 1.65. As the number of sides of an object increases, the roundness value tends towards unity.

Figure 3.8 shows the standard reference material NIST1017b (National Institute of Standards and Technology, NIST) before and after thresholding. Figure 3.9 shows automatic sampling for this system with a size range between  $100\text{-}400 \mu\text{m}$  and 0.31 % solids is adequate. Once 5 images are captured and analyzed (approximately 2.5 min), the particle size sensor can accurately measure the mean size of the standard reference material to  $\pm 5 \mu\text{m}$  of the mean size measured by NIST. After 10 images (approximately 5 min), the sensor has a reasonably smooth prediction of the particle size distribution, shown in Figure 3.9. The factors that will influence this particular sensor's speed to accurately measure the particle size distribution are the percent of solids in the system and the size range. The flow loop and

flow cell geometry influences the particle sample size to the viewing area of the microscope. Consequently, the particle size and shape sensor cannot measure the particle size density on a volume basis.

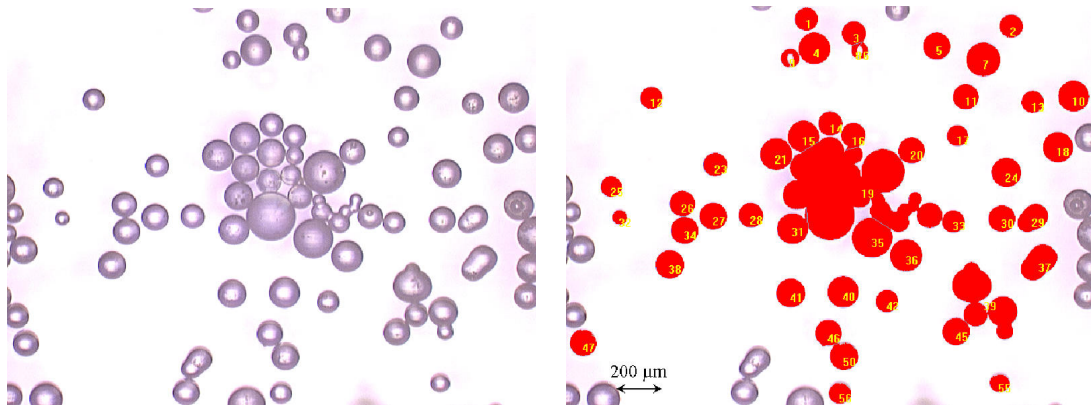


Figure 3.8: Standard reference material NIST1017b in the flowcell in Figure 3.7 once particles settle (left). Results from digital image analysis (right).

Figure 3.10 shows for particles between the range of 200-900  $\mu\text{m}$  and 0.31 % solids, the sensor requires more than 10 images to obtain a smooth particle size distribution. However, after 5 images, the sensor can accurately measure the mean size within  $\pm 10 \mu\text{m}$  of the mean size measured by NIST.

Figure 3.11 shows for particles between the range of 40-180  $\mu\text{m}$  and 0.08 % solids, the sensor requires at most 5 images to obtain a smooth particle size distribution. However, the distribution does not converge to the distribution measured by NIST, though the sensor captures trimodal characteristics similar to those measured by NIST.

Figure 3.12 shows a mixture of two standard reference materials, NIST1018b and NIST1004a. At first, 4.0 g of NIST1018b is added to 1300.0 g water (0.31 % solids) and 50 images are collected during a 40.6 min period. After the 40.6 min period, 0.5 g of NIST1004a is added to the system and another 50 images are captured and digitized. Figure 3.13 shows the cumulative particle size distribution as a function of time. For the solids concentration used in this study, the sensor converges to the new bimodal distribution after 20 images. Figure 3.13 shows that the sensor can detect transient changes in the particle size distribution and converges to a distribution given 10-20 images.

### 3.5 Data Acquisition and Control

Data from the various measurement types described in the previous sections are received via the data acquisition system. Voltage signals are sent to the control valve and size and shape sensor flow line via the signal conditioning system. In addition, the PC archives the

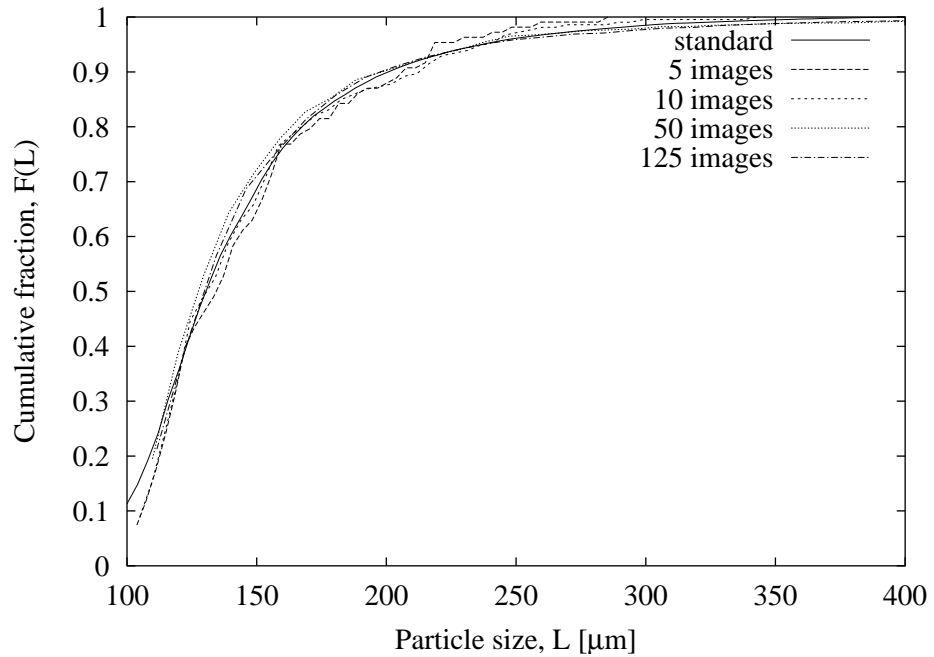


Figure 3.9: Cumulative particle size distribution for the standard reference material NIST1017b in Figure 3.8 after 5, 10, 50 and 125 images are collected compared with NIST's measurement.

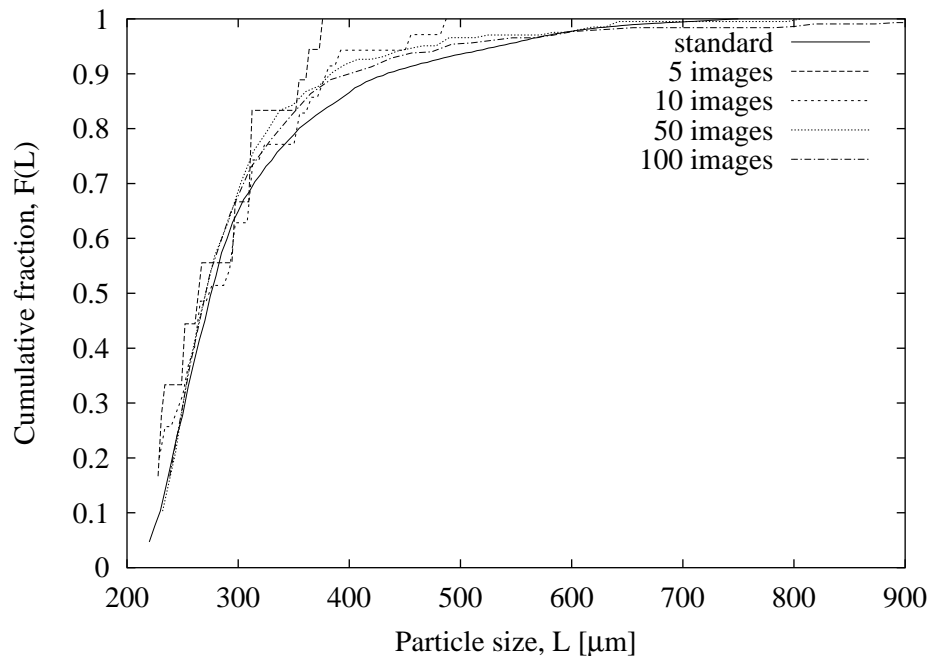


Figure 3.10: Cumulative particle size distribution for the standard reference material NIST1018b after 5, 10, 50 and 100 images are collected compared with NIST's measurement.

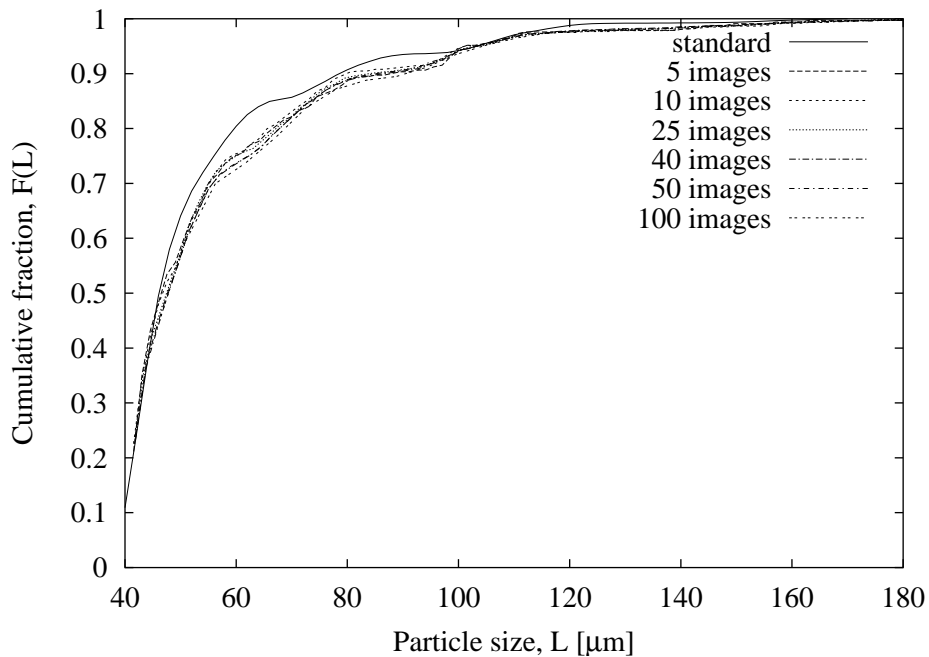


Figure 3.11: Cumulative particle size distribution for the standard reference material NIST1004a after 5, 10, 25, 40, 50 and 100 images are collected compared with NIST's measurement.

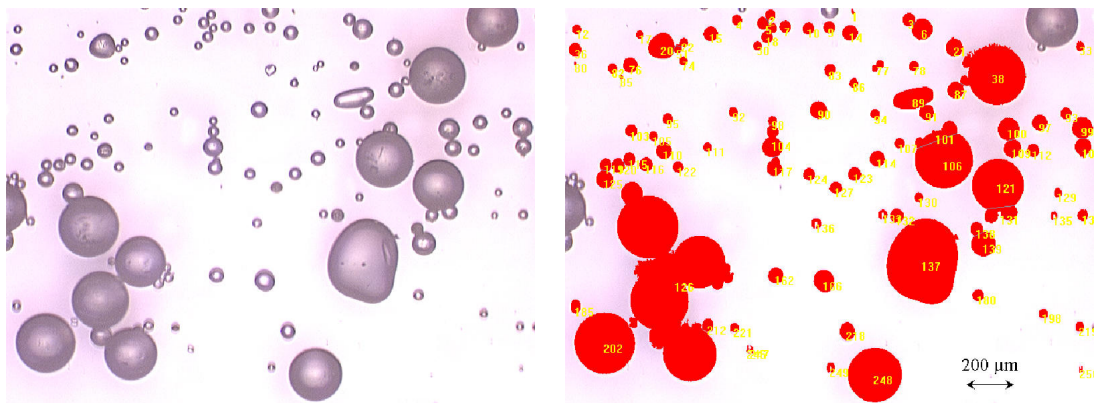


Figure 3.12: Standard reference materials NIST1018b and NIST1004a.

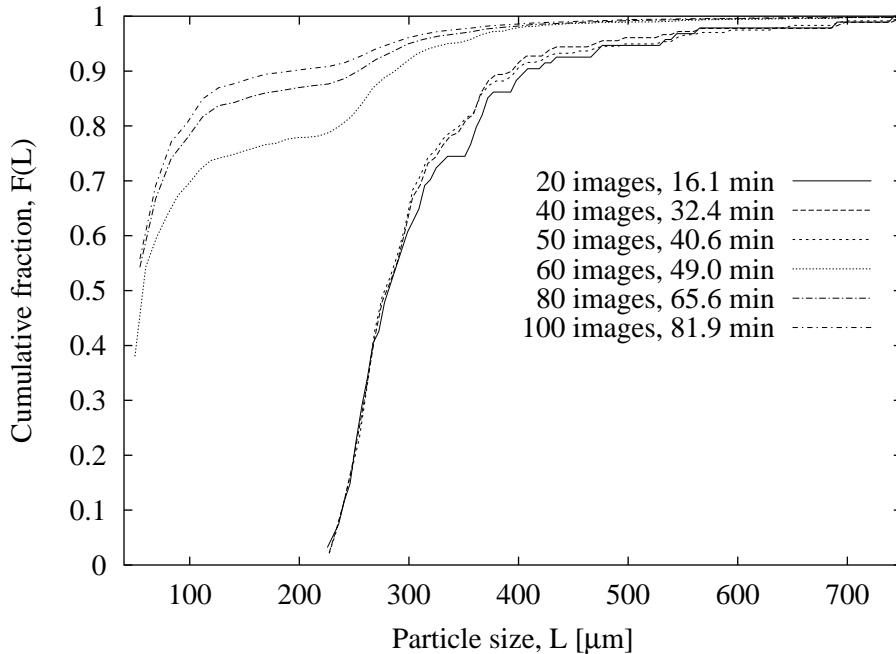


Figure 3.13: Cumulative particle size distribution for a mix of standard reference materials NIST1018b and NIST1004a in Figure 3.12 after 20, 40, 50, 60, 80 and 100 images are collected.

measurements, sends the signals after making control calculations, performs image analysis, and presents all data graphically on-line. This section describes the data acquisition software and signal conditioning hardware in more detail.

### 3.5.1 PC

A Hewlett Packard Vectra Pentium 200 MHz PC using the Windows 95 operating system is used to monitor and control the lab crystallization experiments. The data acquisition and control program is written in the LabVIEW G programming language. The G programming language has drivers that establish communication with the PCI-1200 board and RS232 serial port. The G programming language also has drivers that establish communication with Image-Pro Plus and allows dynamic data exchange between the two applications. The G programming language performs mathematical and linear algebra operations. The mathematical operations are used for sensor calibrations, the PID velocity algorithm calculations for the slave loop of the temperature controller, and the crystal habit controller. The target calculation and state estimation routine described in Appendix A are also performed using G. The LabVIEW environment archives the data, graphically presents on-line data to the screen, and allows the user to change controller parameters and setpoints on-line during the experiment.

### 3.5.2 Signal Conditioning System

The 5B series (National Instruments) backplane consists of digitizing input/output modules. The analog input modules digitize inputs from the RTD and colorimeter sources. The analog output modules send current outputs to the control valve and microscope crystal slurry sample pump. The 5B series modules and backplane communicate via a signal conditioning SC-2053 cable adaptor (National Instruments) to a PCI-1200 board that allows the PC to receive and send signals to the backplane with a maximum sampling rate of 100 kHz. The 5B series backplane allows a maximum of 8 analog input signals, 2 analog output signals and 6 digital input signals. The digital input options are not used in this study. Each module is plugged into the backplane. The RTD, colorimeter, control valve, and pump wires are wired into ports at the base of the connection point of the respective module in the backplane.

The 5B34 isolated RTD input module (National Instruments) receives a 4-20 mA signal from 100  $\Omega$  platinum 2, 3 or 4-wire RTDs operating over a range of 0-100°C and converts to a 0-5 V signal to be read by the PCI-1200 card. The 5B31 isolated voltage input module (National Instruments) receives a 0-10 V signal from the colorimeter and relays the same signal in the same voltage range to the PCI-1200 card. The 5B39 isolated output module (National Instruments) receives a 0-10 V signal from the PCI-1200 card and sends a 4-20 mA from the 5B series backplane to the microscope crystal slurry pump and control valve.

## 3.6 Operating Procedures

Figure 3.14 shows a schematic layout of the cooling and heating system for the bench-scale crystallization apparatus.

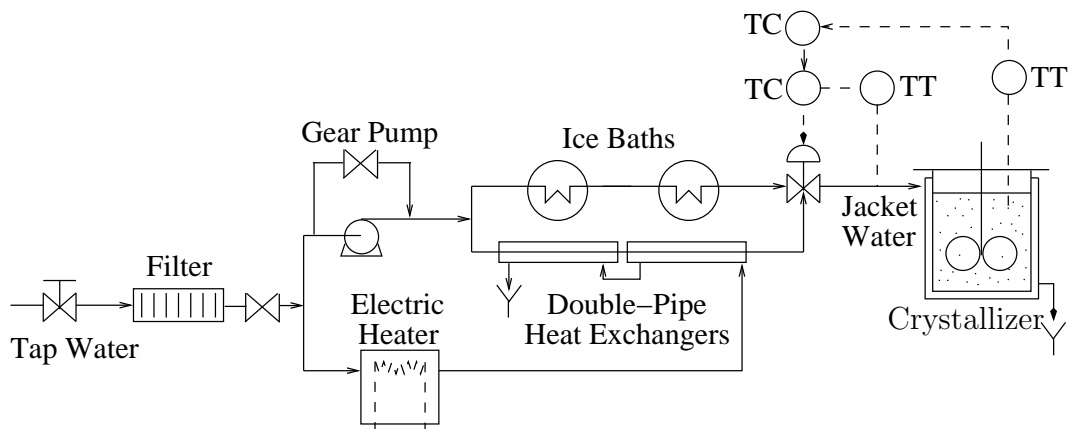


Figure 3.14: Laboratory heating and cooling system for the crystallizer jacket water.

The following set of operating procedures describes start-up for the crystallization

apparatus.

1. The crystallizer is loaded with the initial amounts of material. For the pharmaceutical crystallization, this is usually 63.6 g pharmaceutical, 1600.0 g IPA and 153.1 g water, measured on an electronic balance (Mettler, Model PM116). For the sodium chlorate crystallization, the loading is 1600.0 g NaClO<sub>3</sub> and 1600.0 g H<sub>2</sub>O.
2. The vessel is placed in the fume hood and the headplate with impeller, draft tube, densitometer exit line with filter, and densitometer return line is placed on top of the vessel and screwed down. The crystallizer temperature probe is placed into the crystallizer through a sample port in the headplate. The impeller drive unit is positioned on the coupling and turned on. The vessel is then wrapped in insulating foam.
3. The jacket water inlet and outlet lines are connected to the vessel jacket inlet and outlet ports. The tap water supply valve (Figure 3.14) is turned on. The electric heater (Advantage Sentra, Model S-925) is turned on and the hot water setpoint is set to 80°C for the pharmaceutical crystallization and 50°C for the sodium chlorate crystallization. The gear pump (Baldor, Model 220/56C) and 3-way 0.5 in. control valve (Badger Meter, Model 1002) are turned on. The containers housing the copper coiled tubing for the cold water line are filled with ice.
4. During the initial dissolution period, the master loop of the temperature control scheme is run open-loop. The secondary slave loop is run closed-loop by running a PID velocity algorithm with a controller gain,  $K_c = 0.1 \text{ V}\cdot^\circ\text{C}$  and integral time,  $\tau_{int} = 10 \text{ sec}$ . The setpoint to the slave loop, temperature control for the jacket inlet line is set to 60°C for the pharmaceutical crystallization and 33°C for the sodium chlorate crystallization, and held for approximately 1 hr after the material has completely dissolved. The densitometer water bath (Haake) is set to 75°C, corresponding to approximately 55°C in the cell housing the oscillating u-tube. The colorimeter needs approximately 15 min to warm up, so it is turned on during this period. The colorimeter wavelength is set to 450 nm for the pharmaceutical crystallization.
5. Once the material has completely dissolved, the densitometer is turned on and the pump (Masterflex) to the densitometer is turned on and set to 30 mL·min<sup>-1</sup>. The glass sleeve and transmittance probe is screwed into the headplate of the crystallizer. The transmittance reading is set to 100 % by adjusting the coarse and fine adjustment knobs on the colorimeter.
6. The MPC controller is programmed by entering the initial crystallizer temperature which is the steady-state value resulting from the inlet jacket setpoint of 60°C. The next inputs in the temperature control program are the *hold period* for this initial temperature, the *rate period* over which the crystallizer will cool or heat to the next temperature, and the *next temperature*. The program allows up to 8 linear cooling

profiles and holds, but can be expanded if desired. A filename for the temperature, concentration, transmittance and voltage to control valve data is entered. For the pharmaceutical crystallization, the solution is cooled to 50°C at 10°C·hr<sup>-1</sup> and held for 1 hr, after which the experiment cooling profiles are described in more detail in Chapter 5. For the sodium chlorate crystallization, the solution is held at 33°C for 0.5 hr and then cooled to 25°C as quickly as possible and held at 25°C for 0.5 hr. The solution is then cooled at 0.25°C·hr<sup>-1</sup> for 8 hr. More details are given in Chapter 7.

7. The slave loop PID control program is stopped by choosing the stop virtual instrument command in LabVIEW. The cascaded MPC-PID temperature control program is started immediately after stopping the PID control program by choosing the start virtual instrument command in LabVIEW.
8. If shape control is implemented, the program requires a filename for recording the impurity loads and impurity injection times. The directory name Image-Pro Plus uses for storing the imaging results is entered so the LabVIEW program can find the crystal shape data as it is collected. The shape control experiments are unseeded. The pump (Masterflex) for the microscope is connected to an inlet port and an outlet port in the headplate of the crystallizer and turned on. The pump is switched to automatic by turning the automatic/manual switch to external. The operator is required to view the cell through the microscope and note when nucleation occurs. The pump is occasionally back-flushed to remove air bubbles that collect in the flowcell. Once crystals nucleate, the Image-Pro Plus macro program is started and the *collect images* switch on the LabVIEW panel is switched to on. Based on the image data, the shape controller settings (controller gain,  $K_c = 0.00556 \text{ mL}\cdot\%\text{}^{-1}$  and integral time,  $\tau_{int} = 10 \text{ min}$ ), and the percentage of cubes in the crystallizer, the shape control program calculates a volume of the sodium dithionite solution to inject. The sodium dithionite solution consists of 18.0 g of sodium dithionite pentahydrate ( $\text{Na}_2\text{S}_2\text{O}_6\cdot5\text{H}_2\text{O}$ ) in 100.0 mL  $\text{H}_2\text{O}$ . The impurity is injected via an automatic pipette (Wheaton) with capacity 0.5-5.0 mL. Once the load is injected, the operator hits the impurity inject button on the control panel and the volume is re-set to 0 mL. If the impurity is not injected, the program continues to indicate the cumulative volume of impurity, yet to be injected.
9. The mass (8.4 mg) of the pharmaceutical seeds are measured using a microbalance (Fisher Scientific) and suspended in 3.0 mL IPA. 0.5 mL of the pharmaceutical seeds in IPA solution are injected with the automatic pipette at a crystallizer temperature 49.157 °C.
10. Once the run is completed, the stop virtual instrument command is implemented. The gear pump, control valve, electric water heater, impeller drive unit, and tap water supply valve are switched off. The densitometer inlet stream is disconnected and is pumped clean. Once clean, the densitometer and pump are switched off and the densitometer return line is disconnected. The transmittance probe is removed

from the crystallizer headplate and the colorimeter is switched off. The crystallizer temperature probe is removed from the crystallizer headplate. The jacket water inlet and outlet lines are disconnected and the crystallizer vessel is removed from the fume hood.



## Chapter 4

# Model Summary and Solution

*It's not a question of . . . Sa-Say that again.*

— Bindlish, R.

This chapter outlines the population, mass and energy balance equations used in this study. In particular, the population balance for growth in batch crystallization with boundary and initial conditions and no crystal size spreading mechanisms is given. Then, the population balance for growth with random fluctuations, the population balance equation with growth-dependent dispersion, and the population balance equation with size-dependent growth, all describe crystal size spreading in batch crystallization, are given.

Given the available measurements concentration, transmittance, crystal mean size and variance, we do not seek the particle size density (PSD),  $f(L, t)$  as a function of time. Instead, properties of the PSD, such as the mean, the variance, and the second moment are sufficient. The method of moments, a technique for solving the population, mass and energy balance equations is described. The size-dependent growth model cannot be solved using the method of moments, instead we use orthogonal collocation. Orthogonal collocation for solving a seeded batch crystallization with no nucleation is briefly described. Examples solutions for an isothermal seeded batch crystallization with no secondary nucleation using the random fluctuation and size-dependent growth models are given.

## 4.1 The Population, Mass, and Energy Balance Equations

The PSD of a slurry in a batch crystallizer is modeled by the population balance equation (PBE). The PBE is a partial differential equation in time,  $t$  and crystal size,  $L$

$$\frac{\partial f(L, t)}{\partial t} = -G \frac{\partial f(L, t)}{\partial L} \quad (4.1)$$

in which  $f(L, t)$  is the PSD and  $G$  is the size-independent crystal growth rate.

The solution phase concentration in the crystallizer is described by a mass balance of the crystallizing solute

$$\frac{d\hat{C}}{dt} = -3\rho_c k_v h G \int_0^\infty f(L, t) L^2 dL \quad (4.2)$$

in which  $\hat{C}$  is the concentration (mass of solute per total mass of the mother liquor),  $\rho_c$  is the crystal density,  $k_v$  is the volume shape factor converting  $L^3$  into crystal volume and  $h$  converts solvent mass to slurry volume.

The bulk temperature can be predicted from an energy balance

$$\rho V \hat{C}_p \frac{dT}{dt} = -3\rho_c k_v V \Delta \hat{H}_c G \int_0^\infty f(L, t) L^2 dL - UA(T - T_j(t)) \quad (4.3)$$

in which  $T$  is the bulk temperature,  $\rho$  is the slurry density,  $V$  is the slurry volume,  $C_p$  is the heat capacity of the slurry,  $\Delta H_c$  is the heat of crystallization which is assumed to be constant,  $U$  is the overall heat transfer coefficient,  $A$  is the surface area available for heat transfer, and  $T_j(t)$  is the time-dependent outlet jacket temperature. Equation 4.3 shows that the energy balance is a function of two independent processes: internal heat generation due to crystallization and heat removal by the coolant in the jacket.

The driving force for the nucleation and growth rates is the difference between the bulk concentration and the saturation concentration calculated at the bulk temperature. The kinetic expressions for nucleation and growth are taken to be empirical power-laws in supersaturation. The nucleation kinetics are described by the following empirical expression.

$$B = k_b \left( \frac{\hat{C} - \hat{C}_{\text{sat}}(T(t))}{\hat{C}_{\text{sat}}(T(t))} \right)^b \quad (4.4)$$

The growth kinetics are described by

$$G = k_g \left( \frac{\hat{C} - \hat{C}_{\text{sat}}(T(t))}{\hat{C}_{\text{sat}}(T(t))} \right)^g \quad (4.5)$$

The zero size boundary condition for Equation 4.1 is

$$f(0, t) = \frac{B}{G} \quad (4.6)$$

and the initial conditions for the population, mass, and energy balances are

$$f(L, 0) = f_0(L) \quad (4.7)$$

$$\hat{C}(0) = \hat{C}_0 \quad (4.8)$$

$$T(0) = T_0 \quad (4.9)$$

The PSD of a slurry in a batch crystallizer with apparent growth-rate dispersion can be modeled with a variety of PBEs. In the case for which the number of particles that diffuse at size  $L$  is proportional to  $\partial f / \partial L$ , the PBE is

$$\frac{\partial f(L, t)}{\partial t} = -G \frac{\partial f(L, t)}{\partial L} + D \frac{\partial^2 f(L, t)}{\partial L^2} \quad (4.10)$$

in which  $D$  is the diffusion coefficient (discussed in Appendix C).

The PSD of a slurry in a batch crystallizer in which particles grow in discrete sizes,  $L = i\Delta, i \in \{1, 2, 3, \dots\}$  is modeled by the PBE

$$\frac{\partial f(L, t)}{\partial t} = -\tilde{G}\Delta \frac{\partial f(L, t)}{\partial L} + \tilde{G} \frac{\Delta^2}{2} \frac{\partial^2 f(L, t)}{\partial L^2} \quad (4.11)$$

in which  $\tilde{G}$  is the frequency at which crystals grow from size  $L$  to size  $L + \Delta$  and  $\tilde{G}$  is a function of supersaturation.  $\tilde{G}(\Delta^2/2)$  is the growth-dependent diffusivity, and  $\Delta$  is the size of the smallest discrete growth unit. Defining  $G = \tilde{G}\Delta$ , then Equation 4.11 becomes

$$\frac{\partial f(L, t)}{\partial t} = -G \frac{\partial f(L, t)}{\partial L} + G \frac{\Delta}{2} \frac{\partial^2 f(L, t)}{\partial L^2} \quad (4.12)$$

in which  $G$  is described by Equation 4.5.

#### 4.1.1 Seed Size Density

Based on the photomicrograph of the pharmaceutical seeds in Figure B.2, Appendix B it seems reasonable to use the PSD in Figure B.3 as the initial condition for  $f_0(L)$ . However, photomicroscopy at the magnification of 40X used for the seeds is sensitive to detecting crystals at the small end of the scale. As a result, crystals less than 2.5  $\mu\text{m}$  are difficult to detect and so the PSD is biased. If scanning electron micrographs are used to detect the seeds smaller than 2.5  $\mu\text{m}$ , there is still a limit in detecting the smallest crystals. It is possible that a linear density used by Matthews [68] would describe pharmaceutical crystallization. The linear density assumes that the maximum number of crystals are close to zero size. If the linear density is shifted to the right so the maximum number of seeds occur at some finite size greater than zero, we would have to know that there is a minimum size. We have no reason to believe there is a finite minimum seed size greater than zero, so we assume the seed density is zero at the origin. A simple function for the seed density is a quadratic function and is used for the pharmaceutical crystallization studies. The density has a maximum at some non-zero value and is zero at the origin and the maximum seed size.

The third moment of the seed PSD is related to the mass of the seeds by

$$m_s = \rho_c k_v V \int_0^{L_{\max}} f_q(a_2 L^2 + a_1 L + a_0) L^3 dL \quad (4.13)$$

in which  $m_s$  is the mass of seeds,  $\rho_c$  is the crystal density,  $k_v$  is the volume shape factor,  $V$  is the slurry volume,  $L_{\max}$  is the maximum seed size,  $a_2, a_1, a_0$  are the coefficients of the quadratic function and  $f_q$  is a constant. The coefficients  $a_2, a_1, a_0$  are found knowing that the seed density is zero at the origin and  $L_{\max}$  and the density has a maximum at  $L_{\max}/2$ . The initial moments are then

$$\mu_j(0) = \int_0^{L_{\max}} f_q(a_2 L^2 + a_1 L + a_0) L^j dL \quad (4.14)$$

## 4.2 Model Solution

Numerous solution techniques exist for solving partial differential equations. The choice of the solution technique depends mostly on the particle formation mechanisms. In the case of nucleation and size-independent growth, the method of moments is sufficient only if the moments of the CSD are of interest and the time evolution of  $f(L, t)$  is not needed. When the CSD,  $f(L, t)$  is required, collocation is used when nucleation, size-independent growth and size-dependent growth mechanisms occur. The method of characteristics is suitable for solving the PBE with nucleation and size-independent growth [113]. If agglomeration occurs, a range of solution techniques are possible depending on any other mechanisms occurring besides agglomeration. For agglomeration only, Smit et al. [123] and Gelbard and Seinfeld [30] develop some analytical solutions to the PBE for size-independent and size-dependent agglomeration. Discretization techniques have been used by Kumar and Ramkrishna [59] with some success for agglomeration, nucleation and growth kinetics. The method of moments and orthogonal collocation are used in this study and are briefly outlined in the following sections.

### 4.2.1 Method of Weighted Residuals

The method of weighted residuals, reviewed by Finlayson and Scriven [27], solves the differential equation

$$N(f(L, t)) - \frac{\partial f(L, t)}{\partial t} = 0 \quad (4.15)$$

by assuming a trial solution for the population density  $f^*(L, t)$  to be a combination of a function whose dependence on position is known (the basis function  $f_i(L, t)$ ), and an undetermined function of time ( $c_i(t)$ ),

$$f^*(L, t) = f_s(L, t) + \sum_{i=1}^N c_i(t) f_i(L, t) \quad (4.16)$$

The right hand side of equation 4.16 is substituted into equation 4.15. The residual,  $R(L, t)$  for the differential equation is defined to be

$$R(f^*) = N(f^*) - \frac{\partial f^*}{\partial t} \quad (4.17)$$

and is a measure of the extent to which the function  $f^*(L, t)$  satisfies the differential equation, Equation 4.15. As the number of approximating functions  $N$ , increases, the magnitude of the residuals decreases. To approximate this, the weighted integrals of the residuals are set equal to zero over some domain of  $L$ :

$$\int_{L_1}^{L_2} w_j(L) R(L, t) dL = 0 \quad (4.18)$$

in which  $w_j(L)$  is a weighting function. Once the choice of the weighting function is made, equation 4.18 becomes a set of  $N$  ordinary differential equations. The solution to these equations is substituted into equation 4.16. Successive approximations are obtained by increasing  $N$  and solving equation 4.18 again.

The case in which the weighting functions are chosen to be

$$w_j(L) = L^{j-1} \quad (4.19)$$

and integrated with the residual over the entire size domain for one internal coordinate,  $L$ , is called the method of moments [51]. Assuming size-independent growth and applying the weighting function (Equation 4.19) to the batch PBE, Equation 4.1

$$\int_0^\infty L^j \frac{\partial f}{\partial t} = -G \int_0^\infty L^j \frac{\partial f}{\partial L} dL \quad (4.20)$$

By exchanging the order of integration and time differentiation, and using integration by parts and Leibnitz's rule, the population balance equation becomes:

$$\frac{d\mu_j}{dt} + GL^j f \Big|_{L=0}^{L=\infty} - \int_0^\infty jL^{j-1} f dL = 0 \quad (4.21)$$

where  $\mu_j$  is the  $j^{th}$  moment of the distribution:  $\mu_j = \int_0^\infty L^j f dL$ . Also assuming  $f$  to be finite at  $L = 0$  and  $L \rightarrow \infty$ , and no fines dissolution, then the  $j^{th}$  moments,  $\mu_j$ , for the PSD and the mass and energy balances become:

$$\frac{d\mu_0}{dt} = B \quad (4.22)$$

$$\frac{d\mu_j}{dt} = jG\mu_{j-1} \quad j = 1, 2, 3 \quad (4.23)$$

$$\frac{d\hat{C}}{dt} = -3\rho_c k_v h G \mu_2 \quad (4.24)$$

$$\rho V \hat{C}_p \frac{dT}{dt} = -3\rho_c k_v V \Delta \hat{H}_c G \mu_2 - UA(T - T_j(t)) \quad (4.25)$$

The zeroth and first moments are the total number of particles and their total length, respectively. The second and third moments are proportional to the total crystal surface area and volume, respectively. Assuming  $\partial f/\partial L$  to be finite at  $L = 0$  and  $\partial f/\partial L = 0$  as  $L \rightarrow \infty$ , and no fines dissolution, then the  $j^{th}$  moments,  $\mu_j$ , for the PSD in Equation 4.10:

$$\frac{d\mu_0}{dt} = B - D \left. \frac{\partial f}{\partial L} \right|_{L \rightarrow 0} \quad (4.26)$$

$$\frac{d\mu_1}{dt} = G\mu_0 + \frac{DB}{G} \quad (4.27)$$

$$\frac{d\mu_j}{dt} = jG\mu_{j-1} + j(j-1)D\mu_{j-2} \quad j = 2, 3, \dots \quad (4.28)$$

$D$  is replaced by  $G(\Delta/2)$  when solving Equation 4.12 with  $G = k_g S^g$ . The initial conditions are given by Equations 4.8, 4.9 and 4.14. Equations 4.26, 4.27, 4.28, 4.24, and 4.25 are easily solved using general ODE solution codes such as DASSL and LSODE. This study uses the differential equation solver LSODE. An example of a solution to Equations 4.24, 4.26, 4.27, and 4.28, an isothermal system with no secondary nucleation ( $B = 0$ ) and no fines dissolution ( $\partial f/\partial L = 0$ ) is shown in Figure 4.1. The example in Figure 4.1 shows that once the system reaches steady state, the concentration, transmittance and crystal mean size all reach a steady-state value. However, the standard deviation still increases. Due to the assumptions of the constant dispersion model, at equilibrium, the crystals age by partially dissolving, losing mass that is taken up by other crystals. The standard deviation for the growth-dependent dispersion model reaches a steady-state value at equilibrium.

Parameter	Value	Units
$k_g$	$1 \times 10^{-3}$	$\text{m} \cdot \text{min}^{-1}$
$g$	1	dimensionless
$D$	$1 \times 10^{-4}$	$\text{m}^2 \cdot \text{min}^{-1}$
$k_a$	1	dimensionless
$k_v$	1	dimensionless
$C_s$	1	(g solute) · (g solvent) $^{-1}$
$\rho$	1	$\text{g} \cdot \text{cm}^{-3}$
$m_s$	$1 \times 10^{-3}$	g
$V$	1	$\text{m}^3$
$l$	0.1	m

Table 4.1: Kinetic parameters for Equations 4.24, 4.26, 4.27 and 4.28 the constant dispersion model with no secondary nucleation or fines dissolution.

### 4.2.2 Orthogonal Collocation

Collocation is a method used for solving integral equations, differential equations and reducing PDEs to ODEs. Villadsen and Michelsen [138] outline the approach to solving integral

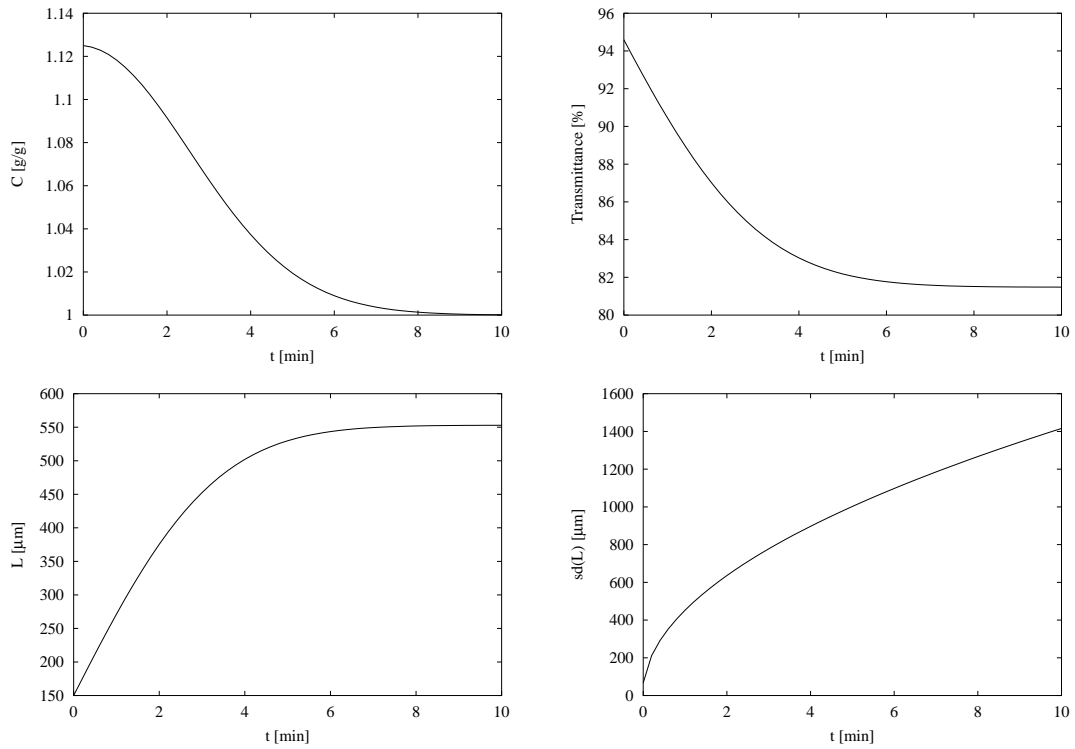


Figure 4.1: Concentration, transmittance, length, and standard deviation as a function of time for the model described by Equations 4.24, 4.26, 4.27 and 4.28 with the parameters given in Table 4.1.

equations, ODEs, and PDEs with collocation. In particular, the article by Villadsen and Stewart [139] shows how to optimally place the collocation points and obtain a more computationally efficient solution than the method of weighted residuals. The accuracy of their orthogonal collocation method is comparable to Galerkin's method. Witkowski [146] provides a discussion on how orthogonal collocation is used for solving the PBE, mass, and energy balances for seeded and unseeded batch crystallization with size-independent growth. Miller [75] extends the discussion for crystallization with size-dependent growth.

For interior collocation, the approximate solution is given by

$$y(x, t) \approx \sum_{i=1}^{NCOL} l_i(x) y(x_i, t) \quad (4.29)$$

in which  $l_i(x)$  is the Lagrange interpolation polynomial and  $y(x_i, t)$  is the function solution evaluated at  $x_i$ . The gradient for  $y(x_i)$  is

$$\left. \frac{dy}{dx} \right|_{x=x_i} \approx \sum_{j=1}^{NCOL} A_{ij} y(x_j) \quad (4.30)$$

in which  $A_{ij}$  is a derivative weight matrix. The integral of  $f(L, t)$  over the domain is required for concentration and transmittance predictions, so its approximate value can be computed from quadrature

$$\int y dx \approx \sum_{j=1}^{NCOL} q_j y(x_j, t) \quad (4.31)$$

in which  $q_j$  is the quadrature weight. Villadsen and Michelsen [138] provide routines for calculating the quadrature weights,  $q_j$  and the elements of the derivative weight matrix,  $A_{ij}$  on the domain  $[0, 1]$ . As in the studies by Witkowski [146], Miller [75] and Matthews [68] and ignoring agglomeration and breakage, it is convenient to partition the PSD into the nucleated crystals and seed crystals. In this work, we study systems that are seeded with no secondary nucleation occurring and systems that are unseeded. In both cases, the PSD consists of one element. We use orthogonal collocation as the solution technique to Equation 4.1 with size-dependent growth. Size-dependent growth can be described by the following *empirical* equation

$$G = k_g S^g (1 + \gamma_2 L)^{\gamma_1} \quad (4.32)$$

in which  $\gamma_1$  is the size-dependency order and  $\gamma_2$  an inverse length weighting factor. Equation 4.32 describes CSD size-spreading. In the case of a seeded crystallization with no secondary nucleation, Miller [75] outlines the model equations to be

$$\frac{df_{S_i}}{dt} = \left( \frac{\zeta_S \Delta G + G_l - G_i}{L_{S_u} - L_{S_l}} \right) \sum_{j=1}^{NCOL} A_{ij} f_{S_j} - \left( \frac{f_{S_i}}{L_{S_u} - L_{S_l}} \right) \frac{\partial G}{\partial \zeta_S} \Big|_{\zeta_{S_i}} \quad (4.33)$$

in which

$$\zeta_S = \frac{L - L_{S_l}}{L_{S_u} - L_{S_l}} \quad (4.34)$$

maps the length scale onto  $[0, 1]$ , and

$$\frac{dL_{S_l}}{dt} = k_g S^g (1 + \gamma_2 L_{S_l})^{\gamma_1} \quad \frac{dL_{S_u}}{dt} = k_g S^g (1 + \gamma_2 L_{S_u})^{\gamma_1} \quad (4.35)$$

and

$$\Delta G = G_u - G_l = G(L_{S_u}) - G(L_{S_l}) \quad (4.36)$$

$L_{S_u}$  is the lowest size of the seed PSD and  $L_{S_l}$  is the highest size of the seed PSD. The initial conditions for the PBE with size-dependent growth are

$$L_{S_l}(0) = L_{S_l0} \quad (4.37)$$

$$L_{S_u}(0) = L_{\max0} \quad (4.38)$$

$$f_{S_i}(0) = f_0 (L_{S_l} + \zeta_{S_i} (L_{S_u} - L_{S_l})) \quad i = 1, \dots, NCOL \quad (4.39)$$

$$\hat{C}(0) = \hat{C}_0 \quad (4.40)$$

$$T(0) = T_0 \quad (4.41)$$

An example of the solution to an isothermal system described by Equations 4.33 and 4.24 is given in Figure 4.2. The behavior in the solution to the size-dependent growth model is similar to the growth-dependent dispersion model. In particular, the standard deviation reaches a steady-state value once the system is at equilibrium, unlike the constant dispersion model. However, the size-dependent growth model predicts a maximum and minimum crystal size which is not a feature of the growth-dependent dispersion model. The size-dependent growth model has the additional assumption that the solute in solution has a preference to become incorporated on larger crystals. The growth-dependent and constant dispersion models assume mass is randomly deposited on any crystal.

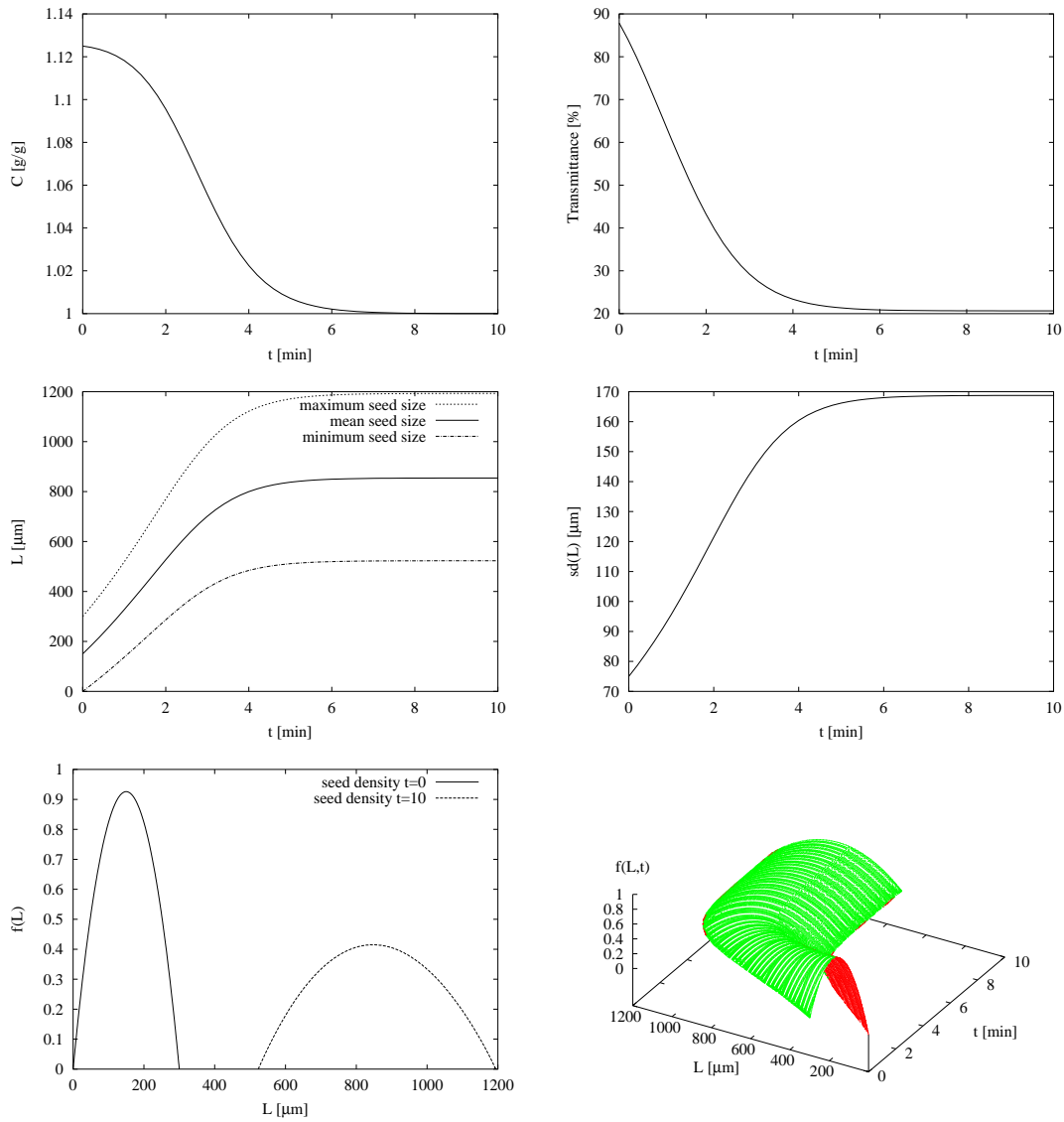


Figure 4.2: Concentration, transmittance, length, standard deviation, and particle size density as a function of time for the model described by Equations 4.24 and 4.33 with the parameters given in Table 4.2.

Parameter	Value	Units
$k_g$	$1 \times 10^{-3}$	$\text{m} \cdot \text{min}^{-1}$
$g$	1	dimensionless
$\gamma_1$	1.7	dimensionless
$\gamma_2$	1	dimensionless
$k_a$	1	dimensionless
$k_v$	1	dimensionless
$C_s$	1	(g solute) · (g solvent) $^{-1}$
$\rho$	1	$\text{g} \cdot \text{cm}^{-3}$
$m_s$	$1 \times 10^{-3}$	g
$V$	1	$\text{m}^3$
$l$	0.1	m

Table 4.2: Kinetic parameters for Equations 4.24 and 4.33, the size-dependent growth model with no secondary nucleation or fines dissolution.



## Chapter 5

# Information-Rich Systems: Industrial Pharmaceutical<sup>1</sup>

*50cent cokes?! REVOLT! This is an outrage! I'm shocked and chagrined, stupidified and mortified.*

— Middlebrooks, S. A.

In this chapter, crystallization kinetics of an industrial pharmaceutical in a batch lab-scale crystallizer are determined for pilot-plant scale crystallization of the pharmaceutical currently produced at GlaxoSmithKline. Dynamic mass and energy balances, coupled with the dynamic population balance equation (PBE) are used to model the bench scale crystallizer. The model assumes growth-rate dispersion occurs via diffusion of infinitesimally small monomer units (molecules or clusters) to the crystal surface. However, data shows once the system is equilibrated, the CSD no longer widens. An alternative model is suggested and assumes growth-rate dispersion occurs via diffusion of monomer units of macro-size to the crystal resulting in a growth-dependent dispersion model. The parameters are identified, however, the predictions do not accurately describe the product CSD mean and standard deviation. We append a reduced dissolution model to the PBE and identify the parameters with predictions that describe all three measurements of solution concentration, slurry transmittance and CSD size and standard deviation. Designing experiments for a seeded crystallization with no secondary nucleation and growth-dependent dispersion is over-specified if the operator requires both a yield and size constraint while minimizing some characteristic of the product CSD. Instead, operating time is minimized and optimal experiments are designed that achieve the maximum mass within a crystal size range. Outside of the size range, the crystals lack bioavailability and have stability problems. Implementation of these optimal experiments are found to agree well with concentration and crystal mean size predictions.

---

<sup>1</sup>Portions of the chapter are in Patience et al. [86, 88]

## 5.1 Introduction

Size spreading of the crystal size density (CSD) during crystallization is a phenomenon in which the width of the CSD at time  $t = t_0$  increases when  $t > t_0$ . To describe the origin of size spreading, consider the steps of crystallization. As described by Kashchiev [57], crystallization involves the steps: (i) achievement of supersaturation, (ii) formation of clusters and nuclei, (iii) cluster coalescence and crystal growth, and (iv) ripening or aging of crystals. In the Szilard model of nucleation, described by Kashchiev [57], molecules, ions, or monomers (units) sequentially add to clusters consisting of  $n$  units. The time evolution of the cluster size density,  $Z(n, t)$ , in a closed system is described by

$$\frac{\partial Z(n, t)}{\partial t} = -\frac{\partial}{\partial n} \left( v(n, t)Z(n, t) - d(n, t)\frac{\partial Z(n, t)}{\partial n} \right) \quad (5.1)$$

in which  $v(n, t)$  is the growth rate of an  $n$ -sized cluster and  $d(n, t)$  is the diffusion coefficient. In growth, molecules, ions, or monomers (units) sequentially add to crystals consisting of  $n$  units, in which  $n$  is greater than the critical number of units ( $n^*$ ) for a cluster to become a stable nucleus. If the system is closed and coalescence between clusters of two or more units with clusters or crystals of  $n$  units does not occur, then the CSD is also described by Equation 5.1 [57]. This governing equation, Equation 5.1, describes cluster and crystal growth as each cluster and crystal having the same mean growth rate,  $v(n, t)$ , however, each crystal's growth randomly fluctuates due to diffusion of units to the crystal surface.

Randolph and White [107] call Equation 5.1 the *random growth diffusivity* model, with  $v(n, t)$  and  $d(n, t)$  constant and model size spreading in crystallization. Alternative models that also describe CSD size spreading are an *intrinsic growth* model described by Berglund and Larson [10], a *size-dependent growth* model described by Abegg et al. [2] and a *growth-dependent diffusion* model described by McCoy [72].

In the intrinsic growth model, each crystal exhibits an individual growth-rate and the growth rate remains constant throughout crystallization. Berglund and Larson [10] use the intrinsic growth-rate model to describe size spreading in a continuous steady-state crystallization of citric acid monohydrate. However, the intrinsic growth-rate model is inadequate for transient systems and requires further development. Jones and Larson [55] measure growth-rate densities as a function of supersaturation. The authors highlight the need that the intrinsic growth-rate model requires more than one internal coordinate besides growth rate such as growth rate constant and order to describe CSD size spreading.

In the size-dependent growth rate model described by Abegg et al. [2], growth is defined as an empirical power law in crystal length. Size-dependent growth is discussed by Kashchiev [57], but the model does not corroborate the model given by Abegg et al [2]. Kashchiev [57] states that the frequencies of monomer attachment and detachment are functions of the number of monomers in the  $n$ -sized cluster, both depending on  $n^{1/3}$ . Kashchiev [57] also gives general formulae for monomer attachment and detachment, useful in industrial crystallization. The general formula given by Kashchiev [57] for the attachment frequency is dependent on the solution properties and independent of  $n$ . The

general formula for the detachment frequency is dependent on  $n$  and the cluster properties. In the Szilard model given by Kashchiev [57], monomer detachment is a strong function of size, especially for small and large clusters. When small, the cluster is unstable and easily loses monomers. When large, the detachment frequency is large due to the large surface area and large number of surface monomers. During most crystallization studies, monomer attachment occurs more often than monomer detachment because of the large size range studied, so growth is not a strong function of size.

When crystals grow at a size-independent frequency  $\tilde{G}$ , and grow in discrete sizes,  $\Delta$ , in which  $\Delta$  is much larger than a unit, the population balance equation (PBE) that describes the CSD is given by

$$\frac{\partial f(L, t)}{\partial t} = \tilde{G}f(L - \Delta, t) - \tilde{G}f(L, t) \quad (5.2)$$

Equation 5.2 is a generalized form of the PBE in which  $f(L, t)$  is the CSD a function of crystal size,  $L$ , and time,  $t$ . Expanding the term  $f(L - \Delta, t)$  in a Taylor series about the point  $(L - \Delta)$  and substitution into Equation 5.2 results in

$$\frac{\partial f(L, t)}{\partial t} = -\tilde{G}\Delta \frac{\partial f(L, t)}{\partial L} + \tilde{G}\frac{\Delta^2}{2} \frac{\partial^2 f(L, t)}{\partial L^2} \quad (5.3)$$

Equation 5.3 is a growth-dependent dispersion model and has been used by McCoy [72] to describe growth and aging in crystallization. McCoy [72] states that the model can naturally describe polymerization kinetics in which monomers of non-infinitesimally small size sequentially add to polymer crystals and inherently produces growth-rate dispersion. Coincidentally, Randolph and White [107] find  $d = 50v$  in Equation 5.1 for sucrose crystallization, and so model growth-dependent dispersion.

Sherwood and Ristić [122] review growth-rate dispersion in crystals formed from secondary nucleation via attrition fragments of a growing crystal and via stripped clusters from the surface of a crystal. Sherwood and Ristić [122] identify two key causes for growth-rate dispersion of secondary nuclei grown in impurity-free solutions. Secondary nuclei are plastically deformed and contain varying numbers of surface dislocations that are growth sources, yielding a variation in growth rate from crystal to crystal. Secondary nuclei have elastic strain that influences the surface of the crystal. Elastic strains vary from crystal to crystal also contributing to a variation in growth rate from crystal to crystal. Lacmann and Tanneberger [60] grow damaged potassium alum crystals. At first, the growth rates are relatively constant over a short period, but the crystals eventually become *healed* and the growth rates decrease to another constant value. Berglund and Larson's [10] data show that individual crystal growth rates are constant over a short period for citric acid monohydrate crystallization. Over a long period the random fluctuation model may be more appropriate than the intrinsic growth model. In bulk crystallization, the effects of lattice dislocations and crystal strain are difficult to determine due to the number of crystals. Sensor technology in industrial crystallization is not ready to measure the magnitude of fluctuations in growth caused by lattice dislocations, elastic strain, and diffusion. The data in Berglund

and Larson's [10] study contain noise that appears to be measurement error, but could easily be random fluctuations. Equation 5.1 is a general equation and still holds for the citric acid monohydrate system. Information regarding the average number of lattice dislocations, elastic strain, impurity effects, and mixing are all inherently built into the growth-rate constant and diffusion coefficient. As described by Kashchiev [57], crystal nucleation and growth are discrete processes and diffusion is a natural phenomenon of the process. Two types of experimental data are generally required to describe crystallization. One piece of information considers the solution phase (temperature and concentration data), the other considers the solid phase (transmittance and CSD data) [134]. Furthermore, batch experiments are more informative than continuous ones [110]. Randolph and White [107] use the one measurement of CSD mean and variance to estimate the parameters,  $v$  and  $d$  in Equation 5.1, however, the authors did not investigate whether the parameters are correlated. Rojkowski [117] uses one measurement, the final product CSD from a continuous crystallizer. Rojkowski [117] uses a *goodness-of-fit* value to discriminate between rival apparent growth-rate dispersion model. The author finds four parameters for the intrinsic growth rate model from this one measurement, however concludes that Equation 5.1 may be more appropriate. In more informative experiments, Monnier et al. [77] studied the crystallization kinetics of adipic acid in water. They used the calorimetric method as an indirect method to measure the supersaturation providing information about the solution phase and used off-line image analysis to give information about the solid phase. Qiu and Rasmussen [99] estimated the kinetics of succinic acid crystallization in aqueous solution. Concentration and final product size distribution are the two measurements used to successfully estimate the parameters.

Recent advances in the pharmaceutical industry have created a large number of drug substances, some of which are complex organic materials requiring solution cooling crystallization as a purification technique. The final form of the crystal always has more than one polymorph due to the complex nature of the organic molecule. As a consequence, once the drug substance is registered and approved, the production of the desired polymorph with desired size, habit, and morphology must be guaranteed. In most cases, a seeded crystallization with no secondary nucleation occurring and using the required polymorph as the seed crystals, produces a final product with the same morphology as the seeds. Secondary nucleation of undesirable polymorphs is avoided by growing the seeds in metastable solutions [9]. However, the crystallization of the seeds does not always produce a product with maximum stability and bioavailability. Usually, the crystal with the greatest bioavailability is the one with the highest solubility. Sometimes, the crystal with the greatest stability is the one with the lowest solubility [128]. Therefore, it is crucial to design a cooling and seeding protocol which maximizes the bioavailability and stability of the final population of crystals. Traditionally, cooling profiles and seeding load protocols have been optimized by experimentally investigating, through factorial designs, the effects of various operating parameters on the crystal product's yield [135, 85]. Although the factorial design method provides a rapid solution to a design objective, the disadvantage is that the approach is not

model-based. The resulting optimal experimental design is limited to implementation only on the equipment used for collecting the data, making scale-up difficult.

An alternative method for optimizing a seeded batch crystallization is to use mathematical models which predict the solution concentration, crystal size, and yield as a function of the operating conditions and cooling profile. Modeling crystallization systems is well-established [110, 145]. The general statement of the open-loop optimal control problem is given by Miller and Rawlings [76]. Temperature is the manipulated variable which is parameterized as piecewise linear in time. Nonlinear state constraints on the supersaturation and linear constraints on the temperature are also applied by Miller and Rawlings [76]. Matthews et al. [69] compute the influence of model parameter uncertainty on optimal cooling profiles. The authors determine temperature constraints in which cooling within these constraints guarantees the optimal result. Chung et al. [21] study the effect of including parameters of the seed size density with the temperature as manipulated variables. Chung et al. [21] show that optimizing over the seed size density has a larger effect on the product crystal size density (CSD) than optimizing over the temperature profile. These modeling and optimal experimental design techniques have been successfully applied to a wide range of organic systems [62], as well as other organic systems such as biological systems [56], enzymatic systems [25], and polymerization systems [31]. The typical objectives for model-based experimental designs include minimizing the mass of nucleated to seed crystals, minimizing the coefficient of variation of the product CSD (defined as the ratio of the CSD standard deviation to the CSD mean), and maximizing the yield.

The objective of this study is to design experiments for a pharmaceutical crystallization with apparent growth-rate dispersion in which seed crystals are grown to a desired size while avoiding secondary nucleation. Three types of data are used that provide detailed dynamics of the transient behavior in batch crystallization. The random fluctuation and growth-dependent dispersion models are used to describe the crystal population dynamics.

## 5.2 Experimental Apparatus

For a crystallization experiment, 63.6 g pharmaceutical is dissolved in 1600 g iso-propyl alcohol (IPA) with 153.1 g H<sub>2</sub>O ( $T^{\text{sat}} = 50.9^\circ\text{C}$ ) at a temperature of 60°C. The solution is held at this temperature for 60 min, then cooled at 10°C·hour<sup>-1</sup> to 50°C and held for 30 minutes. For runs 13 and 14, the solution is then cooled at 1°C·hour<sup>-1</sup> and 2°C·hour<sup>-1</sup>, respectively. For runs 15 and 16, the solution is cooled at 4°C·hour<sup>-1</sup> and 10°C·hour<sup>-1</sup>, respectively. At 49.1°C, 0.5 mL of a pharmaceutical seed solution (8.4 mg seeds in 3.0 mL IPA) are injected into the crystallizer. The temperature profiles from this point are shown in Figure 5.1.

Photo-microscopy and digital image analysis are used to monitor growth kinetics and particle size characteristics of crystals in the size range of 10 μm to 1000 μm using an Olympus BX60 microscope, a Hitachi HV-C20 charged coupled device (CCD) camera and a PC with frame grabber and Image Pro Plus image analysis software. The microscope uses

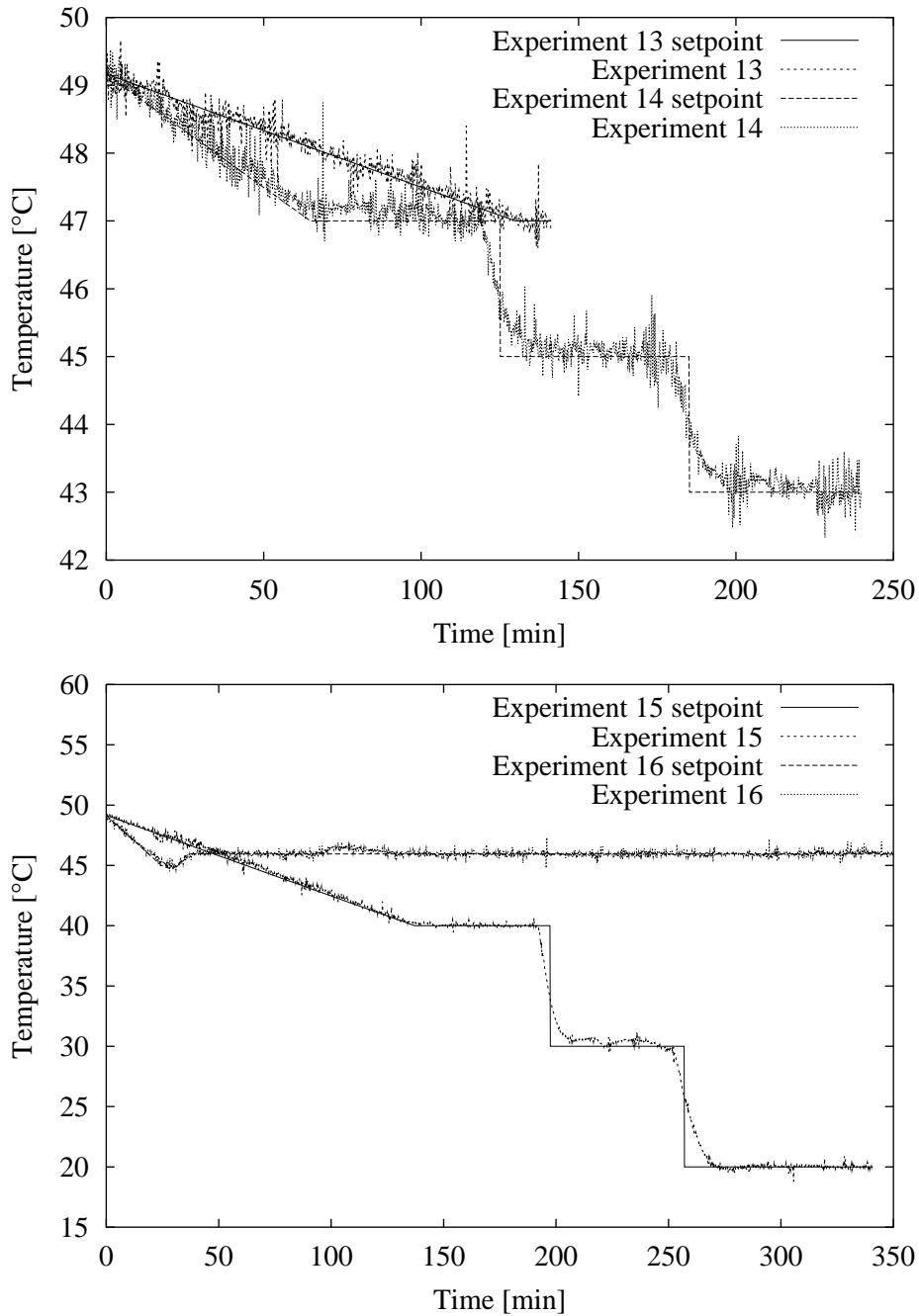


Figure 5.1: Temperature profiles for runs 13–16.

a non-polarized reflected halogen light source with a total magnification of 8X. Samples of 0.5 mL of the crystal slurry are periodically removed from the crystallizer and placed under the microscope for image capture. The CCD camera captures images of  $585 \times 700$  pixels with 256 grayness levels. The particles are then manually traced and a pixel calibration is applied.

On-line measurements of slurry temperature and transmittance and solution concentration are recorded. Temperature measurements are provided by *in-situ* RTD thermocouples. Transmittance measurements are provided by a Brinkman *in-situ* colorimeter probe that is inserted into the headplate of the crystallizer and into the slurry. Concentration measurements are provided by a Paar densitometer.

### 5.3 Crystal Size Densities from Process Vision Measurement

Before using image analysis software on images from photo-microscopy, we study the information present in the process vision measurement (PVM) probe. The PVM probe is a relatively new probe in the field of crystallization monitoring. So far, since its introduction, the probe has only been used for qualitative purposes such as detecting the onset of nucleation and detecting habit changes. Figure 5.2 shows the results of standard imaging software on images provided by the PVM probe. PVM images are typically gray, most objects are blurred and difficult to see with the naked eye. Occasionally, objects reflect light from the strobing light source in the PVM probe in such a way that the crystal is seen as a bright stationary object, providing enough contrast to discern the crystal from the background. Figures 5.2 (i) and (ii) show the results of digitizing with a light thresholding of R=135-255, G=133-254 and B=135-255. Figures 5.2 (iii) and (iv) show the results of digitizing with a light thresholding of R=119-255, G=117-254 and B=119-255. The crystals are either partially digitized or too much of the image is digitized. Even in quality images, PVM imaging software is not able to accurately measure particles for crystals that reflect light well. We avoid investing large amounts of time finding a suitable light threshold to help image analysis routines to accurately digitize PVM images. Instead, we aim to investigate the accuracy of PVM measurements, assuming the PVM image is accurately digitized by manually sizing crystals by hand.

It is not difficult for the human eye to draw a straight line between the two ends of a crystal in a PVM image and call the line a projected length. Figure 5.3 (ii) shows the result of manually digitizing the image in Figure 5.3 (i). Objects that are distinctly visible and are not touching the boundary are considered. Some PVM images do not contain any particles or particles are blurred and touching the boundary. The average number of particles digitized in an image depends on the percent of solids. Figures 5.3 (iii) and 5.3 (iv) show a photo-microscope image before and after digitizing the same slurry from Figures 5.3 (i) and 5.3 (ii). We aim to investigate whether manually digitizing PVM images will result in similar measurements from manually digitizing images of the slurry taken from photo-microscopy.

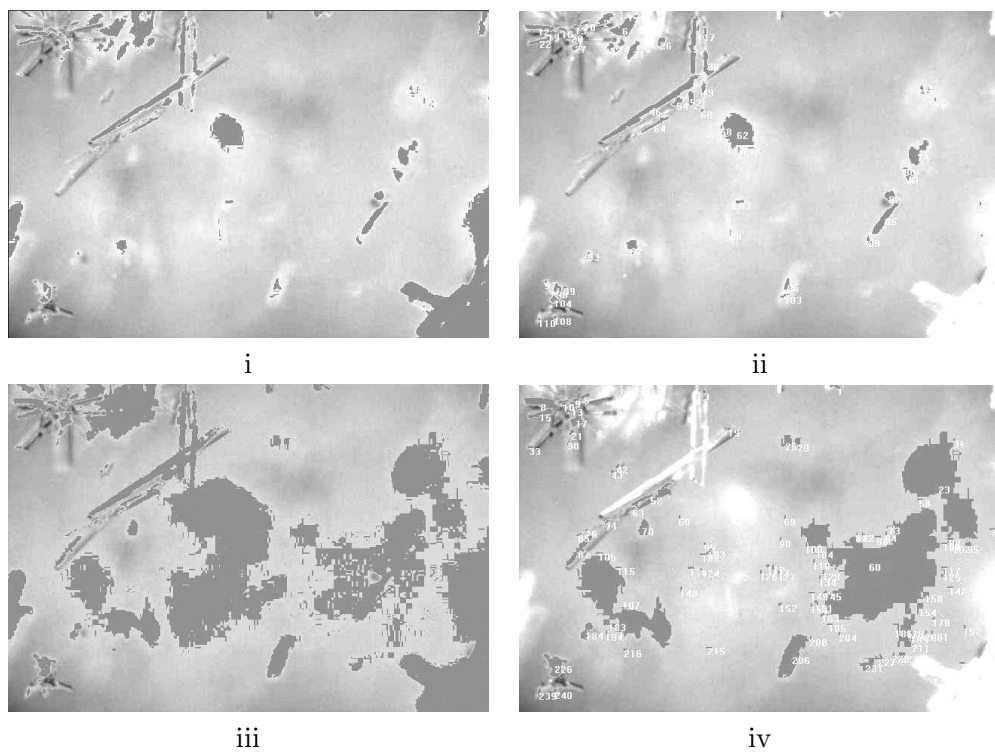


Figure 5.2: Thresholding effects on particle size and count of a PVM image of the industrial pharmaceutical.

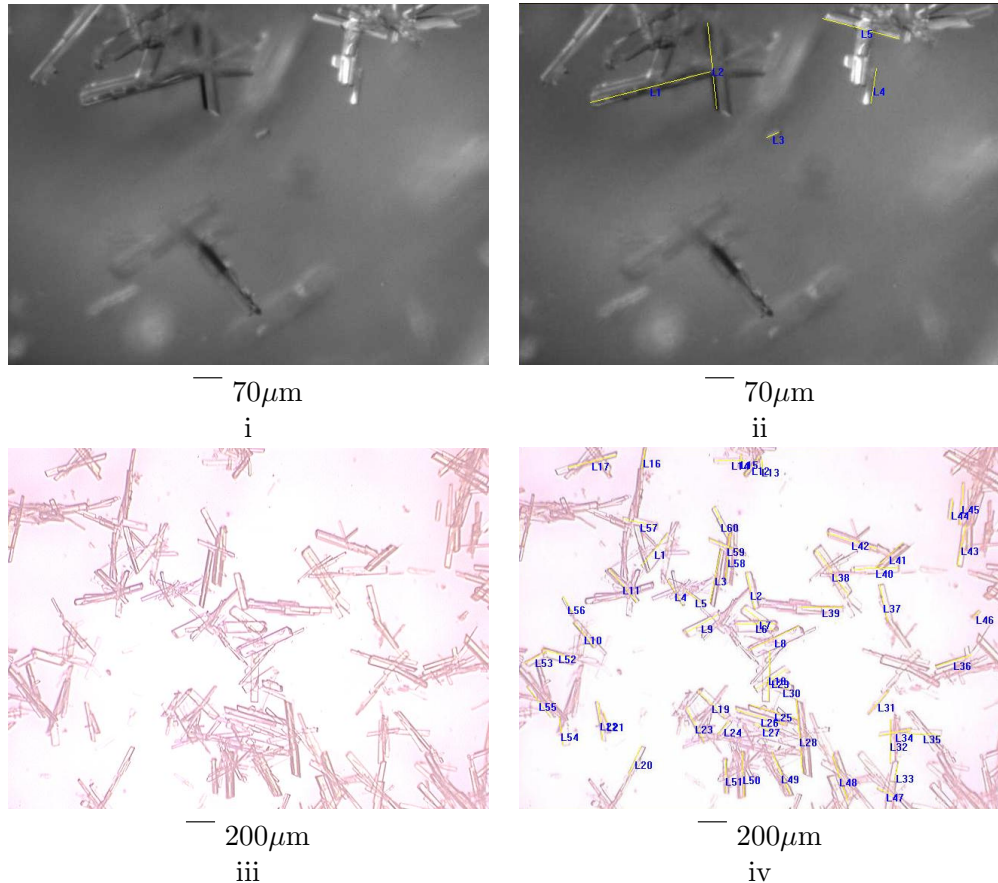


Figure 5.3: Process vision measurement (PVM) images and photo-microscope images of the industrial pharmaceutical at equilibrium. (i) PVM image before manual digitizing. (ii) PVM after manual digitizing resulting in five plengths. (iii) Photo-microscope image before manual digitizing. (iv) Photo-microscope image after manual digitizing.

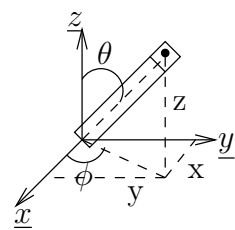


Figure 5.4: The  $x, y, z$  dimensions of a needle as a function of its spherical coordinates in which  $0 \leq \theta \leq \pi$  and  $0 \leq \phi \leq 2\pi$ .

The challenge with PVM images is that the crystals are viewed as two-dimension projections of a randomly-oriented object in three dimensions, shown in Figure 5.4. The goal is to relate the projected length of a particle from the PVM measurement to the observed length of the particle measured when lying on a flat surface. We define the crystal *plength*,  $p$ , as the *projected length* seen in two dimensions from the PVM image. The probability to measure plengths shorter than  $p$  is

$$P(0 < p^* < p) = Q(p) \quad (5.4)$$

The single particle PVM particle plength density (PVMPD) is  $q(p, L)$ . The fraction of plengths between  $p$  and  $(p + dp)$  for a particle with characteristic size  $L$  is  $q(p, L)dp$ , so

$$\int_0^\infty q(p, L)dp = 1 \quad (5.5)$$

Figures 5.5 (i) and (iii) show the  $(x, y)$  and  $(y, z)$  coordinates, seen from the  $z$  and  $x$ -directions, respectively, of the two-dimensional projections of the randomly-oriented needle shown in Figure 5.4. The plength is taken as the distance from the origin to the coordinate in Figures 5.5 (i) and (iii). Figures 5.5 (ii) and (iv) show the single particle PVMPD,  $q(p)$  viewed from the  $z$  and  $x$ -directions for a needle with a unit length one. The PVMPD of the particle population is obtained as a weighted sum of the single particle PVMPDs. The fraction of the overall PVMPD consisting of plengths between  $p$  and  $(p + dp)$  when considering only particles of size  $L$  and  $(L + dL)$  is

$$q(p, L)f(L)LdpdL \quad (5.6)$$

and the PVMPD of the particle population,  $q_{pop}(p)$  is

$$q_{pop}(p)dp = dp \int_0^\infty q(p, L)f(L)LdL \quad (5.7)$$

An approach to the inverse problem of recovering the PSD from a signal such as a light scattering pattern is given by Miller [75] and from a chord length density (CLD) is given by Ruf et al. [119]. Both authors apply a quadrature rule to evaluate the integral in Equation 5.7 which results in a matrix equation

$$q_{pop}(p_i) = \sum_{j=1}^m q(p_i, L_j)w_j f(L_j) \quad i = 1, \dots, n \quad (5.8)$$

Difficulties arise when solving Equation 5.8. No analytical expressions exist for the single particle PVMPDs,  $q(p_i, L_j)$ , and the quadrature weights,  $w_j$ . Before finding numerical values of the single particle PVMPDs, consider Figure 5.6. The results for the manual digitization of images from photo-microscopy are shown in Figure 5.6 (i). The histogram in Figure 5.6 (i) is based on 221 crystals from 2 images resulting in a mean size of 178  $\mu\text{m}$ . The results for the manual digitization of the images from the PVM probe

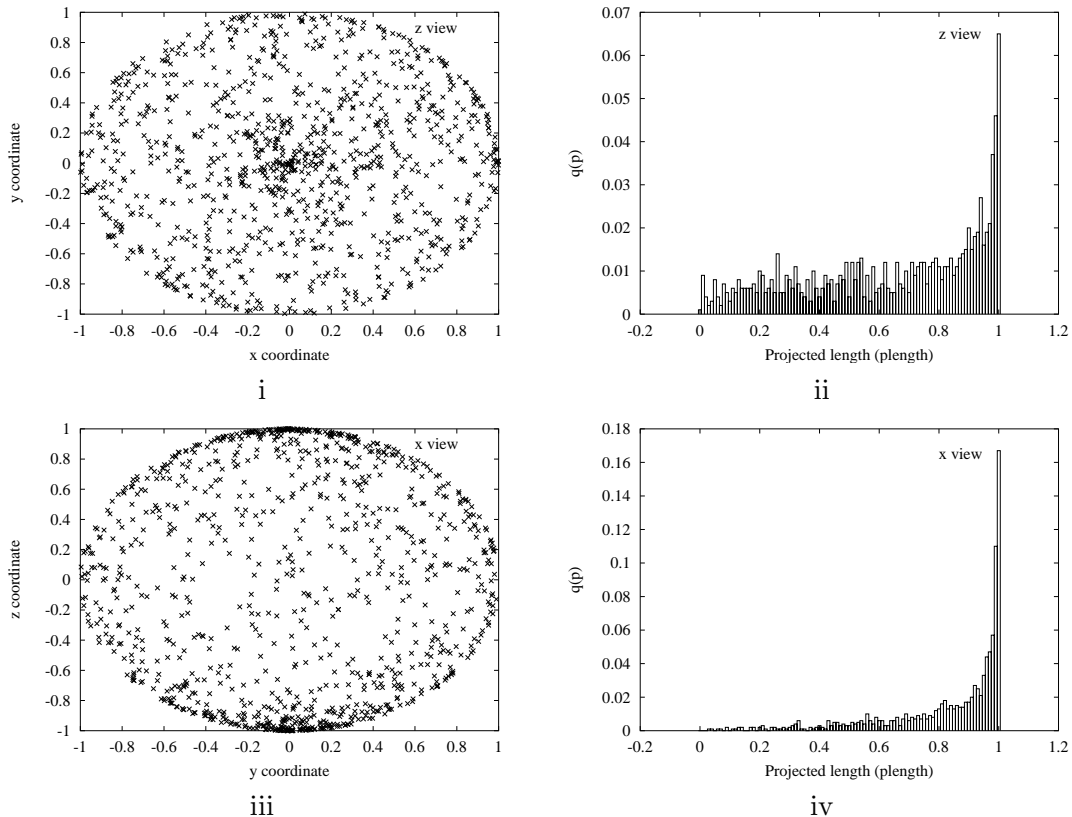


Figure 5.5: (i) The projected lengths in two dimensions of a randomly-oriented needle of unit length as seen from the  $z$ -direction given by the coordinate system in Figure 5.4. (ii) The single particle PVMPPD,  $q(p, L)$ , for a needle seen in the  $z$ -direction. (iii) The projected lengths in two dimensions of a randomly-oriented needle of unit length as seen from the  $x$ -direction given by the coordinate system in Figure 5.4. (iv) The single particle PVMPPD,  $q(p, L)$ , for a needle seen in the  $z$ -direction.

are shown in Figure 5.6 (ii). The histogram in Figure 5.6 (ii) is based on 430 crystals from 80 images and the mean plength is  $129 \mu\text{m}$ . If we take the lengths from the manual digitization of static crystals in Figure 5.6 (i) and randomly orient these lengths according to the coordinate system in Figure 5.4 we obtain the PVMPPDs seen from the  $z$  and  $x$ -directions in Figures 5.6 (iii) and (iv), respectively. The PVMPPD as seen from the  $z$ -direction, Figure 5.6 (iii), has a similar shape to the measured PVMPPD in Figure 5.6 (ii). Thus, we chose to numerically calculate  $q(p_i, L_j)$  based on the  $z$ -direction.

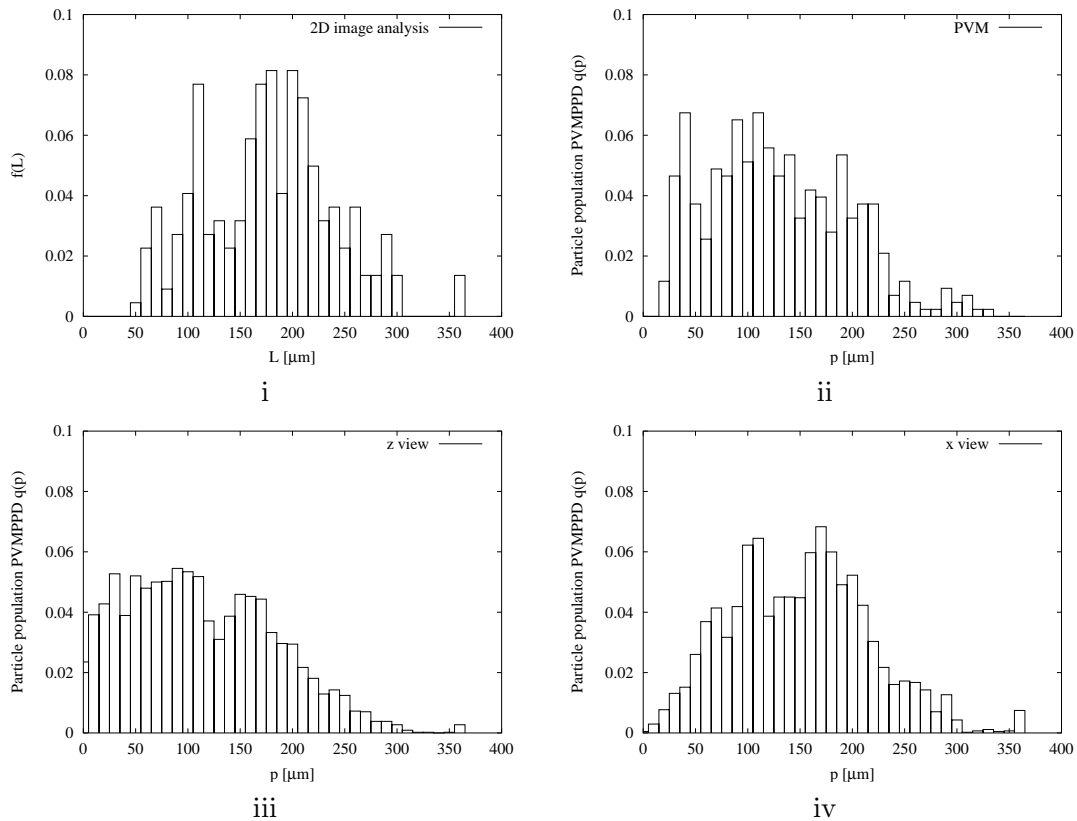


Figure 5.6: (i) Particle size density of crystals in Figure 5.3 (iii). (ii) PVMPPD of particle population of crystals in Figure 5.3 (i). (iii) PVMPPD of particle population based on lengths from Figure 5.6 (i) seen from the  $z$ -direction. (iv) PVMPPD of particle population based on lengths from Figure 5.6 (i) seen from the  $x$ -direction.

To calculate the quadrature weights,  $w_j$ , we first generate values for  $q(p_i, L_j)$  from the  $z$ -direction. For a given  $L_j$ , we generate 10,000 plengths by randomly sampling a value for  $\theta$  and  $\phi$  on a uniform density over  $\pi$  and  $2\pi$ , respectively. The plengths are calculated using  $\phi$  and  $\theta$  and the equations for spherical coordinates. Single particle PVMPPDs are generated for  $L_j$  values in increments of  $16.7 \mu\text{m}$  up to a maximum size of  $334.6 \mu\text{m}$ . A particle population PVMPPD,  $q_{pop}(p)$  is generated by sampling 10,000 lengths from a

uniform density with maximum size  $334.6 \mu\text{m}$ . The lengths are randomly oriented to obtain 10,000 plengths to form the particle population PVMPPD,  $q_{pop}(p)$ . We solve Equation 5.8 for  $w_j$  with  $f(L)$  constant. Using the quadrature weights,  $w_j$ , we now seek  $f(L)$  from the set of plengths,  $q_{pop}(p)$  in Figure 5.6.

The particle population PVMPPD shown in Figure 5.6 (ii) is based on 80 PVM images with 430 crystals. Figure 5.7 shows the recovered CSD using  $q_{pop}(p)$  from Figure 5.6 (ii). The recovered CSD predicts few particles less than  $50 \mu\text{m}$ , agreeing with the CSD measurement from images of the static slurry. However, the inversion technique is sensitive to noise, and does not accurately predict the CSD at large sizes. The effects of the noise are enhanced by the values of  $q(p_i, L_j)$ , generated from random variables. Instead we repeat the calculation for a large number of random variables, greater than 10,000 and examine convergence of the predictions of the mean size of  $f(L)$  as a function of the number of crystals from the PVM images. Figure 5.8 shows that the prediction of the mean size, based on viewing from the  $z$ -direction, converges near the mean size of  $178 \mu\text{m}$ . The mean size prediction, based on viewing from the  $x$ -direction behaves similarly to the measurement based on the  $z$ -direction, however, converges to a different value, lower than the mean of  $178 \mu\text{m}$  from images of static samples.

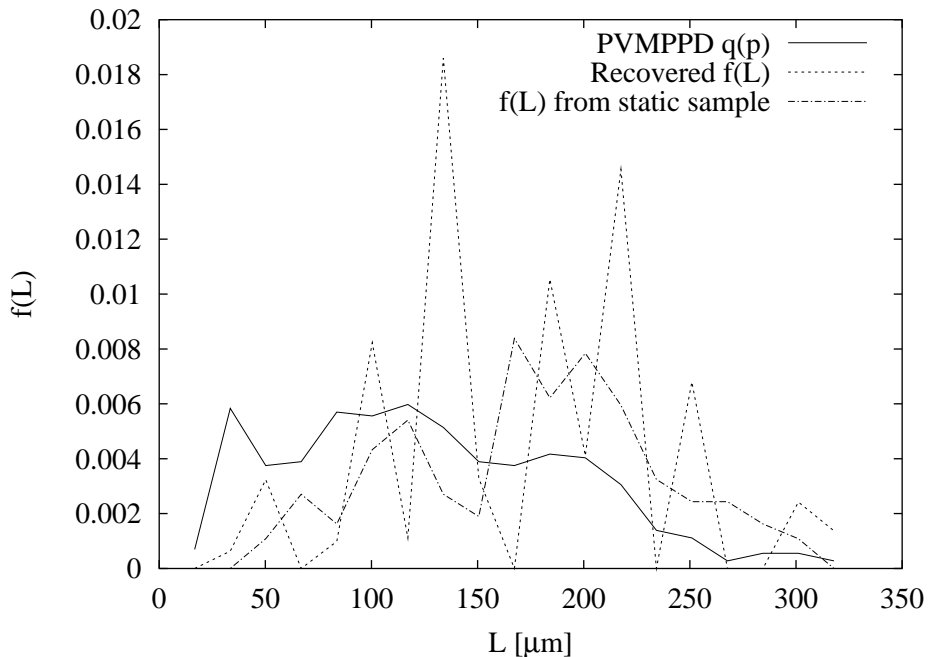


Figure 5.7: Recovery of the CSD from PVM data.

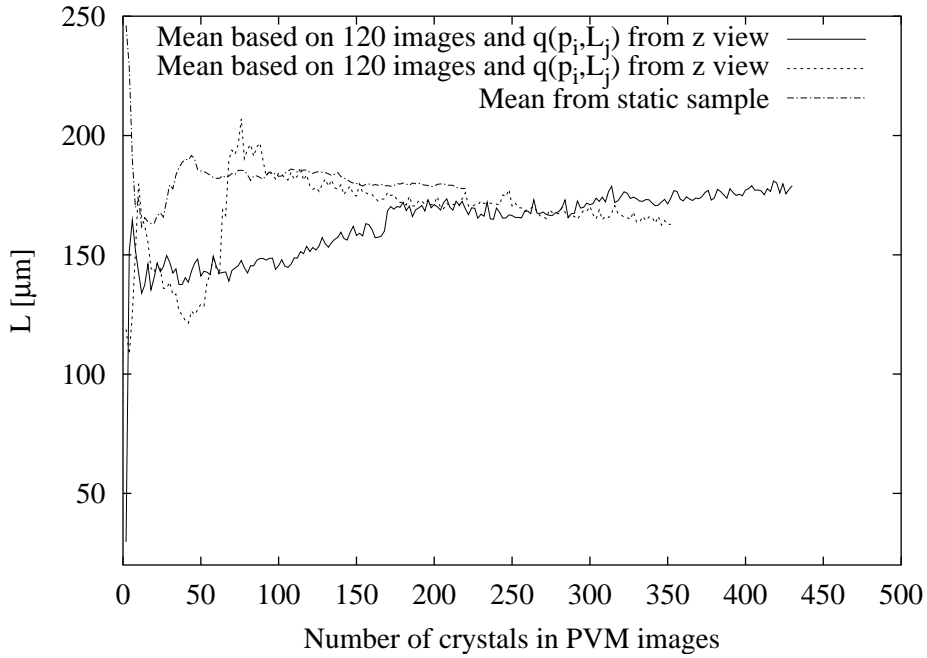


Figure 5.8: Mean size as a function of number of crystals in PVM images.

## 5.4 Initial Estimation of Kinetic Parameters

The CSD of a slurry in a batch crystallizer with random growth-rate dispersion is modeled by the PBE, Equation 4.10. The solution phase concentration in the crystallizer is described by a mass balance of the crystallizing solute given by Equation 4.2. The bulk temperature can be predicted from the energy balance given by Equation 4.3.

We assume secondary nucleation does not occur because of the small supersaturations studied. Photo-microscopy images in Figures 5.9, 5.10, 5.11, and 5.12 for runs 13–16 show no apparent secondary nuclei forming. The CSD is never bimodal and for later times, the images contain no small crystals, indicative of no secondary nucleation. The driving force for the growth rate is the difference between the bulk concentration and the saturation concentration calculated at the bulk temperature. The kinetic expression for growth is taken to be an empirical power-law in supersaturation. The growth kinetics are described by Equation 4.5. The zero size boundary condition for the PBE, Equation 4.10, is

$$f(0, t) = 0 \quad (5.9)$$

and the initial conditions for the population, mass, and energy balances are given by Equations 4.7, 4.8, and 4.9. The seed size density is assumed to be a quadratic function with minimum size zero, and maximum size,  $L_{\max}$  in which  $L_{\max}$  is a parameter to be estimated. The Beer-Lambert law, Equation 2.14, is used to relate the transmittance measurement to

the second moment of the CSD.

$$\frac{I}{I_0} = \exp\left(-\frac{l k_a}{2} \mu_2\right) \quad (5.10)$$

$I$  is the intensity of the light transmitted through the slurry,  $I_0$  is the intensity of the incident light,  $l$  is the beam length, and  $k_a$  is the area shape factor. From Figures 5.9, 5.10, 5.11, and 5.12 we assume the crystals are parallelepiped (Figure 2.3) shaped with length,  $l$ , width,  $w$ , and depth,  $d$ , so the shape factors,  $k_a$  and  $k_v$  are functions of the length-to-width,  $l_w$ , and depth-to-width,  $d_w$ , ratios as

$$k_a = 2(l_w d_w + l_w + d_w) \quad (5.11)$$

$$k_v = l_w d_w \quad (5.12)$$

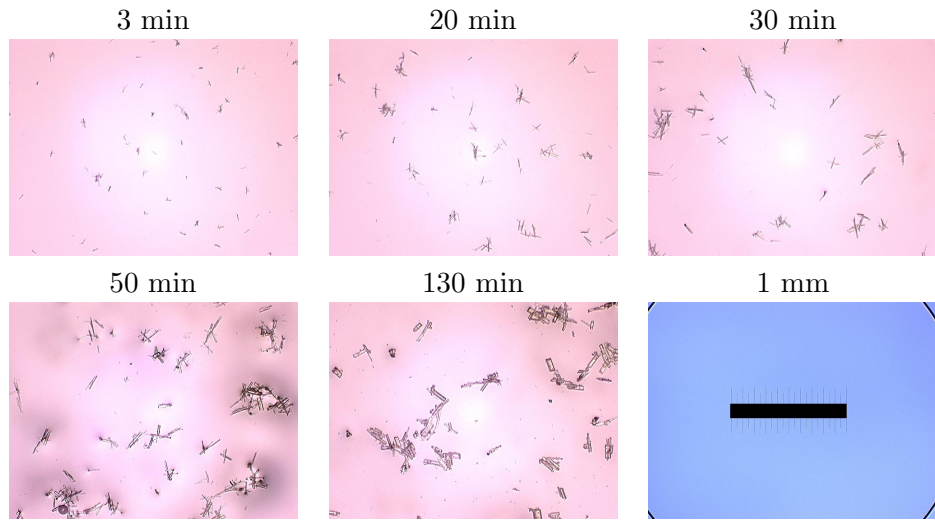


Figure 5.9: Growth of pharmaceutical seed crystals for run 13.

The length-to-width ratio,  $l_w$  is measured off-line using all the images and found to be constant throughout crystallization with an average approximately equal to 5.4 (See Appendix B, Figure B.4). The depth-to-width ratio,  $d_w$ , is not measured using the images because the crystals all align in the same direction making the depth direction impossible to observe. Instead, we aim to estimate  $d_w$ .

The PBE, Equation 4.10, is solved using the method of moments outlined in Chap-

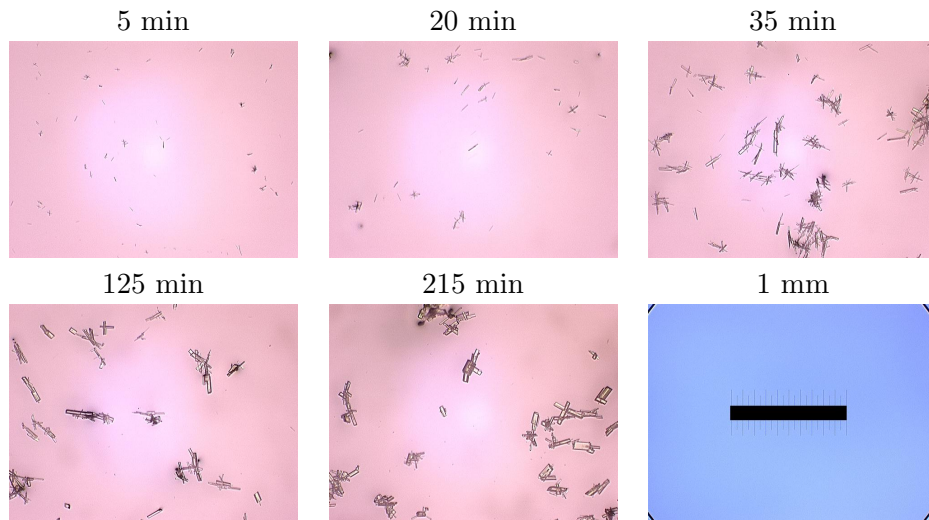


Figure 5.10: Growth of pharmaceutical seed crystals for run 14.

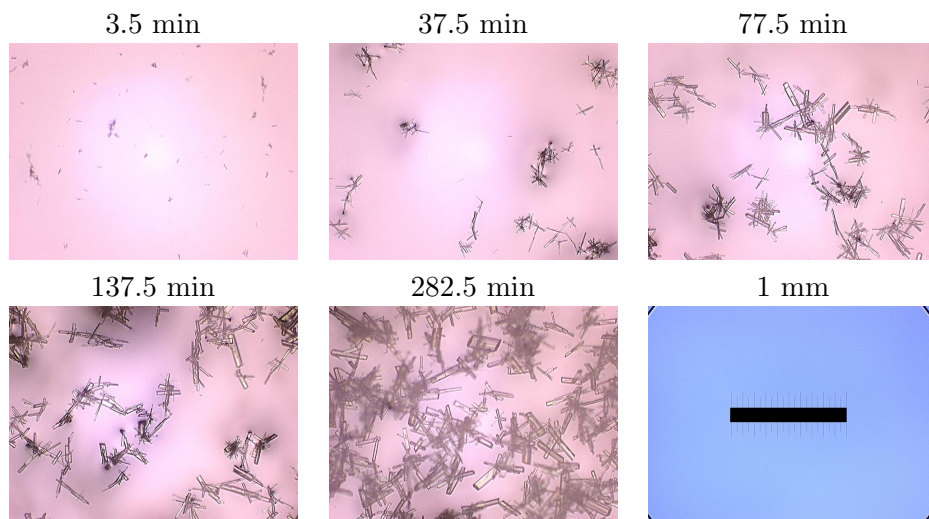


Figure 5.11: Growth of pharmaceutical seed crystals for run 15.

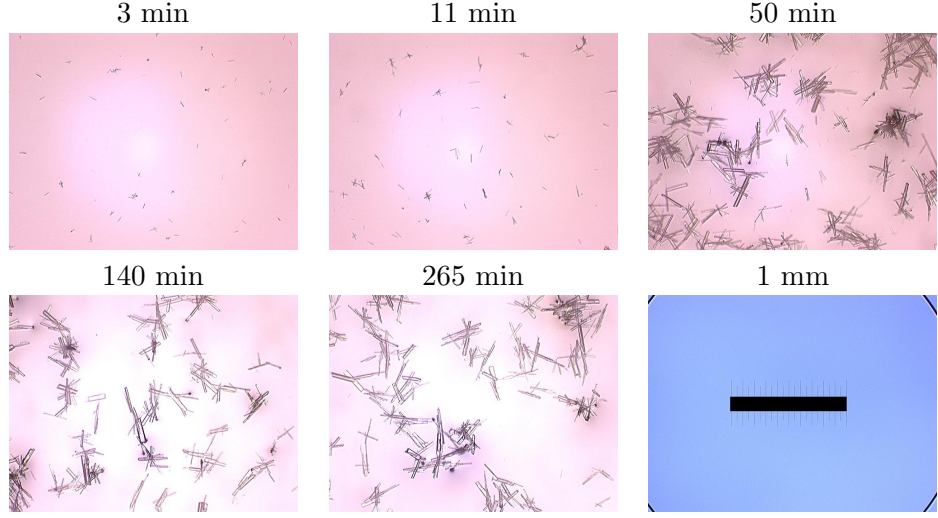


Figure 5.12: Growth of pharmaceutical seed crystals for run 16.

ter 4. The general batch crystallizer model is

$$\frac{d\mu_0}{dt} = 0 \quad (5.13)$$

$$\frac{d\mu_1}{dt} = G\mu_0 \quad (5.14)$$

$$\frac{d\mu_j}{dt} = jG\mu_{j-1} + j(j-1)D\mu_{j-2} \quad j = 2, 3 \quad (5.15)$$

$$\frac{d\hat{C}}{dt} = -3\rho_c k_v h G\mu_2 \quad (5.16)$$

$$\rho V C_p \frac{dT}{dt} = -3\Delta H_c \rho_c k_v V G\mu_2 - UA(T - T_j(t)) \quad (5.17)$$

The initial conditions for the moments, mass, and energy balances, respectively, are

$$\mu_j(t) = \mu_{0j} \quad j = 0, 1, 2, 3 \quad (5.18)$$

$$\hat{C}(t) = \hat{C}_0 \quad (5.19)$$

$$T(t) = T_0 \quad (5.20)$$

The kinetic parameters

$$\theta = \left[ \begin{array}{ll} k_g & : \text{growth rate constant} \\ g & : \text{growth rate order} \\ d_w & : \text{depth-to-width ratio} \\ L_{\max} & : \text{maximum seed size} \\ D & : \text{crystal diffusivity} \end{array} \right] \quad (5.21)$$

are estimated from experimental concentration, slurry transmittance, crystal mean size and standard deviation data collected for the pharmaceutical system by posing an NLP with a maximum likelihood objective function, Equation 2.7.

The residuals are based on the concentration, transmittance, CSD mean and standard deviation ( $k = 4$ ). Given the optimal model parameters,  $\hat{\theta}$ , the maximum-density estimate of the prediction variance for the  $k^{th}$  measurement type,  $\hat{\sigma}_k^2$ , is given by Equation 2.8

The confidence intervals for the model parameters may be determined according to Equation 2.9 with  $\alpha$  equal to 0.025. The sequential quadratic programming code NPSOL [32] is used to solve the unconstrained optimization problem.

The results for runs 13–16 are presented in Figures 5.13, 5.14, 5.15 and 5.16. The parameter estimates and their 95% confidence intervals are presented in Table 5.1. The parameter values are physically realistic, however, the parameters appear to vary as the cooling rate varies. In particular, Run 16 is an extreme experiment with the largest cooling rate as well as a rapid heating period after 35 min. Typically in crystallization systems, the parameter  $g$  is of order 0 to 3 and rate constants are only known to be positive. Runs 13 and 14 have low values for  $g$  being close to zero and a relatively large confidence interval for  $L_{\max}$ . The zero values for  $g$  indicate that the growth is constant for these experiments. The values of supersaturation are low for these experiments, due to the slow cooling rate. If the value of supersaturation is close to zero, within experimental error for the concentration measurement (see Appendix B), then it is difficult to estimate growth. Runs 13 and 14 are not considered informative.

The depth-to-width ratios for runs 13 and 16 differ considerably from the values for runs 14 and 15. The maximum seed size,  $L_{\max}$  agrees with off-line images of the seeds in which the largest size found is approximately  $10 \mu\text{m}$ . We chose to estimate  $L_{\max}$  because the model predictions are sensitive to small errors in  $L_{\max}$  estimated from off-line images of the seeds. However, large confidence intervals are found for  $L_{\max}$  for run 13 because of the few data points for the CSD mean and standard deviation. Therefore, we consider the parameters for run 13 inaccurate. The concentration, transmittance and mean length data are reasonably well-described by the model, however, the standard deviation predictions in Figure 5.16 for run 16 do not describe the data well and we consider the parameters for run 16 inaccurate. The standard deviation data show the system exhibits growth rate dispersion, however, once the supersaturation is zero, the crystal sizes do not disperse. The random fluctuation model, Equation 4.10 is not valid for this system because the second moment in Equation 5.15 increases when  $G$  is zero. The standard deviation data in Figures 5.14 and 5.16 do not show constant dispersion, so alternative models are necessary.

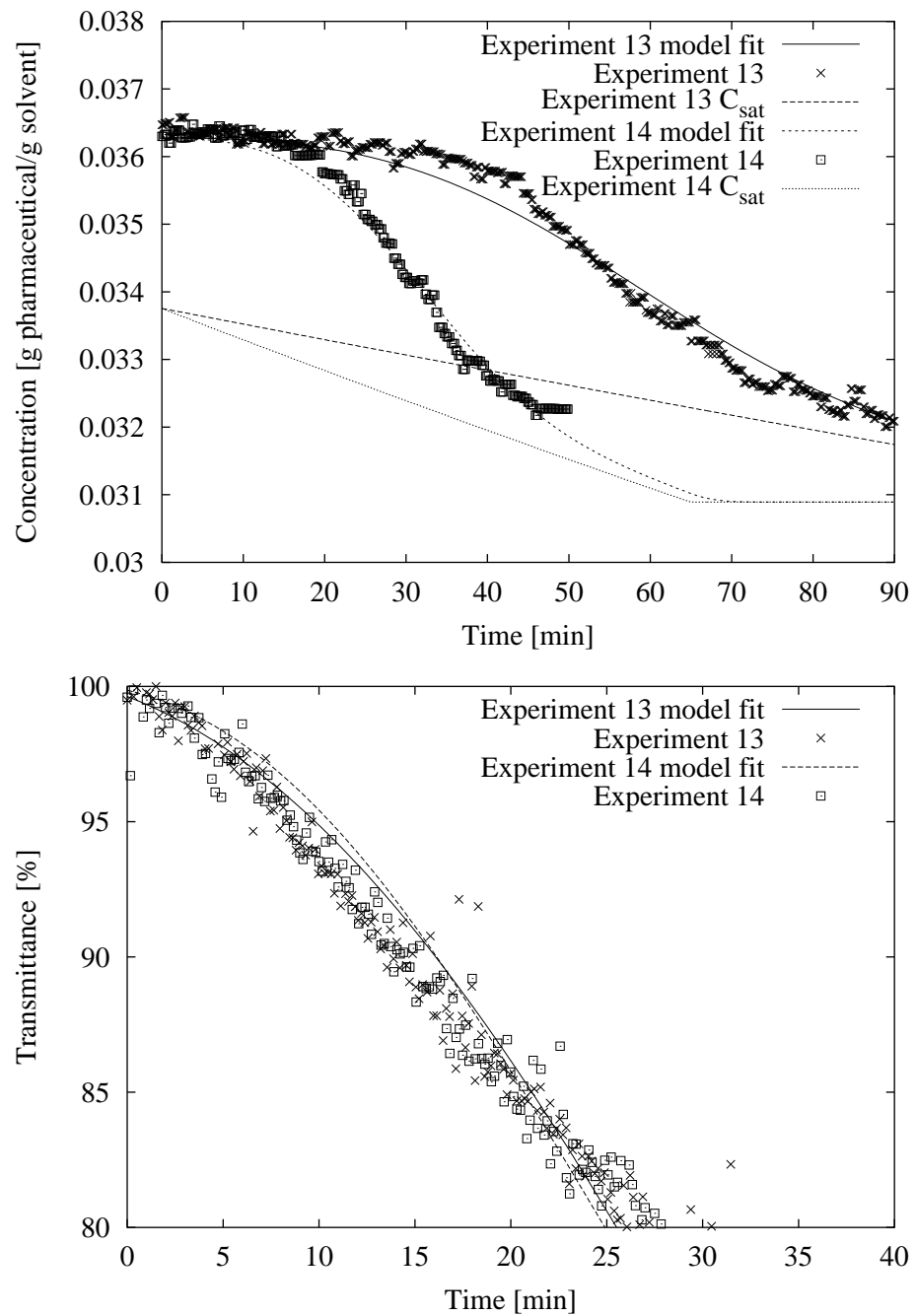


Figure 5.13: Concentration, transmittance and model fit for runs 13 and 14.

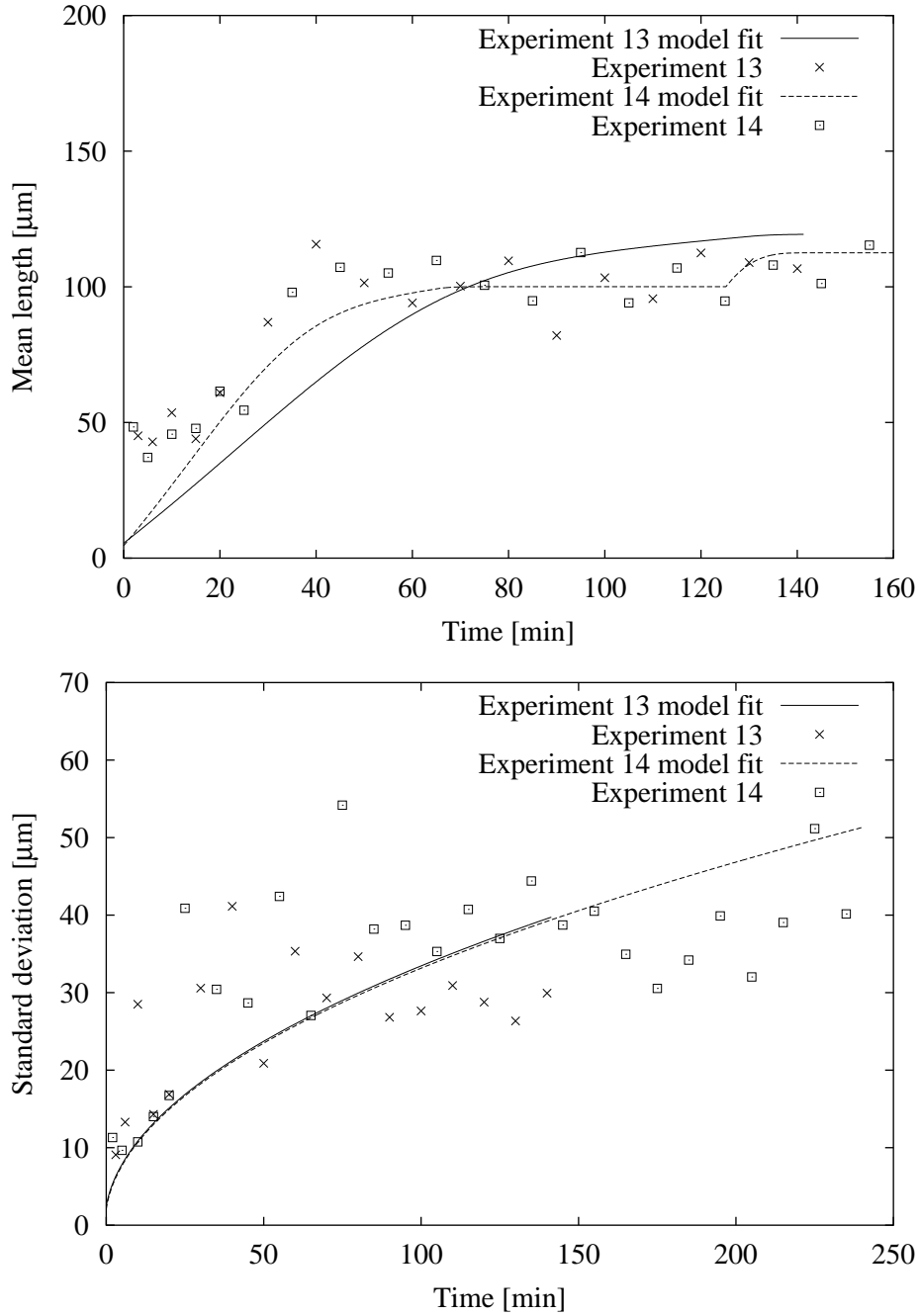


Figure 5.14: Mean length and standard deviation and model fit for runs 13 and 14.

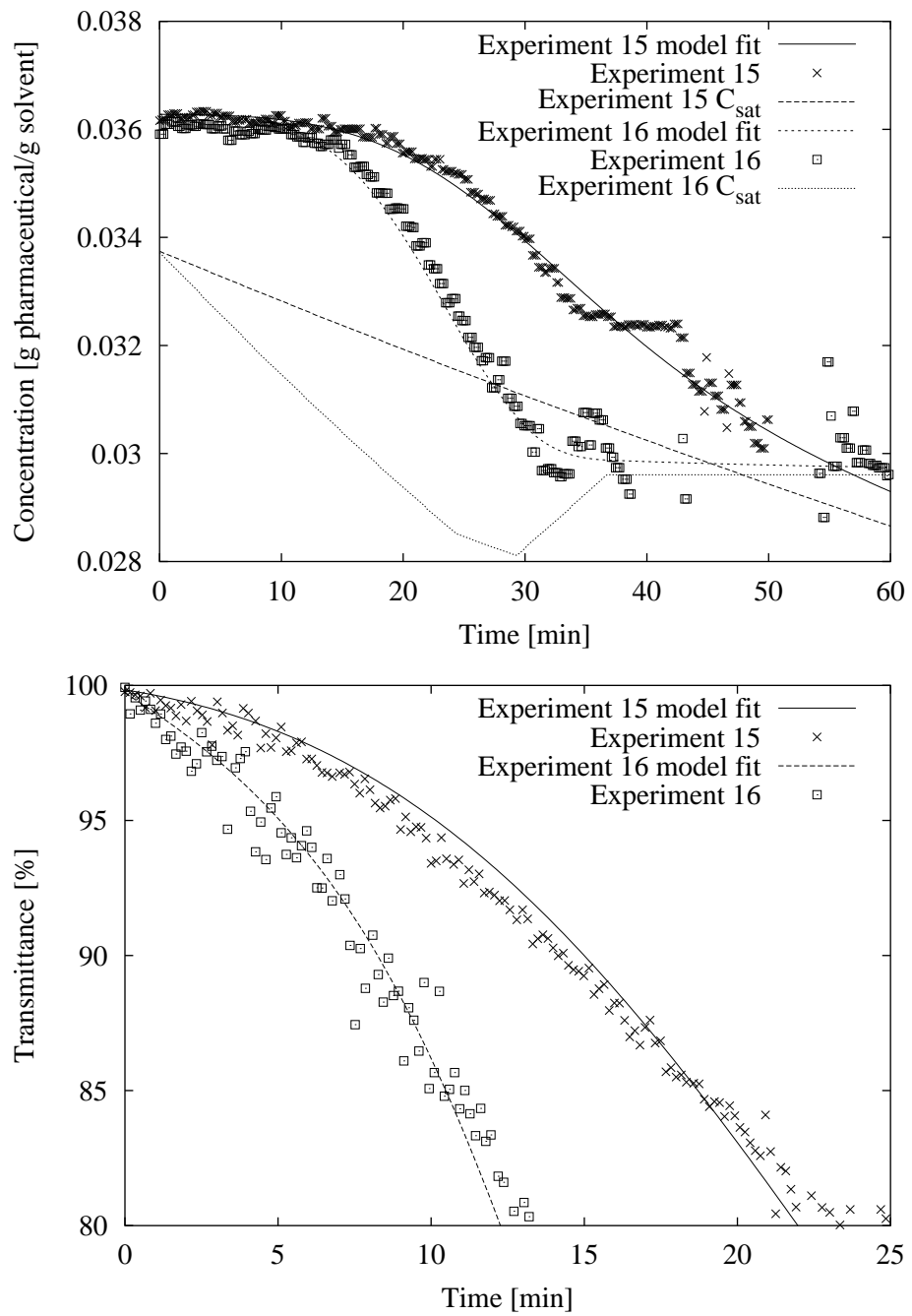


Figure 5.15: Concentration, transmittance and model fit for runs 15 and 16.

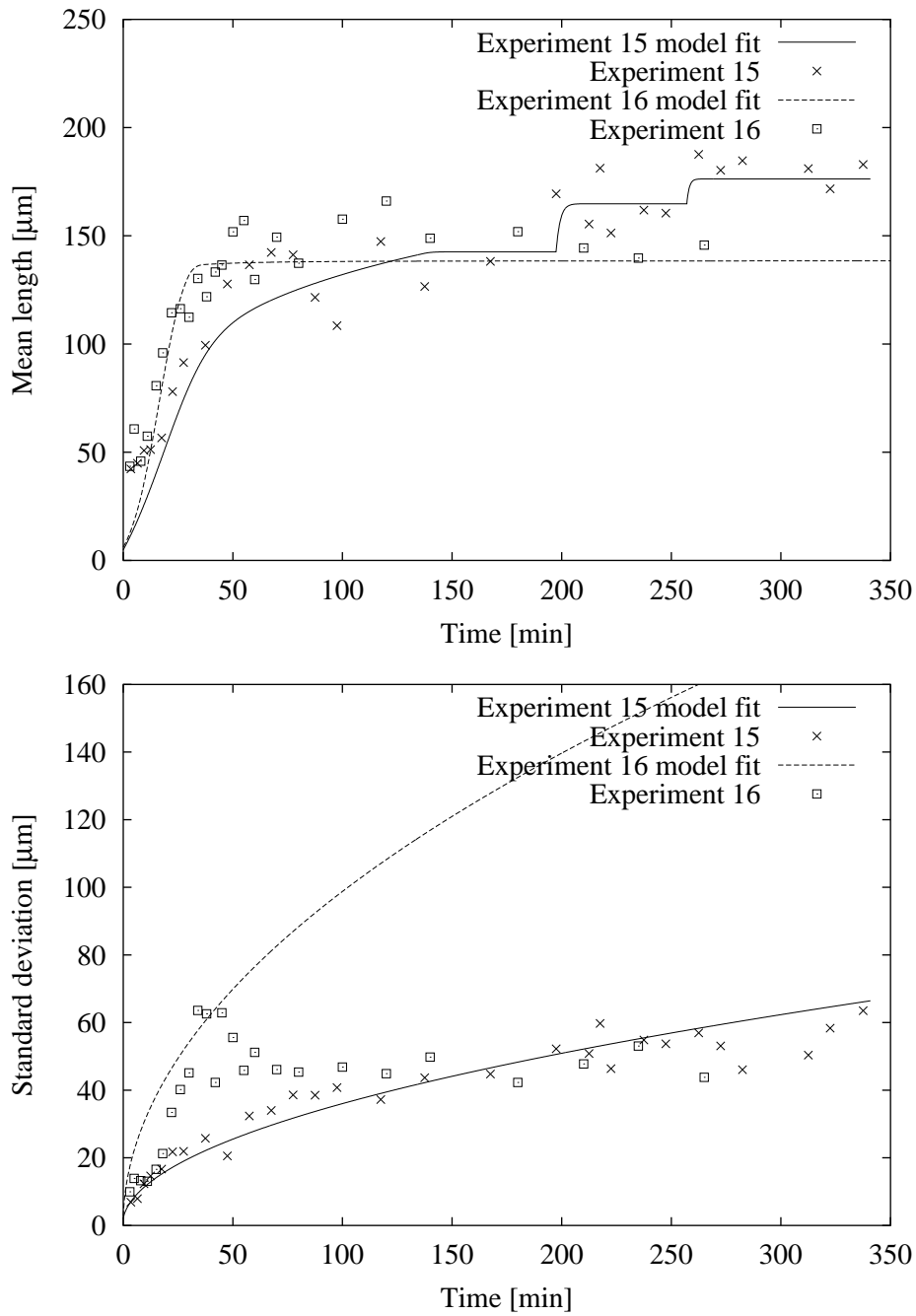


Figure 5.16: Mean length and standard deviation and model fit for runs 15 and 16.

	$\ln(k_g)$ $k_g [=] \text{cm} \cdot \text{min}^{-1}$	$g$	$\ln(d_w)$	$L_{max}$ $\mu\text{m}$	$\ln(D)$ $D [=] \text{cm}^2 \cdot \text{s}^{-1}$
Estimate (Run13)	-7.1	0.70	-3.2	11	-16.7
Interval	$\pm 0.3$	$\pm 0.06$	$\pm 0.2$	$\pm 2$	$\pm 0.4$
Estimate (Run14)	-6.7	0.69	-1.2	9.2	-16.7
Interval	$\pm 0.2$	$\pm 0.07$	$\pm 0.2$	$\pm 0.6$	$\pm 0.3$
Estimate (Run15)	-5.97	1.01	-1.7	9.8	-16.6
Interval	$\pm 0.02$	$\pm 0.07$	$\pm 0.1$	$\pm 0.4$	$\pm 0.1$
Estimate (Run16)	-4.7	1.54	-3.0	12.4	-14.5
Interval	$\pm 0.2$	$\pm 0.09$	$\pm 0.1$	$\pm 0.7$	$\pm 0.3$

Table 5.1: Parameter estimates and approximate 95% confidence intervals from concentration, transmittance, mean crystal length, and standard deviation measured for runs 13-16.

## 5.5 Alternative Model: Growth-dependent Dispersion and Dissolution

The CSD of a slurry in a batch crystallizer in which particles grow in discrete sizes of  $\Delta$  is modeled by the PBE given by Equation 4.12. Equation 4.12 is equivalent to Equation 4.10 with  $D = G(\Delta/2)$  and  $G$  given by Equation 4.5. The crystal diffusivity,  $D$ , in Equation 5.15 is replaced by  $G(\Delta/2)$  when solving Equation 4.12 by the method of moments.

The results for the growth-dependent dispersion model fit to run 16 are presented as fit 1 in Figures 5.17 and 5.18. The parameter estimates and their 95% confidence intervals are presented in Table 5.2. The model predictions for crystal size in Figure 5.18 underestimate the final mean size by 10  $\mu\text{m}$  and overestimate the final standard deviation in Figure 5.18 by 5  $\mu\text{m}$ . At saturation, the densitometer reading is noisy because of filter blinding and back-flushing of the sensor, however the mean reading remains close to the expected solubility concentration. The noisy concentration readings are removed from the objective function and the parameter estimation routine is repeated. The model fits and parameters are presented as fit 2 in Figures 5.17 and 5.18 and Table 5.2. The parameter values are similar to fit 1 except for a noticeable decrease in the value for the crystal growth order,  $g$ . It is difficult to predict concentration near saturation for this model. In particular, there is a rapid heating step between the 30 to 40 min period in which the concentration is close to and possibly less than the saturation concentration. The PBE only predicts growth when the concentration is greater than or equal to the saturation concentration. Once the concentration is equal to the saturation concentration, growth is zero, and the concentration, length and standard deviation predictions no longer change with the time-varying bulk temperature. Consequently, the final mean length size and standard deviation are overestimated. The system continues to increase in temperature so the solution concentration is less than the saturation concentration. The model does not have the predictive

capability for concentration once supersaturation is zero or negative. Model predictions for supersaturation close to zero are sensitive to noise in the concentration measurement and present difficulties in estimating parameters and predicting model states. We propose to add a dissolution model for cases in which predictions are required for concentration less than the saturation concentration.

	$\ln(k_g)$ $k_g [=] \text{cm} \cdot \text{min}^{-1}$	$g$	$\ln(d_w)$	$L_{\max}$ $\mu\text{m}$	$\ln(\Delta/2)$ $\Delta [=] \text{cm}$
Estimate (Run16) Fit 1	-5.71	1.06	-3.0	11.9	-6.9
Interval	$\pm 0.08$	$\pm 0.02$	$\pm 0.1$	$\pm 0.7$	$\pm 0.1$
Estimate (Run16) Fit 2	-6.1	0.80	-2.9	12.6	-7.1
Interval	$\pm 0.1$	$\pm 0.06$	$\pm 0.1$	$\pm 0.6$	$\pm 0.2$
Estimate (Run16) Fit 3	-5.8	0.97	-3.0	12.3	-7.1
Interval	$\pm 0.2$	$\pm 0.08$	$\pm 0.1$	$\pm 0.5$	$\pm 0.2$

Table 5.2: Parameter estimates and approximate 95% confidence intervals from concentration, transmittance, mean crystal length, and standard deviation measured for run 16.

Dissolution is a faster process than growth. A common equation to describe dissolution kinetics is an empirical power law equation similar to Equation 4.5

$$G_d = -k_d \left( \left| \frac{\hat{C} - \hat{C}_{\text{sat}}(T(t))}{\hat{C}_{\text{sat}}(T(t))} \right| \right)^d \quad (5.22)$$

in which  $k_d$  a dissolution rate constant and  $d$ , a dissolution order. We assume the crystal dissolution rate is large and rapid. During dissolution, the crystals liberate as much mass as possible to the bulk solution almost instantly and the under-saturated solution becomes saturated. In Chapter 6 we reduce the PBE model for high-growth systems. Similarly, the reduced model for dissolution in the case when  $\hat{C} < \hat{C}_{\text{sat}}(T)$  is derived as follows. For  $\hat{C} < \hat{C}_{\text{sat}}(T)$ , the model, Equation 4.12 is reduced by removing the large parameter,  $k_d$ , that is not estimable from these data. We take the limit  $k_d \rightarrow \infty$  and assuming  $\hat{C} \rightarrow \hat{C}_{\text{sat}}(T)$ . Given

$$\hat{C} = \hat{C}_{\text{sat}}(T) \quad (5.23)$$

and from Equation 4.2, we have

$$\frac{d\hat{C}}{dt} = \frac{d\hat{C}_{\text{sat}}(T)}{dt} = -3\rho_c k_v h G_d \int_0^\infty f(L, t) L^2 dL \quad (5.24)$$

Applying the chain rule and rearranging Equation 5.24 results in the reduced growth rate expression

$$G_d = \frac{-1}{3h\rho_c k_v} \left( \frac{1}{\mu_2} \right) \left( \frac{d\hat{C}_{\text{sat}}(T)}{dT} \right) \left( \frac{dT}{dt} \right) \quad (5.25)$$

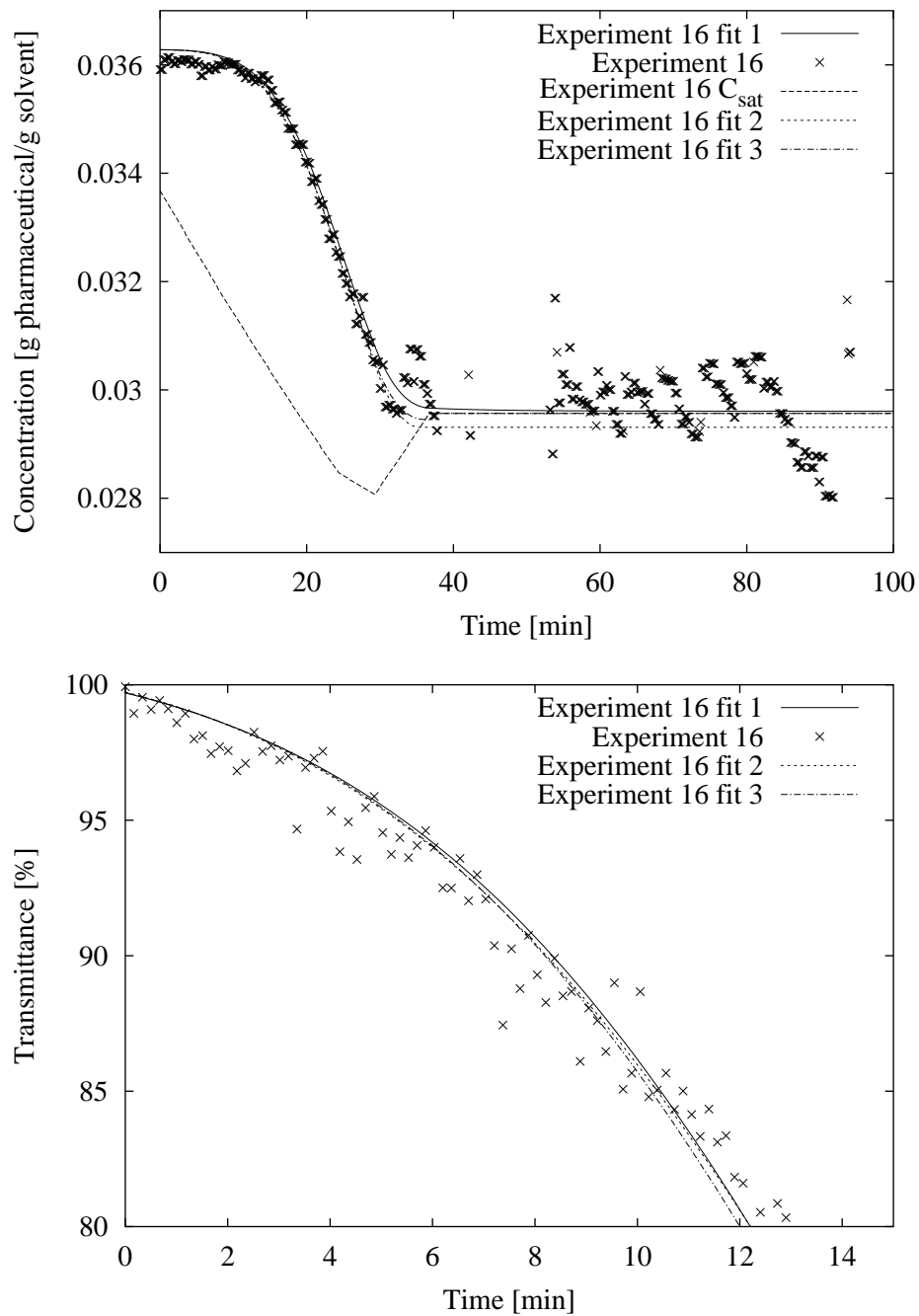


Figure 5.17: Concentration, transmittance and model fits for run 16.

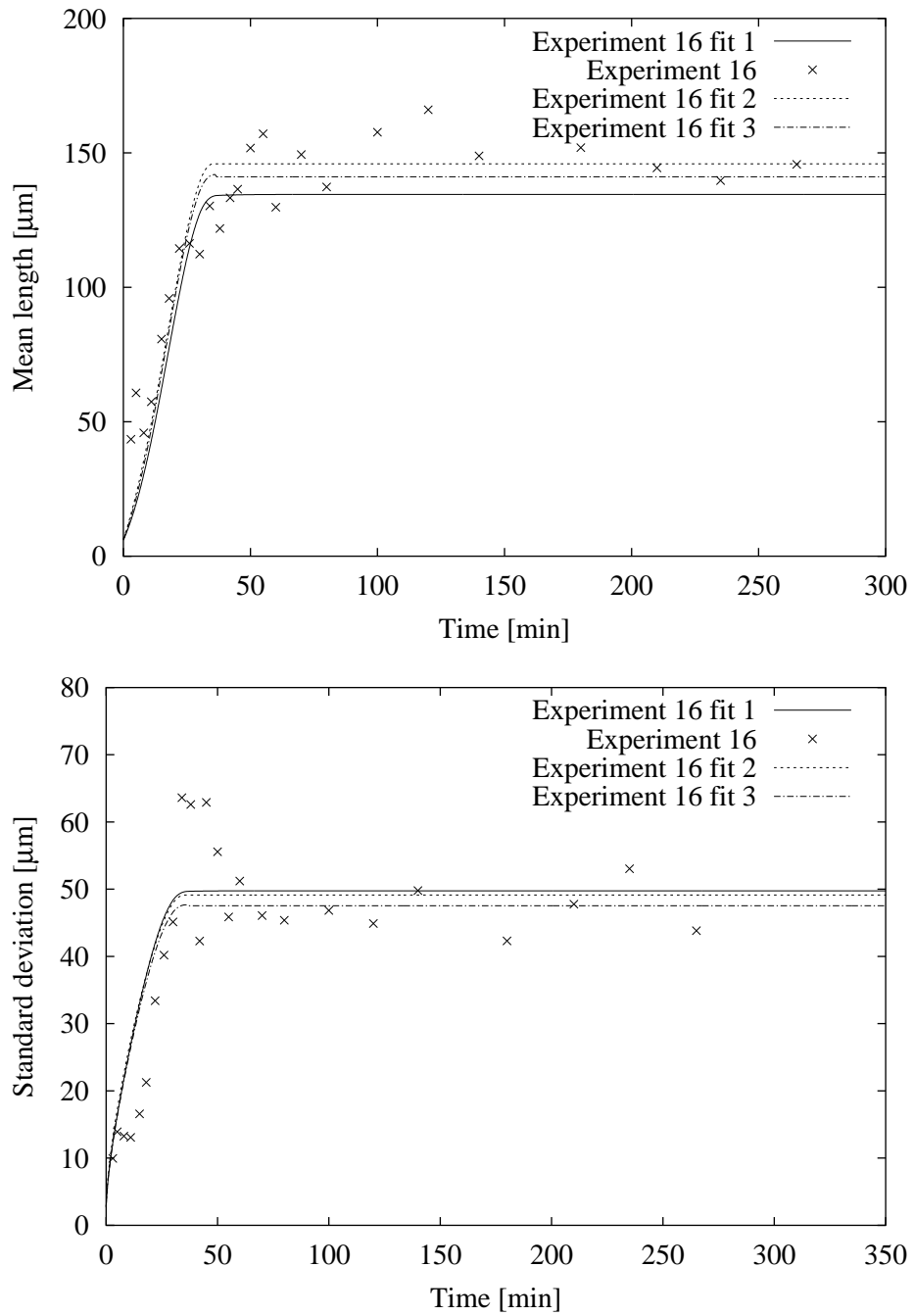


Figure 5.18: Mean length and standard deviation and model fits for run 16.

Substitution of Equation 5.25 into Equations 5.13, 5.14, and 5.15 results in the following expressions for the moments when  $\hat{C} < \hat{C}_{\text{sat}}(T)$

$$\frac{d\mu_0}{dt} = 0 \quad (5.26)$$

$$\frac{d\mu_1}{dt} = -\frac{1}{3h\rho_c k_v} \left( \frac{\mu_0}{\mu_2} \right) \left( \frac{d\hat{C}_{\text{sat}}(T)}{dT} \right) \left( \frac{dT}{dt} \right) \quad (5.27)$$

$$\frac{d\mu_2}{dt} = -\frac{2}{3h\rho_c k_v} \left( \frac{\mu_1}{\mu_2} - \frac{\mu_0}{\mu_2} \left( \frac{\Delta}{2} \right) \right) \left( \frac{d\hat{C}_{\text{sat}}(T)}{dT} \right) \left( \frac{dT}{dt} \right) \quad (5.28)$$

$$\frac{d\mu_3}{dt} = -\frac{1}{h\rho_c k_v} \left( 1 - 2 \frac{\mu_1}{\mu_2} \left( \frac{\Delta}{2} \right) \right) \left( \frac{d\hat{C}_{\text{sat}}(T)}{dT} \right) \left( \frac{dT}{dt} \right) \quad (5.29)$$

The results for the growth-dependent dispersion and dissolution model fit to run 16 are presented as fit 3 in Figures 5.17 and 5.18. The parameter estimates for fit 3 and their 95% confidence intervals are presented in Table 5.2. The concentration predictions in Figure 5.17 for fit 3 show that once the concentration is equal to the saturation concentration, and the solution is heated, the concentration predictions follow the saturation concentration line. During this time between 35 to 40 min, the mean length and standard deviation rapidly decrease. Fit 3 is a better fit than fit 1, the final mean length is accurately described, as well as the concentration and transmittance data. The standard deviation data are the most difficult to describe because the data points rely greatly on the sample size in each image. The standard deviation data, however, provide enough trend to show that this system exhibits growth-dependent dispersion.

### 5.5.1 Size-Dependent Growth Model Fit

The results for the size-dependent growth rate model fit to run 16 are presented in Figures 5.19 and 5.20. The parameter estimates and their 95% confidence intervals are presented in Table 5.3. The size-dependent growth model, Equation 4.32, describes the CSD mean and standard deviation, however, the model fits for concentration and transmittance are not as accurate as the fits for the growth-dependent diffusion model. The size-dependent growth rate model is useful for describing data that exhibits behavior similar to size-dependent dispersion because it predicts CSD standard deviation to remain constant at equilibrium, unlike the random fluctuation and intrinsic growth rate models. However, Equation 4.32 is not derived from any physical mechanism. The model assumes growth as an empirical function in size. The parameter values for  $g$  and  $d_w$  differ significantly from the values for  $g$  and  $d_w$  when using the random fluctuation or growth-dependent dispersion models because the size-dependent growth model is both a function of supersaturation and size. In the size-dependent growth model, growth is influenced by both supersaturation and size, so we would not expect  $\ln(k_g)$  and  $g$  to be similar to the growth-dependent dispersion model. Furthermore, the size of the confidence intervals for  $L_{max}$ ,  $\gamma_1$  and  $\ln(\gamma_2)$  suggests the model is invalid.

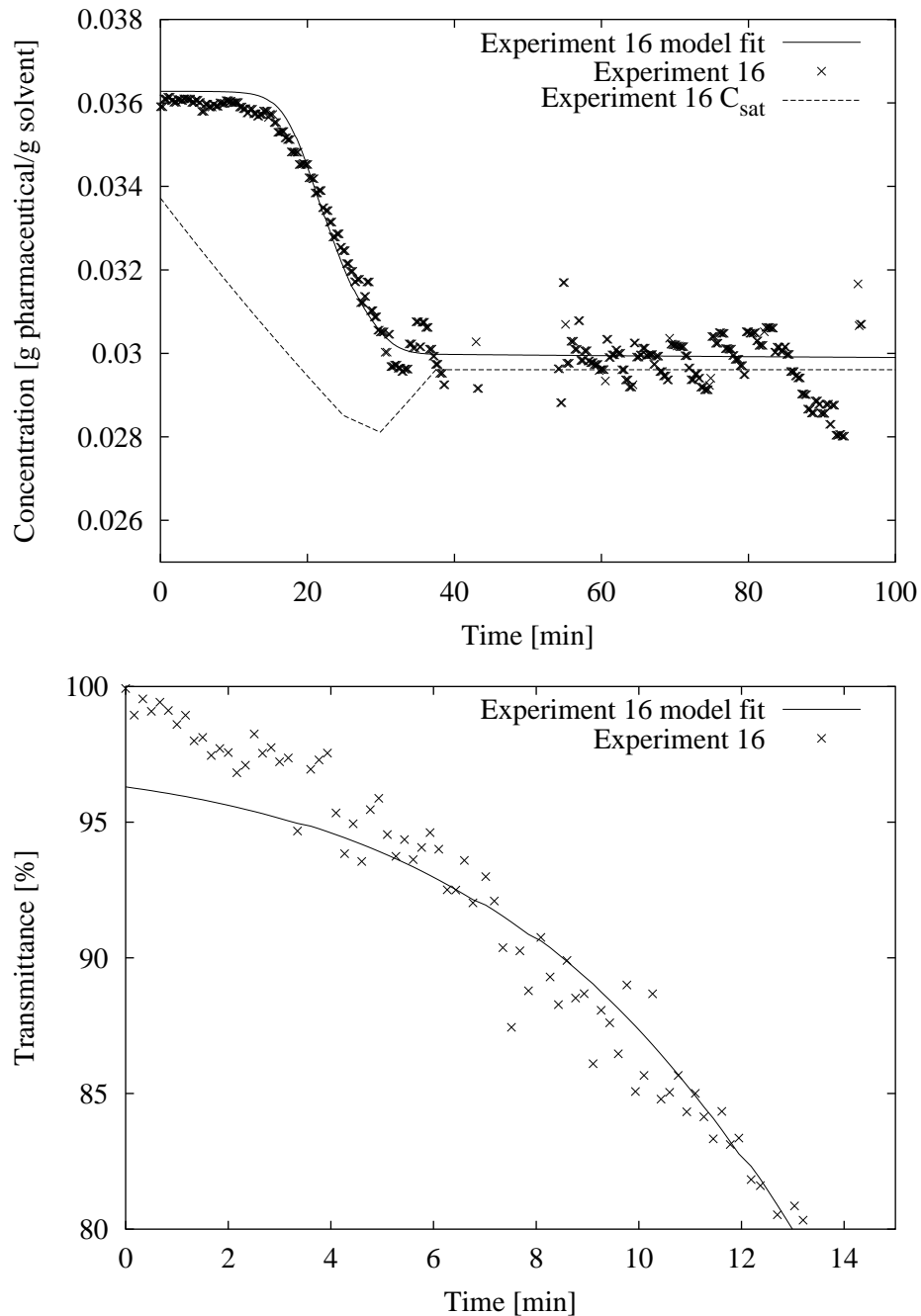


Figure 5.19: Concentration, transmittance data, and size-dependent growth rate model fits.

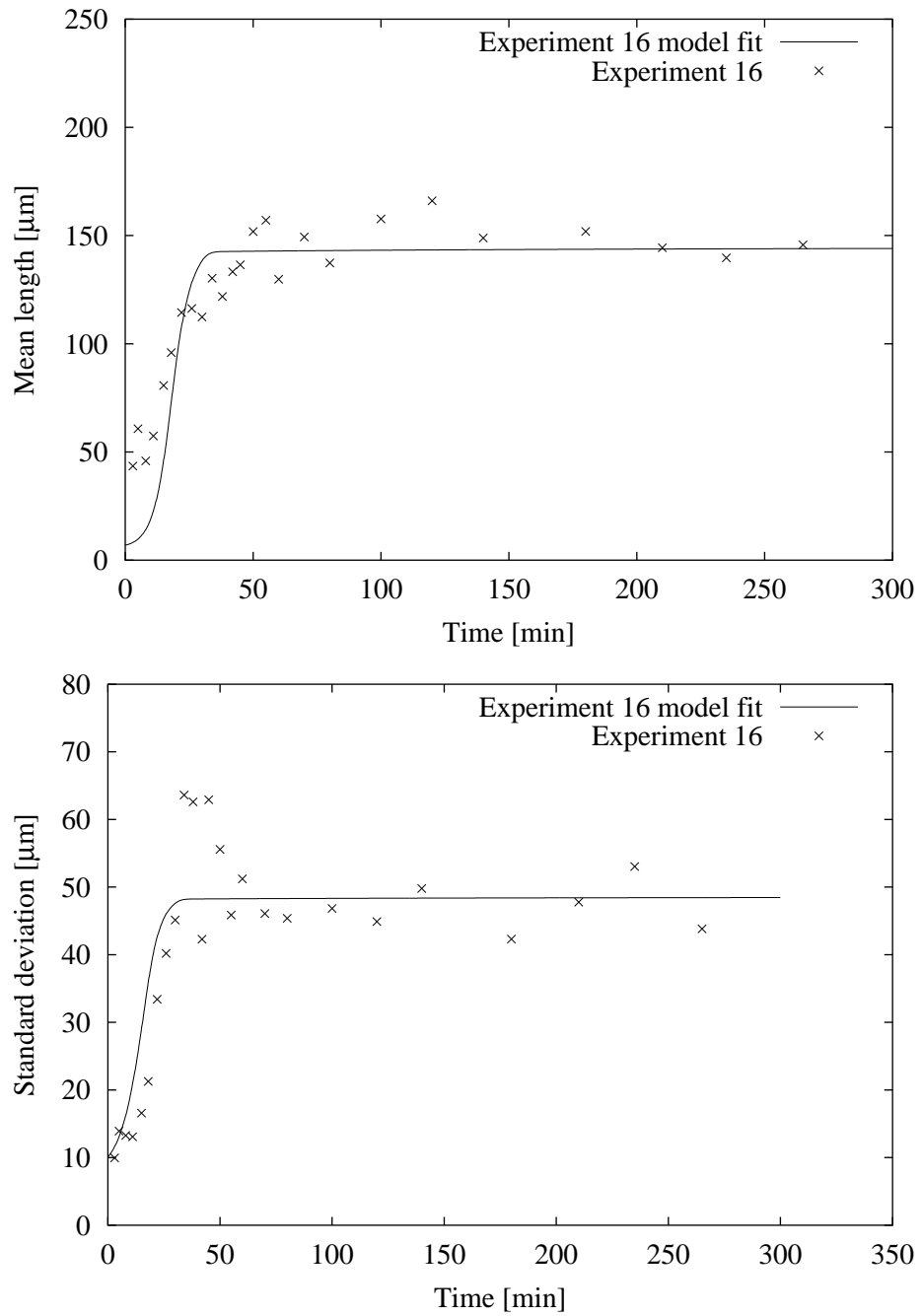


Figure 5.20: Mean length, CSD standard deviation, and size-dependent growth rate model fits.

	$\ln(k_g)$ $k_g [=] \text{cm} \cdot \text{min}^{-1}$	$g$	$\ln(d_w)$	$L_{\max}$ $\mu\text{m}$	$\gamma_1$	$\ln(\gamma_2)$
Estimate (Run16)	-6.6	2.60	2.73	13.9	0.4	14.5
Interval	$\pm 0.1$	$\pm 0.06$	$\pm 0.07$	$\pm 0.2$	$\pm 0.2$	$\pm 0.3$

Table 5.3: Size-dependent growth rate model parameter estimates and approximate 95% confidence intervals from concentration, transmittance, mean crystal length, and CSD standard deviation measured for run 16.

## 5.6 Best Operating Policies

The general statement of the open-loop optimal control problem is given by Miller and Rawlings [76] as an NLP problem. Temperature is the manipulated variable which is parameterized as piecewise linear. Nonlinear state constraints on the supersaturation and linear constraints on the temperature are also applied by Miller and Rawlings [76]. Chung et al. [21] study the effect of including parameters of the seed size density with the temperature as manipulated variables.

In the pharmaceutical industry, it is desirable to manufacture crystals between a specified size range. If the crystals are larger or smaller than the size range, they may not have the required bioavailability or the crystals may have stability issues. Usually, the pharmaceutical industry grows seeds of the approved polymorph and prevents secondary nucleation of undesirable polymorphs by maintaining a supersaturation well below the supersaturation in which secondary nucleation occurs. To maximize the amount of mass of final product into a size range, one possible objective is to minimize the coefficient of variation of the product CSD, with the mean constrained to the middle of the desired range. The coefficient of variation is defined as the ratio of the standard deviation to the mean. For a seeded crystallization with growth-dependent dispersion and no secondary nucleation, minimizing the coefficient of variation with a final mean size constraint is an over-specified problem. Given the initial seed CSD, any cooling profile that is implemented to take the process to the final required mean size will always produce a CSD with the same coefficient of variation. There is no minimum for this class of problem. A feasible objective is to minimize the batch operating time to achieve the final mean size and accept the resulting coefficient of variation of the product CSD.

An example of minimizing the batch operating time while growing the seed crystals to the final mean size of  $110 \mu\text{m}$  is given in Figure 5.21. Figure 5.21 shows the influence of the element size,  $\Delta t$ , over which the optimization problem is solved. For the simple case in which no temperature constraints are imposed, a positive supersaturation throughout the run and supersaturation zero at the end of the run, then the solution to the minimum batch time problem is  $2\Delta t$ .

The profiles in Figure 5.21 are trivial solutions to the minimum batch time process.

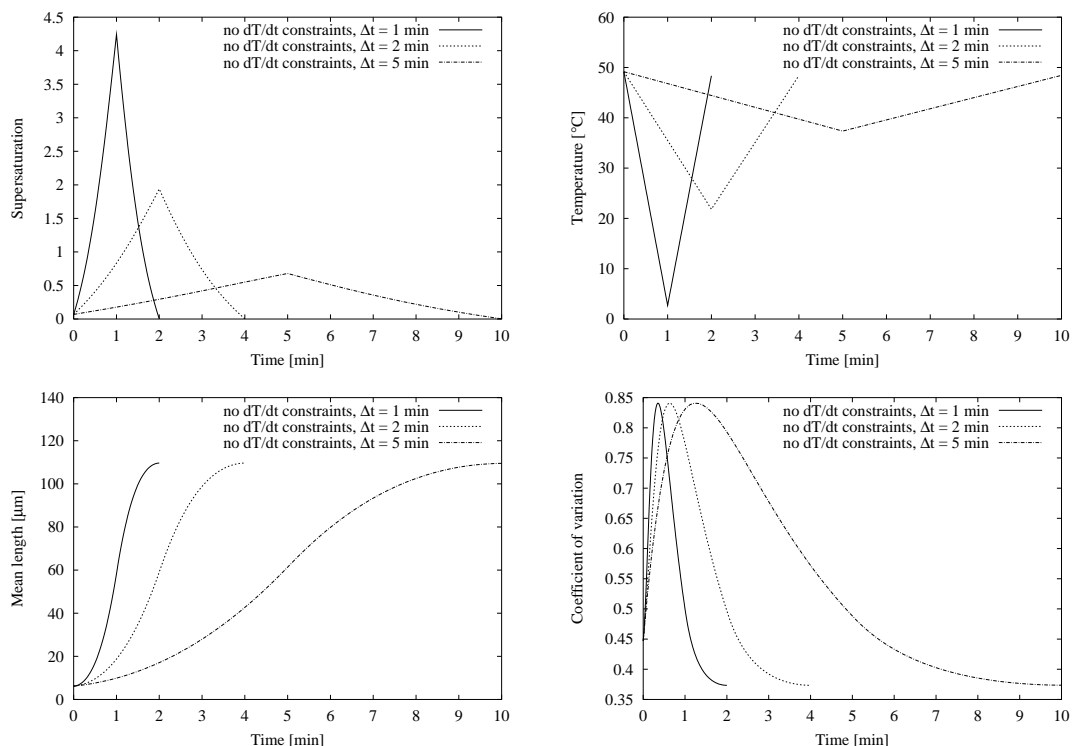


Figure 5.21: Supersaturation, temperature, mean length and CSD coefficient of variation for pharmaceutical crystallization. The profiles are for minimizing batch time with a final mean size constraint of  $110 \mu\text{m}$  and a final mean supersaturation constraint zero, without constraints on the cooling rate and supersaturation constrained to be positive.

Given a finite number of seeds and a final required mean size, then the solute mass required to be removed from solution and thus yield is specified. The first decision variable in the solution to the NLP is a temperature in which almost half the mass of required solute will come out of solution in the first time step. The second and final decision variable is the final temperature required to bring the supersaturation back to zero and remove the remaining solute from solution. In the limit, as the time step,  $\Delta t$ , approaches zero, the solution to the problem for supersaturation is a Dirac-delta function with area equal to the area under the supersaturation curve in Figure 5.21. Figure 5.21 shows once the mean size of the CSD has reached  $110 \mu\text{m}$ , the coefficient of variation is the same for all the profiles.

Figure 5.22 shows the solution to minimizing batch time while imposing a cooling rate constraint less than  $10^\circ\text{C}\cdot\text{hr}^{-1}$ . Figure 5.22 also shows the solution to minimizing batch time while imposing a cooling rate less than  $10^\circ\text{C}\cdot\text{hr}^{-1}$  and supersaturation constraint less than 0.1. The case in which no cooling rate constraints are imposed for a time step of 1 min, from Figure 5.21 is also shown for comparison. The solution for the minimum batch time for the cooling rate constrained profile is 31 min. If we impose a supersaturation constraint,  $S < 0.1$ , the minimum batch time to achieve the same size is 38 min. In the supersaturation constrained case, the cooling profile is identical for the first four minutes, after which the supersaturation constraint becomes active. At this point the cooling rate decreases a little to avoid violating the supersaturation constraint. The temperature continues to cool, drawing out enough mass to grow the crystals to the desired size. Once almost enough mass has been withdrawn from solution to achieve the final size, the temperature increases at a rate equal to the constraint and quenches the reactor to zero supersaturation at the point in which the crystal mean size is  $110 \mu\text{m}$ .

We implement the two experimental designs for the cooling rate constrained case (run 18) and the supersaturation constrained case (run 20). The concentration and transmittance data with predictions based on the parameters in Table 5.2 from the experimental design are shown in Figure 5.23. The mean length and standard deviation data with predictions are shown in Figure 5.24. The concentration data are close to the concentration predictions. The transmittance readings do not closely follow the predictions, however, the data for run 20 is mostly slower than run 18 as predicted. The crystal mean length and standard deviations agree within error with the model predictions. At times, the mean size data do not closely follow the model predictions. In run 20, we detect a lower growth rate than run 18, as expected. The standard deviation data are not expected to agree well with the predictions, because of the difficulty with varying sample sizes. Given the amount of noise in the crystal size data, we are able to achieve the required mean size with  $10 \mu\text{m}$ .

## 5.7 Conclusions

This article has shown that the predictions of the identified crystallizer model show good agreement for the concentration and light transmittance readings for crystallization of an industrial pharmaceutical with growth-dependent dispersion. However, the prediction of

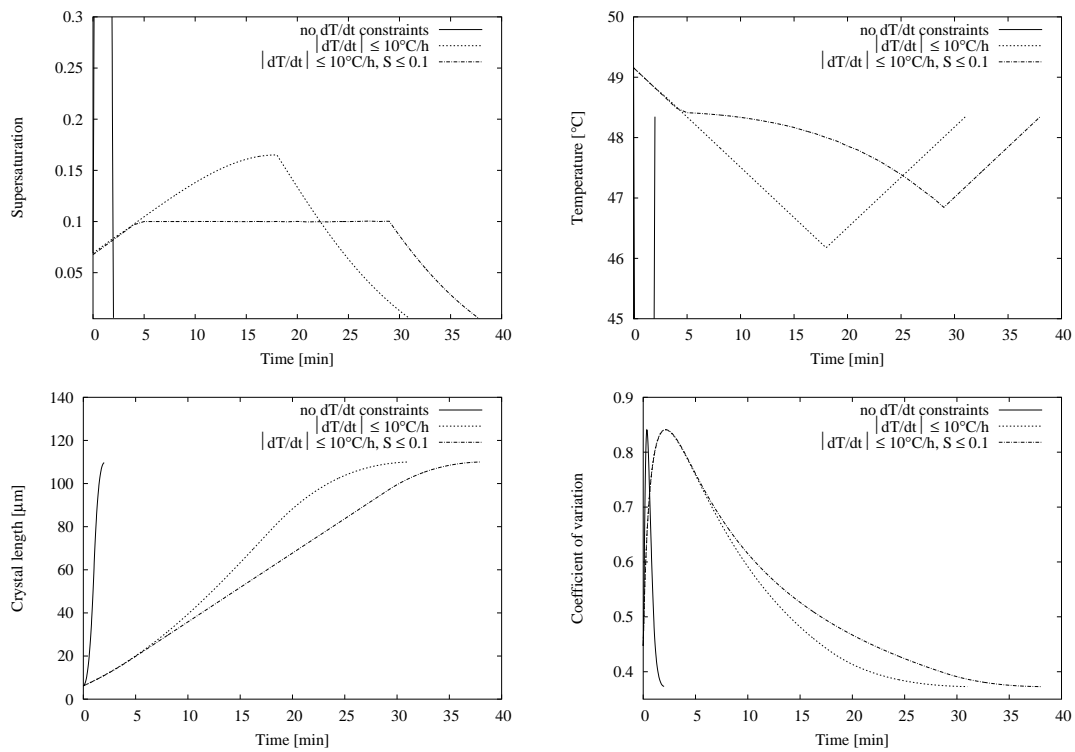


Figure 5.22: Supersaturation, temperature, mean length and CSD coefficient of variation for pharmaceutical crystallization. The profiles are for minimizing batch time with a final mean size constraint of  $110 \mu\text{m}$  and a final mean supersaturation constraint zero, with constraints on the cooling rate and supersaturation constrained between zero and 0.1. The two constrained profiles are compared with the unconstrained cooling rate case for a  $\Delta t$  of 1 min.

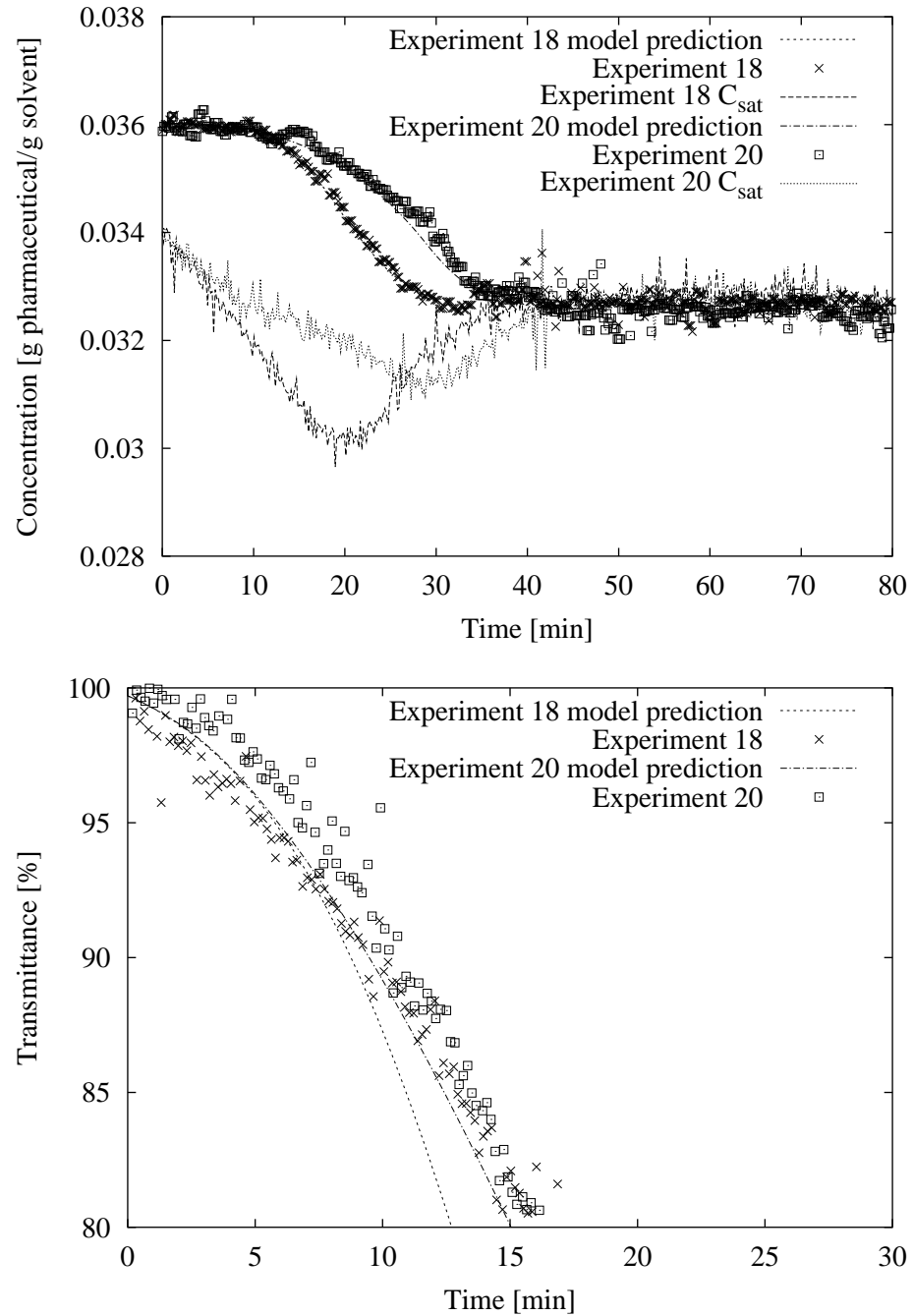


Figure 5.23: Concentration and temperature experimental data for temperature rate constrained and supersaturation constrained experiments with model predictions.

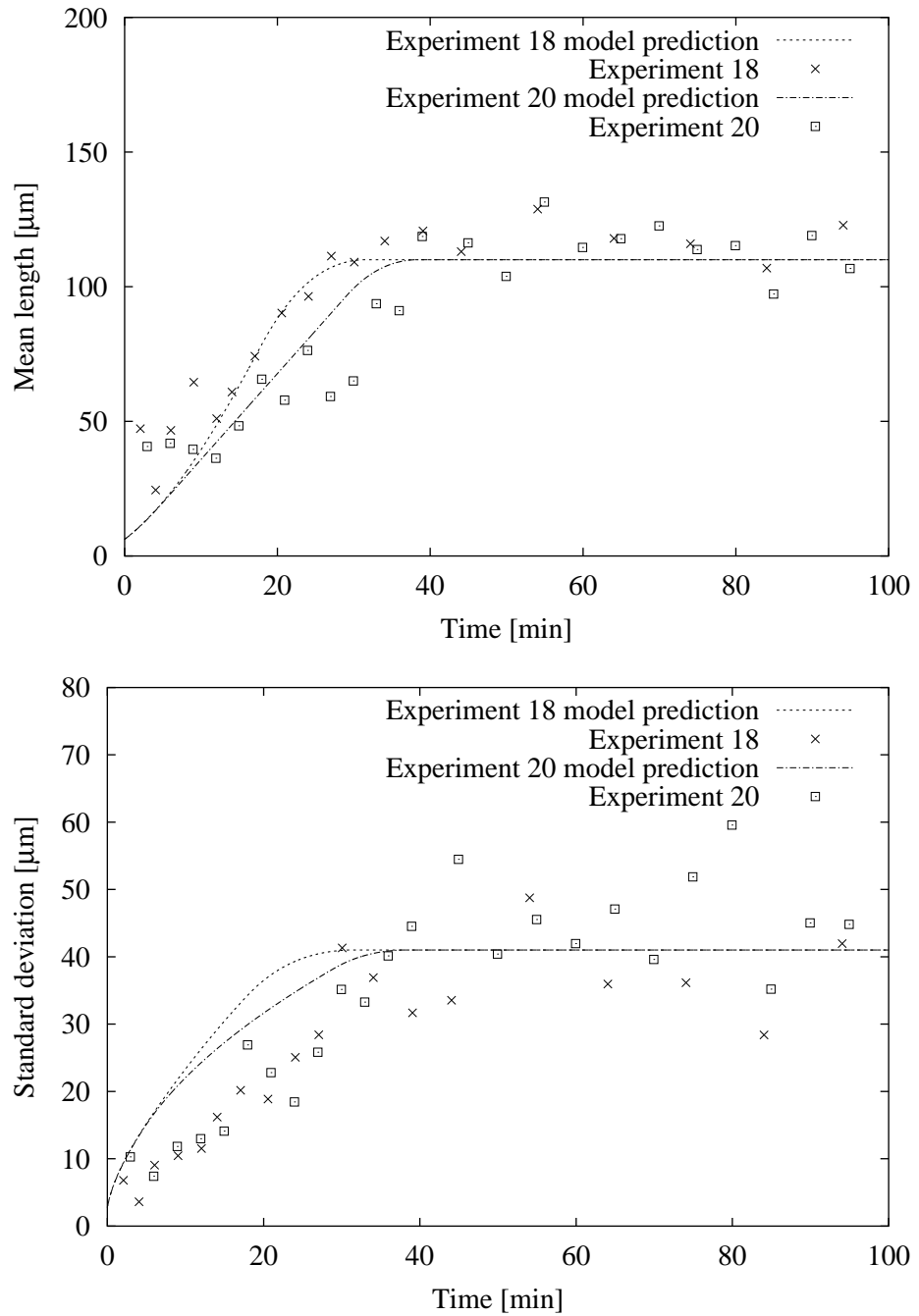


Figure 5.24: Mean length and standard deviation experimental data for temperature rate constrained and supersaturation constrained experiments with model predictions.

the final mean size and CSD standard deviation for image analysis measurements are difficult to describe when a system is suddenly quenched to saturation. Therefore, we derive and append a reduced dissolution model to the PBE and obtain good agreement with all the measurements, concentration, light transmittance, and CSD mean size and standard deviation from image analysis of photo-micrographs of the crystal slurry.

Minimizing the coefficient of variation of the product CSD is a standard experimental design objective, however, when subject to terminal constraints such as yield or final mean size, the objective is over-specified for growth-dependent dispersion systems with no secondary nucleation. Instead, the minimization of the operating time subject to a final CSD mean size is appropriate. The effects of cooling rate and supersaturation constraints on the minimal operating time are investigated for the pharmaceutical. These optimal experimental designs are implemented and the concentration and CSD mean size predictions are found to closely agree with the data.

Increased seed loads can, of course, be used to increase the final yield if required. However, designing experiments with increased yield for a minimal operating time to achieve a final size constraint would require model identification of experiments outside of the temperature range and seed load studied.

## Chapter 6

# Information-Poor Systems: Industrial Polymer Precursor<sup>1</sup>

*There is no lower bound for stupidity*

— Pannocchia, G.

In this chapter, crystallization kinetics of para-xylene in batch pilot-scale scraped-surface crystallizers are determined for commercial crystallization of a xylene mixture currently produced in Amoco plants. Dynamic mass and energy balances coupled with the dynamic population balance are used to model the scraped-surface crystallizer. The model assumes that crystal nucleation occurs at the walls of the crystallizer and that crystal growth occurs in the bulk. The parameters in the kinetic models are estimated from on-line measurements of bulk temperature and slurry transmittance. Concentration measurements show that the xylene mixture is always saturated (supersaturation is essentially zero) during all crystallization runs. Therefore, a reduced, 2-parameter, high growth rate model is developed to describe these crystallizers. The kinetic parameters for the reduced model are highly correlated and a new batch experiment with an alternative temperature profile is determined that removes the correlation and allows both parameters to be determined uniquely.

---

<sup>1</sup>Portions of the chapter are published in Patience et al. [89]

## 6.1 Introduction

Xylene mixtures, consisting of ortho-xylene, para-xylene, meta-xylene and ethyl-benzene, are produced mainly from petroleum. Selected naphtha streams from reformed petroleum are used to produce the xylene mixture. Para-xylene is a base chemical for the production of terephthalic acid (TPA) and dimethylterephthalate (DMT). These products are used for the production of fibers, films and polyethyleneterephthalate (PET) bottle manufacturing.

Many physical properties of the individual xylene isomers are similar. Consequently, the production of individual xylene isomers of high purity is difficult. Crystallization is one of the practical methods for the commercial production of pure para-xylene. Several commercial crystallization processes have been developed to separate para-xylene from its isomer mixture, often named after the company that applied the process. Among these is the Amoco process [61, 127, 48], which is studied in this work. Other processes, such as the Chevron, Arco, Phillips and Exxon processes, are described in more detail by Ransley [108] and Arkenbout [4]. A schematic diagram for the Amoco process is shown in Figure 6.1. The Amoco process uses two or more scraped-surface crystallizers (SSCs) in the first stage to bring the temperature of the xylene mixture to the para-xylene/meta-xylene eutectic point. The first-stage crystallization process is followed by a solid-liquid separation process using centrifuges. The cold xylene filtrate (usually called the mother liquor), from the first stage cools the feed stream and is sent to the isomerization process. To achieve the maximum production rate from a certain feed stock, the first-stage mother liquor should contain the eutectic para-xylene/meta-xylene concentration. The solid cake para-xylene crystals and the adherent mother liquor are melted and pumped to the second-stage crystallizer. The product from the second-stage crystallizer is pumped to the final centrifuges. A portion of the second-stage mother liquor is returned to the second-stage crystallizers to control the solids concentration and the remainder is pumped with the feed to the first-stage crystallizers. The cake from the second-stage crystallizer is melted to form the final para-xylene product. This process described in Figure 6.1, however, is not necessarily practiced commercially today. As the costs for melting the cake from the first stage and using second-stage crystallization become higher, process alternatives become attractive. One alternative is to re-slurry the first-stage cake with a higher purity para-xylene stream coming from a later stage of purification [19].

Pure para-xylene crystals can be separated in one stage since para-xylene forms a eutectic with meta-xylene. However, the separation of the mother liquor from the para-xylene crystals is difficult and is greatly influenced by the crystal size density, and so the process variables governing nucleation and growth are of importance. Understanding and improving the crystallization process leads to a better solid-liquid separation process. Even with new alternatives such as the re-slurrying step instead of the second-stage crystallizers, controlling the crystal size density from the first stage is still of importance.

A typical temperature-time data set for the para-xylene scraped-surface crystallizer in Figure 3.2 is shown in Figure 6.3. The difference between the middle temperature ( $T_1$ )

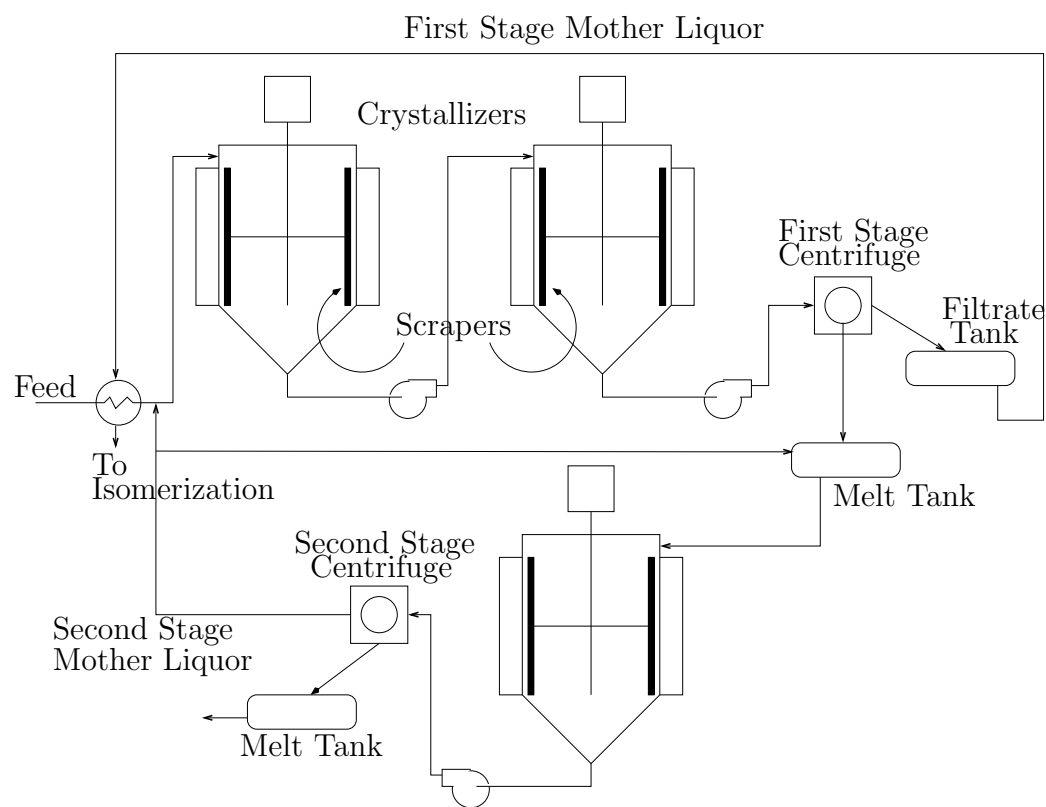


Figure 6.1: The Amoco para-xylene crystallization process.

and the top temperature (T2) is less than 0.1 K and the maximum difference between the middle and recirculation temperature is not more than 0.2 K. Therefore, the temperature is assumed to be homogeneous in the crystallizer and the modeling in this work is based on the middle temperature, T1. The small difference between the three temperature measurements, T1, T2, and T3 shows good mixing conditions inside the crystallizer. The outlet jacket temperature is warmer than the inlet jacket temperature by 0.4 to 0.8 K. Since the difference is not large, the outlet jacket temperature is accepted to be the jacket temperature in the simulations.

Typical off-line concentration data taken from the sample port (Figure 3.2) are shown in Figure 6.2. The equilibrium concentration (solid line) is calculated from Equation B.3. These concentration data will be used later for model reduction.

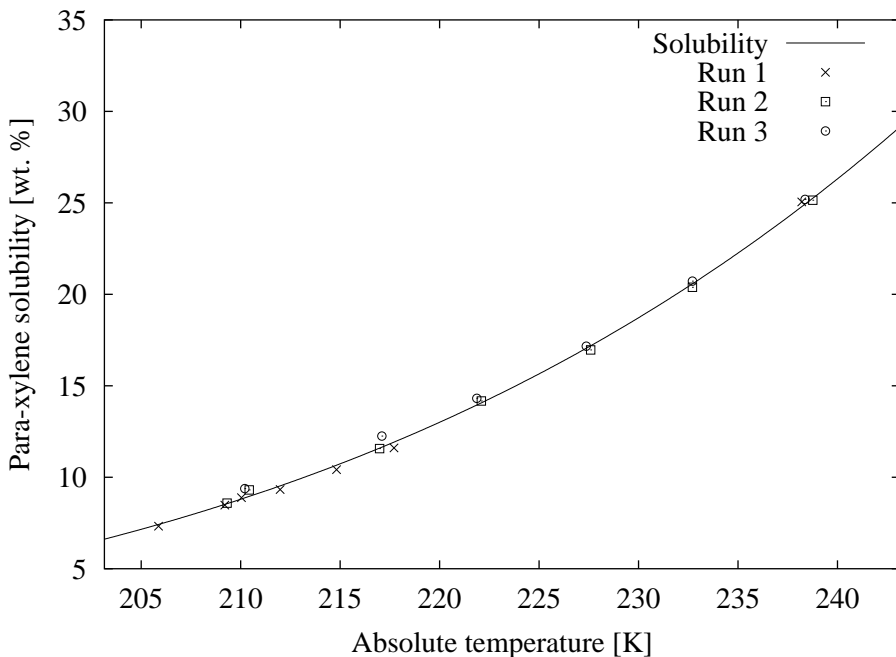


Figure 6.2: Comparison between the experimental gas chromatography (GC) measurements (symbols) and the equilibrium concentration (solid line) for three different runs. The solubility is calculated from Equation B.3 and the physical properties of para-xylene in Table B.2.

The objective of this work is to model SSCs incorporating both crystal nucleation and growth kinetics using dynamic temperature and transmittance data.

## 6.2 Initial Estimation of Kinetic Parameters

The PSD of a slurry in a batch SSC is modeled by the PBE, Equation 4.1. The solution phase is described by the mass balance given by Equation 4.2. The bulk temperature is described by an energy balance given by Equation 4.3. An average value for the overall

heat transfer coefficient,  $U$  is calculated from the experimental data and found to be 5085  $\text{W}\cdot\text{m}^{-2}\cdot\text{K}^{-1}$ . For these experiments<sup>2</sup> the volume shape factor,  $k_v$  is taken to be 1.

The kinetic expressions are taken to be empirical power-laws in supersaturation. It is assumed in this model that nucleation is mainly occurring on the wall of the crystallizer due to the high temperature difference between the coolant and the bulk, while growth occurs in the bulk. Therefore, the driving force for nucleation is the difference between the bulk concentration and the saturation concentration calculated at the wall temperature. It is assumed that the wall temperature is the same as the jacket temperature because the values of the heat conductivities of the material of construction and the para-xylene layer on the wall are  $12.75 \text{ W}\cdot\text{m}^{-1}\cdot\text{K}^{-1}$  and  $0.29 \text{ W}\cdot\text{m}^{-1}\cdot\text{K}^{-1}$ , respectively, and the resistance through the 8 mm thick wall is negligible compared to the heat transfer through the bulk. The para-xylene forms a uniform layer on the wall with an average thickness of 0.5 mm, measured from heat transfer data. This suggests that the wall resistance can be neglected and the wall temperature can be taken as the jacket temperature. The nucleation kinetics are described by the following empirical expression, similar to Equation 4.4.

$$B = k_b \left( \frac{\hat{C} - \hat{C}_{\text{sat}}(T_j(t))}{\hat{C}_{\text{sat}}(T_j(t))} \right)^b \quad (6.1)$$

The driving force for the growth rate is the difference between the bulk concentration and the saturation concentration calculated at the bulk temperature. The growth kinetics are described by Equation 4.5. The parameters  $k_b$ ,  $b$ ,  $k_g$ , and  $g$  are inferred from experimental data.

The Beer-Lambert law, Equation 2.14 is used to relate the transmittance measurement to the second moment,  $\mu_2$  of the PSD.

$$\frac{I}{I_0} = \exp \left( -\frac{l k_a}{2} \mu_2 \right) \quad (6.2)$$

$I$  is the intensity of the light transmitted through the slurry,  $I_0$  is the intensity of the incident light,  $l$  is the beam length (m), and  $k_a$  is the area shape factor. For these experiments, the area shape factor is 6.

The zero-size boundary condition, Equation 4.6 is used in the PBE for modeling the SSC. The PBE, Equation 4.1 is solved using the method of moments described in section 4.2.1.

The general batch crystallizer model Equations 4.1, 4.2 and 4.3 require the first four moments to be determined, Equations 4.22 and 4.23. The integral terms in the mass and energy balances (Equations 4.2 and 4.3) are replaced by  $\mu_2$  resulting in Equations 4.24

---

<sup>2</sup>At the time of these experiments, we were unable to obtain images of the crystal slurry, so we assume a simple cubic geometry.

and 4.25. The initial conditions for moments, mass and energy balances, respectively, are

$$\mu_j(t) = 0, \text{ for } j = 0, 1, 2, 3 \quad (6.3)$$

$$\hat{C}(t) = \hat{C}_0, \quad (6.4)$$

$$T(t) = T_0, \quad (6.5)$$

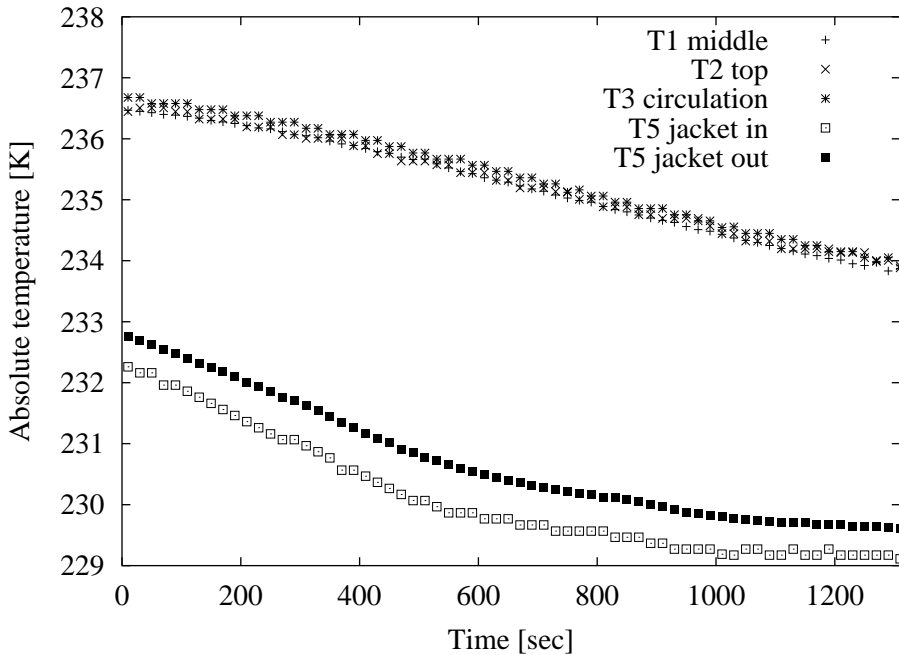


Figure 6.3: Typical collected temperature data from the pilot-plant scraped-surface crystallizer in Figure 3.2, run 15. Cooling rate =  $0.2 \text{ }^{\circ}\text{F} \cdot \text{min}^{-1}$ .

The kinetic parameters given in Equations 6.1 and 4.5 are estimated from experimental data for xylene mixtures. The parameter vector of the model has the form:

$$\theta = \begin{bmatrix} k_g & : & \text{growth rate constant} \\ g & : & \text{growth rate order} \\ k_b & : & \text{nucleation rate constant} \\ b & : & \text{nucleation rate order} \end{bmatrix} \quad (6.6)$$

The parameters were estimated by posing an NLP with the Bayesian objective function of Equation 2.7. The method may be summarized in the following statement of the unconstrained NLP.

$$\begin{aligned} \min_{\theta} \quad & \Phi_{\text{be}}(\mathbf{Y}, \tilde{\mathbf{Y}}(\theta); \hat{\sigma}) \\ \text{subject to:} \quad & \text{crystallizer model} \end{aligned} \quad (\text{NLP2})$$

The sequential quadratic programming code NPSOL [32] was used to solve this unconstrained optimization problem.

The results for two replicated runs (14 and 15)<sup>3</sup> are presented in Figures 6.4 and 6.5. The two experiments, 14 and 15 are almost identical and show good reproducibility. The parameter estimates and their 95% confidence intervals are presented in Table 6.1. The temperature data are reasonably well described by the model, which under-predicts slightly at early times and over-predicts slightly for latter times. The transmittance data are also well described by the model in the region of single light scattering (transmittance >74%). The parameter values are physically realistic. Typically, in crystallization systems,  $b$  and  $g$  are of the order of 0 to 3 whereas the rate constants,  $k_b$  and  $k_g$  are only known to be positive. Second derivatives for calculating the Hessian at the local optimum are difficult to obtain because the objective function is essentially flat in at least one direction of the parameter space. The Gaussian approximation to the Hessian is used instead of second order finite differences and converges to a solution using a step-size of  $10^{-3}$  to  $10^{-6}$ . The size of the confidence intervals suggests that the model is over-parameterized or there are insufficient data and/or measurement types to identify uniquely the four parameters. Thus, revisions of the model are required.

Table 6.1: Parameter estimates and approximate 95% confidence intervals resulting from the temperature and transmittance measurements for runs 14 and 15.

	$\ln(k_g)$	$g$	$\ln(k_b)$	$b$
Estimate (Run14)	-2.85	0.68	9.75	0.05
Interval	$\pm 297$	$\pm 37$	$\pm 12$	$\pm 6$
Estimate (Run15)	3.61	0.80	10.80	0.44
Interval	$\pm 1000$	$\pm 113$	$\pm 14$	$\pm 7$

### 6.3 Model Reduction: High Growth Rate Limit

The concentration measurements in Figure 6.2 show that the bulk concentration of para-xylene is within gas chromatography (GC) experimental error of the equilibrium concentration during the entire crystallization run. We assume, therefore, the para-xylene growth rate is large and rapid growth depletes any supersaturation in the bulk of the crystallizer almost instantly and deposits the para-xylene solid on the available crystals in the bulk and nuclei scraped from the walls. We do not expect to be able to operate this class of crystallizer outside of this high growth regime.

In order to reduce the model and remove the large parameter,  $k_g$ , that is not estimable from these data, we take the limit  $k_g \rightarrow \infty$  and we know  $C \rightarrow C_{\text{sat}}(T)$ , which is verified in Figure 6.2. Given

$$\hat{C} = \hat{C}_{\text{sat}}(T) \quad (6.7)$$

---

<sup>3</sup>These are different runs 14 and 15 in Chapter 5

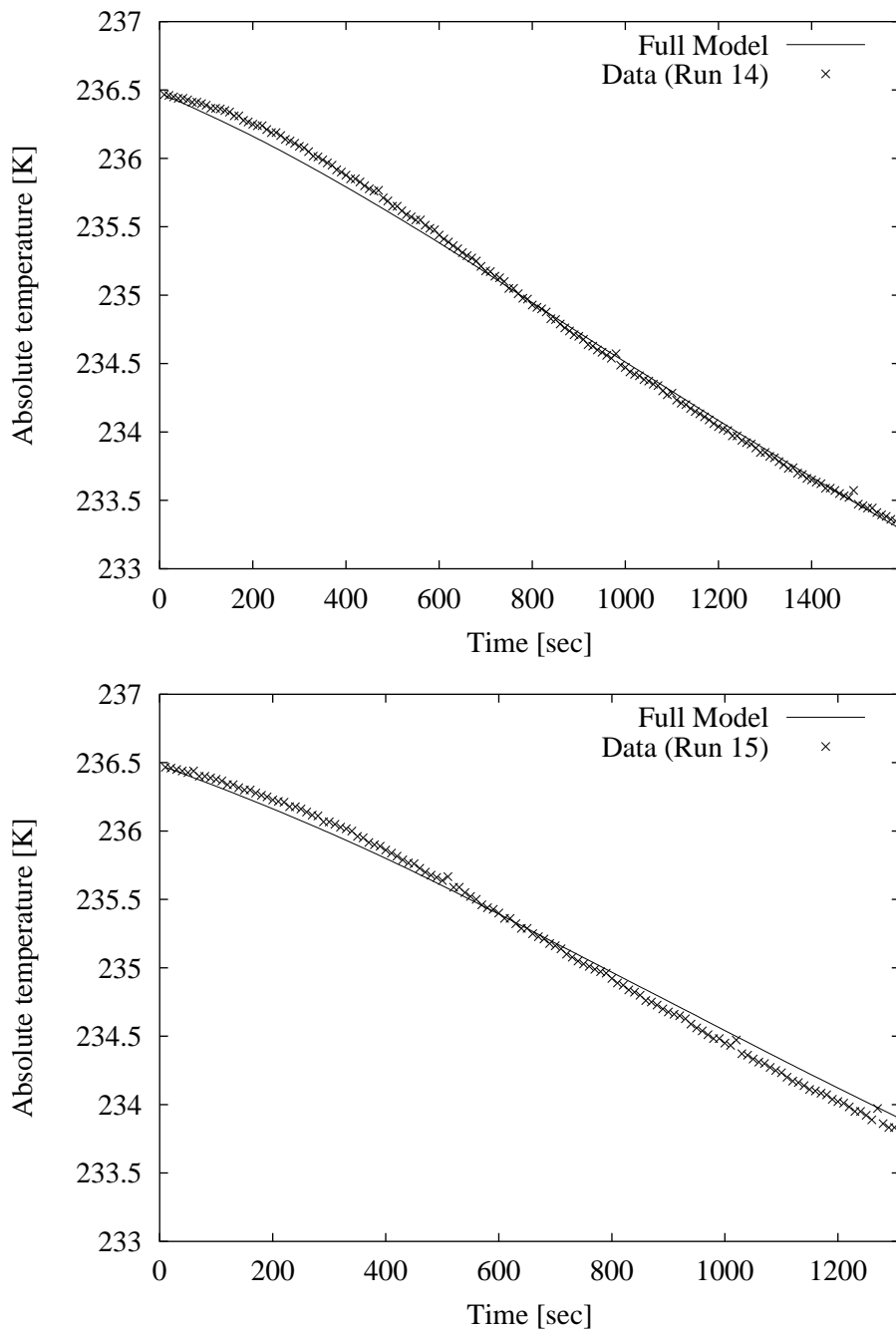


Figure 6.4: Temperature profile at T1 and full model fit for runs 14 and 15.

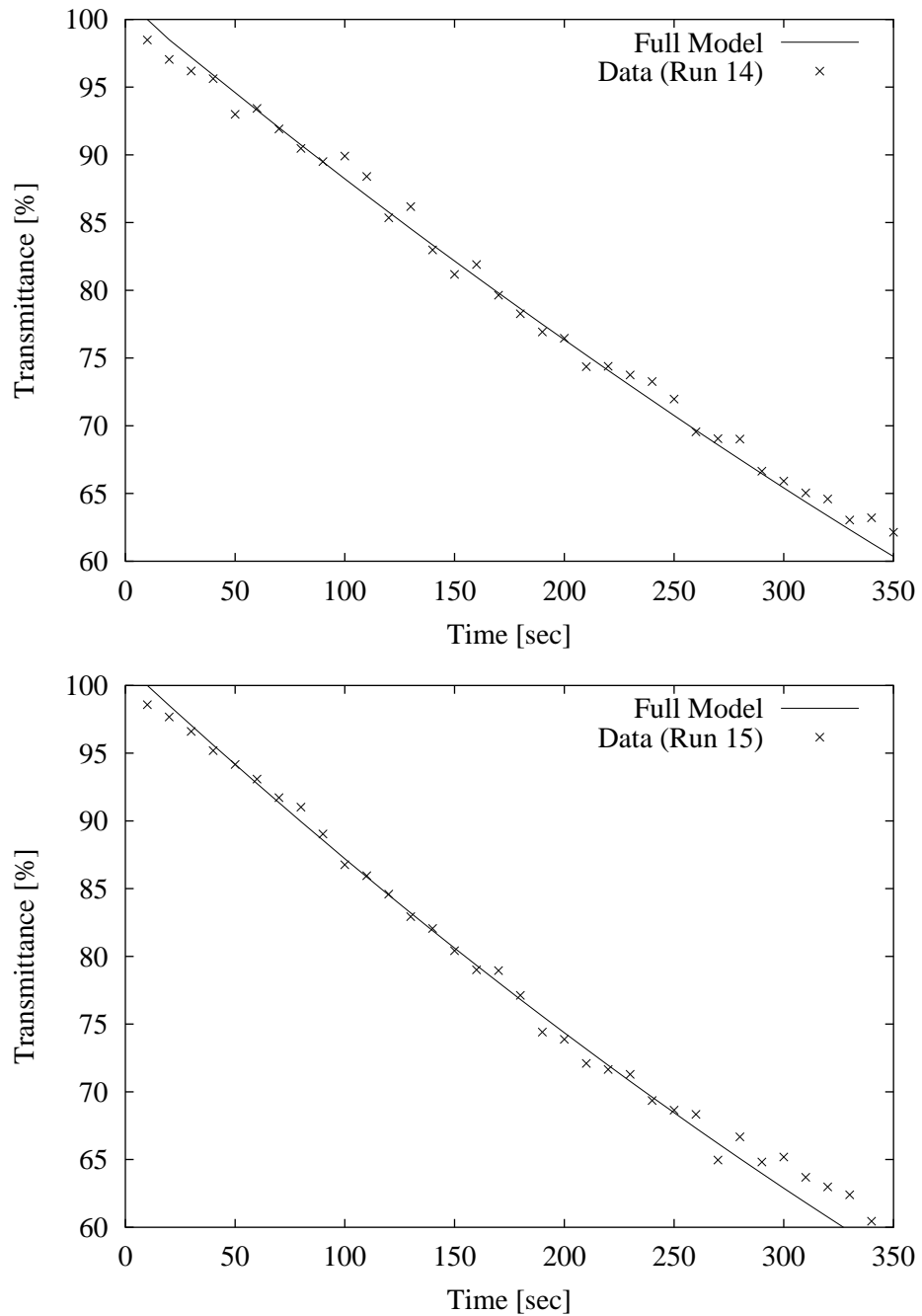


Figure 6.5: Transmittance profile and full model fit for runs 14 and 15.

and from Equation 4.2, we have

$$\frac{d\hat{C}}{dt} = \frac{d\hat{C}_{\text{sat}}(T)}{dt} = -3\rho_c k_v h G \int_0^\infty f(L, t) L^2 dL \quad (6.8)$$

The derivative of the saturation concentration with respect to temperature can be found analytically from the solubility expression, Equation B.3 and  $C_{\text{sat}} = 100N$ , in which  $N$  is the mole fraction of para-xylene. Applying the chain rule and rearranging Equation 6.8 results in the reduced growth rate expression

$$G = \frac{-1}{3h\rho_s k_v} \left( \frac{1}{\mu_2} \right) \left( \frac{d\hat{C}_{\text{sat}}(T)}{dT} \right) \left( \frac{dT}{dt} \right) \quad (6.9)$$

where  $\mu_2$  is the second moment of the PSD. Randolph and Larson [106] provide the steady state version of the high growth limit, which is discussed in section 6.4. Substituting Equation 6.9 into Equation 4.3 results in

$$\rho V \hat{C}_p \frac{dT}{dt} = \frac{-UA(T - T_j(t))}{1 - \left( \frac{\Delta\hat{H}_c}{\rho\hat{C}_p h} \right) \left( \frac{d\hat{C}_{\text{sat}}(T)}{dT} \right)} \quad (6.10)$$

Substitution of Equation 6.9 into Equations 4.22 and 4.23 results in the following expressions for the moments

$$\frac{d\mu_0}{dt} = B \quad (6.11)$$

$$\frac{d\mu_1}{dt} = -\frac{1}{3h\rho_c k_v} \left( \frac{\mu_0}{\mu_2} \right) \left( \frac{d\hat{C}_{\text{sat}}(T)}{dT} \right) \left( \frac{dT}{dt} \right) \quad (6.12)$$

$$\frac{d\mu_2}{dt} = -\frac{2}{3h\rho_c k_v} \left( \frac{\mu_1}{\mu_2} \right) \left( \frac{d\hat{C}_{\text{sat}}(T)}{dT} \right) \left( \frac{dT}{dt} \right) \quad (6.13)$$

$$\frac{d\mu_3}{dt} = -\frac{1}{h\rho_c k_v} \left( \frac{d\hat{C}_{\text{sat}}(T)}{dT} \right) \left( \frac{dT}{dt} \right) \quad (6.14)$$

The initial derivatives for the first and second moments in the reduced model are undefined because  $\mu_i(0) = 0$ . Instead, values of the initial rate of change of first and second moments are evaluated analytically by taking the limit as step-size tends to zero in the implicit Euler approximation

$$Y|_{k+1} = Y|_k + h_s f(Y|_k, t|_k) \quad (6.15)$$

$Y|_k$  is the estimate of the solution to the differential equation  $y' = f(y, t)$  at time  $t|_k$  and  $h_s$  is the step size, so

$$f(Y|_k, t|_k) \equiv \lim_{h_s \rightarrow 0} \left[ \frac{Y|_{k+1} - Y|_k}{h_s} \right] \quad (6.16)$$

Applying the forward Euler method (Equation 6.15) and the definition of the derivative (Equation 6.16) to the first three reduced model moment equations for the initial derivative (where  $\mu_i|_0 = 0$ ) results in

$$\frac{d\mu_0}{dt} \Big|_{t=0} \equiv \lim_{h_s \rightarrow 0} \frac{\mu_0|_1}{h_s} = \lim_{h_s \rightarrow 0} B|_0 \quad (6.17)$$

$$\frac{d\mu_1}{dt} \Big|_{t=0} \equiv \lim_{h_s \rightarrow 0} \frac{\mu_1|_1}{h_s} = \lim_{h_s \rightarrow 0} \frac{-1}{3h\rho_ck_v} \left( \frac{d\hat{C}_{\text{sat}}}{dT} \right) \left( \frac{dT}{dt} \right) \frac{\mu_0|_0}{\mu_2|_0} \quad (6.18)$$

$$\frac{d\mu_2}{dt} \Big|_{t=0} \equiv \lim_{h_s \rightarrow 0} \frac{\mu_2|_1}{h_s} = \lim_{h_s \rightarrow 0} \frac{-1}{3h\rho_ck_v} \left( \frac{d\hat{C}_{\text{sat}}}{dT} \right) \left( \frac{dT}{dt} \right) \frac{\mu_1|_0}{\mu_2|_0} \quad (6.19)$$

In the limit as  $h_s \rightarrow 0$ ,  $\mu_i|_1 = \mu_i|_0$  so  $(d\mu_i/dt)|_0 = (\mu_i|_1 - 0)/h_s = \mu_i|_0/h_s$ . Solving for  $\mu_i|_0$  in Equations 6.17, 6.18, and 6.19 and setting  $(d\mu_i/dt)|_0 = \mu_i|_0/h_s$  results in the analytical expressions for the first three initial derivatives of the reduced model

$$\frac{d\mu_0}{dt} \Big|_{t=0} = B \quad (6.20)$$

$$\frac{d\mu_1}{dt} \Big|_{t=0} = \left[ \frac{-(B)^2}{6h\rho_ck_v} \left( \frac{d\hat{C}_{\text{sat}}(T)}{dT} \right) \left( \frac{dT}{dt} \right) \Big|_{t=0} \right]^{\frac{1}{3}} \quad (6.21)$$

$$\frac{d\mu_2}{dt} \Big|_{t=0} = \left[ \frac{-\sqrt{2B}}{3h\rho_ck_v} \left( \frac{d\hat{C}_{\text{sat}}(T)}{dT} \right) \left( \frac{dT}{dt} \right) \Big|_{t=0} \right]^{\frac{2}{3}} \quad (6.22)$$

and  $(\frac{dT}{dt})|_{t=0}$  can be evaluated from Equation 6.10. The nucleation rate does not change in the reduced model and still can be calculated from Equation 6.1. The growth rate is calculated from Equation 6.9. In the reduced model, only the nucleation rate parameters  $k_b$  and  $b$  are estimated.

$$\theta = \begin{bmatrix} k_b & : \text{ nucleation rate constant} \\ b & : \text{ nucleation rate order} \end{bmatrix} \quad (6.23)$$

The results for runs 14 and 15 using the reduced model are presented in Figures 6.6 and 6.7. The reduced model parameter estimates and 95% confidence intervals are presented in Table 6.2. The fit to the experimental data for the reduced model is essentially identical to the fit for the full model verifying the accuracy of the reduced model for this crystallizer.

## 6.4 High Growth Limits for MSMPR Crystallizers

Randolph and Larson [106] discuss mixed-suspension, mixed-product removal (MSMPR) systems in which the exit concentration approaches  $\hat{C}_{\text{sat}}$  and the per pass yield is independent of throughput, named *class II* systems. The authors assume constant temperature and show that the growth rate for this particular system is inversely proportional to the

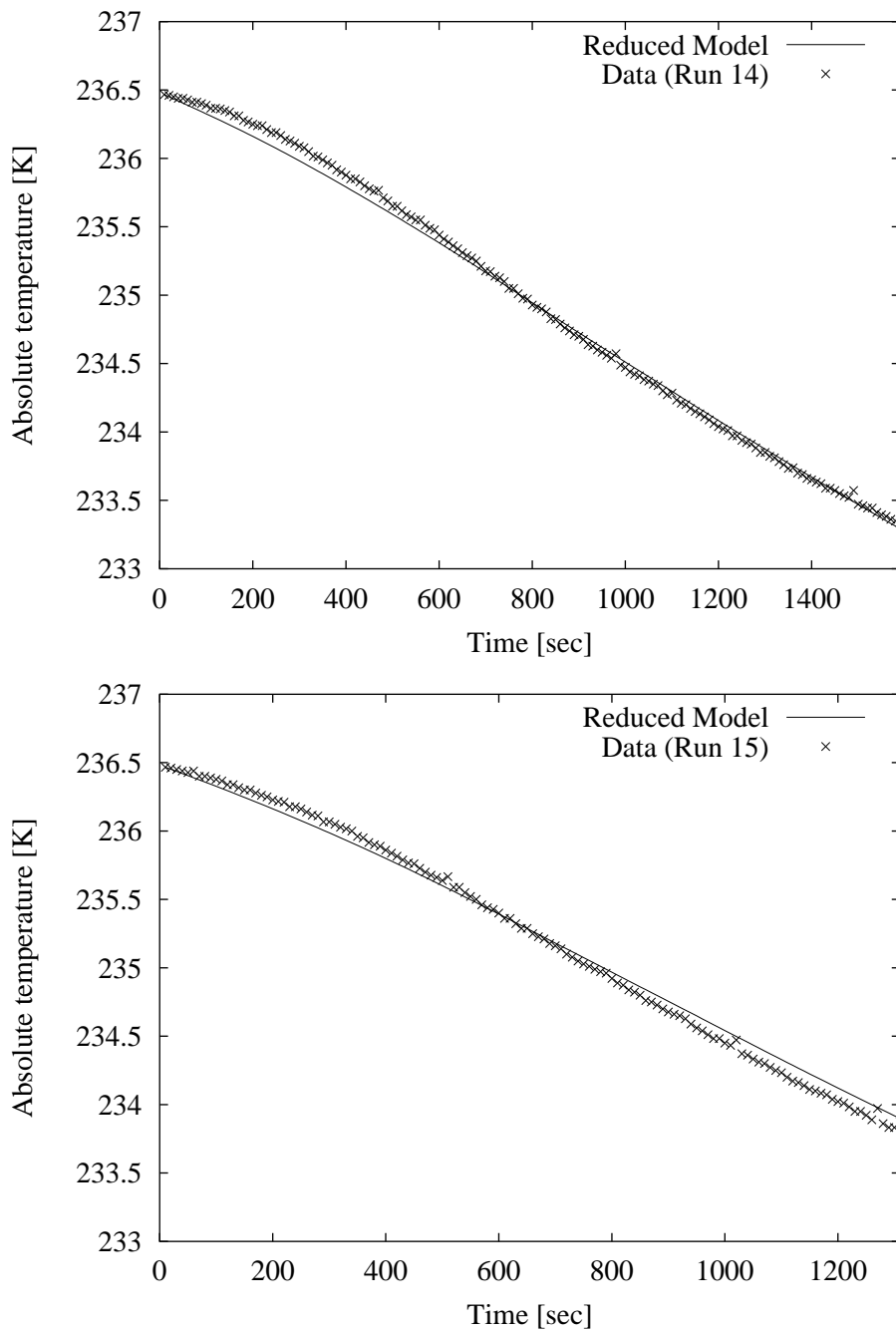


Figure 6.6: Temperature profile at T1 and reduced model fit for runs 14 and 15.

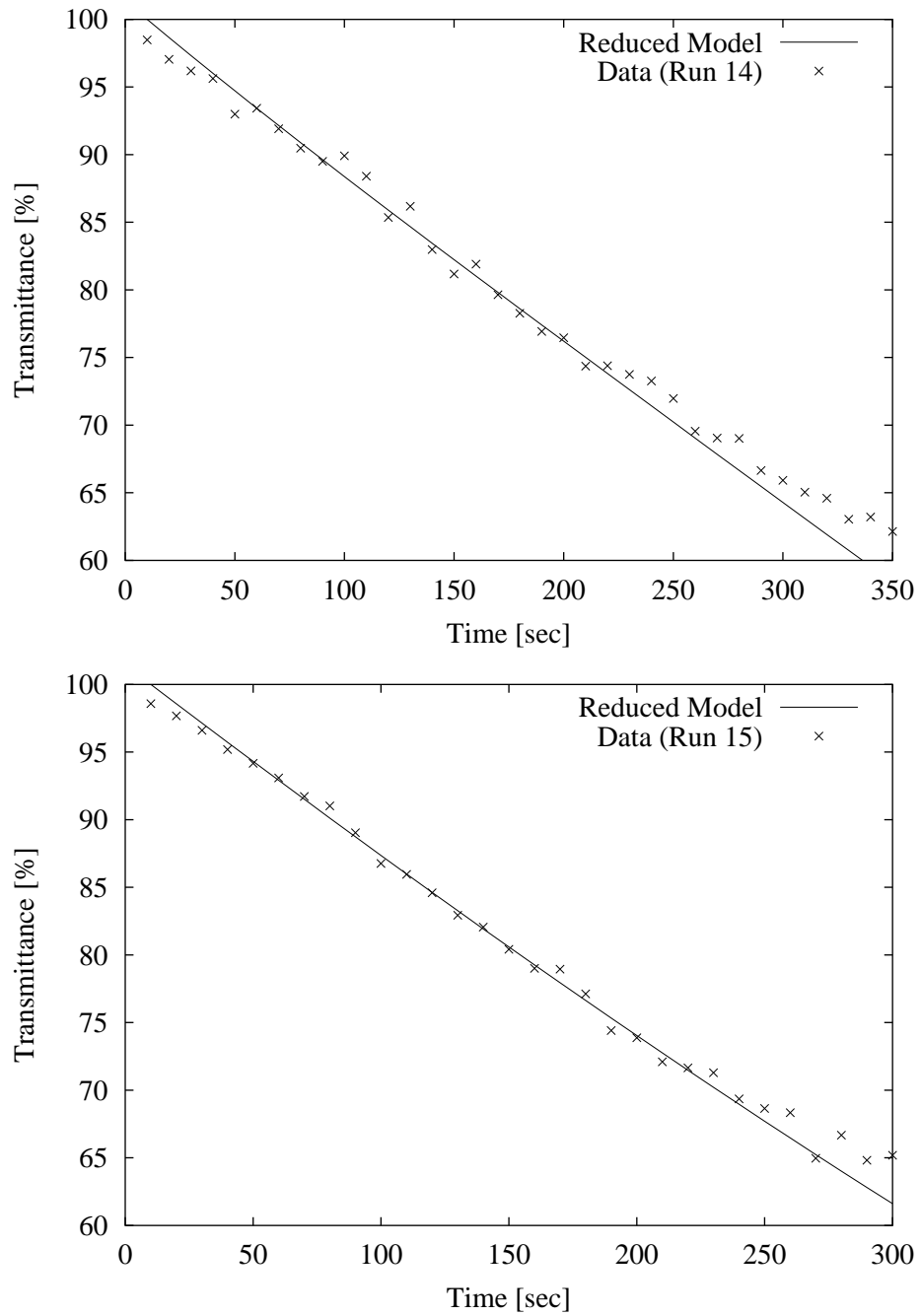


Figure 6.7: Transmittance profile and reduced model fit for runs 14 and 15.

Table 6.2: Parameter estimates and approximate 95% confidence intervals resulting from the temperature and transmittance measurements for runs 14 and 15 and the simultaneous fit of the simulated data and run 15 using the reduced model. Confidence regions are summarized in Figures 6.8 and 6.13.

	$\ln(k_b)$	$b$
Estimate (Run 14)	24.99	7.80
Interval	$\pm 45$	$\pm 23$
Estimate (Run 15)	21.71	5.94
Interval	$\pm 16$	$\pm 8$
Estimate (Simulated and Run 15)	10.66	0.36
Interval	$\pm 0.10$	$\pm 0.06$

surface area of crystals in suspension. Here we show that the reduced model in the high growth limit in this study is a more general form and does not necessarily need the constant temperature assumption.

For the continuous case, Equation 6.8 has the additional terms for the inlet and exit streams

$$\frac{d\hat{C}}{dt} = \frac{d\hat{C}_{\text{sat}}(T)}{dt} = \frac{\hat{C}_{\text{in}}}{\tau} - \frac{\hat{C}_{\text{sat}}}{\tau} - 3\rho_c k_v h G \int_0^\infty f(L, t) L^2 dL \quad (6.24)$$

Similar inlet and exit temperature terms are added to Equation 6.10 for the energy balance. Rearranging Equation 6.24 for growth rate and noting the conversion between volume and area shape factor,  $6k_v = k_a$

$$G = \frac{2 \left( \frac{d\hat{C}_{\text{sat}}(T)}{dt} - \left( \frac{\hat{C}_{\text{in}} - \hat{C}_{\text{sat}}}{\tau} \right) \right)}{-\rho_c k_a h \mu_2} \quad (6.25)$$

Assuming constant temperature so  $d\hat{C}_{\text{sat}}/dt = 0$ , Equation 6.25 becomes Equation(4.5-3) in Randolph and Larson [106].

## 6.5 Analysis of Confidence Regions for the Reduced Model

The confidence regions for the reduced model for runs 14 and 15 are shown in Figure 6.8. Figure 6.9 shows the objective function near the respective optima. The objective surface remains essentially flat in one direction and is steep in the orthogonal direction. The shapes of the confidence regions show that the parameters  $k_b$  and  $b$  are highly correlated. Again, the size of the intervals of the parameters in Table 6.2 and the confidence region suggest that either further model revisions are required or a new experimental design is required.

Consider the high values for the nucleation rate constant  $k_b$  in Table 6.2 and the supersaturation at the wall shown in Figure 6.10. The value for the supersaturation ratio

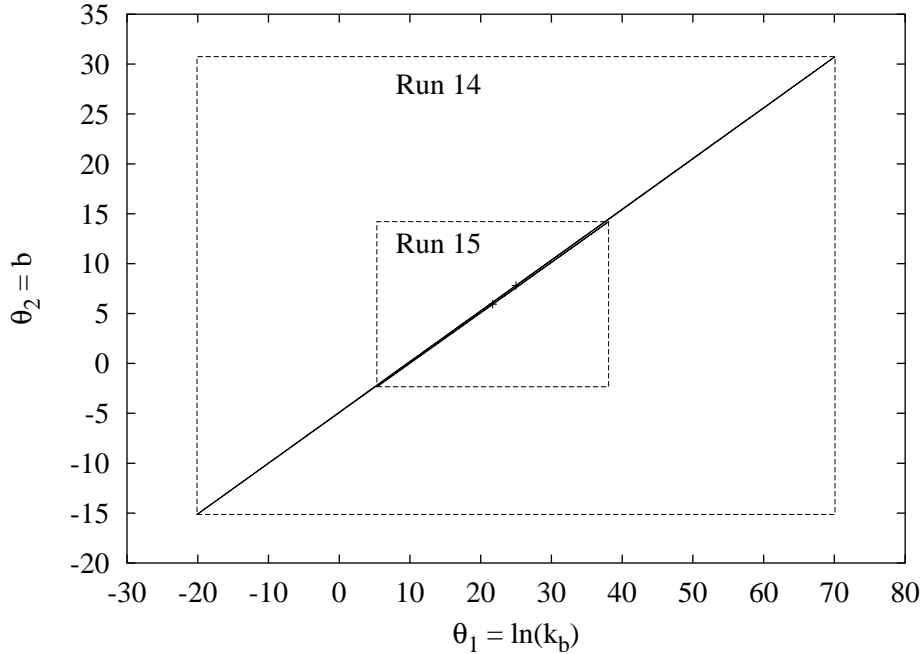


Figure 6.8: Parameter approximate 95% inference regions for runs 14 and 15 data using the reduced model.

at the wall is small and does not change significantly throughout the run and is almost identical for both runs 14 and 15. Taking the product of the supersaturation ratio raised to the power of  $b$  and a high rate constant results in a relatively constant value for the nucleation rate,  $B$ . Consider the expression for the rate of nucleation

$$B = \exp(\ln(k_b)) S_w^b = \exp(\theta_1) S_w^{\theta_2} \quad (6.26)$$

in which  $S_w = (\hat{C} - \hat{C}_{\text{sat}}(T_j(t))) / \hat{C}_{\text{sat}}(T_j(t))$ . For a truly constant nucleation rate experiment, the correlation would be:

$$dB = B(d\theta_1 + \ln(S_w)d\theta_2) = 0 \quad (6.27)$$

so

$$\frac{d\theta_2}{d\theta_1} = \frac{-1}{\ln(S_w)} \quad (6.28)$$

Equation 6.28 is the value of the slope of the line that results from the limit of the narrow ellipse as it becomes a line for correlated parameters with a correlation coefficient of 1.0. The value of the slope is calculated from the intervals from Figure 6.8 and is compared with the predictions of the supersaturation at the wall for both runs 14 and 15 in Figure 6.10 and Equation 6.28. The values for the slopes of the ellipses obtained from the inference regions for the reduced model for runs 14 and 15 are 0.51 and 0.50, respectively. The values

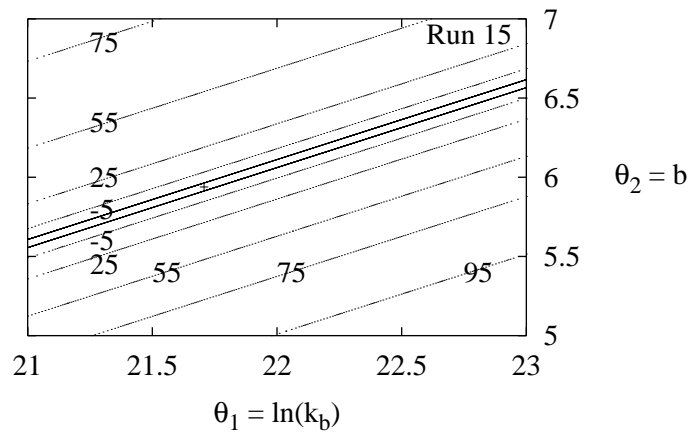
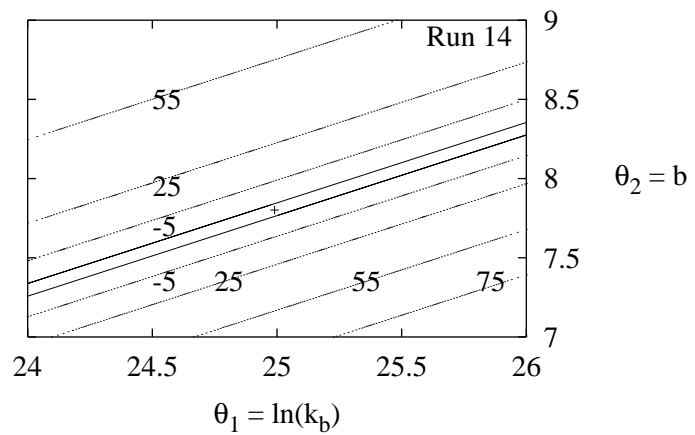


Figure 6.9: Objective function ( $\Phi_{be}$ ) contours and a portion of the 95% inference regions for runs 14 and 15 data.

for Equation 6.28 from the model fits for runs 14 and 15 are both 0.56 and are close to the values from the ellipses. We conclude that the experiments were conducted with an approximately constant nucleation rate and that is the cause of the parameter correlation and is, therefore, not an informative experimental design.

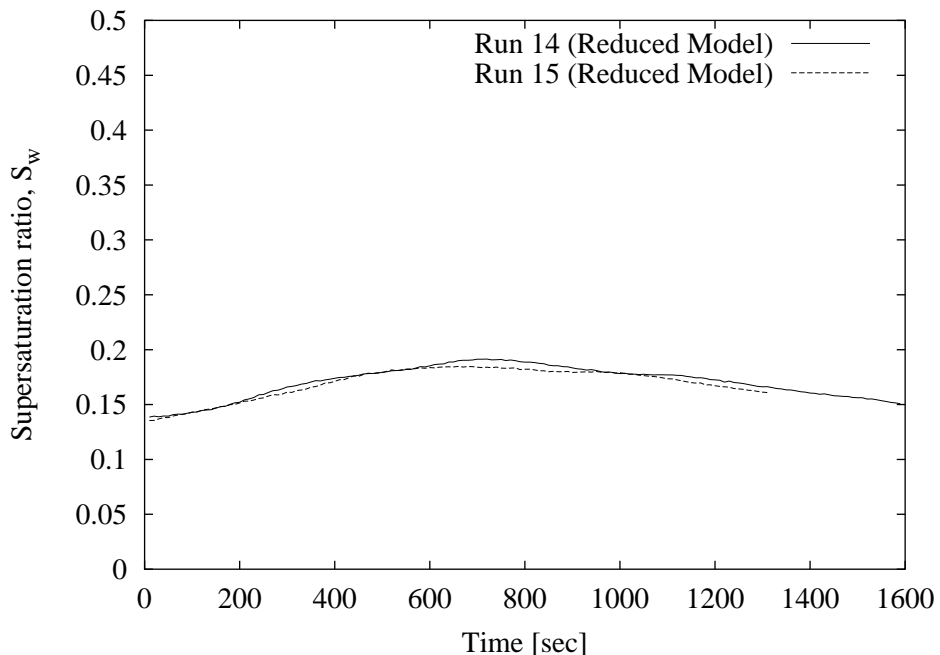


Figure 6.10: Supersaturation profiles at the wall predicted using the reduced model for runs 14 and 15.

## 6.6 Experimental Design

There are two options in which one can eliminate the parameter correlation. The first approach would be to make the transmittance data more informative. In the high growth regime, the parameters  $k_b$  and  $b$  only affect the transmittance predictions and the temperature predictions are unaffected. If a single run is required to uniquely identify  $k_b$  and  $b$ , then the supersaturation must be significantly varied with time during the run. The experiment would require that the inlet jacket temperature slowly decrease from its initial temperature of approximately 232 K and then, while transmittance is still greater than 74%, a rapid decrease to a lower final temperature would create a large supersaturation at the wall.

A second and simpler approach is to use two experiments at constant but different supersaturations. The data from runs 14 and 15 and a second experiment in which the supersaturation at the wall is different from the supersaturation at the walls for runs 14 and 15 can be used to provide experiments with varied supersaturations. A large supersaturation at the wall can be generated, for example, by stepping the inlet jacket temperature to its final

temperature at the beginning of the run. Simulated data of the crystallizer temperature and transmittance responses are created by using a set of parameters in the confidence region in Figure 6.8, namely  $\ln(k_b) = 10.74$  and  $b = 0.41$ , and an inlet jacket temperature of 220 K. The temperature and transmittance responses for the simulated data along with the simultaneous fit from run 15 are shown in Figures 6.11 and 6.12. Notice that only few transmittance points can be used for parameter estimation on these rapid cooling profile experiments. The step in the inlet jacket temperature results in a more rapid decrease in the crystallizer temperature compared to run 15. The large supersaturation created at the wall generates many nuclei quickly and so the transmittance profile is steeper than the transmittance profile for run 15.

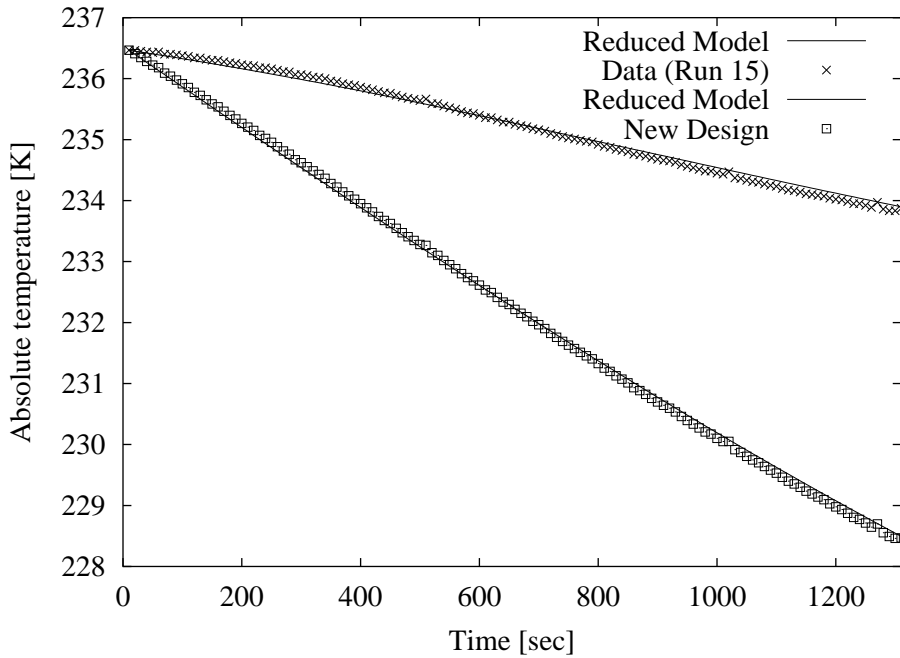


Figure 6.11: Temperature profile at T1 and reduced model fit for run 15 and simulated data.

The parameter estimation routine converged to a local optimum with parameters  $\ln(k_b) = 10.66 \pm 0.10$  and  $b = 0.36 \pm 0.06$ . The confidence region and objective surface are shown in Figure 6.13. The original parameters that generated the simulated data are contained in the linear 95% confidence region. The objective surface shows that the two parameters in the reduced model are much less correlated when two experiments run with significantly different supersaturations are used for parameter estimation.

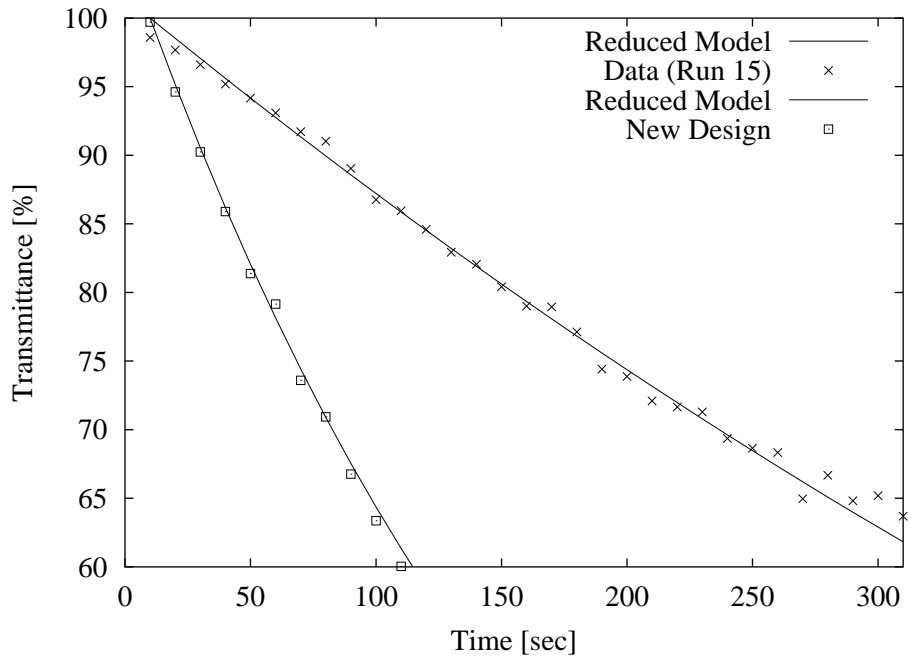


Figure 6.12: Transmittance profile and reduced model fit for run 15 and simulated data.

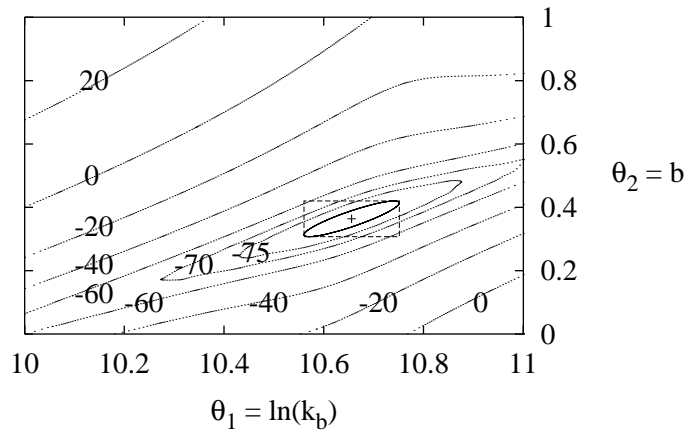


Figure 6.13: Objective function ( $\Phi_{be}$ ) contours and the 95% inference region for run 15 and simulated data.

## 6.7 Conclusions

This chapter has shown that the predictions of the identified crystallizer models show good agreement with the temperature and light transmittance measurements for crystallization of para-xylene in a batch pilot-scale SSC, assuming nucleation occurs at the wall of the crystallizer, and growth occurs in the bulk. The data show that the para-xylene crystallization system is a high-growth rate process and the bulk supersaturation is essentially zero at all conditions. Therefore, the growth rate constant is assumed large and a reduced model is derived. The nucleation order and the rate constant are the only adjustable parameters in the reduced model. Good agreement with all the data was also obtained with the reduced model, but the reduced model's two parameters remain correlated. The correlation between the nucleation order and rate constant is attributed to the near constant nucleation rate in the available experiments. The parameters can be largely decoupled and determined precisely in a single experiment if data can be collected while the supersaturation at the wall is time-varying. Alternatively, repeated experiments at constant but differing values of supersaturation can be used. Given the available Amoco experiments and an additional experiment with a step to a low inlet jacket temperature, simulated data show that the parameters are decoupled. It is recommended that this temperature profile be implemented in subsequent parameter estimation studies.

Alternative models can, of course, describe the nucleation kinetics in the crystallizer. Using the data in this study, statistical model discrimination techniques could be used to discriminate between rival models, such as primary versus secondary nucleation models. This topic could be the focus of further research to understand the crystallization mechanism occurring in an industrial SSC.

## Chapter 7

# Particle Shape-Monitoring and Control in Crystallization Processes<sup>1</sup>

*5 minutes to go. Time to start making things up!*

— Campbell, J. C.

In this chapter, we implement feedback control of crystal habit in an unseeded semi-batch crystallization of sodium chlorate. We develop a measurement technology that uses direct digital imaging of a sample stream. Simple measurements such as particle boxed area and aspect ratio are used to infer the habit of the crystals, however, images are replete with bad data and cause these measurements to be extremely noisy. Given prior information regarding the crystal habit, a user-defined algorithm is developed that can distinguish the cubic and tetrahedral habits of sodium chlorate. The flowrate of an impurity stream is manipulated that can influence the particle habit. Through a simple PID control policy, a predominantly tetrahedral habit is maintained in the face of unmeasured disturbances using video images processed in real time to produce the feedback signal used for control.

---

<sup>1</sup>Portions of the chapter are published in Patience and Rawlings [90]

## 7.1 Introduction

Limitations of sensors for the on-line measurement of solid-phase properties have restricted the development and implementation of improved design, monitoring and control methods for crystallizers and other particulate processes. Light scattering is an attractive measurement technique because it is on-line and rapidly provides a signal that is sometimes suitable for control. Heffels et al. [40, 42] exploit the particle shape information present in forward light scattering techniques. Although simple shapes such as cubes and ellipsoids can be detected, it remains to be seen whether the technique can handle simultaneously size and shape determination in the presence of significant process noise as expected with more complicated materials. Image analysis has recently become a popular technique to monitor crystal size and shape in crystallization processes. Plummer and Kausch [93] use image analysis to measure the real time crystal size density (CSD) of polyoxymethylene as it crystallizes on a static stage under a microscope. Monnier et al. [77] use image analysis to measure the final CSDs of adipic acid in water crystallization. Puel et al. [98] use image analysis to measure two characteristic lengths of hydroquinone crystals as a function of time. The technique is not yet fully automated, however, and the crystal slurry is manually sampled and placed under the microscope and imaging requires an operator to occasionally interrupt automatic sizing and discard measurements before taking more samples. In their review, Braatz and Hasebe [17] discuss the recently available in-situ Lasentec Particle and Vision Measurement (PVM) system. This sensor provides two dimensional images of crystals in random orientation, however, the authors state that the quality of the images limits the ability of imaging software to automatically identify individual particles but is suitable for qualitative troubleshooting. Image analysis has not yet been demonstrated to automatically monitor in real-time the size and shape characteristics of crystals in a suspension crystallizer. The strong advantage of image analysis in the above applications, however, is that it requires almost no assumptions about particle size or shape and does not require inversion of a signal and inference of the resultant particle size or shape density. Although image analysis is a direct observation technique, it is a two dimensional measurement and care must be taken if one is to infer a three dimensional shape.

Limited information regarding shape can be extracted from two dimensional binarized images of objects given adequate sampling. Podczeck [95] reviews the history of the range of methods to assess the shape of particles from a two dimensional image. Podczeck [94] motivates the need to define new shape factors that are simple to calculate and incorporate commonly used measurements such as aspect ratio and defines one shape factor based on a combination of the object's elongation and other shape factors that describe an object's deviation from a square, circle and triangle. Bernard-Michel et al. [11] use Fourier descriptors of an object contour to classify more than 10 distinctly different shapes. These shape descriptors are not available with commercial image analysis software routines. The particles used in these studies are not broken and are not agglomerated. The particles are carefully arranged under the microscope without touching other particles making it easy

to digitize correctly all particles in the image. If commercial packages are implemented on-line, the user is often limited with software designer supplied functions. Typically, only simple measurements are available with commercial image analysis packages such as aspect ratio, roundness (the deviation of the object's shape from a circle) and boxed area. It can be difficult to extract meaningful shape information from aspect ratio and roundness measurements, let alone using more detailed shape descriptors for an image of particles sampled from a particulate process. Particles sampled from a suspension crystallizer, for example, can contain broken, agglomerated, aggregated, and irregularly grown crystals besides the correctly grown crystals and in all cases, the shape measurements are replete with bad data and contain significant noise. Bharati and MacGregor [12] use multiway principal component analysis to decompose highly correlated data present in images obtained from a LANDSAT satellite as it passes over geographical regions of the earth. These techniques are useful to determine the most informative software designer supplied measurements for shape in commercial image analysis software packages.

The habit of a crystal is determined by the various growth rates of the different faces of the crystal under different internal and external conditions. Internal conditions that affect the habit of a crystal include factors such as impurity content and liquid occlusions, while external factors include temperature and solution flow around a crystal. Some pharmaceuticals potentially exhibit multiple polymorphs because of their typical complex chemical structure, and these polymorphs often have different shapes. Shape may be an important characteristic to monitor in pharmaceuticals in order to detect morphology changes. However, it should be noted that polymorph assessment based on shape must be verified with x-ray diffraction. Because of these characteristics, shape is becoming an increasingly important variable to monitor in crystallization processes. Given the above mentioned limitations in on-line measuring of crystal size with light scattering or image analysis, on-line measurement of shape is even more challenging.

In this chapter, we present a simple technique that can identify suitable data from a noisy signal produced on-line by commercially available image analysis software. A controller successfully uses this signal to regulate the flowrate of a habit modifier stream to maintain a desired crystal habit. We demonstrate these methods on a simple chemical system: sodium chlorate ( $\text{NaClO}_3$ ) crystallization using sodium dithionite ( $\text{Na}_2\text{S}_2\text{O}_6$ ) as a habit modifier.

## 7.2 Chemical System and Experimental Apparatus

Small concentrations of sodium dithionite in a supersaturated sodium chlorate solution influence the relative growth rates of crystal faces by competitively binding to potential growth sites on the  $\bar{1}\bar{1}\bar{1}$  faces. The dithionite impurity consists of two sulfur atoms bound to each other and each sulfur atom is bound to three oxygen atoms. Each set of the three oxygen atoms are bound in a tetrahedral arrangement with similar bond angles to a chlorate molecule. One end of the dithionite molecule can fit into a sodium chlorate crystal

structure with the other end of the dithionate molecule protruding from the structure. The protruding end of the dithionate molecule inhibits subsequent addition of chlorate molecules and slows the growth rate of the face. A figure of the atomic structure of sodium dithionate molecule in the sodium chlorate lattice is shown in Ristić et al. [115]. The 100 faces form many hydrogen bonds with water, becoming hydrated, making it difficult for dithionate ions to competitively bind to 100 faces and so dithionate preferentially bonds to the  $\bar{1}\bar{1}\bar{1}$  faces.

The PSD of sodium chlorate crystallization in a batch crystallizer is described by the PBE

$$\frac{\partial f(l, w, t)}{\partial t} = -G_l \frac{\partial f(l, w, t)}{\partial l} - G_w \frac{\partial f(l, w, t)}{\partial w} \quad (7.1)$$

Two characteristic dimensions (two internal co-ordinates) are used to describe the crystal size and habit, namely the maximum and minimum lengths ( $l$  and  $w$ , respectively) on the 100 face of the sodium chlorate crystal. The chemical composition of the crystals in this study are assumed to be pure. For modeling and monitoring purposes, the presence of impurities and occlusions in sodium chlorate crystals are neglected. One way to model the evolution of a population of sodium chlorate crystals in the presence of a habit modifier is to assume the habit modifier changes the net rates of diffusion of sodium chlorate to the various faces. In this way, the growth rate for the width dimension is both a function of the sodium chlorate concentration and the dithionate concentration.

$$G_w = k_g S^g, \quad C_{\text{imp}} < C_{\text{imp}}^* \quad (7.2)$$

$$= 0, \quad \text{otherwise} \quad (7.3)$$

The growth rate for the length direction is also a function of the supersaturation and is not influenced by the habit modifier.

Ristić et al. [114] measure a segregation coefficient of 2 for sodium chlorate crystallization in the presence of sodium dithionate concentrations less than 1200 ppm. For a segregation coefficient 2 and impurity concentration of 100 ppm, our experiments with 1600 g NaClO<sub>3</sub> in 1600 g H<sub>2</sub>O, cooling to 23°C results in 20.8 g NaClO<sub>3</sub> crystallizing out. The final impurity concentration after crystallization for these conditions is 97 ppm, so it is reasonable to assume the crystals are relatively pure.

Ristić et al. [115] found that sodium chlorate crystallized in impurity-free solution forms predominantly the 100 faces responsible for the cubic shape, shown in the top left of Figure 7.1. In the presence of at least 50 ppm sodium dithionate, growth of the  $\bar{1}\bar{1}\bar{1}$  faces are slowed and the 100, 110 and 111 faces grow out (top right of Figure 7.1) resulting in a tetrahedral shape with  $\bar{1}\bar{1}\bar{1}$  faces. If sodium dithionate is no longer present in the solution phase and provided enough supersaturation is remaining in solution, the tetrahedral sodium chlorate crystal will grow back to the natural cubic shape [114].

The experimental apparatus used in this study is similar to that described by Matthews and Rawlings [70] shown in bottom of Figure 7.1. The crystallizer is a 2.2 L,

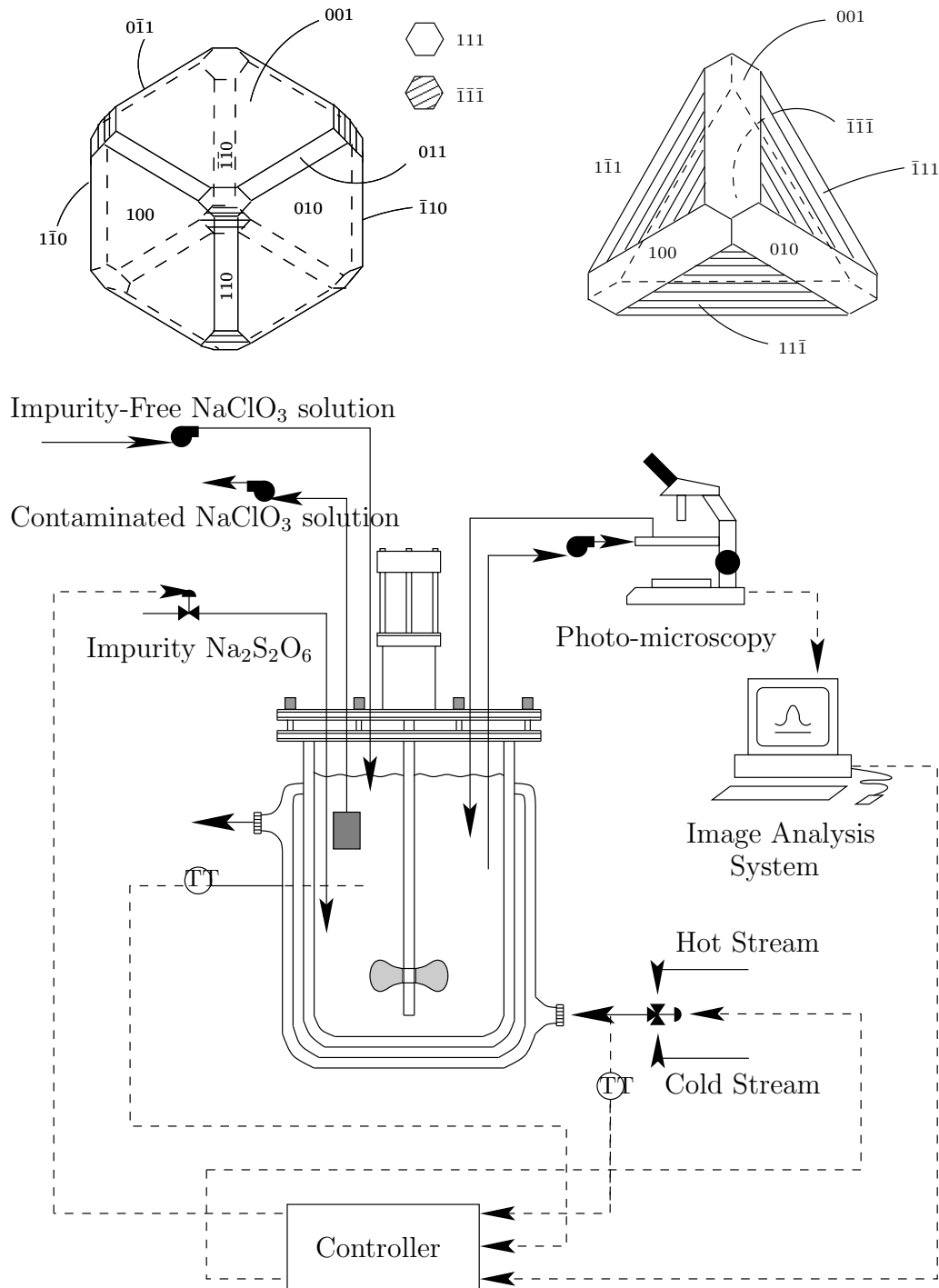


Figure 7.1: The habit of sodium chlorate (NaClO<sub>3</sub>). (Top left) Typical cubic structure. (Top right) Growth towards a tetrahedral structure in the presence of sodium dithionite (Na<sub>2</sub>S<sub>2</sub>O<sub>6</sub>), 111 faces begin to dominate the structure. (Bottom) Experimental apparatus.

glass, jacketed vessel. The temperature of the crystallizer is controlled by a model predictive controller. For a crystallization experiment, 1600 g sodium chlorate is dissolved in 1600 g H<sub>2</sub>O ( $T^{\text{sat}} = 24.4^\circ\text{C}$ ) at a temperature of 33°C. The solution is held at this temperature for 30 minutes, then rapidly cooled at 16°C·hour<sup>-1</sup> to 25°C and held for 30 minutes. Then the solution is cooled at 0.25°C·hour<sup>-1</sup> until completion of the experiment. 2 mL of sodium dithionite solution (18 g Na<sub>2</sub>S<sub>2</sub>O<sub>6</sub> in 100 g H<sub>2</sub>O) is injected into the crystallizer after cubic crystals nucleate, resulting in an impurity concentration of 225 ppm. When the crystals grow to the tetrahedral shape, an impurity-free solution of sodium chlorate ( $T^{\text{sat}}=23.5^\circ\text{C}$ ) is fed to the reactor and a solids-free solution is removed from the reactor at equal rates of 80 mL·min<sup>-1</sup>. The crystals grow back to their original cubic shape during this semi-batch phase once the sodium dithionite concentration is low enough to no longer slow the growth of the  $\bar{1}\bar{1}\bar{1}$  faces. The flowstreams to and from the crystallizer are stopped once the cubic shape is seen under the microscope and then another 225 ppm of sodium dithionite is injected into the crystallizer.

Photo-microscopy and digital image analysis are used to monitor growth kinetics and particle size and shape characteristics of crystals in the size range of 50  $\mu\text{m}$  to 1000  $\mu\text{m}$  using an Olympus BX60 microscope, a Hitachi HV-C20 charged coupled device (CCD) camera and a PC with frame grabber and Image Pro Plus image analysis software. The microscope uses a non-polarized reflected halogen light source with a total magnification of 8X. The crystal slurry is pumped continuously from the crystallizer through a circulation loop. Periodically, the flow is automatically stopped and an image of the settled particles at the bottom of a 10mm x 10mm x 100mm rectangular glass flow cell is captured and digitized. The CCD camera captures images of 585  $\times$  700 pixels with 256 grayness levels. A Sobel filter, an Image Pro Plus supplied function, is applied to the image to enhance transparent crystals and increase the probability of detecting a cube. A red/green/blue threshold of 000/084/002 is applied. Any pixel darker than this color is considered to be background and any pixel lighter is part of an object. The brightness, contrast and gamma corrections are set to their default values of 50%, 50% and 1.0. The particles are then sized according to a pixel calibration using an image of a stage micrometer at the same magnification. Upon completion of image capture and digitization, the flow loop is restarted and the sample returns to the crystallizer. During image capture, 20-30 seconds are required to stop the flow, let the particles settle, digitize the image, size the particles and re-start the flow. The stop-flow cell is used for two reasons: first, the CCD camera is not able to capture quality images of the slurry as the particles are moving. Second, we obtain a preferred orientation of the crystals on the 100 and  $\bar{1}\bar{1}\bar{1}$  faces instead of a random orientation. Obtaining shape information from a moving, randomly oriented object requires further analysis.

## 7.3 Results and Discussion

### 7.3.1 Raw Measurement and Standard Image Analysis

Figures 7.2 shows the results of an experiment in which sodium chlorate crystals nucleate heterogeneously and grow in impurity-free solution. Once impurity is injected (occurs between Figures 7.2i and 7.2ii) the crystals continue to grow and evolve to the tetrahedral shape (Figures 7.2ii to 7.2iii). Once the crystals are tetrahedrons, the impurity is flushed from the system and the crystals continue to grow and return to the original cubic shape (Figure 7.2iv). Figure 7.2iv shows the rough  $\bar{1}\bar{1}\bar{1}$  surfaces of the former tetrahedral habit in Figure 7.2iii. Figure 7.3 shows the two habits of sodium chlorate as seen using the *in-situ* PVM probe.

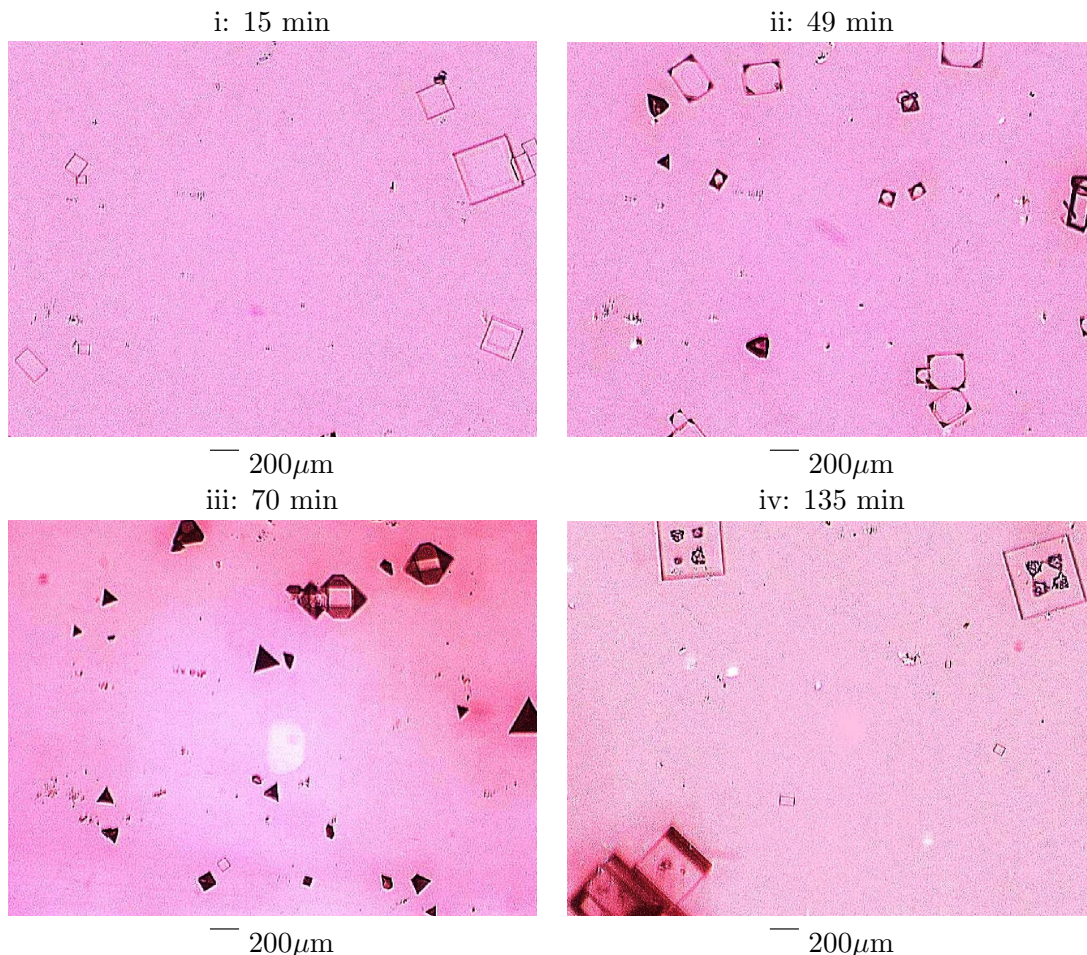


Figure 7.2: Nucleation and growth of sodium chlorate at  $23.5^\circ\text{C}$ . Impurity injected at 30 min and contaminated solution flush started at 80 min.

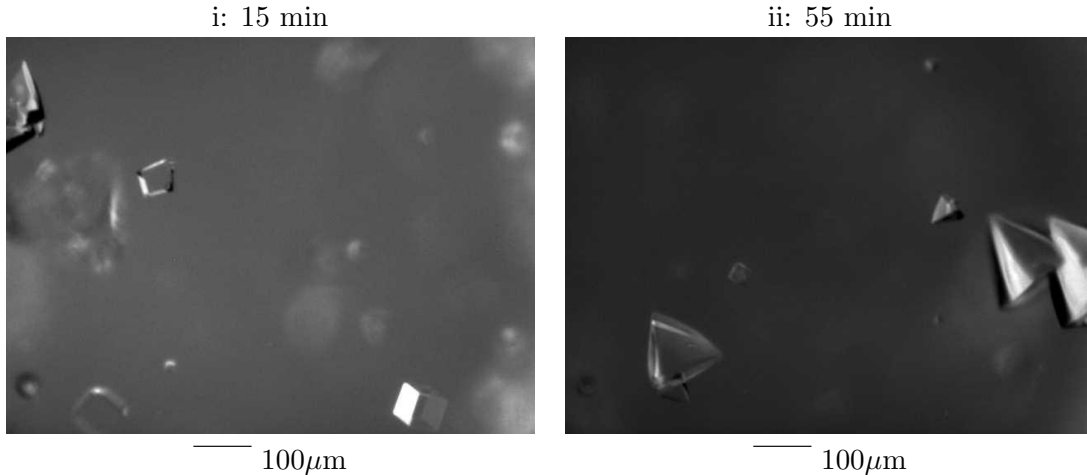


Figure 7.3: Nucleation and growth of sodium chlorate as seen by process vision measurement (PVM). Impurity is injected after 20 min.

The image analysis algorithm by Image Pro is similar to the algorithm presented by Pons [96]. Objects that are in contact with the border are eliminated and objects that have holes are filled. An *auto-split* split option analyzes all existing outlines and attempts to automatically split clustered objects. Two clustered objects are separated if their intersection can be identified by two concave points. If the resulting split results in convex objects, then the split is considered, otherwise the object remains un-split. Auto-splitting has the advantage of separating touching crystals, but can split agglomerated crystals or crystals with irregular protrusions unnecessarily. The sensor has been tested with glass beads manufactured by the National Institute of Standards and Technology (NIST) and found to give particle size densities agreeing with those measured by NIST. Measurements such as an aspect ratio and a boxed area provide a description of particle shape. The aspect ratio used in this study is defined as the ratio between the major and minor characteristic lengths of an object. The boxed area is defined as the ratio of the area of an object to the area of the minimum size bounding box of the object. For an equilateral triangle, the values for aspect ratio and boxed area are  $3\sqrt{3}/4$  and 0.5, respectively. For a square, the values are  $\sqrt{2}$  and 1.0, respectively. A roundness measurement also describes shape, though in this study, the measurement is correlated with boxed area. A summary of the measurements is given in Table 7.3.1.

Unless the light thresholding and focusing are set manually and individually for each image, and particles in the image are chosen, split correctly and sized manually and individually, then data from automated image analysis for sodium chlorate crystallization are going to contain many erroneous points. The raw measurement of boxed area as a function of time in Figure 7.4 shows no trends as the impurity is injected or when the

		square	triangle
boxed area	$\frac{\text{object area}}{\text{bounding box area}}$	1.0	0.5
aspect ratio	$\frac{L_{\max}}{L_{\min}}$	$\sqrt{2}$	$\frac{3\sqrt{3}}{4}$
roundness	$\frac{\text{per}^2}{4\pi \text{area}}$	$\frac{4}{\pi}$	$\frac{9}{\pi\sqrt{3}}$

Table 7.1: Definitions and values of boxed area, aspect ratio and roundness measurements for a square and equilateral triangle.

impurity is flushed from the solution, even though images clearly show changes back and forth between the cubic and tetrahedral shapes as the impurity is injected and flushed from the system. Figures 7.5, 7.6, and 7.7 show the aspect ratio, roundness and object diameter as a function of time for the same experiment. The noise is caused by many factors. Particles may be touching and are not split. Particles may be broken or agglomerated. Perfect transparent crystals may not be completely detected and when the object is digitized the boundary of the object may not be completely closed.

### 7.3.2 Refined Image Analysis

Sodium chlorate crystals can produce a family of images ranging from squares to equilateral triangles when viewed from above after they settle on a flat surface. For simplicity we focus here on distinguishing squares and equilateral triangles. Figure 7.8 shows squares and equilateral triangles that have saw tooth waves of increasing amplitude added to the boundaries of the shapes. Adding these waves to the boundaries of squares and triangles mimics the noise in determining the particle boundary of a sodium chlorate crystal under the microscope. The noise in the boundary of a square or equilateral triangle object is caused by the degree of camera focusing and the light threshold setting. These factors can change the object size and shape measurements by many pixels.

The boxed area and aspect ratio are functions of  $w/l$ , which is a function of the impurity concentration. A sodium chlorate crystal resting on its 100 face, is seen as a square, regardless of the value of  $w/l$ . Therefore, the boxed area and aspect ratio are constant functions of  $w/l$  with values 1.0 and  $\sqrt{2}$ , respectively. A sodium chlorate crystal resting on its  $\bar{1}\bar{1}\bar{1}$  is seen as an equilateral triangle when  $w/l$  is zero, and some other shape as a function of  $w/l$ . Figures 7.9 and 7.10 show the analytical values of boxed area and aspect ratio as a function of  $w/l$  and the 100 and  $\bar{1}\bar{1}\bar{1}$  faces. We assume that if  $w/l$  is zero, then it is impossible for a sodium chlorate crystal to rest on its 100 face. In fact, the 100 is the edge of the tetrahedron and the crystal would tip over and be seen as an equilateral triangle. If  $w/l$  is one, then we assume it is impossible for a sodium chlorate crystal to rest

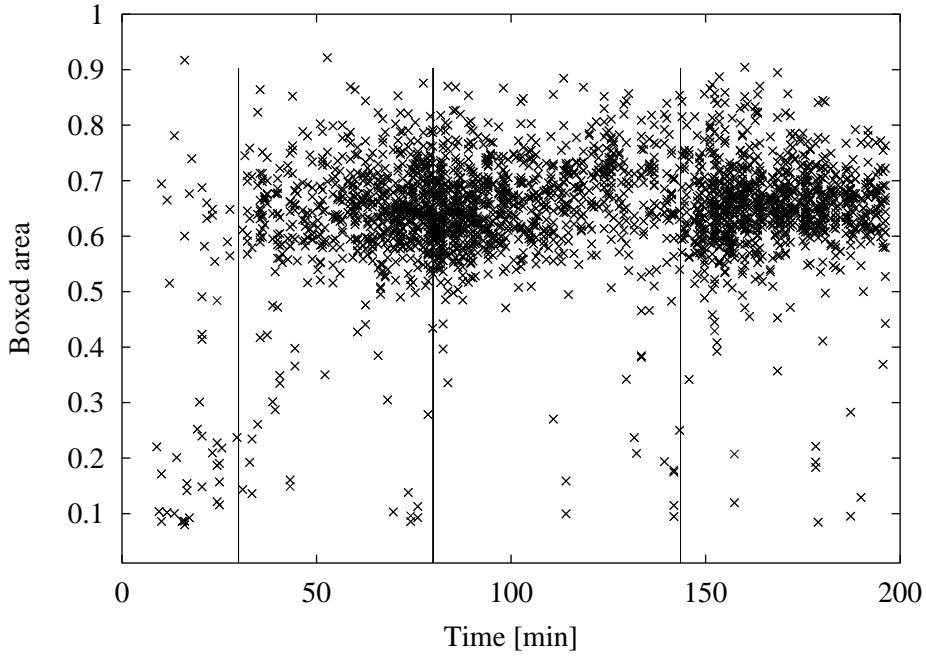


Figure 7.4: Raw data boxed area as a function of time. Impurity injected at 30 min, contaminated solution flush started at 80 min and stopped at 144 min. A second dosage of impurity is injected at 144 min.

on its  $\bar{1}\bar{1}\bar{1}$  face. In fact, the  $\bar{1}\bar{1}\bar{1}$  face is a point of the cube and the crystal would tip over and be seen as a square. Figure 7.11 shows the fraction of the total surface area of the crystal that is  $\bar{1}\bar{1}\bar{1}$  faces. We assume that the probability of the crystal landing on its  $\bar{1}\bar{1}\bar{1}$  face is proportional to the fraction of total surface that is  $\bar{1}\bar{1}\bar{1}$  and is a function of  $w/l$ .

In the boxed area–aspect ratio plane, Figure 7.12, the region in which a measurement from Image Pro Plus for the objects in Figure 7.8 in an image is considered to be a square is based on squares 1-7, 9-10 in Figure 7.12 at two sizes. The region for detecting a triangle is based on triangles 11-14 at two sizes in Figure 7.8. The region  $\mathbf{X}$ , namely the aspect ratios and boxed areas for the shapes in Figure 7.8, is given by the ellipsoid

$$(\mathbf{X} - \bar{\mathbf{X}})^T \mathbf{V}_{\mathbf{XX}}^{-1} (\mathbf{X} - \bar{\mathbf{X}}) \leq s \quad (7.4)$$

in which  $\mathbf{V}_{\mathbf{XX}}$  is the covariance matrix of  $\mathbf{X}$  for the objects in Figure 7.8 and  $s$  is a scaling factor. The values for  $s$  (25 for squares and 5 for triangles) are pre-chosen in preliminary shape experiments to get the desired trend in shape change and then these values are used throughout the experiments in this study. The trajectory of boxed area–aspect ratio as a function of  $w/l$  is shown in Figure 7.12. The trajectory is calculated by using the values of boxed area (Figure 7.9) and aspect ratio (Figure 7.10) of each face as a function of  $w/l$  and are weighted by the function in Figure 7.11.

As each image is analyzed by Image Pro Plus as a function of time, the routine

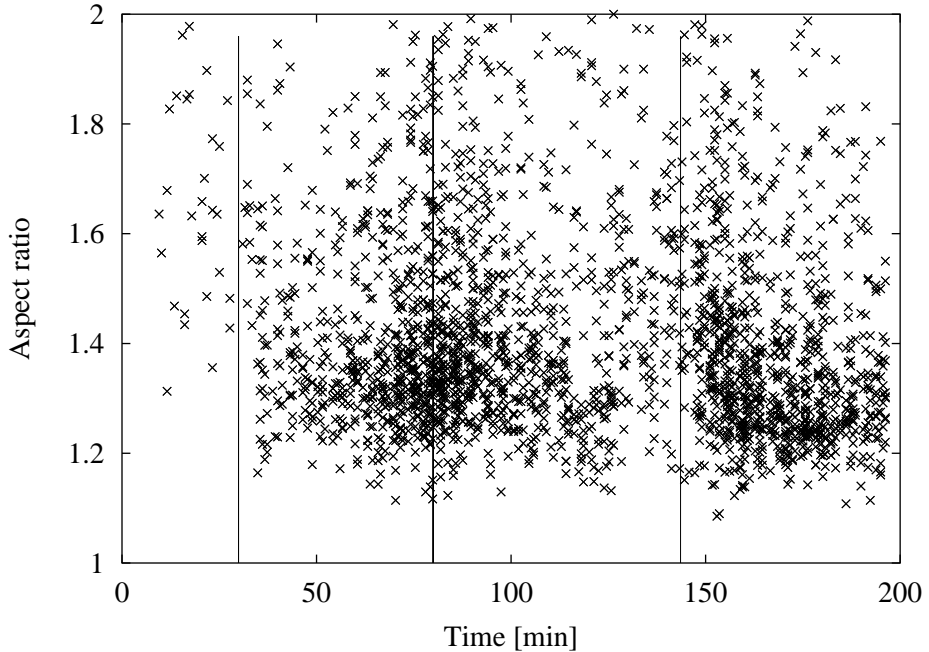


Figure 7.5: Raw data aspect ratio as a function of time. Impurity injected at 30 min, contaminated solution flush started at 80 min and stopped at 144 min. A second dosage of impurity is injected at 144 min.

then examines each object and if its aspect ratio and boxed area lie in either ellipse, then the data for that object is accepted, otherwise it is rejected. Figure 7.13 shows the raw data in Figure 7.4 plotted in the boxed area–aspect ratio plane with the elliptical regions in Figure 7.12. Clearly, most of the data are rejected because the objects are unclassifiable departures from a square (cube) or equilateral triangle (tetrahedron). Figure 7.14 shows the final result of the boxed area as a function of time after the data (objects) have been classified as either squares or triangles. A sodium chlorate crystal of shape intermediate between a cube and tetrahedron can be viewed and sized as a square if the crystal rests on its 100 face. However, if the crystal with an intermediate shape between a cube and tetrahedron rests on its  $\bar{1}\bar{1}\bar{1}$  face during image capture it is likely that it is a rejected object.

Figure 7.14 shows as the impurity is injected, an increased number of tetrahedra are present in the crystallizer and as the contaminated solution is flushed the density of tetrahedra decreases, supported by images. With this algorithm, we are able to generate a signal that detects shape transition and particle size in a semi-batch crystallizer given on-line image analysis data from commercial software. Figures 7.15, 7.16, and 7.17 show the remaining data for aspect ratio, roundness and maximum crystal diameter as a function of time after data are removed based on the classification regions in Figure 7.12. Figure 7.18 shows boxed area as a function of time for a replicate experiment. The classification technique is valid and may be used as an on-line signal for feedback control.

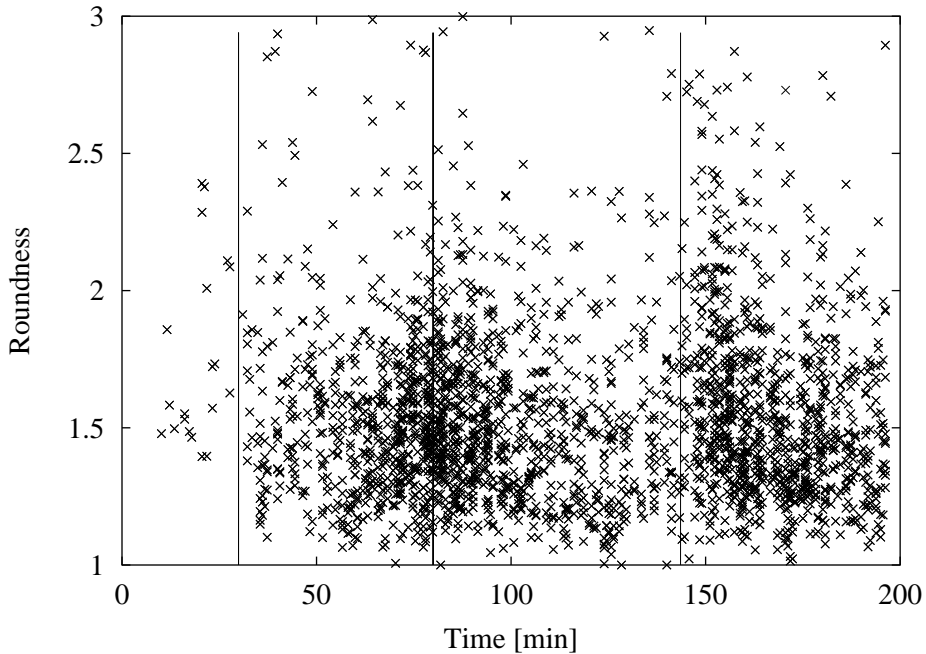


Figure 7.6: Raw data roundness as a function of time. Impurity injected at 30 min, contaminated solution flush started at 80 min and stopped at 144 min. A second dosage of impurity is injected at 144 min.

### 7.3.3 Feedback Control

An impurity-free sodium chlorate solution stream is fed to the reactor and a solids-free solution is removed from the reactor at equal rates, of  $80 \text{ mL}\cdot\text{min}^{-1}$ . The impurity-free solution entering the reactor acts as a disturbance by flushing the habit modifier from the system and preventing the crystal from remaining in the tetrahedral shape.

For basic industrial control of shape, the percentage of cubes or tetrahedra may be all that is required to implement feedback control. The boxed area measurement is convenient for detecting the percentage of cubes or tetrahedra because of the discontinuity in the measurement. To remove the effects of low sampling of objects in one image, the percentage of cubes in the crystallizer at a point in time is based on the most recent 10 images. The sampling rate of 20-30 seconds is adequate to capture the system dynamics, shown at the bottom of Figure 7.14. A simple proportional-integral (PI) feedback controller uses the percentage of cubes signal to regulate the habit modifier concentration to maintain a desired shape.

To illustrate a simple control example, it is desired that the percentage of cubes remains below 40%. If more than 40% of the particles are cubes, then the controller adjusts the habit modifier level until the percentage is below 40%. The fresh feed reactant stream disturbance ( $T^{\text{sat}}=24^\circ\text{C}$ ) is fed to the crystallizer and a solids-free stream removed from the crystallizer at equal rates after 60 minutes. The exit stream is removing the added habit

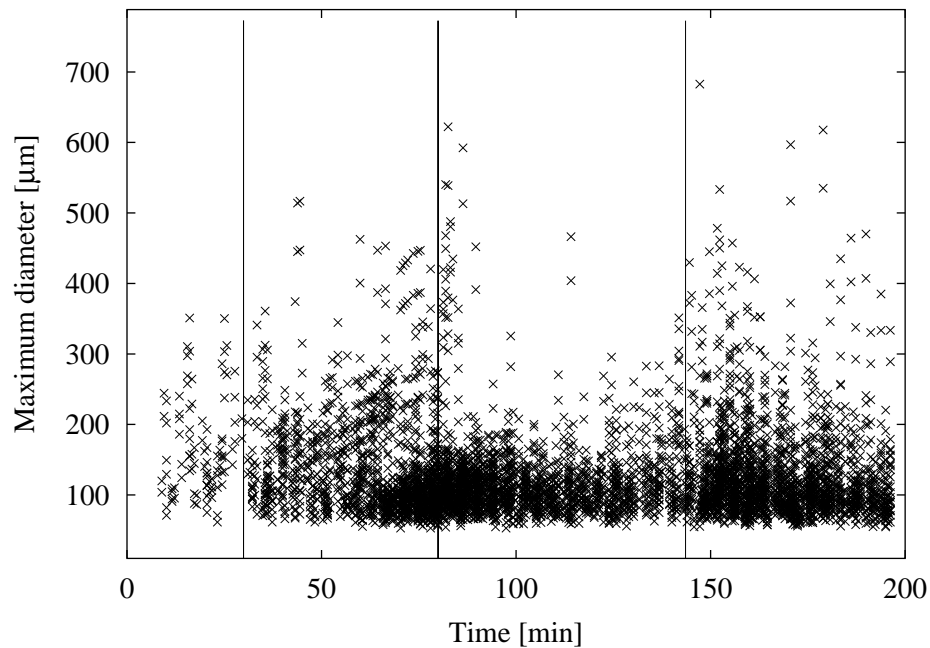


Figure 7.7: Raw data maximum crystal length,  $l$  as a function of time. Impurity injected at 30 min, contaminated solution flush started at 80 min and stopped at 144 min. A second dosage of impurity is injected at 144 min.

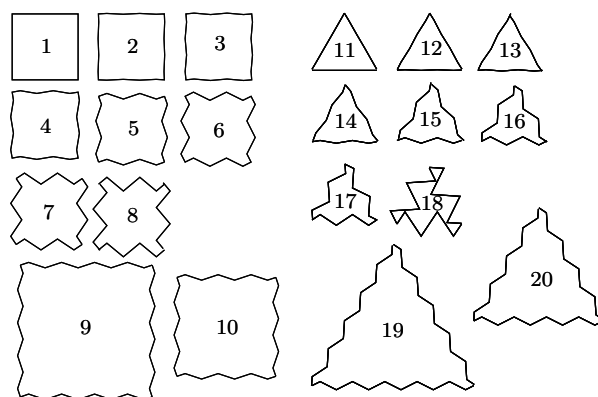


Figure 7.8: Possible sodium chlorate views in two dimensions when the crystal rests either on the 100 face (square) or  $\bar{1}\bar{1}\bar{1}$  face (triangle).

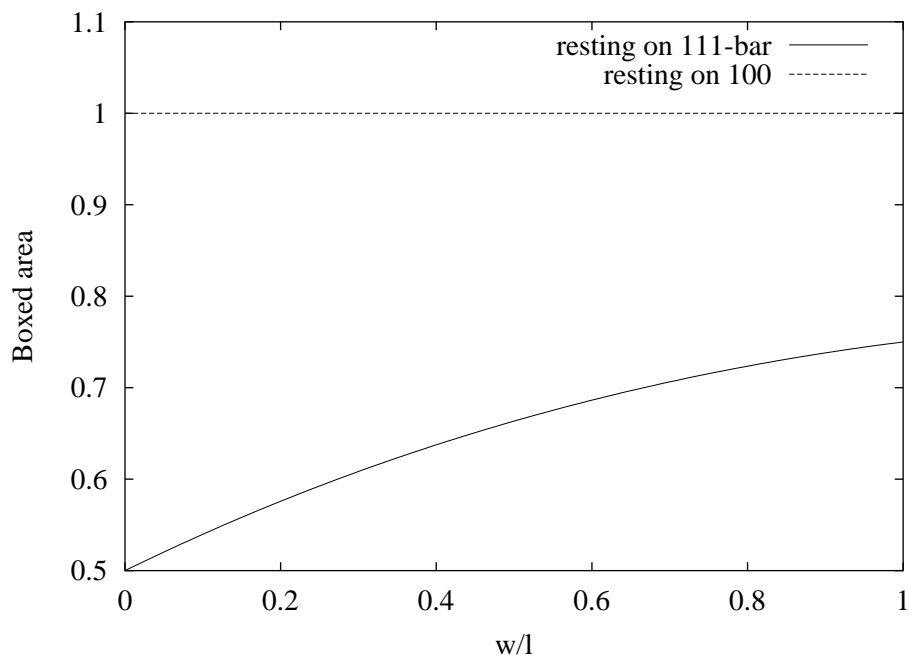


Figure 7.9: Boxed area as a function of  $w/l$  for a sodium chlorate crystal resting on its 100 and  $\bar{1}\bar{1}\bar{1}$  faces.  $w$  is the length across the 100 face from the top of one  $\bar{1}\bar{1}\bar{1}$  face to the diametrically opposite  $\bar{1}\bar{1}\bar{1}$  face.  $l$  is the length across the 100 face perpendicular to the  $w$  length.

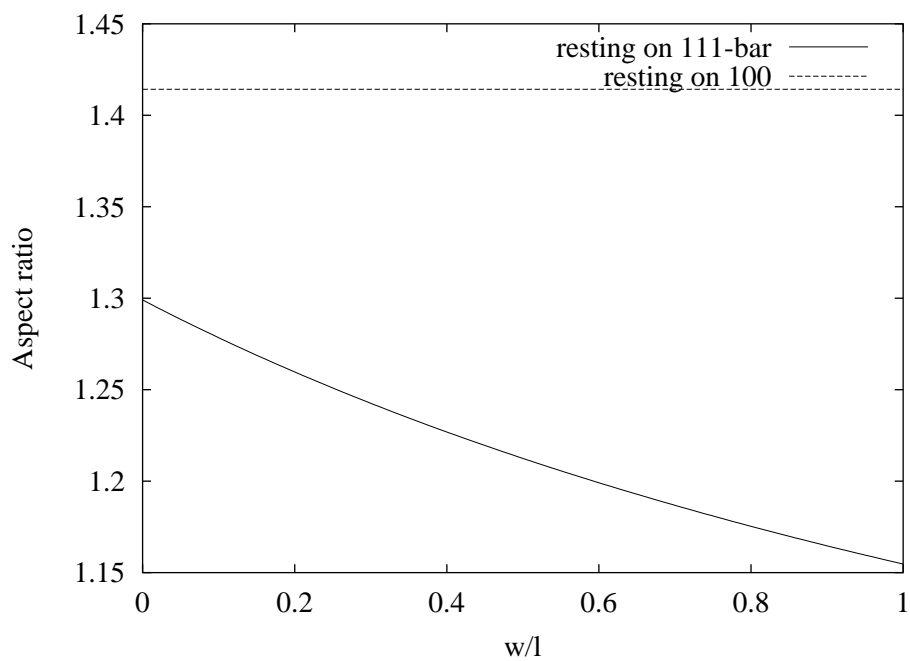


Figure 7.10: Aspect ratio as a function of  $w/l$  for a sodium chlorate crystal resting on its 100 and  $\bar{1}\bar{1}\bar{1}$  faces.  $w$  is the length across the 100 face from the top of one  $\bar{1}\bar{1}\bar{1}$  face to the diametrically opposite  $\bar{1}\bar{1}\bar{1}$  face.  $l$  is the length across the 100 face perpendicular to the  $w$  length.

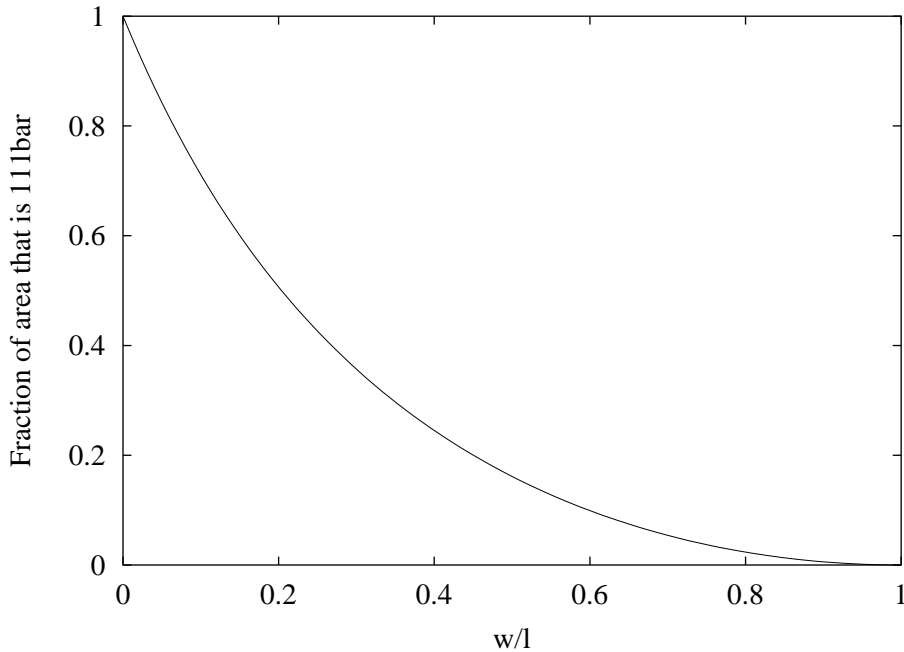


Figure 7.11: The ratio of the total surface area of all four  $\bar{1}\bar{1}\bar{1}$  faces to the total surface area of the whole sodium chlorate crystal as a function of  $w/l$ .

modifier so the controller is required to maintain the level of habit modifier over the course of crystallization. Figure 7.19 shows that without any prior knowledge of the nucleation and growth kinetics of the sodium chlorate system, the controller is able to determine a critical concentration of 140-150 ppm sodium dithionite required to maintain the percentage of cubes less than 40%.

## 7.4 Conclusions

This chapter has shown that a simple user defined algorithm can be implemented with existing commercially available image analysis software to monitor transient crystal shape changes in a suspension crystallizer. The raw signal from image analysis is replete with bad data resulting in a noisy signal, but with prior knowledge of the crystal shape, a simple automated classification scheme can be used to determine which data result from correctly sized crystals. This signal can be used for basic control of crystal shape in a suspension crystallizer.

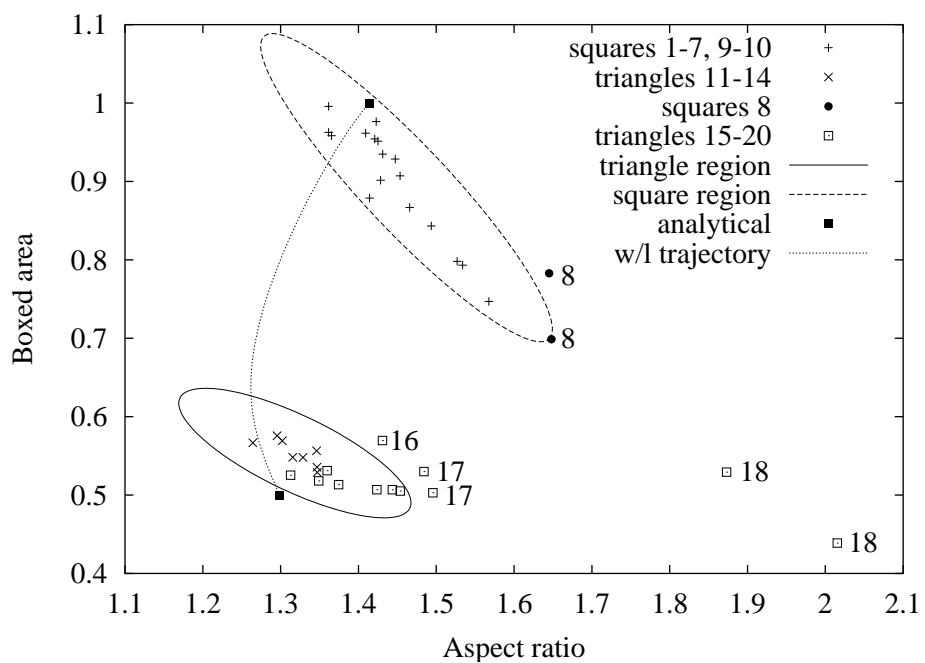


Figure 7.12: Likelihood regions in which Image Pro Plus will detect a square and equilateral triangle using boxed area and aspect ratio. The ellipse for detecting a square is based on squares 1-7, 9-10 at two sizes. The ellipse for detecting a triangle is based on triangles 11-14 at two sizes.

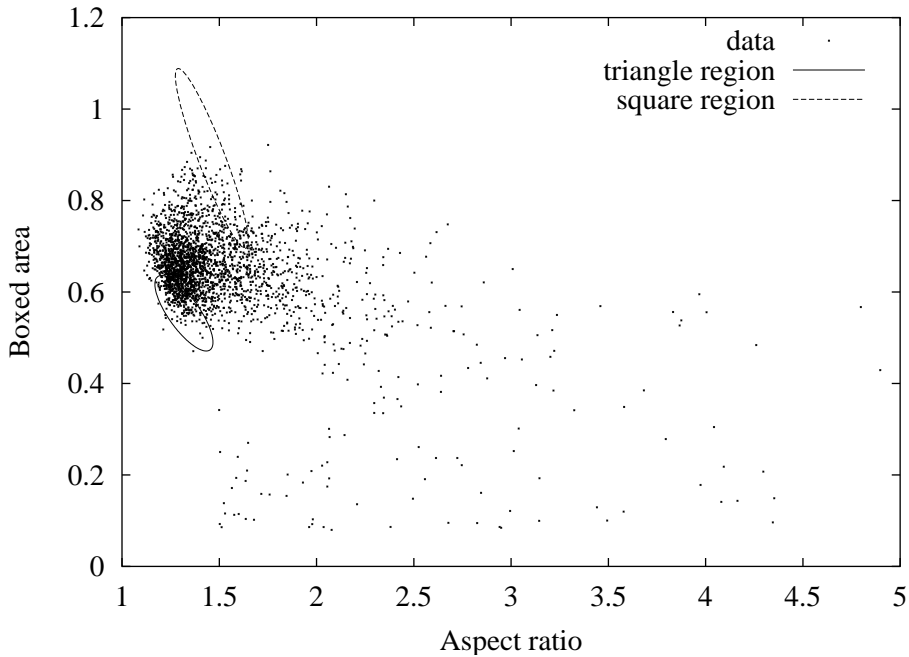


Figure 7.13: Raw data in boxed area - aspect ratio plane with regions indicating where an object is a square or triangle.

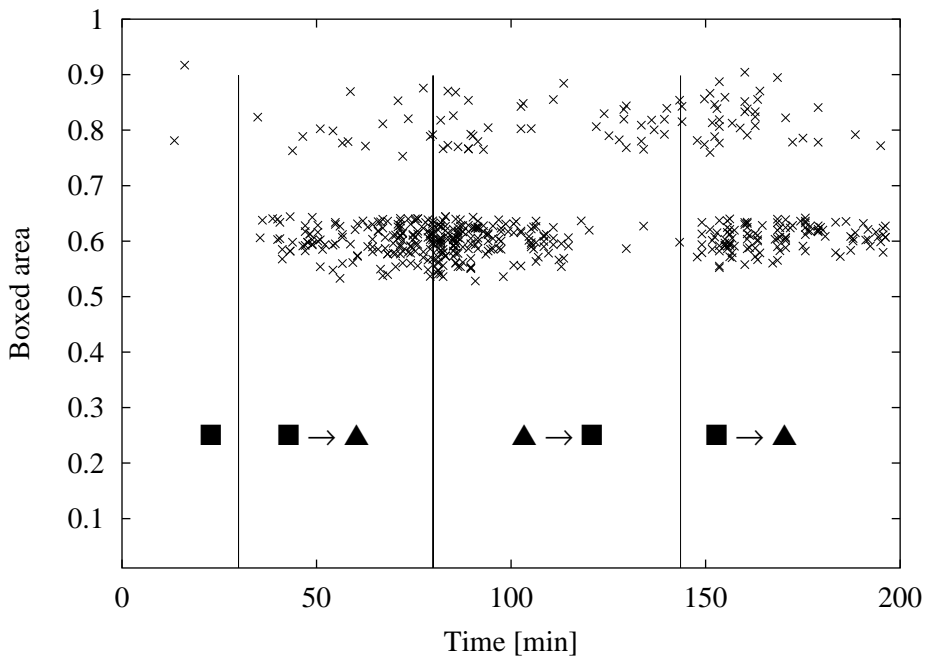


Figure 7.14: Boxed area as a function of time. Impurity injected at 30 min, contaminated solution flush started at 80 min and stopped at 144 min. A second dosage of impurity is injected at 144 min.

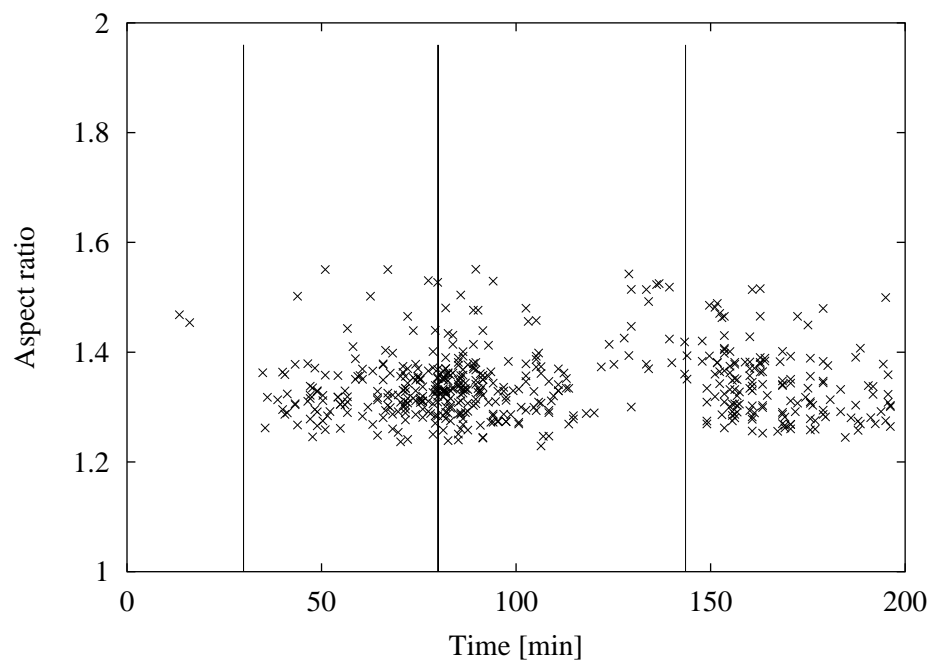


Figure 7.15: Aspect ratio as a function of time. Impurity injected at 30 min, contaminated solution flush started at 80 min and stopped at 144 min. A second dosage of impurity is injected at 144 min.

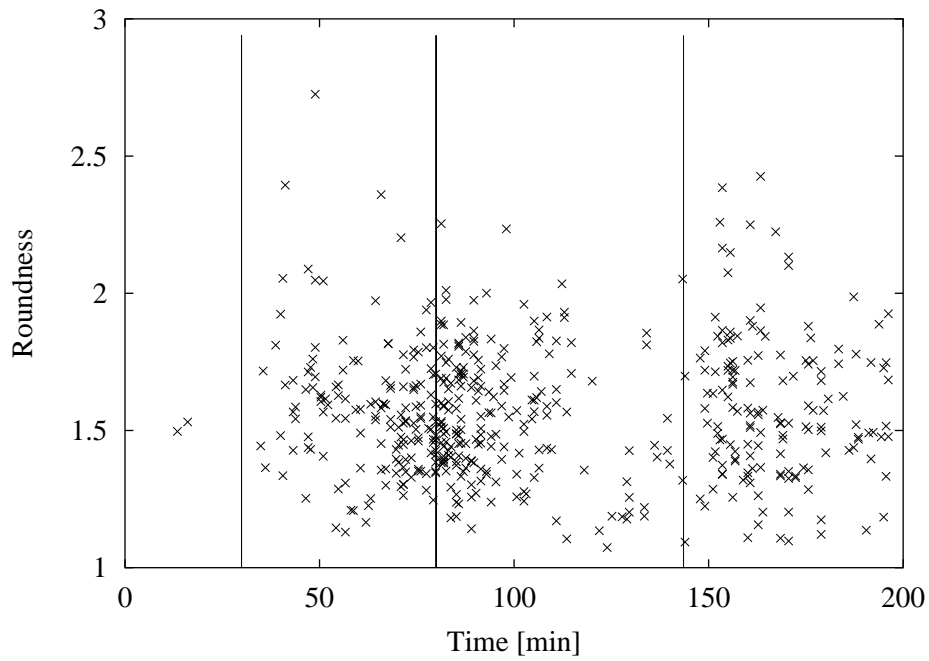


Figure 7.16: Roundness as a function of time. Impurity injected at 30 min, contaminated solution flush started at 80 min and stopped at 144 min. A second dosage of impurity is injected at 144 min.

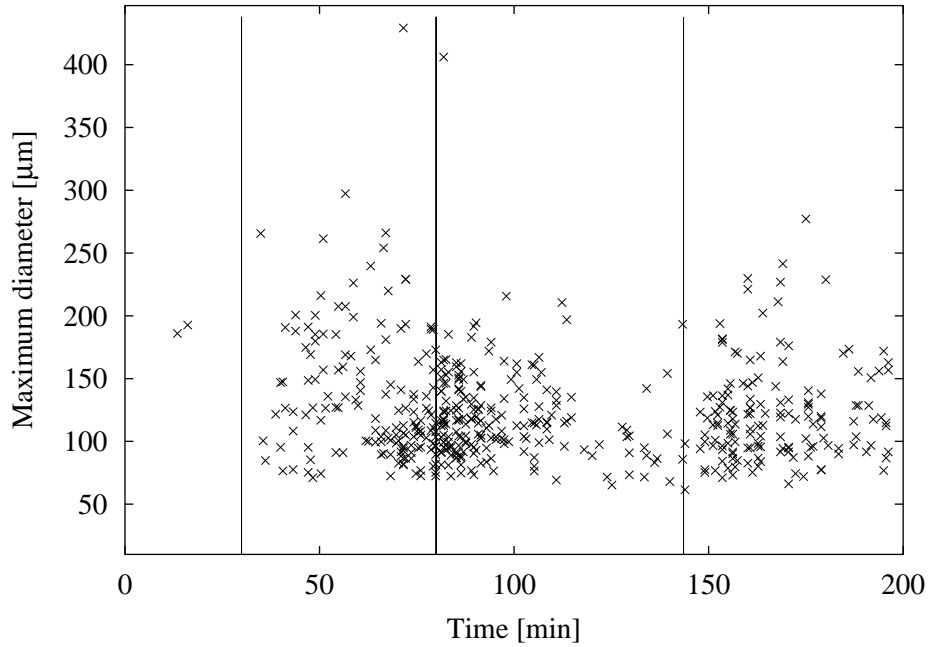


Figure 7.17: Maximum crystal diameter,  $l$  as a function of time. Impurity injected at 30 min, contaminated solution flush started at 80 min and stopped at 144 min. A second dosage of impurity is injected at 144 min.

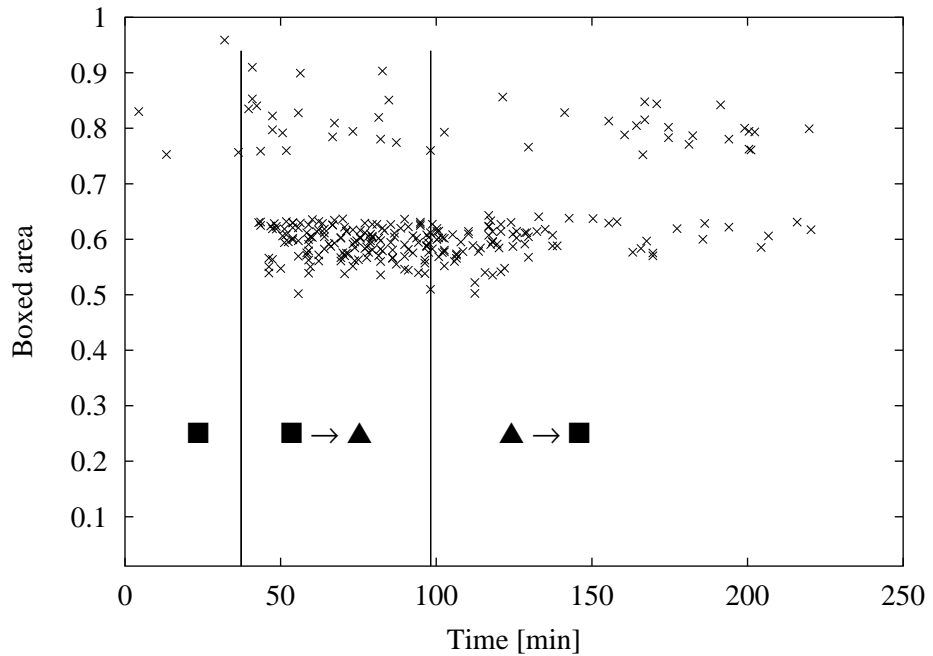


Figure 7.18: Boxed area as a function of time for a replicated experiment of the experiment in Figure 7.14.

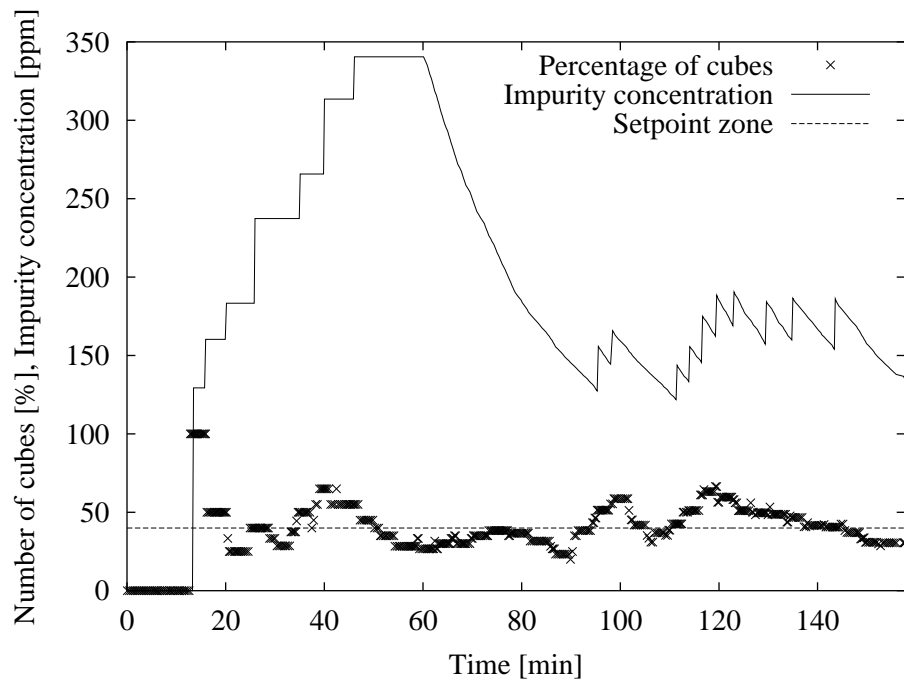


Figure 7.19: Feedback control of particle shape based on on-line measurements of shape. After 60 minutes, an impurity-free solution of sodium chlorate is fed to the reactor and a solids-free solution removed at equal rates for the remainder of the experiment.

## Chapter 8

### Conclusions

*NO! The point is ...*

— Matthews, H. B.

This dissertation has outlined a procedure for solving the common industrial crystallization problems of obtaining adequate models and installing reliable sensors. The population balance approach is the standard starting point for initial model identification stage. To obtain reliable parameter estimates, data of more than one measurement type describing both the solid and solution phases are required. Data from dynamic batch experiments need to be collected for a range of different operating conditions. From this point, the researcher will have identified a weakness in the model that requires further attention, such as incorporation of dynamic habit models, dissolution models, and model reduction. From this point, further experiments are implemented to test the validity of the model. Finally, an objective is defined and experiments are designed. After the first stage of experimentation, many issues besides modeling may be open that require further attention before proceeding with experimental design. The sensors may not be adequate to measure or detect crystal size or habit. The experiments or lack of measurements may not be informative to uniquely identify the system parameters. This study addresses modeling and measurement issues encountered during the steps towards experimental design of crystallization systems.

## 8.1 Experimental Design for Systems with Growth-Dependent Dispersion

This portion of the study has shown that the predictions of a growth-dependent dispersion model with dissolution model shows good agreement with on-line measurements of solution concentration, slurry transmittance, CSD mean and standard deviation. The parameters for the seeded crystallization of an industrial pharmaceutical with no secondary nucleation are estimated. For a seeded crystallization with growth-dependent dispersion and no secondary nucleation, minimization of product crystal size density properties such as the coefficient of variation, by manipulating the cooling profile is not possible with a final size or yield constraint. If growth-rate dispersion occurs via random fluctuations instead of growth-dependent dispersion, then the the coefficient of variation can be minimized subject to the size constraint. In the case of growth-dependent dispersion, batch operating time is minimized subject to the final size constraint and the yield is fixed. The optimal profile has been implemented and found to agree with the model predictions producing a CSD with the desired mean size.

## 8.2 High-Growth Systems

This portion of the study used a population balance to describe the crystallization kinetics of para-xylene crystallization in a scraped-surface crystallizer with nucleation occurring at the walls and growth in the bulk. Growth rates are not estimable from these data and so a reduced population balance model is developed that describes crystallization kinetics of high-growth systems in scraped-surface crystallizers with nucleation occurring at the walls of the crystallizer. The nucleation parameters are not estimable from the one set of experimental conditions, however, we suggest alternative experiments that improve the confidence in parameter estimates. The ability to solve common industrial crystallization problems requires more than one measurement type and operating condition to utilize the standard population balance approach and optimal control to its maximum capability.

## 8.3 Monitoring and Controlling Crystal Habit

This portion of the study has shown that user-defined algorithms can be integrated with standard video-microscopy and image analysis software to provide on-line measurements of crystal habit. It is possible to use the shape sensor for feedback control of crystal habit. For a semi-batch crystallization of sodium chlorate in the presence of no sodium dithionite impurity results in a cubic crystal habit. For a semi-batch crystallization of sodium chlorate in the presence of at least 50 ppm sodium dithionite results in a tetrahedral crystal habit. Two types of proto-typical control problems can be studied with this system with the impurity load as a manipulated or disturbance variable, or the residence time of the reactor as the manipulated or disturbance variable. In the case studied here, the impurity load is

used as a manipulated variable. During crystallization, a solids-free solution is removed from the crystallizer and an impurity-free solution is fed to the crystallizer at equal rates and acts as a disturbance, driving the shape towards a cubic habit. Standard control techniques are capable of controlling crystal size and shape with state-of-the-art photomicroscopy sensors. The challenge will always be obtaining prior information such as the expected crystal habit of the specific system and which signals or measurements are appropriate to quantify a particular habit.

## 8.4 Future Work

Many issues in crystallization remain open with the improving sensor technology. In-situ and on-line crystal size and shape sensors are providing vast amounts of data in the form of strobed video images. In-situ solution concentration sensors are improving in sensitivity and provide accurate measurements of meta-stable zone widths and in some cases detect polymorphic transformations. The large quantity of video images provided by imaging sensors present problems in data extraction and data reduction if they are ever to be used for the successful implementation of advanced on-line control strategies.

The new process vision measurement probes and in-situ light scattering probes measure characteristics of randomly-oriented objects. Photomicroscopy used in this study measures size characteristics of settled particles. Development of models regarding the inference of size and shape characteristics from the projected shape of randomly oriented objects requires attention. In two dimensions as a crystal settles, it may be possible to distinguish its habit from other crystals, however, once randomly oriented, the two-dimension projection of an ellipsoid may be confounded with the two-dimension projection of a sphere. If the process vision measurement probe provides little quantitative information, a study investigating image analysis of images from two video microscopes should be attempted.

Attempts should also be made at monitoring polymorphic transformations on-line with x-ray diffraction. The large quantity data from x-ray diffraction scattering patterns will also be handled by the new tools emerging from the field of data reduction. Closed-loop control technologies have not been applied to many industrial crystallization systems. The author is encouraged by the results of the sensor technologies and models used in this study. Soon, the technologies will be used in the successful implementation of closed-loop control strategies.



# Notation

## Upper Case Letters

$A$	— jacket heat transfer area, $\text{m}^2$
$A_p(L)$	— projected surface area of a particle of size $L$ .
$A_{ij}$	— derivative weight matrix for collocation
$A, B, C$	— model matrices in state space notation
$B$	— crystal birth rate, $1\cdot\text{s}^{-1}\cdot\text{kg solvent}^{-1}$
$B$	— crystal nucleation rate, $1\cdot\text{s}^{-1}\cdot\text{kg solvent}^{-1}$
$\hat{C}$	— liquid phase concentration, $\text{kg}\cdot\text{kg}^{-1}$ solvent
$\hat{C}_{\text{sat}}$	— liquid phase saturation concentration, $\text{kg}\cdot\text{kg}^{-1}$ solvent
$\hat{C}_{\text{sat0}}$	— saturation concentration curve shift parameter, $\text{kg}\cdot\text{kg}^{-1}$ solvent
$C_n$	— equilibrium concentration of $n$ -sized cluster
$C_{\text{imp}}$	— impurity concentration, ppm
$C_p$	— slurry heat capacity, $\text{J}\cdot\text{K}$
$\hat{C}_p$	— slurry heat capacity, $\text{J}\cdot\text{kg}^{-1}\cdot\text{K}$
$\hat{C}_0$	— liquid phase concentration at zero time, $\text{kg}\cdot\text{kg}^{-1}$ solvent
$D$	— crystal death rate, $1\cdot\text{s}^{-1}\cdot\text{kg solvent}^{-1}$
$D$	— crystal diffusivity $\text{m}^2\cdot\text{s}^{-1}$
$F(L, t)$	— particle size distribution, $1\cdot\text{m}^{-3}$ .
$G$	— crystal growth rate, $\text{m}\cdot\text{s}^{-1}$
$G'$	— crystal growth frequency, $1\cdot\text{s}^{-1}$
$G_l$	— crystal growth rate of $l$ coordinate, $\text{m}\cdot\text{s}^{-1}$
$G_w$	— crystal growth rate of $w$ coordinate, $\text{m}\cdot\text{s}^{-1}$
$\hat{H}$	— enthalpy, $\text{J}\cdot\text{kg}^{-1}$
$\Delta\tilde{H}_c$	— heat of crystallization, $\text{J}\cdot\text{mol}^{-1}$
$\Delta\hat{H}_c$	— heat of crystallization, $\text{J}\cdot\text{kg}^{-1}$
$\mathbf{H}_{\theta\theta}$	— Hessian

$I$	— incident light intensity
$I_0$	— transmitted light intensity
$K$	— kinetic energy, kJ
$L$	— characteristic particle length, m
$L_0$	— characteristic length at which crystals are nucleated, m
$L_{\max}$	— maximum seed size, m
$L_x, L_d$	— Kalman filter gain
$N$	— horizon length
$N_i$	— number of $i$ molecules
$P_{xy}(t)$	— probability for a process starting at $x$ is in $y$ at time $t$
$Q$	— net rate of heat added to the system from the surroundings, W
$Q$	— state penalty, dimensionless
$Q(L)$	— light extinction efficiency factor
$R$	— gas constant, $8.314 \text{ kJ}\cdot\text{kg}^{-1}\cdot\text{K}^{-1}$
$R$	— mass generation, $\text{kg}\cdot\text{s}^{-1}$
$S$	— supersaturation ratio, dimensionless
$S$	— surface area, $S=S_k+S_s+S_e$
$S$	— input penalty, dimensionless
$S_w$	— supersaturation ratio at the wall, dimensionless
$T$	— bulk crystallizer temperature, $^{\circ}\text{C}$
$T_0$	— bulk crystallizer temperature at zero time, $^{\circ}\text{C}$
$T_j$	— cooling jacket fluid temperature, $^{\circ}\text{C}$
$U$	— overall heat transfer coefficient, $\text{W}\cdot\text{m}^2\cdot\text{K}$
$U$	— internal energy, kJ
$\hat{U}$	— internal energy, $\text{kJ}\cdot\text{kg}^{-1}$
$\hat{V}$	— volume, $\text{m}^3\cdot\text{kg}^{-1}$
$V$	— crystallizer volume, $\text{m}^3$
$\mathbf{V}_{\mathbf{XX}}$	— ellipsoid covariance
$W$	— work done by the system on the surroundings, W
$W_s$	— shaft work transferred by means of moving parts, W
$\mathbf{X}$	— ellipsoid
$X(t)$	— state of stochastic system at time $t$

$\bar{\mathbf{X}}$	— ellipsoid focal points
$Z_n$	— $n$ -sized cluster concentration, $\text{m}^{-3}$

## Lower Case Letters

$a_i$	— activity of solute $i$ , $\text{mol}\cdot\text{kg}^{-1}$ , $\text{mol}\cdot\text{L}^{-1}$ , mole fraction
$a_2, a_1, a_0$	— coefficients of quadratic seed size density
$b$	— nucleation rate order, dimensionless
$\mathbf{b_l}, \mathbf{b_u}$	— upper and lower bound vectors for temperature constraints
$c_i$	— activity of solute $i$ , $\text{mol}\cdot\text{kg}^{-1}$ , $\text{mol}\cdot\text{L}^{-1}$ , mole fraction
$d_k$	— output disturbance at time $k$
$d_w$	— depth-to-width ratio, dimensionless
$e_{ik}(\theta)$	— prediction error of the $i^{\text{th}}$ measurement of the $k^{\text{th}}$ type
$f_0(L)$	— particle size density at zero time, $1\cdot\text{m}^{-3}\cdot\text{m}^{-1}$
$f_q$	— coefficient for quadratic seed size density function
$f(L, t)$	— particle size density, $1\cdot\text{m}^{-3}\cdot\text{m}^{-1}$
$f(l, w, t)$	— particle size density, $1\cdot\text{m}^{-3}\cdot\text{m}^{-2}$
$f_{nm}(t)$	— transition frequency of $n$ -sized cluster to $m$ -sized cluster, $\text{s}^{-1}$
$f_n$	— transition frequency of $n$ -sized cluster to $n + 1$ -sized cluster, $\text{s}^{-1}$
$g$	— growth rate order, dimensionless
$g_n$	— transition frequency of $n$ -sized cluster to $n - 1$ -sized cluster, $\text{s}^{-1}$
$g(x(t_i))$	— supersaturation state constraint
$h$	— conversion from solvent mass to slurry volume
$\bar{h}_j$	— partial molar enthalpy, $\text{J}\cdot\text{mol}^{-1}$
$j_n(t)$	— rate of appearance of $n$ -sized cluster
$k_a$	— area shape factor, dimensionless
$k_b$	— nucleation rate constant, $1\cdot\text{s}^{-1}\cdot\text{kg solvent}^{-1}$
$k_g$	— growth rate constant, $\text{m}\cdot\text{s}^{-1}$
$k'_g$	— growth rate constant, $1\cdot\text{s}^{-1}$
$k_v$	— volume shape factor, dimensionless
$l$	— light transmission path length, m
$l$	— length of 100 face of sodium chlorate, m
$l_w$	— length-to-width ratio, dimensionless

$l_i(x)$	— Lagrange interpolation polynomial
$m$	— mass, kg
$m_s$	— mass of seeds, kg
$n$	— number of moles, number of units in cluster
$n_k$	— number of measurements of $k^{\text{th}}$ type
$\mathbf{n}$	— unit vector normal to the surface
$p$	— pressure, Pa, random variable distributed uniformly on [0,1]
$p$	— plength, projected length from PVM imaging, $\mu\text{m}$
$q$	— volumetric flowrate, $\text{m}^3 \cdot \text{s}^{-1}$
$q_i$	— quadrature weight for collocation
$q_{xy}$	— infinitesimal rate parameter of a stochastic process
$q(p, L)$	— single particle PVM particle plength density
$q_{pop}(p)$	— particle population PVM plength density
$\mathbf{r}_k$	— reference trajectory
$r_i$	— rate of reaction $i$ , $\text{s}^{-1}$
$t$	— time, s
$t_f$	— batch time, s
$\mathbf{u}_k$	— input vector at time $k$
$\mathbf{v}$	— vector of internal and external velocities
$w$	— length perpendicular to $l$ on 100 face, m
$w$	— mass flowrate $\text{kg} \cdot \text{s}^{-1}$
$w_j$	— quadrature weight
$\mathbf{x}_k$	— state vector at time $k$
$\hat{\mathbf{x}}_k^-, \hat{\mathbf{x}}_k$	— state estimate at time $k$ given $y_k$ up to times $k - 1$ and $k$
$\mathbf{x}$	— three-dimensional vector of spatial coordinates
$\mathbf{y}_k$	— output measurement vector
$\mathbf{y}$	— vector of internal state variables
$\mathbf{z}$	— vector of spatial and state variables

## Greek Letters

$\alpha$	— confidence level of $\chi_p^2$
$\alpha_{ij}$	— birth rate from state $x_i$ to $x_j$ , $\text{s}^{-1}$

$\beta(L, L')$	— agglomeration kernel, $s^{-1}$
$\theta$	— parameter vector
$\hat{\theta}$	— optimal model parameter vector
$\gamma_1$	— size-dependency order
$\gamma_2$	— inverse length weighting factor
$\Delta$	— monomer unit size, m
$\lambda_i$	— birth rate from state $x_i$ to $x_{i+1}$ , $s^{-1}$
$\mu_i$	— death rate from state $x_i$ to $x_{i-1}$ , $s^{-1}$
$\mu_j$	— $j^{\text{th}}$ moment of the PSD, $m^k \cdot g \text{ solvent}^{-1}$
$\Delta\mu$	— chemical potential difference, $\text{kJ} \cdot \text{kmol}^{-1}$
$\rho$	— slurry density, $\text{kg} \cdot \text{m}^{-3}$
$\rho_c$	— crystal density, $\text{kg} \cdot \text{m}^{-3}$
$\rho < \bar{v} >$	— cross sectional flowrate, $\text{kg} \cdot \text{m}^{-2} \cdot \text{s}^{-1}$
$\sigma$	— relative supersaturation
$\hat{\sigma}_k^2$	— variance for $k^{\text{th}}$ measurement type
$\tau$	— turbidity, $\text{m}^{-1}$ , residence time, min
$\tau_i$	— time in which $X(t)$ jumps from state $x_{i-1}$ to $x_i$
$\Phi$	— potential energy, kJ
$\hat{\Phi}$	— potential energy, $\text{kJ} \cdot \text{kg}^{-1}$
$\Phi_{be}$	— maximum likelihood objective function
$\chi_p^2$	— chi-squared statistic
$\zeta$	— scaled dimensionless length
$\omega$	— frequency of coalescence between clusters of size $n$ and $m$
$\omega_k, \xi_k, \nu_k$	— identically independent Normally distributed random variables with zero mean
$\Omega$	— particle phase space

## Caligraphic Letters

$\mathcal{S}$	— finite or countably infinite state space for the stochastic process $X(t)$
$\mathcal{U}$	— uniform density on $[0,1]$



## Appendix A

# Model-Predictive Control of Crystallizer Temperature

A cascaded control system is used to control the temperature of the crystallizer. A master controller determines the setpoint of the temperature of the inlet jacket to the crystallizer. A slave controller receives the inlet temperature setpoint to the crystallizer and controls the temperature by manipulating the blend of hot and cold water at the jacket inlet. The slave loop for control of the jacket inlet is fast and a standard feedback PI control system is adequate. The response of the change in the crystallizer temperature to a setpoint change in the inlet jacket temperature (Figure A.1) is sluggish due to poor heat transfer through the glass wall of the crystallizer. Standard cascaded PID feedback control is inadequate, the temperature of the crystallizer generally lags behind the setpoint trajectory.

Model-predictive control improves performance since the controller acts on future predictions of future deviations from the setpoint trajectory. Miller [75] uses quadratic dynamic matrix control (QDMC) as discussed by Garcia and Morshedi [28] for the master controller to determine the setpoint to the inlet of the jacket of the crystallizer. QDMC uses a linear step response model and a quadratic performance objective, and it explicitly incorporates input constraints in the QP. The QP must be solved on-line. Feedback is incorporated by estimating a disturbance as the difference between the measured value of the output and its predicted value. However, no weighting is given to the *disturbance* as to whether it is a true disturbance or measurement noise and as discussed previously, stability of QDMC has not been addressed theoretically [71]. Formulating an infinite horizon control law guarantees the stability property, but if constraints need to be handled repeated optimization calculations are required on-line at each sample time. The response of the crystallizer temperature to a step in the jacket temperature is a simple first order with dead time model, so tuning the controller via simulation prior to the experiment helps to avoid violating input constraints when the controller is implemented on-line.

Consider a plant model with an equal number of inputs and outputs and a constant output disturbance that acts as an integrator. The disturbance,  $d_k$  that acts as an integrator is shown to be offset free given that  $\mathbf{A}$  has no eigenvalues at 1 and the steady-state gain

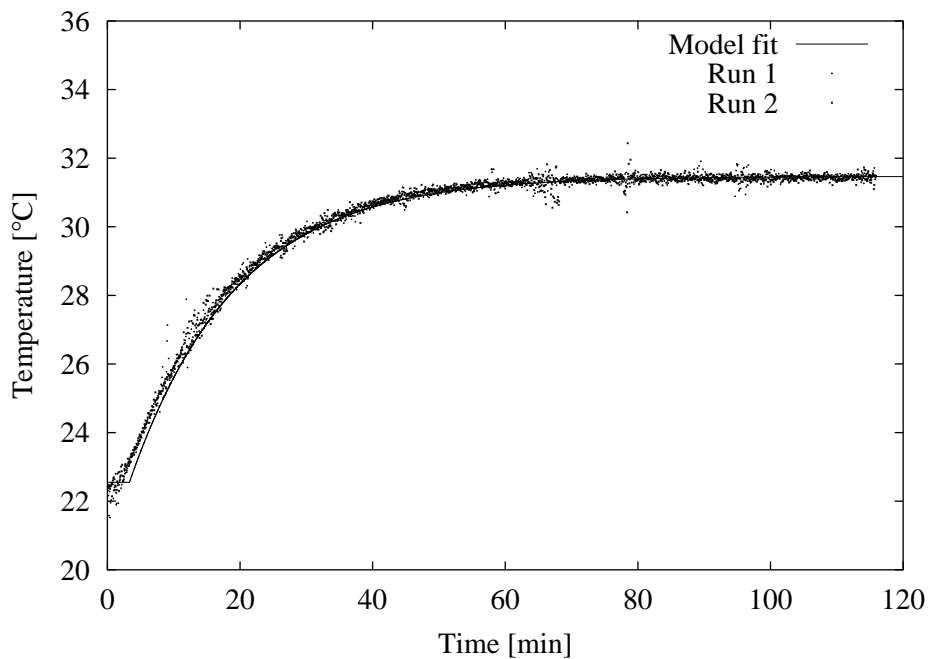


Figure A.1: Response of the crystallizer to a 10°C step change in the inlet jacket temperature with a fit of a first order with dead-time model. The fit of the model  $dT_{\text{crystallizer}}/dt = -(1/\tau)T_{\text{crystallizer}}(t) + (K/\tau)T_{\text{inlet}}^{\text{set}}(t - \alpha)$  where  $\alpha = 2.17$  min,  $\tau = 15.95$  min and  $K=0.90$  °C/°C is also shown.

matrix has full rank [109]. The plant model is

$$x_{k+1} = Ax_k + Bu_k + \omega_k \quad (\text{A.1})$$

$$d_{k+1} = d_k + \xi_k \quad (\text{A.2})$$

$$y_k = Cx_k + d_k + \nu_k \quad (\text{A.3})$$

where  $\omega$ ,  $\xi$  and  $\nu$  are independently, identically Normally distributed, zero mean random variables. Augmenting the state  $x_k$  and disturbance  $d_k$ ,

$$\begin{bmatrix} x \\ d \end{bmatrix}_{k+1} = \begin{bmatrix} A & 0 \\ 0 & I \end{bmatrix} \begin{bmatrix} x \\ d \end{bmatrix}_k + \begin{bmatrix} B \\ 0 \end{bmatrix} u_k + \begin{bmatrix} I & 0 \\ 0 & I \end{bmatrix} \begin{bmatrix} \omega \\ \xi \end{bmatrix}_k \quad (\text{A.4})$$

$$y_k = \begin{bmatrix} C & I \end{bmatrix} \begin{bmatrix} x \\ d \end{bmatrix}_k + \nu_k \quad (\text{A.5})$$

The estimator with disturbance model is

$$\hat{x}_{k+1}^- = A\hat{x}_k + Bu_k \quad (\text{A.6})$$

$$\hat{d}_{k+1}^- = \hat{d}_k \quad (\text{A.7})$$

$$\hat{x}_k = \hat{x}_k^- + L_x (y_k - (C\hat{x}_k^- + \hat{d}_k^-)) \quad (\text{A.8})$$

$$\hat{d}_k = \hat{d}_k^- + L_d (y_k - (C\hat{x}_k^- + \hat{d}_k^-)) \quad (\text{A.9})$$

where  $\hat{x}_k^-$ ,  $\hat{x}_k$  are the state estimates at time  $k$  given the output measurements  $y_k$  up to times  $k-1$  and  $k$ , respectively.  $L_x$  and  $L_d$  are the Kalman filter gains, computed by solving the discrete steady-state Riccati equation for the linear quadratic estimation problem after specifying the covariances of  $w$ ,  $\xi$  and  $v$ .

Batch suspension crystallizers are typically operated with a pre-determined cooling temperature profile. A controller must be designed that considers not just the current reference signal or a final setpoint, but the controller must also consider future reference signals extending from the current time  $k$  to  $k+N-1$ , where  $N$  is the horizon length. The reference trajectory,  $\mathbf{r}_k$ , is

$$r_{j|k} = \begin{cases} r_j, & k \leq j < k+N-1 \\ r_{k+N-1}, & k+N-1 \leq j \end{cases} \quad (\text{A.10})$$

where we assume that the reference trajectory after  $k+N$  is constant, see Figure A.2. The infinite horizon tracking problem at time  $k$  is

$$\min_{\mathbf{u}_k} \Phi(\mathbf{x}_k, \mathbf{r}_k, \mathbf{u}_k) \quad (\text{A.11})$$

in which

$$\Phi(\mathbf{x}_k, \mathbf{r}_k, \mathbf{u}_k) = \sum_{j=k}^{\infty} (\mathbf{y}_j - \mathbf{r}_j)^T \mathbf{Q} (\mathbf{y}_j - \mathbf{r}_j) + (\mathbf{u}_j - \mathbf{u}_{j-1})^T \mathbf{S} (\mathbf{u}_j - \mathbf{u}_{j-1}) \quad (\text{A.12})$$

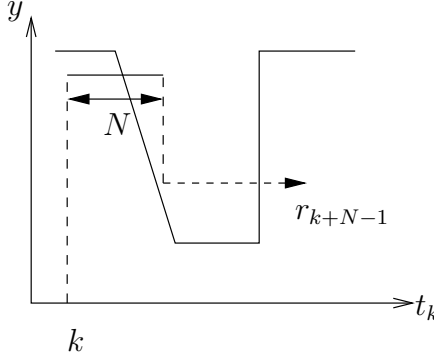


Figure A.2: Moving horizon reference trajectory.

subject to the model, Equations A.4 and A.5. Augmenting the current state, the future trajectory and the previous input results in the following augmented state equation

$$\begin{bmatrix} x_{k+1} \\ r_{k+1|k+1} \\ r_{k+2|k+1} \\ \vdots \\ r_{k+N-1|k+1} \\ r_{k+N|k+1} \\ u_k \end{bmatrix} = \begin{bmatrix} A & 0 & 0 & \cdots & 0 & 0 & 0 \\ 0 & 0 & I & \cdots & 0 & 0 & 0 \\ 0 & 0 & 0 & \cdots & 0 & 0 & 0 \\ \vdots & \vdots & \vdots & \ddots & \vdots & \vdots & \vdots \\ 0 & 0 & 0 & \cdots & 0 & I & 0 \\ 0 & 0 & 0 & \cdots & 0 & I & 0 \\ 0 & 0 & 0 & \cdots & 0 & 0 & 0 \end{bmatrix} \begin{bmatrix} x_k \\ r_{k|k} \\ r_{k+1|k} \\ \vdots \\ r_{k+N|k} \\ r_{k+N-1|k} \\ u_{k-1} \end{bmatrix} + \begin{bmatrix} B \\ 0 \\ 0 \\ \vdots \\ 0 \\ 0 \\ I \end{bmatrix} u_k$$

$$\tilde{\mathbf{z}}_{k+1} = \tilde{\mathbf{A}}\tilde{\mathbf{z}}_k + \tilde{\mathbf{B}}\mathbf{u}_k \quad (\text{A.13})$$

The regulation problem becomes

$$\min_{\tilde{\mathbf{u}}_k} \Phi(\tilde{\mathbf{x}}_k, \tilde{\mathbf{r}}_k, \tilde{\mathbf{u}}_k) \quad (\text{A.14})$$

in which

$$\Phi(\tilde{\mathbf{z}}_k, \tilde{\mathbf{r}}_k, \tilde{\mathbf{u}}_k) = \sum_{j=k}^{\infty} \tilde{\mathbf{z}}_j^T \tilde{\mathbf{Q}} \tilde{\mathbf{z}}_j + 2\tilde{\mathbf{z}}_j^T \tilde{\mathbf{M}} \tilde{\mathbf{u}}_j + \tilde{\mathbf{u}}_j^T \tilde{\mathbf{R}} \tilde{\mathbf{u}}_j \quad (\text{A.15})$$

and

$$\tilde{\mathbf{x}}_k = \mathbf{x}_k - \mathbf{x}_k^s \quad (\text{A.16})$$

$$\tilde{\mathbf{u}}_k = \mathbf{u}_k - \mathbf{u}_k^s \quad (\text{A.17})$$

$$\tilde{\mathbf{r}}_{j|k} = \mathbf{r}_{j|k} - \mathbf{r}_{k+N-1|k} \quad j = k, \dots, k + N - 1 \quad (\text{A.18})$$

$$\tilde{\mathbf{r}}_k = \mathbf{r}_k - \mathbf{r}_k^s \quad (\text{A.19})$$

$$\tilde{Q} = \begin{bmatrix} C^T QC & -C^T Q & 0 & \cdots & 0 \\ -QC & Q & 0 & \cdots & 0 \\ 0 & 0 & 0 & \cdots & 0 \\ \vdots & \vdots & \vdots & \ddots & \vdots \\ 0 & 0 & 0 & \cdots & 0 \\ 0 & 0 & 0 & \cdots & S \end{bmatrix} \quad (\text{A.20})$$

$$\tilde{R} = S \quad (\text{A.21})$$

$$\tilde{M} = \begin{bmatrix} 0 \\ 0 \\ 0 \\ \vdots \\ -S \end{bmatrix} \quad (\text{A.22})$$

The solution to the problem is

$$\mathbf{u}_k = K(\mathbf{z}_k - \mathbf{z}_k^s) + \mathbf{u}_k^s \quad (\text{A.23})$$

where  $K$  is computed from the solution to the discrete steady-state Riccati equation for the linear quadratic regulation problem. This method has advantages compared to QDMC. It is computationally less expensive than QDMC because an on-line QP need not be solved at every sample time. The method also incorporates a linear Kalman filter so less control action is implemented on a noisy signal. However, the method does not handle input or output constraints,  $K$  must be computed from simulations for different temperature profiles before commencing the experiment to ensure the input and output constraints are not violated. Future predicted deviations from the required trajectory are penalized equally as current deviations. Figures A.3 and A.4 show the performance of a cascaded MPC-PID temperature controller for the experimental apparatus. The regulator does not behave erratically to noise and rejects output disturbances. The regulator is tuned so that it does not violate input constraints, and the regulator is able to incorporate information of the future and act accordingly. The controller now knows that the heat transfer is poor and that the system has a large amount of relative inertia, so the manipulated variable is spiked moments before the step change and when turning corners from a ramp to a hold. As the crystallizer temperature approaches the new setpoint after the step in the temperature trajectory, the manipulated variable gradually levels off and holds the crystallizer at the new temperature. The response splits the trajectory with some early and late errors, however, the response is better than pure feedback in a cascaded PID-PID setup.

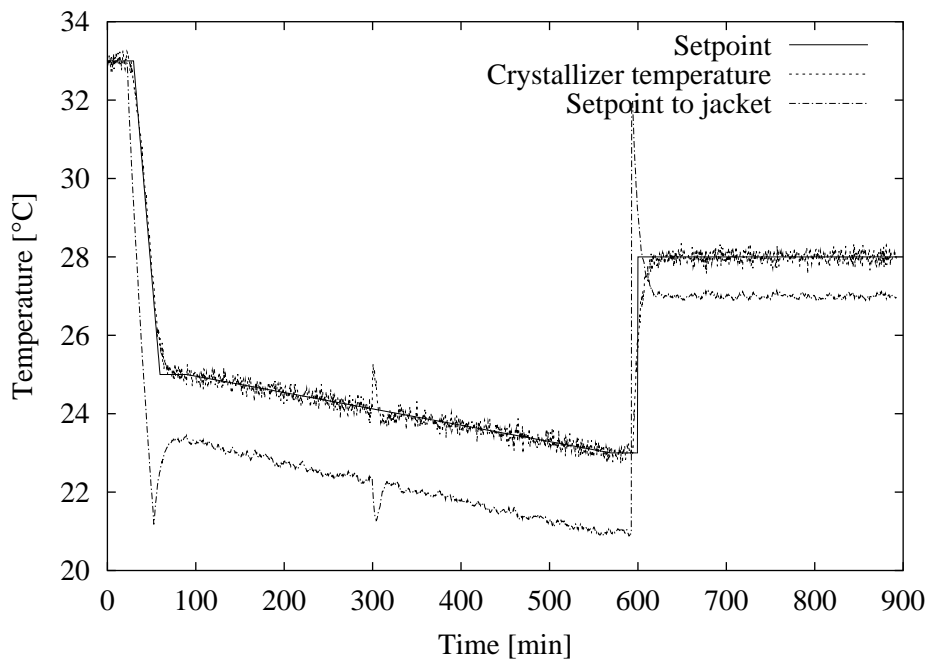


Figure A.3: Performance of cascaded horizon tracking-PID controller,  $Q=0.5$ ,  $S=5$ .

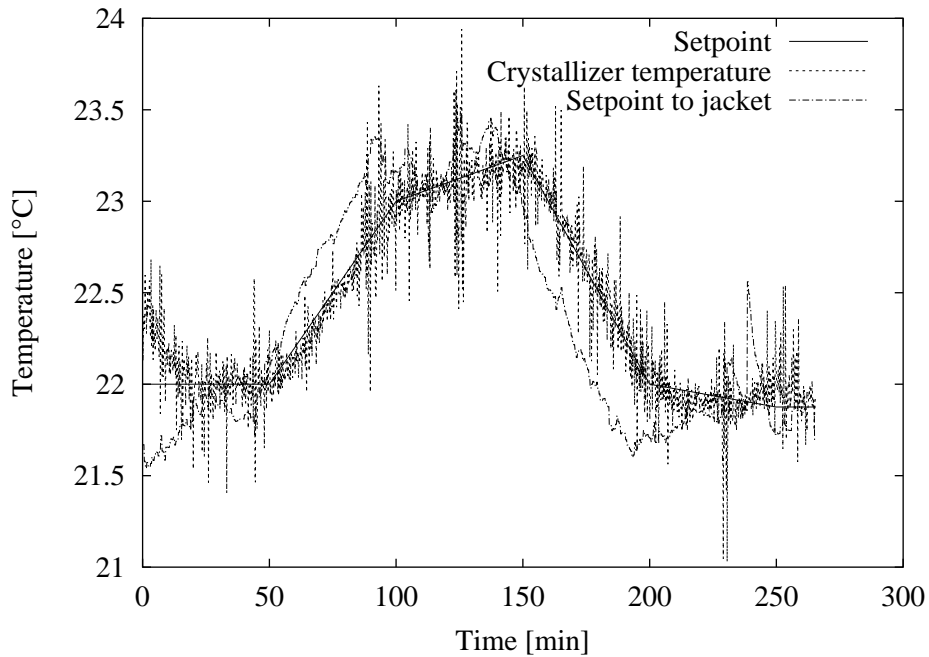


Figure A.4: Typical temperature profile for pharmaceutical crystallization.

## Appendix B

# Physical Properties

### B.1 Physical Parameters of the Pharmaceutical System

The pharmaceutical solubility ( $\text{g}\cdot\text{g solvent}^{-1}$ ) in iso-propyl alcohol (IPA) and water 93/7 % $v/v$  is related to the absolute temperature,  $T$ , via the following expression

$$\log_{10} \hat{C}_{sat}(T) = 242.86 - 208.01 \log_{10} T + 44.13 ((\log_{10} T)^2) \quad (\text{B.1})$$

Equation B.1 was determined from solubility data collected during solubility experiments at GlaxoSmithKline (GSK). Solutions of known concentration are cooled at 0.5, 0.25, ...  $^{\circ}\text{C}\cdot\text{min}^{-1}$  and the temperature at which nucleation occurs is recorded. The temperatures at which nucleation occurs are plotted as a function of the respective cooling rates. The solubility temperature for the solution concentration is extrapolated to 0  $^{\circ}\text{C}\cdot\text{min}^{-1}$ . These data are compared with data collected from long term equilibrium experiments in the batch crystallizer apparatus and are shown in Figure B.1. The correlation is a best fit model in the 20-75  $^{\circ}\text{C}$  temperature range. The following correlation, Equation B.2, is a fit based on all the data from GlaxoSmithKline and the data collected from long term equilibrium experiments, to compare the change in fitted solubility with the original fit.

$$\log_{10} \hat{C}_{sat}(T) = 141.848 - 128.196 \log_{10} T + 28.327 ((\log_{10} T)^2) \quad (\text{B.2})$$

The two fits and the solubility data in Figure B.1 show the magnitude of error in the saturation concentration measurement.

The pharmaceutical seeds were crystallized in a batch crystallizer, separated from the mother liquor by filtration and the fine particles were collected during sieving at GlaxoSmithKline (King of Prussia, PA). Figure B.2 shows the seeds under 40x magnification and Figure B.3 shows the PSD (measured by image analysis) of the seeds in Figure B.2. Table B.1 shows the other physical parameters used in the study.

### B.2 Physical Parameters of the Para-xylene System

Solubility data for para-xylene in xylene mixtures are calculated based on the assumption that the xylene mixture behaves as an ideal solution and the crystallized solid phase is pure

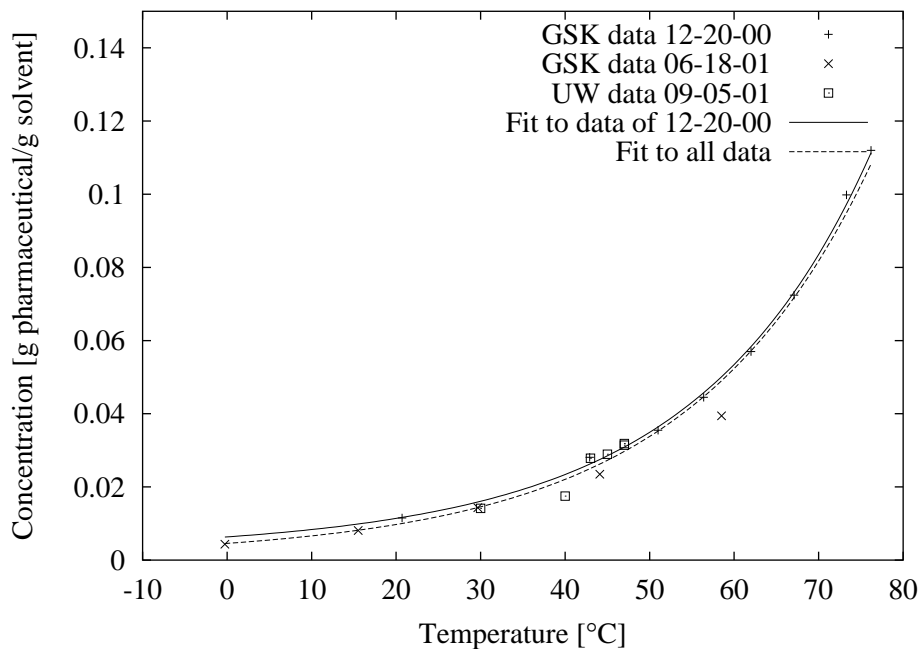


Figure B.1: Equilibrium concentration fits using Equation B.1 for the data of 12-20-00 and using Equation B.2 for all the data.

Table B.1: Physical properties of the pharmaceutical-IPA-water system.

Physical parameter	Value	Analysis technique	Source
Crystal density $\rho_c$	$1.4 \text{ g}\cdot\text{mL}^{-1}$	helium displacement	GSK
IPA density $\rho_{IPA}$	$0.7854 \text{ g}\cdot\text{mL}^{-1}$	displacement	[91]
$H_2O$ density $\rho_{H_2O}$	$0.9982 \text{ g}\cdot\text{mL}^{-1}$	displacement	[91]
Crystal length-to-width $l_w$	5.4204	image analysis	

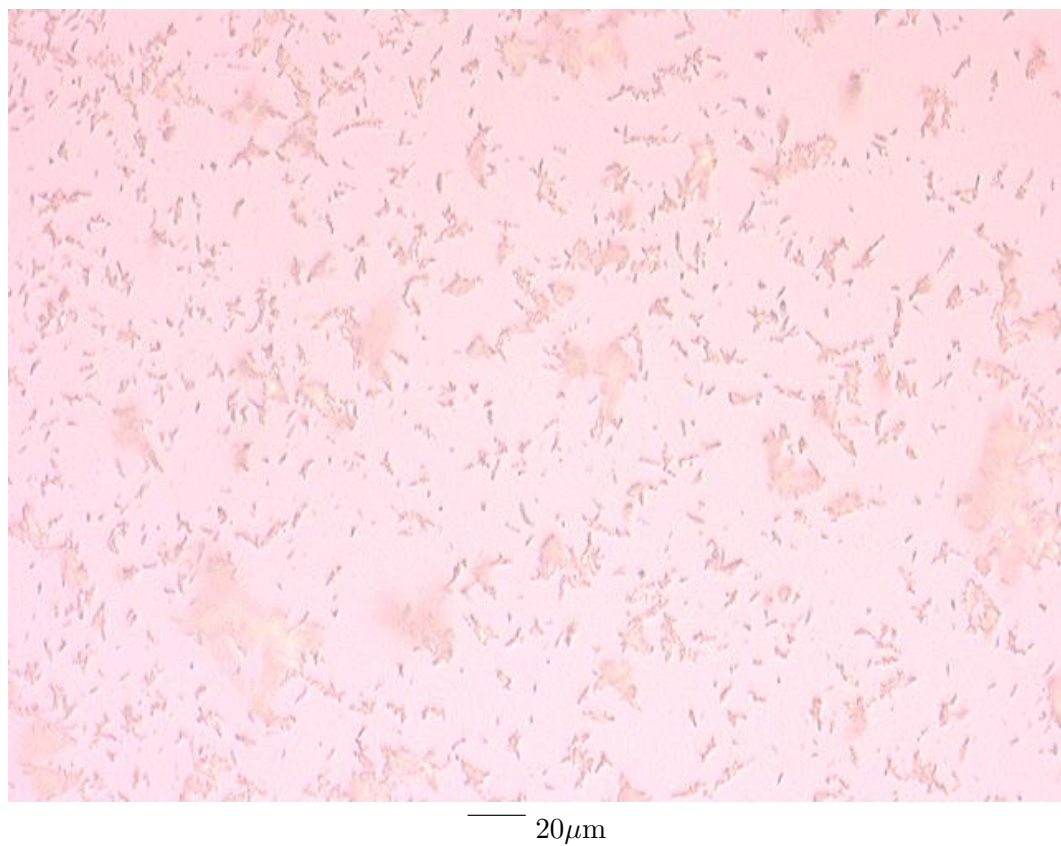


Figure B.2: Photomicrograph of pharmaceutical seed crystals.

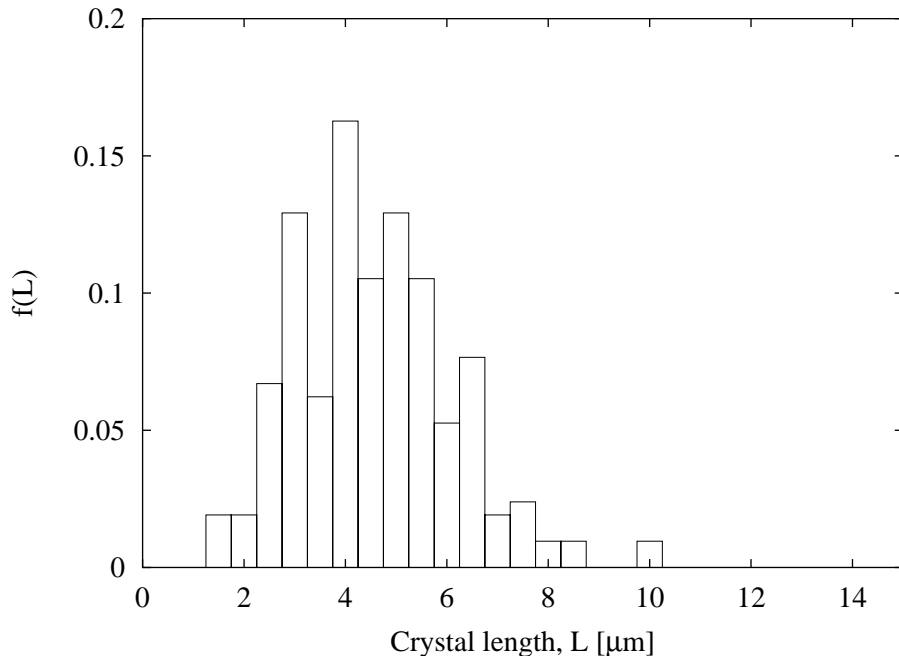


Figure B.3: Particle size density (measured using image analysis) of pharmaceutical seeds in Figure B.2.

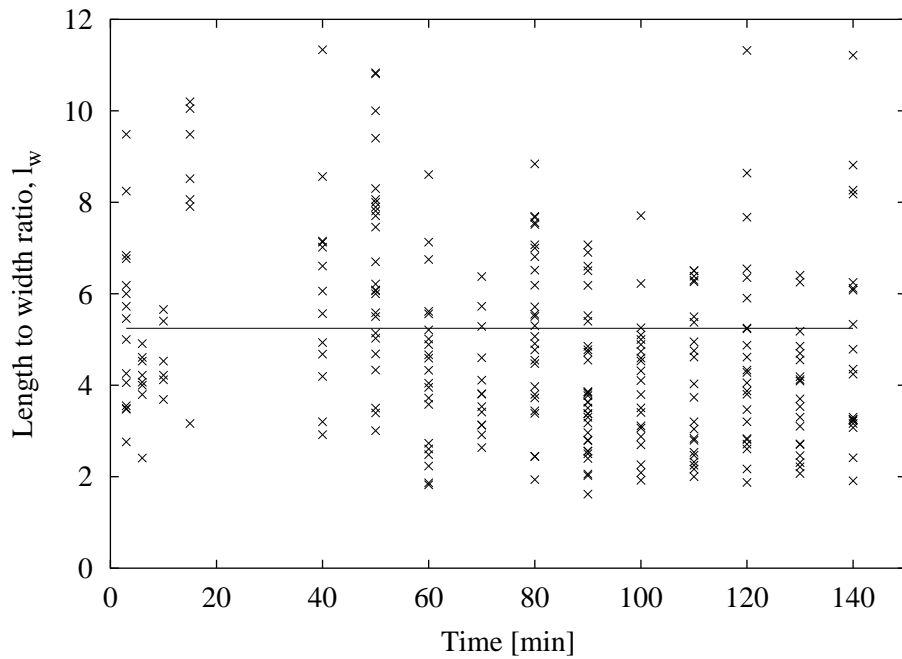


Figure B.4: Length to width ratio as a function of time for pharmaceutical crystallization.

para-xylene. The presence of non-xylene compounds like toluene is considered to behave similarly to the other xylene compounds [73]. The experimental data provided by Haddon and Johnson [37] and Porter and Johnson [97] show that para-xylene has non-ideal behavior and its solubility deviates from the solubility predicted by the correlation based on an ideal solution. Within the studied range of temperatures in the present work the para-xylene solubility can be predicted by the following equation [45]

$$\ln\left(\frac{1}{N}\right) = \frac{\Delta H_f}{RT_m} \left(\frac{T_m}{T} - 1\right) - \frac{\Delta C_p}{R} \left(\frac{T_m}{T} - 1\right) + \frac{\Delta C_p}{R} \ln\left(\frac{T_m}{T}\right) \quad (\text{B.3})$$

where  $N$  is the mole fraction of para-xylene in the mixture at temperature  $T$  (K),  $\Delta H_f$  is the latent heat of fusion ( $\text{J}\cdot\text{mol}^{-1}$ ),  $T_m$  is the melting point (K),  $\Delta C_p$  is the difference in heat capacities of the solid and the liquid phase ( $\text{J}\cdot\text{mol}^{-1}\cdot\text{K}^{-1}$ ) and  $R$  is the gas constant. The physical properties for para-xylene are shown in Table B.2, Mullin [80]. Equation B.3 is plotted in Figure 6.2.

Table B.2: Physical properties of para-xylene used in Equation B.3.

Physical parameter	Value	Analysis technique	Source
Freezing point, $T_m$	286.4 K	calorimetry	[80]
Heat of fusion, $\Delta H_f$	17113 $\text{J}\cdot\text{mol}^{-1}$	calorimetry	[80]
Heat capacity, $\Delta C_p$	24.3 $\text{J}\cdot\text{mol}^{-1}\cdot\text{K}^{-1}$	calorimetry	[80]
Crystal density, $\rho_c$	1.084 $\text{g}\cdot\text{mL}^{-1}$	displacement	[91]
Xylene liquid density, $\rho$	0.905 $\text{g}\cdot\text{mL}^{-1}$	displacement	[91]

### B.3 Physical Parameters of the Sodium Chlorate System

Solubility data for sodium chlorate are presented in Table B.3. Segregation coefficients of sodium dithionite in sodium chlorate solution to crystal are presented in Table B.4. For the experiments in which the concentration of sodium dithionite is 225 ppm in a solution of 1600 g sodium chlorate and 1600 g water solution, only 6 mg of sodium dithionite are taken up in the crystals at equilibrium if the cooling is stopped at 23.5°C. Thus, the concentration of sodium dithionite that remains in solution is 221 ppm. Due to the low segregation coefficients, it is necessary to flush the contaminated sodium chlorate solution from the system and replace it with impurity-free solution if habit modification back and forth between cubic and tetrahedral shapes is required. Habit modification back and forth between the two habits is not possible in a batch system.

Table B.3: Sodium chlorate solubility in water, Mullin [80].

Temperature °C	0	10	20	30	40	60	80	100
Solubility g <sub>NaClO<sub>3</sub></sub> /100 g <sub>H<sub>2</sub>O</sub>	80	89	101	113	126	155	189	233

Table B.4: Segregation coefficients for sodium dithionite in sodium chlorate-water system, Ristić et al. [114].

Na <sub>2</sub> S <sub>2</sub> O <sub>6</sub> concentration in NaClO <sub>3</sub> /H <sub>2</sub> O [ppm]	<500	1,000	10,000
Segregation coefficient, C <sub>solution</sub> <sup>Na<sub>2</sub>S<sub>2</sub>O<sub>6</sub></sup> : C <sub>crystal</sub> <sup>Na<sub>2</sub>S<sub>2</sub>O<sub>6</sub></sup>	2	1	0.2

## **Appendix C**

# **Model Formulation**

Many researchers have reviewed crystallization and particle modeling extensively [100, 143, 132, 133, 23, 110, 17]. These reviews provide mathematical equations that can be used to predict the response of a system to various inputs. The model can then be used for system design, optimization and improve control of the process. Model development for particulate processes involves conservation of particle populations, mass, and energy, coupled with constitutive relations of material behavior.

### **C.1 Population Balance**

The objective of crystallization modeling is to obtain an accurate mathematical description of the population of crystals in the continuous phase of a well-mixed system. Once the model and parameters are established, other objectives such as simulation, optimization and process control can be performed. Crystallization is a dispersed phase, heterogeneous system that poses many difficulties. Not only do temperature and solute concentration affect the rate of crystal growth, but other quality characteristics of each crystal, such as crystal defects and the history of crystal defects can influence the growth rate of a crystal [83, 13]. Characteristic variables that describe the quality of each crystal can vary from system to system. The population balance approach for chemical reactors was first described by Rudd [118]. Rudd showed that using the residence time method approach for predicting the average catalytic activity in a well-mixed continuous reactor cannot always be applied. For example, a catalyst receiving its activity from a radiation source within the reactor. Here the activity is not a function of the residence time in the reactor, but instead the length of time since its last activation by the radiation. Rudd [118] proposes a generalization of the residence time method, called the event space method, where instead of formulating a model based on particle age, one can consider a generalized describing variable, such as catalyst particle activity. Hulbert and Katz [51] extended the work with population balances to include an arbitrary number of characteristic variables such as particle dimensions and intrinsic growth rate, and apply population balance modeling to particle nucleation, growth and agglomeration. Randolph and Larson [105] derived a general size distribution equation, coupled with mass and energy balances, which described the transient

behavior of particles in an arbitrary suspension. It was shown that long term transients in product size distribution from an MSMPR crystallizer (i.e. continuous) can occur in spite of steady-state heat and mass inputs to the system. This transient behavior is attributed to nucleation kinetics.

The deterministic population balance equation is derived by Randolph and Larson [106] as a conservation equation for the number of particles in a population,  $f(\mathbf{z}, t)$ , where  $\mathbf{z}$  is a vector of variables that includes three spatial external coordinates,  $\mathbf{x}$ , and internal coordinates,  $\mathbf{y}$  that describe the state of the particle, such as quality and intrinsic growth rate. If we consider the subregion of particle phase space,  $\Omega$ , and  $d\Omega$  is an infinitesimal volume in the particle phase space, then the total number of particles per unit volume of crystallizer is

$$\int_{\Omega} f(\mathbf{z}, t) d\Omega \quad (\text{C.1})$$

The population balance for particles in the fixed subregion of phase space can be stated as

$$\text{Accumulation} = \text{Input} - \text{Output} + \text{Generation}$$

Therefore, the derivative of Equation C.1 will depend on the rates of birth,  $B$ , and death,  $D$ , in  $\Omega$  and may be stated simply as

$$\frac{d}{dt} \int_{\Omega} f(\mathbf{z}, t) d\Omega = \int_{\Omega} (B - D) d\Omega \quad (\text{C.2})$$

Using the Leibnitz formula (in 3 dimensions), the left hand side of Equation C.2 may be expanded to a volume and a surface integral, and then the divergence theorem is used to convert the surface integral to a volume integral as follows

$$\begin{aligned} \frac{d}{dt} \int_{\Omega} f(\mathbf{z}, t) d\Omega &= \int_{\Omega} \frac{\partial f(\mathbf{z}, t)}{\partial t} d\Omega + \int_{\Sigma} (\mathbf{n} \cdot \mathbf{v}) f(\mathbf{z}, t) d\Sigma \\ &= \int_{\Omega} \left[ \frac{\partial f(\mathbf{z}, t)}{\partial t} + (\nabla \cdot f(\mathbf{z}, t)) \mathbf{v} \right] d\Omega \end{aligned} \quad (\text{C.3})$$

Recalling that  $\mathbf{z}$  is partitioned into internal,  $\mathbf{y}$  or  $L$ , and external coordinates,  $\mathbf{x}$  or  $x, y, z$

$$\mathbf{z} = \begin{bmatrix} \mathbf{x} \\ \mathbf{y} \end{bmatrix} = \begin{bmatrix} x \\ y \\ z \\ L \end{bmatrix}$$

The velocity  $\mathbf{v}$  is defined as the vector sum of external velocities  $v_x, v_y, v_z$  (cartesian components of fluid velocities) and internal velocities  $v_L$  (particle growth rate).

$$\mathbf{v} = \mathbf{v}_{ext} + \mathbf{v}_{int} = \begin{bmatrix} v_x \\ v_y \\ v_z \\ v_L \end{bmatrix}$$

Substituting the right hand side of Equation C.3 into Equation C.2 allows the population balance to be written as

$$\int_{\Omega} \left[ \frac{\partial f(\mathbf{z}, t)}{\partial t} + (\nabla \cdot f(\mathbf{z}, t) \mathbf{v}) - (B - D) \right] d\Omega = 0 \quad (\text{C.4})$$

As the region  $\Omega$  was arbitrary, the integrand must vanish identically. Thus, the population balance is given as

$$\frac{\partial f(\mathbf{z}, t)}{\partial t} + (\nabla \cdot f(\mathbf{z}, t) \mathbf{v}) - (B - D) = 0 \quad (\text{C.5})$$

Equation C.5 is a number continuity equation in particle phase space. When Equation C.5 is combined with mass and energy balances, particle number formation kinetics can be completely described. Equation C.5 can be further simplified for well-mixed systems so  $f(\mathbf{z}, t)$ ,  $B$ , and  $D$  have no spatial dependence. Equation C.5 can be integrated over the volume of the crystallizer to give

$$\int_V \left( \frac{\partial f(\mathbf{z}, t)}{\partial t} + (\nabla \cdot f(\mathbf{z}, t) \mathbf{v}_{\text{int}}) + (\nabla \cdot f(\mathbf{z}, t) \mathbf{v}_{\text{ext}}) - (B - D) \right) dV = 0 \quad (\text{C.6})$$

Assuming the system is well-mixed,  $f(\mathbf{z}, t)$ ,  $B$  and  $D$  are all functions of internal coordinates, so

$$f(\mathbf{z}, t) = f(\mathbf{y}, t) = f(L, t)$$

The volume integral in Equation C.6 involving the external velocity can be expressed as a surface integral using the divergence theorem

$$\int_V (\nabla \cdot \mathbf{v}_{\text{ext}} f(L, t)) dV = \int_S (\mathbf{n} \cdot \mathbf{v}_{\text{ext}}) f(L, t) dS \quad (\text{C.7})$$

The term  $S$  may be considered as a sum of three components,  $S = S_k + S_s + S_e$  where  $S_k$  is the surface area where flow into and out of the volume occurs,  $S_s$  is the free surface of liquid in the vessel and  $S_e$  is the total particle-fluid interface.

$$\int_{S_k} (\mathbf{n} \cdot \mathbf{v}_{\text{ext}}) f(L, t) dS = \frac{w_{\text{eff}}}{\rho_{\text{eff}}} f_{\text{eff}}(L, t) - \frac{w_{\text{feed}}}{\rho_{\text{feed}}} f_{\text{feed}}(L, t) \quad (\text{C.8})$$

$$\int_{S_s + S_e} (\mathbf{n} \cdot \mathbf{v}_{\text{ext}}) f(L, t) dS = f(L, t) \frac{dV}{dt} \quad (\text{C.9})$$

where  $dV/dt$  is the total rate of change of solids free volume. Integration of Equation C.6 over  $\mathbf{x}$  or  $V$  and substitution of Equations C.8 and C.9 for the external velocity terms results in

$$\begin{aligned} & V \left( \frac{\partial f(L, t)}{\partial t} + (\nabla \cdot v_L f(L, t)) - (B - D) \right) \\ &= - \left[ \frac{w_{\text{eff}}}{\rho_{\text{eff}}} f(L, t) - \frac{w_{\text{feed}}}{\rho_{\text{feed}}} f_f(L, t) \right] - f(L, t) \frac{dV}{dt} \end{aligned} \quad (\text{C.10})$$

Equation C.10 can describe batch, semi-batch and continuous crystallizers with appropriate values of  $w/\rho = q$ , specification of the internal variables and functional forms of  $v_L$ ,  $f(L, t)$ ,  $B$ , and  $D$  and supply the necessary initial and boundary conditions. Additional length coordinates, crystal shape, purity, and intrinsic growth can be included as elements of  $\mathbf{y}$ , but for most crystallization systems, the variable that best describes a crystal is the length,  $L$ . If crystal breakage, agglomeration and fines dissolution are ignored, and nucleated crystals appear at a single small size,  $L_0$ , then Equation C.10 becomes

$$V \frac{\partial f(L, t)}{\partial t} + V \frac{\partial(Gf(L, t))}{\partial L} - VB\delta(L - L_0) + f(L, t) \frac{dV}{dt} = -[q_e f(L, t) - q_f f_f(L, t)] \quad (\text{C.11})$$

where  $G = v_L = \partial L / \partial t$  is the crystal growth rate,  $B$  is the nucleation rate density, and  $\delta(L - L_0)$  is the Dirac delta function acting at  $L_0$ . As  $L \rightarrow L_0$ , Equation C.11 may be integrated over  $L_0^-$  to  $L_0^+$  to show that nucleation may be removed and specified as a boundary condition, and assuming a constant volume system, results in Equation C.12

$$\frac{\partial f(L, t)}{\partial t} + \frac{\partial(Gf(L, t))}{\partial L} = -\frac{[q_e f(L, t) - q_f f_f(L, t)]}{V} \quad (\text{C.12})$$

with the boundary condition

$$f(L_0, t) = \frac{B}{G|_{L_0}} \quad (\text{C.13})$$

The fundamental driving force for crystallization is the difference in chemical potential of the solution (phase 1) and the solidifying solute, or crystal (phase 2). For a binary system, this is written as

$$\Delta\mu = \mu_2 - \mu_1 \quad (\text{C.14})$$

In a crystallizing system  $\Delta\mu < 0$ . It is common to express the crystallizing driving force as a positive quantity, so an *affinity of reaction*,  $\phi$  is defined. The driving force for crystallization in a binary system is then rewritten as

$$\phi = -\Delta\mu = \mu_1 - \mu_2 \quad (\text{C.15})$$

Chemical potential is defined in terms of fugacity, and hence activity by

$$\mu = \mu_{0x} + RT \ln a_x \quad (\text{C.16})$$

$$= \mu_{0m} + RT \ln a_m \quad (\text{C.17})$$

$$= \mu_{0c} + RT \ln a_c \quad (\text{C.18})$$

Chemical potential is independent of the of the units used to express the solution concentration, but the standard potentials and activities are different for the mole fraction ( $x$ ), molal ( $m$ ) and molar ( $c$ ) concentration based units.

Combining Equations C.15 and C.16, the fundamental dimensionless driving force for crystallization is derived in Equation C.19. The same standard state ( $\mu_0$ ) is chosen for both the solute in the crystal and in the solution.

$$\frac{\phi}{RT} = \ln \left( \frac{a_x}{a_{x,eq}} \right) = \ln \left( \frac{a_m}{a_{m,eq}} \right) = \ln \left( \frac{a_c}{a_{c,eq}} \right) = \nu \ln \sigma_a \quad (\text{C.19})$$

where  $\nu$  is the stoichiometric coefficient and  $\sigma_a$  is the supersaturation ratio based on activities. Equation C.19 can be simplified by linearizing the natural logarithm about  $\sigma_a = 1.0$ . The result, Equation C.20, is valid for low relative supersaturations ( $\sigma_a < 1.1$ ).

$$\frac{\phi}{RT} \approx \nu(\sigma_a - 1) = \nu S_a \quad (\text{C.20})$$

where  $S_a$  is the supersaturation. Activity is not easily measured because activity coefficients (molal, molar or mole fraction basis) for supersaturated solutions are not usually available. In general, they are assumed to be 1.0 and the resulting supersaturation,  $S_a$ , is expressed in Equation C.23.

$$\Delta c_i = c_i - c_{i,eq} \quad (\text{C.21})$$

$$S_a \approx \frac{c_i}{c_{i,eq}} \quad (\text{C.22})$$

$$S_a = \sigma_a - 1 \approx \frac{\Delta c_i}{c_{i,eq}} = S \quad (\text{C.23})$$

where  $c_i$  and  $c_{i,eq}$  are the solute and equilibrium solute concentrations of specie  $i$ . Care must be taken in choice of units used for concentration when calculating supersaturation, and in the case where activity coefficients are unknown preference is given to supersaturation expressed in molal units because of their simplicity and temperature independence compared to the molar and mole fraction based units [82].

It is common in macroscopic modeling of growth and nucleation to express  $G$  and  $B$  as empirical functions proportional to supersaturation raised to a power. Some examples of expressions for growth and nucleation as functions of supersaturation are given in Table 2.1.

### C.1.1 Population Balance with Diffusion

Kashchiev [57] derives a master equation to describe the time evolution of a population of clusters consisting of  $n$  atoms, molecules or monomer units. This approach, called the cluster approach shown in Figure C.1, is used to describe nucleation kinetics. The cluster approach requires the following three assumptions:

1. There exist clusters in the solution phase which consist of  $n$  atoms, molecules or monomers (units),  $n = 1, 2, \dots$

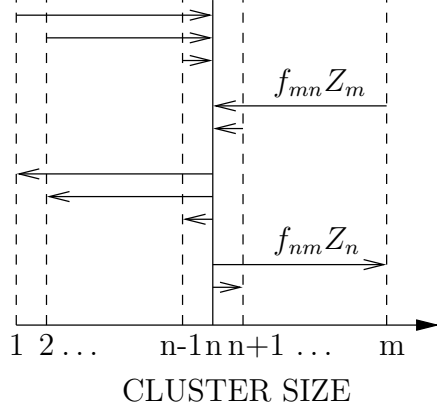


Figure C.1: Possible changes in the size of a cluster of  $n$  units [57].

2. Transformations of  $n$ -sized clusters into  $m$ -sized ones at time  $t$  occur with time-dependent frequencies,  $f_{nm}(t)$  ( $s^{-1}$ ),  $n, m = 1, 2, \dots$
3.  $n$ -sized clusters have the same size and shape.

Assuming no non-aggregative mechanisms occur, the evolution of the  $n$ -sized cluster concentration,  $Z_n(t)$  ( $m^{-3}$ ) is described by

$$\frac{dZ_n(t)}{dt} = \sum_{m=1}^M [f_{mn}(t)Z_m(t) - f_{nm}(t)Z_n(t)] \quad (\text{C.24})$$

$Z_n(t)$  represents the actual cluster size distribution averaged over a unit volume. The rate of appearance of  $n$ -sized clusters at time  $t$  is defined by

$$j_n(t) = \sum_{m=m'+1}^M \sum_{m'=m'}^n [f_{m'm}(t)Z_{m'}(t) - f_{mm'}(t)Z_m(t)] \quad (\text{C.25})$$

Using Equations C.24 and C.25 it can be shown that

$$\frac{dZ_n(t)}{dt} = j_{n-1}(t) - j_n(t) \quad (\text{C.26})$$

For shorthand notation, rewrite

$$Z_n(t) = Z_n \quad j_n(t) = j_n \quad f_n(t) = f_n$$

Substituting a truncated Taylor's series for  $j_{n-1}$

$$j_{n-1} \approx j_n + \left[ \frac{\partial j_n}{\partial n} \right] [(n-1) - n]$$

into Equation C.26 results in the continuity equation for  $Z_n$

$$\frac{dZ_n}{dt} = -\frac{\partial j_n}{\partial n} \quad (\text{C.27})$$

Kashchiev [57] states that  $n$  can be treated as a continuous variable when

$$1 \ll n \ll 2 \min\{f_{nm}\}t \quad (\text{C.28})$$

In this case, summation and finite difference terms can be replaced by integrals and derivatives, for example Equations C.24 and C.25.

$$\frac{\partial Z_n}{\partial t} = \int_1^M [f_{mn}(t)Z_m(t) - f_{nm}Z_n] dm \quad (\text{C.29})$$

$$j_n = \int_n^M \int_1^n [f_{m'm}Z_{m'} - f_{mm'}Z_m] dm' dm \quad (\text{C.30})$$

Phase transition consists of three stages: an early nucleation stage, an advanced coalescence stage and a late aging stage. At the early stage, nucleation predominantly occurs in which various sized clusters form via addition of atomic, molecular or monomer units. During the second stage, clusters grow by coalescing with other various sized clusters. At the second stage most of the monomers have been captured by the growing clusters, thus decreasing the supersaturation and reducing the rate of cluster nucleation. During the third stage, clusters decay by liberating units and clusters grow by addition of other clusters or by addition of liberated units from decaying clusters. In a closed system, the process ends when clusters reach a mean size and concentration that ensure a thermodynamic equilibrium.

During the early stage of nucleation, the chances of clusters of size  $n = 2, 3, \dots$  coming into contact with each other are small because their concentrations are low. The chances that they lose dimers and trimers are also low. Due to the high concentrations of monomer units in the early stage of nucleation, it is a reasonable approximation that

$$f_{nm} = 0$$

for  $|n - m| > 1$ . The Szilard model for nucleation, described by Kashchiev [57], models cluster growth as a sequence of bimolecular reactions in which units attach or detach from  $n$ -sized clusters. Kashchiev [57] describes when the Szilard model is valid. Figure C.2 shows the Szilard model. For the Szilard model, Equation C.24 becomes

$$\frac{dZ_n}{dt} = f_{n-1}Z_{n-1} - g_nZ_n - f_nZ_n + g_{n+1}Z_{n+1} \quad (\text{C.31})$$

and Equation C.25 becomes

$$j_n = f_nZ_n - g_{n+1}Z_{n+1} \quad (\text{C.32})$$

Determining the values of  $f_n$  is easier than determining the values of  $g_n$ .  $f_n$  is the attachment frequency and depends strongly on the properties of the bulk phase. Determining the values of the detachment frequency  $g_n$  is difficult because it requires knowledge of the parameters characterizing the  $n$ -sized clusters. Determining the values of  $g_n$  for the smallest cluster

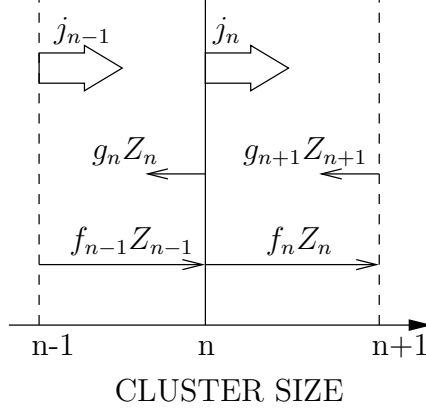


Figure C.2: Szilard model of nucleation in which a cluster of size  $n$  can only grow as a result of a unit attachment or detachment [57].

is especially difficult [57]. Instead, we seek to eliminate  $g_n$ . At equilibrium let  $C_n$  be the equilibrium concentration of  $n$ -sized clusters. At equilibrium Equation C.32 becomes

$$f_n C_n - g_{n+1} C_{n+1} = 0 \quad (\text{C.33})$$

Substituting Equation C.33 for  $g_n$  into Equation C.31 and rearranging results in

$$\frac{dZ_n}{dt} = f_{n-1} C_{n-1} \left( \frac{Z_{n-1}}{C_{n-1}} - \frac{Z_n}{C_n} \right) - f_n C_n \left( \frac{Z_n}{C_n} - \frac{Z_{n+1}}{C_{n+1}} \right) \quad (\text{C.34})$$

Using a truncated Taylor's series for  $Z_{n+1}/C_{n+1}$

$$\frac{Z_{n+1}}{C_{n+1}} \approx \frac{Z_n}{C_n} + \frac{\partial(Z_n/C_n)}{\partial n} ((n+1) - n)$$

and similarly for  $Z_n/C_n$  and substituting into Equation C.34 results in

$$\frac{dZ_n}{dt} = -f_{n-1} C_{n-1} \frac{\partial Z_{n-1}/C_{n-1}}{\partial n} + f_n C_n \frac{\partial Z_n/C_n}{\partial n} \quad (\text{C.35})$$

Substituting the following truncated Taylor's series for the first term on the right hand side of Equation C.35

$$f_{n-1} C_{n-1} \frac{\partial Z_{n-1}/C_{n-1}}{\partial n} \approx f_n C_n \frac{\partial Z_n/C_n}{\partial n} + \frac{\partial}{\partial n} \left( f_n C_n \frac{\partial Z_n/C_n}{\partial n} \right) ((n-1) - n)$$

and after rearranging and eliminating terms reduces to the expression

$$\frac{dZ_n}{dt} = \frac{\partial}{\partial n} \left( f_n C_n \frac{\partial Z_n/C_n}{\partial n} \right) \quad (\text{C.36})$$

Comparing Equation C.36 with Equation C.27, the term for the net flux of clusters through size  $n$  is

$$j_n = -f_n C_n \frac{\partial Z_n/C_n}{\partial n} = -f_n \frac{\partial \ln C_n}{\partial n} Z_n - f_n \frac{\partial Z_n}{\partial n} \quad (\text{C.37})$$

Equation C.37 shows that the flux of clusters through size  $n$  consists of two terms. The second term on the right of Equation C.37,  $f_n \partial Z_n / \partial n$ , is the *diffusion* flux of clusters, which describes the random movement of monomer units to and from the crystal surface or cluster. The other term,  $f_n (\partial \ln C_n / \partial n) Z_n$ , represents the *velocity* of cluster growth.

As clusters grow, the concentration of monomers decreases and the concentration of  $n$ -sized clusters increases. The likelihood of  $n$ -sized clusters coalescing with other clusters of size  $n \geq 2$  increase. In a similar way, Kashchiev [57] derives an equation for the concentration of  $n$ -sized clusters,  $Z_n$ , in which clusters coalesce and grow besides addition of monomer units.

$$\frac{\partial Z_n}{\partial t} = \frac{\partial}{\partial n} \left[ f_n \frac{\partial Z_n}{\partial n} - v_n Z_n \right] + \frac{1}{2} \int_1^n \omega_{m,n-m} Z_{n-m} Z_m dm - Z_n \int_1^{M-n} \omega_{nm} Z_m dm \quad (\text{C.38})$$

Equation C.38 describes both the early nucleation stage and advanced coalescence stage. As the concentration of monomers decreases, and when coalescence no longer occurs, the particles can also age. Clusters can liberate monomers and decrease in size and the liberated monomers attach to other clusters and grow. This stage is sometimes referred to the *Ostwald Ripening* stage. Equations C.36 and C.37 can also describe aging of clusters in a closed system without coalescence [57]. So if coalescence does not occur between clusters, Equations C.36 and C.37 can describe *all* stages of the first-order phase transition.

For a given system and during nucleation, there exists a critical cluster size (or number of monomer units),  $n^*$ , that is a stable nucleus. Beyond this size, the cluster is unlikely to diminish back to a size  $n < n^*$ , unless the bulk supersaturation is negative. Nucleation rates,  $J(t)$ , can be estimated via

$$J(t) = j^* - Z^* \frac{dn^*}{dt} \quad (\text{C.39})$$

in which  $j^*$  is given by Equation C.37 for  $n = n^*$  and  $Z^*$  is the concentration of  $n^*$ -sized clusters.  $n^*$  is a function of the time-dependent supersaturation and is often difficult to estimate or measure. Instead, Kashchiev [57] points out that Equation C.39 can be used to predict a *detectable* nucleation rate with a known detectable nucleus size,  $n'$ , so  $dn'/dt = 0$  and  $J'(t)$  is equal to Equation C.37.

The population balance equation with diffusion is developed by writing a particle number density balance over a stationary volume element in the dispersed phase space. We reduce the dimension of the system to one dimension by assuming we only need one characteristic length to describe the size of a particle.

Consider Figure C.3. The number of particles per unit volume that grow at a rate of  $G$  to the size  $L$  is  $Gf(L)|_L$ . The number of particles per unit volume that grow at a rate of  $G$  to the size  $L + \Delta L$  is  $Gf(L)|_{L+\Delta L}$ . The number of particles per unit volume that diffuse with a diffusion coefficient of  $D$ , based on Equation C.37, to the size  $L$  is  $D\partial f/\partial L|_L$ . The number of particles per unit volume that diffuse with a diffusion coefficient of  $D$  to the size

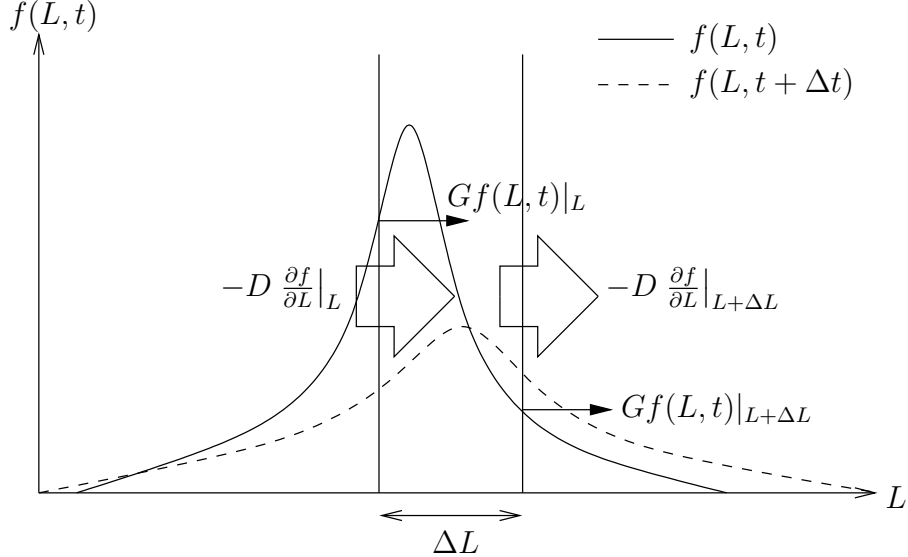


Figure C.3: Region of length  $\Delta L$  fixed in particle size space through which particles grow and diffuse into and out of.

$L + \Delta L$  is  $D\partial f/\partial L|_{L+\Delta L}$ . The rate of particles that accumulate between the size range  $L$  to  $L + \Delta L$  is  $\Delta L \partial f/\partial t$ . The population balance then becomes

$$\Delta L \frac{\partial f(L, t)}{\partial t} = Gf(L, t)|_L - Gf(L, t)|_{L+\Delta L} + -D \frac{\partial f}{\partial L}\Big|_L - -D \frac{\partial f}{\partial L}\Big|_{L+\Delta L} \quad (\text{C.40})$$

By dividing this entire equation by  $\Delta L$  and taking the limit as this dimension approaches zero, we get

$$\frac{\partial f(L, t)}{\partial t} = -G \frac{f(L, t)}{\partial L} + D \frac{\partial^2 f(L, t)}{\partial L^2} \quad (\text{C.41})$$

### C.1.2 Population Balance for Particles with Discrete Sizes

The population balance equation that describes the growth as discrete steps in particle size is developed by writing a particle number density balance over a stationary volume element in the dispersed phase space. We reduce the dimension of the system to one dimension by assuming we only need one characteristic length to describe the size of a particle.

Consider Figure C.4. The number of particles per unit volume that grow at a rate of  $\tilde{G}$  to the size  $L$  is  $\int \tilde{G}f(\bar{L} - \Delta, t)d\bar{L}$ . The number of particles per unit volume that grow at a rate of  $\tilde{G}$  to the size  $L + \Delta$  is  $\int \tilde{G}f(\bar{L}, t)d\bar{L}$ . The rate of particles that accumulate between the size range  $L$  to  $L + \Delta L$  is  $\Delta L \frac{d}{dt} \int_L^{L+\Delta L} f(\bar{L}, t)d\bar{L}$ . The population balance then becomes

$$\Delta L \frac{d}{dt} \int_L^{L+\Delta L} f(\bar{L}, t)d\bar{L} = \int_{L-\Delta}^{L-\Delta+\Delta L} f(\bar{L} - \Delta) \tilde{G} d\bar{L} - \int_L^{L+\Delta L} f(\bar{L}, t) \tilde{G} d\bar{L} \quad (\text{C.42})$$

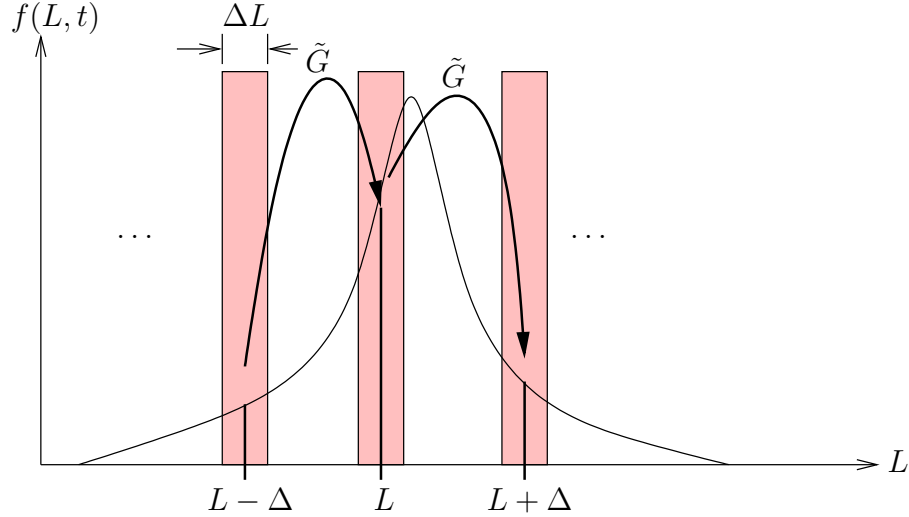


Figure C.4: Region of length  $\Delta L$  fixed in particle size space through which particles of discrete sizes  $\{\Delta, 2\Delta, \dots, L - \Delta, L, L + \Delta, \dots\}$  grow into and out of.

Using Leibnitz's rule for differentiating an integral

$$\begin{aligned} \Delta L \int_L^{L+\Delta L} \frac{\partial f(\bar{L}, t)}{\partial t} d\bar{L} &+ f(L + \Delta L, t) \frac{d(L + \Delta L)}{dt} - f(L, t) \frac{dL}{dt} \\ &= \int_{L-\Delta}^{L-\Delta+\Delta L} f(\bar{L} - \Delta) \tilde{G} d\bar{L} - \int_L^{L+\Delta L} f(\bar{L}, t) \tilde{G} d\bar{L} \end{aligned} \quad (\text{C.43})$$

Noting that the second and third terms on the left hand side of Equation C.43 cancel each other because  $dL/dt = d(L + \Delta L)/dt$ , so Equation C.43 becomes

$$\Delta L \int_L^{L+\Delta L} \left[ \frac{\partial f(\bar{L}, t)}{\partial t} + f(\bar{L}, t) \tilde{G} \right] d\bar{L} = \int_{L-\Delta}^{L-\Delta+\Delta L} f(\bar{L} - \Delta) \tilde{G} d\bar{L} \quad (\text{C.44})$$

Dividing Equation C.44 by  $\Delta L$  and taking the limit so the length dimension approaches zero, Equation C.44 becomes

$$\frac{\partial f(L, t)}{\partial t} + \tilde{G}f(L, t) - \tilde{G}f(L - \Delta, t) = 0 \quad (\text{C.45})$$

Equation C.45 is a generalized form of the population balance. Expanding the term  $f(L - \Delta, t)$  in a Taylor series about the point  $(L - \Delta)$  to obtain

$$f(L - \Delta, t) \approx f(L, t) + f'(L, t) ((L - \Delta) - L) f''(L, t) \frac{((L - \Delta) - L)^2}{2!} + \dots \quad (\text{C.46})$$

$$\approx f(L, t) - \Delta f'(L, t) + \frac{\Delta^2}{2} f''(L, t) \quad (\text{C.47})$$

Substituting Equation C.46 into Equation C.45 and rearranging results in

$$\frac{\partial f(L, t)}{\partial t} + \tilde{G}f(L, t) - \tilde{G} \left( f(L, t) - \Delta f'(L, t) + \frac{\Delta^2}{2} f''(L, t) \right) = 0 \quad (\text{C.48})$$

and

$$\frac{\partial f(L, t)}{\partial t} = -\tilde{G}\Delta \frac{\partial f(L, t)}{\partial L} + \tilde{G}\frac{\Delta^2}{2} \frac{\partial^2 f(L, t)}{\partial L^2} \quad (\text{C.49})$$

Letting  $G = \tilde{G}\Delta$  and rewriting Equation C.49 as

$$\frac{\partial f}{\partial t} = -G \frac{\partial f(L)}{\partial L} + \frac{\Delta}{2} G \frac{\partial^2 f(L, t)}{\partial L^2} \quad (\text{C.50})$$

in which  $G = k_g S^g$ . Equation C.50 has the second order derivative term that describes apparent crystal growth dispersion. This equation is similar in form to Equation C.41 and describes temperature-dependent diffusion. For Equation C.50 at equilibrium, crystal sizes do not disperse. For Equation C.41 at equilibrium crystal sizes disperse, however the mean of the PSD remains constant.

## C.2 Continuous Phase Mass Balance

The crystallization system consists of the suspended solution and solid phases. Mass and energy balances along with the constitutive equations (Table 2.1 in Chapter 2) for nucleation and growth are required to complete the description of the crystallization process.

The solute mass balance accounts for accumulation of solute in the system, flow of solute into and out of the system and mass transfer to the solid phase via nucleation and crystal growth. Bird, Stewart and Lightfoot [14] state the macroscopic mass balance applied to flow systems

$$\frac{dm_{tot}}{dt} = \rho_1 \langle \bar{v}_1 \rangle S_1 - \rho_2 \langle \bar{v}_2 \rangle S_2 - R \quad (\text{C.51})$$

in which  $m_{tot} = V \rho_c k_v \mu_3$  is the total mass of crystals,  $\rho_c$  the crystal density,  $k_v$  the volumetric shape factor, and  $\bar{v}$  the average velocity across the cross-sectional area  $S$ . The reaction term,  $R$ , accounts for the consumption of continuous phase solute mass via chemical reactions or phase changes. So  $dm_{tot}/dt = V \rho_c k_v d\mu_3/dt$  assuming the crystal density and volumetric shape factor are constant.

For a batch system, the PBE, Equation C.12 with  $q_e = q_f = 0$  is

$$\frac{\partial f(L, t)}{\partial t} + \frac{\partial(Gf(L, t))}{\partial L} = 0 \quad (\text{C.52})$$

Multiplying Equation C.52 by  $L^3$  and integrating over  $L$

$$\int_0^\infty L^3 \frac{\partial f(L, t)}{\partial t} dL = - \int_0^\infty L^3 \frac{\partial(Gf(L, t))}{\partial L} dL \quad (\text{C.53})$$

Using integration by parts on the right hand side of Equation C.53

$$\int_0^\infty L^3 \frac{\partial(Gf(L, t))}{\partial L} dL = -3 \int_0^\infty L^2 Gf(L, t) dL \quad (\text{C.54})$$

and substitution of the result of Equation C.54 into Equation C.53 is

$$\frac{d\mu_3}{dt} = -3 \int_0^\infty L^2 G f(L, t) dL \quad (\text{C.55})$$

Therefore the mass balance for a batch crystallizer becomes

$$\frac{dm_{tot}}{dt} = \frac{d(\varepsilon CV)}{dt} = -3\rho_c k_v V \int_0^\infty L^2 G f(L, t) dL \quad (\text{C.56})$$

$\varepsilon$  is the fraction of the slurry that is solid. The right hand side of Equation C.56 is the rate of disappearance of solute by crystallization, (-R).

### C.3 Energy Balance

The energy balance accounts for accumulation of internal, kinetic and potential energy in the system, the rate of change of internal (U), kinetic (K) and potential ( $\Phi$ ) energy in and out of the system, the net rate of heat addition to the system from the surroundings, and the net rate of work done by the system on the surroundings. Bird, Stewart and Lightfoot [14] state the first law of thermodynamics applied to flow systems assuming gravity or an external force does not change with time as

$$\frac{d}{dt}(U_{tot} + K_{tot} + \Phi_{tot}) = -\Delta \left[ \left( \hat{U} + \frac{1}{2} \frac{\langle \bar{v}^3 \rangle}{\langle \bar{v} \rangle} + \hat{\Phi} + p\hat{V} \right) w \right] + Q - W \quad (\text{C.57})$$

where Q is the net rate of heat added to the system from the surroundings and W is the net work done by the system on the surroundings. Assuming the potential and kinetic energy terms are negligible, the energy balance becomes

$$\frac{dU_{tot}}{dt} = -\Delta \left[ \left( \hat{U} + p\hat{V} \right) w \right] + Q - W \quad (\text{C.58})$$

The work term,  $W$ , consists of the work done by the system if the volume of the system changes,  $p dV/dt$ , and work transferred by means of moving parts (e.g. a turbine or compressor),  $W_s$ . Equation C.58 becomes

$$\frac{dU_{tot}}{dt} = -\Delta \left[ \left( \hat{U} + p\hat{V} \right) w \right] + Q - \left( W_s + p \frac{dV}{dt} \right) \quad (\text{C.59})$$

Enthalpy per unit mass,  $\hat{H}$  is defined as

$$\hat{H} = \hat{U} + p\hat{V} \quad (\text{C.60})$$

and Equation C.59 becomes

$$\frac{dU_{tot}}{dt} = -\Delta \left[ \hat{H}w \right] + Q - \left( W_s + p \frac{dV}{dt} \right) \quad (\text{C.61})$$

For a batch crystallizer,  $w = 0$ , and the energy balance, Equation C.61, simplifies to

$$\frac{dU_{\text{tot}}}{dt} = Q - \left( W_s + p \frac{dV}{dt} \right) \quad (\text{C.62})$$

Taking time differentials of Equation C.60 and rearranging

$$\frac{dU}{dt} = \frac{dH}{dt} - p \frac{dV}{dt} - V \frac{dp}{dt} \quad (\text{C.63})$$

Substitution of Equation C.63 for  $dU_{\text{tot}}/dt$  into Equation C.62 and rearranging

$$\frac{dH_{\text{tot}}}{dt} - V \frac{dp}{dt} = Q - W_s \quad (\text{C.64})$$

The crystallizer is kept at atmospheric pressure, so one can assume constant pressure and the energy balance is further simplified to

$$\frac{dH_{\text{tot}}}{dt} = Q - W_s \quad (\text{C.65})$$

For a two phase system,  $H_{\text{tot}}$ , can be considered as the sum of the enthalpies of the liquid ( $I$ ) and solid ( $II$ ) phases. Neglecting the surface interface energy ( $H^{\text{surf}} = 0$ ), the total enthalpy is then the sum of the enthalpies of the liquid and solid phases

$$H_{\text{tot}} = H^I + H^{II} \quad (\text{C.66})$$

or in terms of differentials

$$dH_{\text{tot}} = dH^I + dH^{II} \quad (\text{C.67})$$

Enthalpy can be expressed as a function of temperature, pressure and moles i.e.  $H = H(T, p, n_j)$ . For constant pressure, the *fundamental property relation* for the differential enthalpy of phase  $I$  is

$$dH^I = \left( \frac{\partial H^I}{\partial T} \right)_{p, n_j} dT + \sum_j \left( \frac{\partial H^I}{\partial n_j} \right)_{T, p, n_{i \neq j}} dn_j^I \quad (\text{C.68})$$

and similarly there exists an expression for phase  $II$ . The partial molar enthalpy,  $\bar{h}_j$ , is defined as

$$\bar{h}_j = \left( \frac{\partial H}{\partial n_j} \right)_{T, p, n_{i \neq j}} \quad (\text{C.69})$$

and the specific heat capacity at constant pressure is related to enthalpy as

$$C_p = \left( \frac{\partial H}{\partial T} \right)_{p, n} \quad (\text{C.70})$$

For a binary system,  $j = 1, 2$ . The system is closed and assuming that the solid phase  $II$  consists of pure component 1 (i.e. 1 is the crystallizing species), then

$$dn_1^I = -dn_1^{II} \quad (\text{C.71})$$

and

$$dn_j^I = dn_j^{II} = 0, \quad j = 2, \dots \quad (\text{C.72})$$

Substitution of Equations C.71 and C.72 into the fundamental relationship for phases  $I$  and  $II$  (Equation C.68) and substituting the result into Equation C.67,  $dH_{\text{tot}}$  then becomes

$$dH_{\text{tot}} = (C_p^I + C_p^{II})dT + (\bar{h}_1^I - \bar{h}_1^{II})dn_1^I \quad (\text{C.73})$$

Taking time derivatives of Equation C.73 and substituting this for  $dH_{\text{tot}}/dt$  in the energy balance, Equation C.65 becomes

$$\frac{dH_{\text{tot}}}{dt} = \Delta\tilde{H}_c \frac{dn_1^I}{dt} + \rho V \hat{C}_p \frac{dT}{dt} = Q - W_s \quad (\text{C.74})$$

where

$$\rho V \hat{C}_p = C_p^I + C_p^{II} \quad (\text{C.75})$$

and

$$\Delta\tilde{H}_{\text{crys}} = \bar{h}_1^I - \bar{h}_2^{II} \quad (\text{C.76})$$

It should be noted that  $\bar{h}_i^I$  is not constant during the course of crystallization since the number of moles of the crystallizing species changes as a function of time. The crystallizer is insulated so that the heat transfer is only between the coolant and the slurry, so  $Q$  in Equation C.74 becomes  $UA(T_j - T)$ , where  $U$  is the overall heat transfer coefficient,  $A$  is the jacket heat transfer area, and  $T_c$  the temperature of the coolant. No shaft work is done by the system on the surroundings, and Equation C.74 becomes

$$\rho V \hat{C}_p \frac{dT}{dt} = -\Delta\tilde{H}_c \frac{dn_1^I}{dt} + UA(T_j - T) \quad (\text{C.77})$$

Substituting the right hand side of Equation C.56 into Equation C.77 for the rate of disappearance of solute by crystallization ( $rV = R = dn_1^I/dt$ ) and rearranging

$$\rho V \hat{C}_p \frac{dT}{dt} = -3\rho c k_v V \Delta\hat{H}_c \int_0^\infty L^2 G f(L, t) dL + UA(T_j - T) \quad (\text{C.78})$$

The following boundary and initial conditions are applied to the material, energy and population balances:

$$f(L, t = 0) = f_0(L) \quad (\text{C.79})$$

$$C(t = 0) = C_0 \quad (\text{C.80})$$

$$T(t = 0) = T_0 \quad (\text{C.81})$$



## Appendix D

# Stochastic Modeling of Chemical Kinetics and Crystallization Processes<sup>1</sup>

## D.1 Model Formulation

If the population is large, single microscopic events such as incorporation of growth units into a crystal lattice and biparticle collisions are not significant. Microscopic events tend to occur on short time scales relative to those required to make a significant change in the macroscopic PSD. If fluctuations about the average PSD are large, then the PBE is no longer valid. Large fluctuations about the average density occur when the population modeled is small. Examples of small populations in particulate systems in which fluctuations are significant include such varied applications as aggregation of platelets and neutrophils in flow fields, growth and aggregation of proteins, and aggregation of cell mixtures [63]. The PBE is not valid also in modeling precipitation reactions in micelles in which the micelles act as micro-scale reactors containing a small population of fine particles [67, 5].

Besides applications of modeling relatively small populations and small length scales, crystal nucleation and growth rate dispersion are other phenomena which the PBE cannot always accurately describe because of their naturally random behavior. A nucleation event occurs once a critical number of molecules cluster and forms a stable aggregate, called a nucleus. Brownian dynamics govern the events required to form a stable aggregate of ions or molecules. Growth rate dispersion is the term used to describe the apparent spreading in the length dimension of the PSD as a population of crystals evolves. Possible mechanisms that cause apparent growth rate dispersion are Ostwald ripening, poorly-mixed systems, inherent growth rates that randomly vary from crystal to crystal, and size-dependent growth. Madras and McCoy [66] consider a second-order derivative term in the PBE to model Ostwald ripening. Randolph and White [107] use a second-order derivative term in the PBE to model growth fluctuations due to poor mixing. Brownian dynamics also governs the events occurring in Ostwald ripening and random individual growth rates.

---

<sup>1</sup>Some portions of this appendix are in Haseltine et al. [39]

The stochastic framework, on the other hand, models crystal nucleation, growth and agglomeration as random, discrete processes. Ramkrishna and Borwanker [102, 103] introduce the stochastic framework to modeling particulate processes. The authors show that the PBE is one of an infinite sequence of equations, called product densities, that describe the mean behavior and fluctuations about the mean behavior of the PSD. The PBE is, in fact, the expectation density of the infinite sequence of equations satisfied by the product density equations. As the population decreases, higher order product density equations are required to describe the time behavior and fluctuations about the expected behavior of the population. Ramkrishna and Borwanker [102, 103] show that the relative magnitude of the random fluctuations is proportional to  $1/\sqrt{N}$ , where  $N$  is the number of particles in the system. This result can also be found in standard probability and stochastic processes theory [29]. Ramkrishna [101] provides a detailed analysis of the PBE.

One approach to solving the stochastic model for any population of crystals is the Monte Carlo simulation method. Kendall [58] first applied the concept of exponentially distributed time intervals between birth and death events in a single-specie population. Shah et al. [121] use the same approach as Kendall and simulate breakage and agglomeration in a dispersed-phase system. The rates of agglomeration and breakage are proportional to the number of particles in the system and the size-dependency mechanism of breakage and agglomeration. Laurenzi and Diamond [63] apply the same technique as Shah et al. [121] to model aggregation kinetics of platelets and neutrophils in flow fields. Hsu et al. [50, 49] formulate a stochastic model for an MSMPR crystallizer, and use this model to analyze the influence of the initial size distribution and size-dependent growth on the crystallizer dynamics and the moments of the PSD. The steady-state representation of the MSMPR crystallizer can also be recovered from the resultant dynamic model under the condition of no random variation. Gooch and Hounslow [35] apply a Monte Carlo technique similar to Shah et al. [121] to model breakage and agglomeration. Gooch and Hounslow calculate the event time interval from the numerical solution to the zeroth moment equation with  $\Delta N = 1$  for breakage, and  $\Delta N = -1$  for agglomeration. Manjunath et al. [67] and Bandyopadhyaya et al. [5] use the stochastic approach to model precipitation in small micellar systems. The model specifies the minimum number of solubilized ions and molecules to form a stable nucleus. Once a particle nucleates, growth is rapid and depletes the micelle of growth units. Brownian collisions govern the interaction between micelles. Solubilized ions and molecules are transferred during collisions.

The PBE is a macroscopic approach to describing the time averaged evolution of the particle size density, driven by microscopic events such as molecular incorporation of molecules into a crystal lattice and collisions between crystal lattices. Stochastic modeling is concerned with the random nature of these events and constructs probability functions that can describe the expectation of particular crystal events occurring [47].

Consider a system that can be either in a finite or countably infinite set  $\mathcal{S}$  of states. In crystallization these states can be the particle size and  $\mathcal{S}$  is the state space of the system.

Let  $X(t)$  denote the state of the system at time  $t$ , defined by

$$X(t) = \begin{cases} x_0, & 0 \leq t < \tau_1 \\ x_1, & \tau_1 \leq t < \tau_2 \\ x_2, & \tau_2 \leq t < \tau_3 \\ \vdots & \end{cases} \quad (\text{D.1})$$

The process defined by Equation D.1 is called a *jump process*. If  $X(t)$  does not explode, i.e. if

$$\lim_{n \rightarrow \infty} \tau_n = \infty \quad (\text{D.2})$$

then Equation D.1 *does* define  $X(t)$  for all  $t \geq 0$ . Let  $P_{xy}(t)$  denote the probability that a process starting in state  $x$  is in state  $y$  at time  $t$ . Then

$$P_{xy}(t) = P_x(X(t) = y)$$

and

$$\sum_y P_{xy}(t) = 1$$

To calculate the probability of being in states  $x_1, x_2, \dots, x_n, x, y \in \mathcal{S}$  at times  $s_1 \leq s_2 \leq \dots \leq s_n \leq s \leq t$  the *transition function*  $P_{xy}(t)$  must satisfy the *Markov Property*

$$P(X(t) = y | X(s_1) = x_1, \dots, X(s_n) = x_n, X(s) = x) = P_{xy}(t - s) \quad (\text{D.3})$$

It can be shown that a Markov jump process is Markovian if and only if

$$P_x(\tau_1 > t + s | \tau_1 > s) = P_x(\tau_1 > t) \quad s, t \geq 0 \quad (\text{D.4})$$

and the only distribution function that satisfies this relation is the exponential distribution. From the Markov property for  $0 \leq t_1 \leq \dots \leq t_n$  and  $x_1, \dots, x_n \in \mathcal{S}$

$$\begin{aligned} P(X(t_1) = x_1, \dots, X(t_n) = x_n) &= P(X(t_1) = x_1) P_{x_1, x_2}(t_2 - t_1) \dots \\ &\quad \dots P_{x_{n-1}, x_n}(t_n - t_{n-1}) \end{aligned} \quad (\text{D.5})$$

In particular, for  $s \geq 0$  and  $t \geq 0$

$$P_x(X(t) = z, X(t+s) = y) = P_{xz}(t) P_{zy}(s)$$

Since

$$P_{xy}(t+s) = \sum_z P_x(X(t) = z, X(t+s) = y)$$

one can conclude that

$$P_{xy}(t+s) = \sum_z P_{xz}(t)P_{zy}(s), \quad s \geq 0, t \geq 0 \quad (\text{D.6})$$

Equation D.6 is known as the *Chapman-Kolmogorov* equation. If  $\mathcal{S}$  is finite or countably infinite, the Chapman-Kolmogorov equation can be differentiated with respect to  $s$ , obtaining,

$$P'_{xy}(t+s) = \sum_z P_{xz}(t)P'_{zy}(s), \quad s \geq 0, t \geq 0 \quad (\text{D.7})$$

In particular

$$P'_{xy}(t) = \sum_z P_{xz}(t)q_{zy}, \quad t \geq 0 \quad (\text{D.8})$$

where

$$q_{zy} = P'_{zy}(0), \quad x, y \in \mathcal{S} \quad (\text{D.9})$$

and

$$\sum_{y \neq x} q_{xy} = -q_{xx} \quad (\text{D.10})$$

$q_{xy}$  is the *infinitesimal parameter* of the process. The infinitesimal parameter describes the rate at which the process moves from state  $x$  to state  $y$ . Equation D.8 is known as the *forward equation* and equivalently there is the *backward equation*, Equation D.11

$$P'_{xy}(t) = \sum_z q_{xz}P_{zy}(t), \quad t \geq 0 \quad (\text{D.11})$$

Solving the backward or forward equation with chosen values or functions for the infinitesimal parameters for a respective system, one can then determine solutions for  $P_{xy}(t)$ . For example, the *birth and death process* on  $\mathcal{S} = \{1, 2, \dots, d\}$  or  $\mathcal{S} = \{1, 2, \dots\}$  has infinitesimal parameters such that

$$q_{xy} = 0, \quad |x - y| > 1$$

A birth and death process starting at  $x$  can in one jump go only to states  $x - 1$  or  $x + 1$  or remain in  $x$ . Figure D.1 shows the transition diagram for a birth and death process with infinite state space.

**Example 1: MSMPR Stochastic Model** Consider an MSMPR crystallizer, in which the feed stream contains seeds of certain size distribution. The MSMPR is ideally mixed and maintained at steady state so the growth of the crystals is constant and that the product stream is representative of that in the crystallizer. Agglomeration and breakage are neglected. The nucleation inside the crystallizer produces initial crystals and seeds of

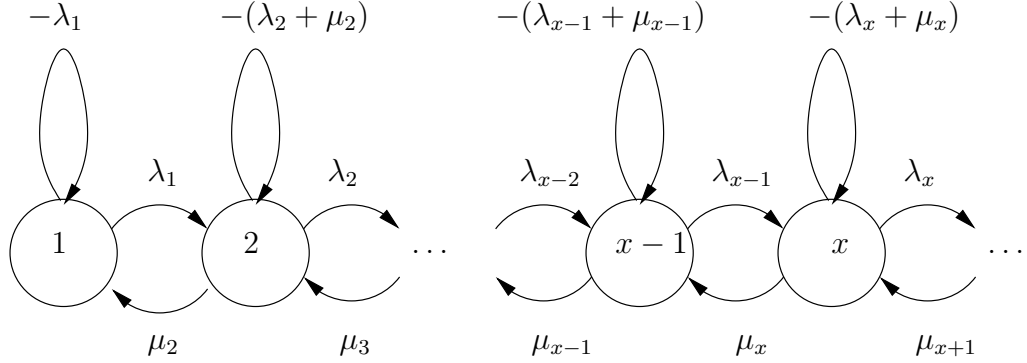


Figure D.1: Transition diagram of birth and death process

various sizes. The crystals are partitioned into  $\Omega$  states, such that a crystal in state  $y$ , where  $y = 1, 2, \dots, \Omega$  has a size of  $y\delta$  and  $\delta$  is the discrete size increment between two adjacent states and  $\Omega$  is the maximum attainable state of crystals. During some time interval,  $t + \Delta t$ , a crystal in the  $y^{\text{th}}$  state may either grow to another state, exit the crystallizer or remain in the same state  $y$ . Assuming  $\Delta t$  to be small enough, the following transition probabilities for a crystal hold [50].

$$\Pr[\text{state } x \text{ at } t \text{ is in state } x+1 \text{ at } t + \Delta t] = \lambda_x \Delta t + o(\Delta t)$$

$$\Pr[\text{state } x \text{ at } t \text{ exits from the crystallizer at } t + \Delta t] = \mu_x \Delta t + o(\Delta t)$$

$$\Pr[\text{state } x \text{ at } t \text{ stays in the same state at } t + \Delta t] = 1 - (\lambda_x + \mu_x) \Delta t + o(\Delta t)$$

and  $\lambda_x$ 's are the transition intensities among the states, and  $\mu_x$ 's are the exit transition intensities. It is assumed that only one event occurs in a time interval  $\Delta t$  and the probability that more than one event occurs is given by the function  $o(\Delta t)$ . As the time intervals become small ( $\Delta t \rightarrow 0$ ) only one event can occur within time  $\Delta t$  with probability 1. The function  $o(\Delta t)$  is such that

$$\lim_{\Delta t \rightarrow 0} \frac{o(\Delta t)}{\Delta t} = 0$$

Using the backward Equation D.11, the master density equation that describes the MSMPR for the transition diagram D.2 becomes

$$P'_{xy}(t) = q_{xx}P_{xy}(t) + q_{x,x+1}P_{x+1,y}(t) = -(\lambda_x + \mu_x)P_{xy}(t) + \lambda_x P_{x+1,y}(t) \quad (\text{D.12})$$

The forward equation for the first state is

$$P'_{11}(t) = -(\lambda_1 + \mu_1)P_{11}(t) \quad (\text{D.13})$$

Subject to the initial conditions

$$P_{xy}(0) = \begin{cases} 1, & y=x, \\ 0, & y > x \end{cases} \quad x=1,2,\dots \quad (\text{D.14})$$

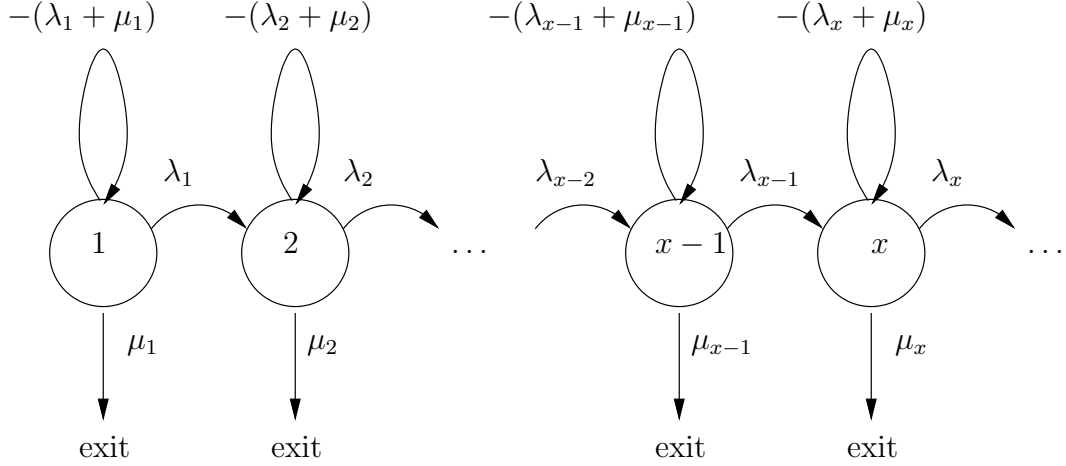


Figure D.2: Transition diagram of the crystal growth process in a mixed-suspension mixed-product removal (MSMPR) [50] reactor.

and assuming that the transition intensities are constant (i.e.  $\lambda_x = \lambda, \forall x$  and  $\mu_x = \mu, \forall x$ ), assuming that the exit transition intensities are constant and equal to the residence time of the crystallizer  $\tau$ , and using the *lack-of-memory* or Markov property, Equation D.12 (with D.13 and D.14) has the solution

$$P_{xy}(t) = \frac{(\lambda t)^{y-x}}{(y-x)!} \exp(-(\lambda + (1/\tau))t), \quad y \geq x; \quad x = 1, 2, \dots \quad (\text{D.15})$$

which is indicative of the decaying exponential size distribution of an MSMPR crystallizer. Hsu and Fan [49] also incorporated size-dependent growth into the stochastic model for an MSMPR crystallizer.

**Example 2: Batch Crystallizer Stochastic Model** Consider the transition diagram in Figure D.3 for a pure birth process  $X(t)$ ,  $0 \leq t < \infty$ , on the non-negative integers such that

$$\lambda_x > 0, \quad x \geq 0$$

where  $\lambda_x$  is the crystal growth rate for state  $x$ , assuming no dissolution. Since a pure birth process can only move to the right

$$P_{xy}(t) = 0, \quad y < x, t \geq 0$$

Also  $P_{xx}(t) = P_x(\tau_1 > t)$  and hence

$$P_{xx}(t) = e^{\lambda_x t}, \quad t \geq 0$$

The forward equation for  $y \neq 0$  is

$$P'_{xy}(t) = \lambda_{y-1} P_{x,y-1}(t) - \lambda_y P_{xy}(t), \quad t \geq 0 \quad (\text{D.16})$$

Solutions to Equation D.16 are given in table D.1 for some common examples.

Process	Infinitesimal Parameter	Solution to forward equation
Poisson process	$\lambda_x = \lambda$	$P_{xy}(t) = \frac{(\lambda t)^{y-x} e^{-\lambda t}}{(y-x)!}$
Yule process	$\lambda_x = \lambda x$	$P_{xy}(t) = \binom{y-1}{y-x} e^{-x\lambda t} (1 - e^{-\lambda t})^{y-x}$
Pure birth process	$\lambda_x \neq \lambda_{x+1}$	$P_{x,x+1}(t) = \frac{\lambda_x}{\lambda_{x+1} - \lambda_x} (e^{-\lambda_x t} - e^{-\lambda_{x+1} t})$
Pure birth process	$\lambda_x = \lambda_{x+1}$	$P_{x,x+1}(t) = \lambda_x t e^{-\lambda_x t}$

Table D.1: Solutions to the forward equation (Equation D.16) of some common pure birth processes [47].

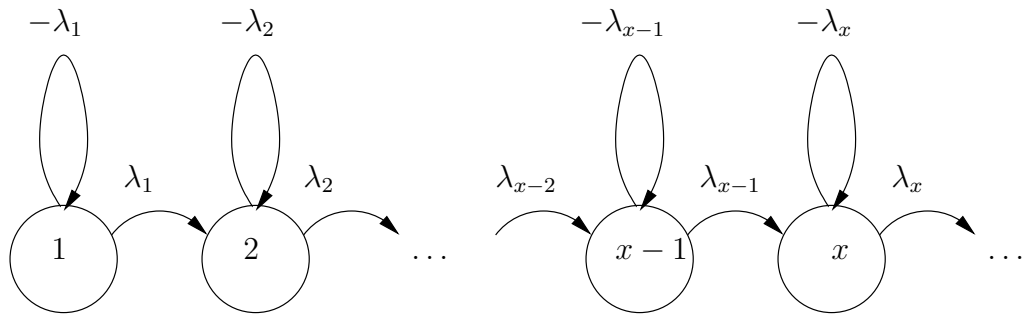


Figure D.3: Transition diagram of the crystal growth process in a batch crystallizer with no dissolution [47]

**Example 3: Batch Agglomeration Stochastic Model** Batch crystallizers are difficult to model using a probabilistic/stochastic approach, because supersaturation is not constant. In the MSMPR model, growth rate and hence supersaturation are assumed constant. For the batch system a separate mass balance must be coupled with the probability equations to determine the values of  $\lambda_x$  as a function of time. However, in a seeded batch agglomerator where there is no crystal growth, agglomeration of particles via size-independent or size-dependent growth is independent of the mass of solvent in solution and so the mass balance does not need to be coupled with the probabilistic model.

The following model for a batch agglomeration process is proposed by the author and is not complete. Consider the transition diagram Figure D.4 for a batch agglomerator. The system is assumed to be seeded with particles in the first three states. As particles grow (from state  $y$ , say) they do not necessarily have to move from consecutive state to state, jump processes to any state  $(y + 1), (y + 2), \dots$  are possible. It is assumed that particles  $x$  and  $y$  agglomerate to a new state  $(x + y)$  at a rate of  $\alpha_{xy}$  and there is correspondingly a loss of one particle from state  $y$  at a transition rate  $\alpha_{xy}$ . For the first three states 1, 2, 3 there are  $3^2$  possible permutations of binary agglomeration events. For  $\Omega$  states,  $\Omega^2$  possible agglomeration events are possible. The crystals are partitioned into  $\Omega$  states, such that a

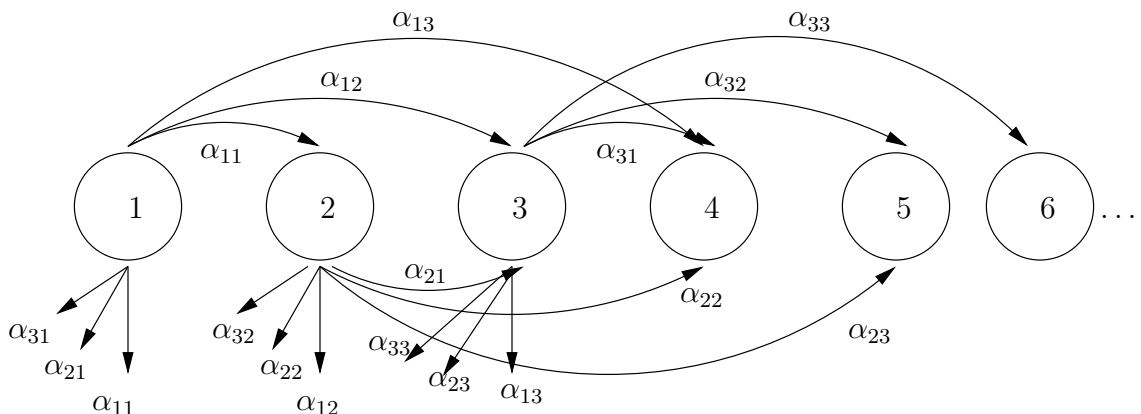


Figure D.4: Transition diagram of the agglomeration process. Arrows are drawn considering only the first 3 states.

crystal in state  $y$ , where  $y = 1, 2, \dots, \Omega$  has a size of  $y\delta$  and  $\delta$  is the discrete size increment between two adjacent states and  $\Omega$  is the maximum attainable state of crystals. During some time interval,  $t + \Delta t$ , a crystal in the  $y^{\text{th}}$  state may either grow to another state, exit the crystallizer or remain in the same state  $y$ . Assuming  $\Delta t$  to be small enough, the

following transition probabilities for a crystal hold

$$\begin{aligned} \Pr[\text{state } x \text{ at time } t \text{ exits at time } t + \Delta t] &= \left[ \lim_{n \rightarrow \infty} \sum_{y=1}^n (\alpha_{yx} + \alpha_{xy}) \right] \Delta t + o(\Delta t) \\ \Pr[\text{state } x \text{ at time } t \text{ stays in } x \text{ at time } t + \Delta t] &= 1 - \left[ \lim_{n \rightarrow \infty} \sum_{y=1}^n (\alpha_{yx} + \alpha_{xy}) \right] \Delta t \\ &\quad + o(\Delta t) \\ \Pr[\text{state } x \text{ at time } t \text{ is in state } x+1 \text{ at time } t + \Delta t] &= \alpha_{x1}\Delta t + o(\Delta t) \\ \Pr[\text{state } x \text{ at time } t \text{ is in state } x+2 \text{ at time } t + \Delta t] &= \alpha_{x2}\Delta t + o(\Delta t) \\ &\vdots \\ \Pr[\text{state } x \text{ at time } t \text{ is in state } x+n \text{ at time } t + \Delta t] &= \alpha_{xn}\Delta t + o(\Delta t) \end{aligned}$$

Using the backward Equation D.11, the master density equation for agglomeration is

$$\begin{aligned} P'_{xy}(t) &= \alpha_{y-1,1}P_{y-1,y}(t) + \alpha_{y-2,2}P_{y-2,y}(t) + \dots + \alpha_{1,y-1}P_{1,y}(t) \\ &\quad + \left( 1 - \lim_{n \rightarrow \infty} \sum_{k=1}^n (\alpha_{ky} + \alpha_{yk}) \right) P_{yy}(t), \quad y \geq x \end{aligned} \quad (\text{D.17})$$

A similar balance for  $P_{11}(t)$  yields

$$P'_{11}(t) = - \lim_{n \rightarrow \infty} \sum_{k=1}^n (\alpha_{k1} + \alpha_{1k}) P_{11}(t) \quad (\text{D.18})$$

Solution of Equation D.17 (with D.18 and D.14), allows calculation of the moments of the PSD of the batch agglomerator. The difficulty lies in the choice of  $\alpha_{ki}$  and  $\alpha_{ik}$  and whether the limit operations exist. For size-dependent agglomeration,  $\alpha_{kj}, \alpha_{jk}$  is a function of  $k$  and  $j$ , dependent on the state. Furthermore, the equations are non-linear and offer no advantage over solving numerically the deterministic population balance equation with agglomeration. Section D.2 outlines a Monte Carlo algorithm if one wishes to track the evolution of each individual particle instead of the evolution of the density over  $X(t)$ .

## D.2 Model Solution

In stochastic models, the random behavior of individual particles is simulated. In deterministic models, it is assumed that the system behaves as a continuum. The deterministic model for crystallization assumes that the number of particles is large and the time evolution of growth of a particle is continuous. The stochastic case states that the time evolution of the growth of a particle is a random-walk process and the growth of a particle appears to be piece-wise continuous. Many PDEs that describe deterministic systems have a complementary stochastic differential equation (SDE) that is proven to describe the same process [29].

For example the following PDE

$$\frac{\partial f}{\partial t} = -G \frac{\partial f}{\partial L} + \frac{1}{2} D \frac{\partial^2 f}{\partial L^2} \quad (\text{D.19})$$

has the SDE analogue for the  $i^{th}$  particle

$$dL_i(t) = Gdt + \sqrt{D}dW_i(t) \quad (\text{D.20})$$

which has the solution

$$L_i(t + \Delta t) = L_i(t) + G\Delta t + \sqrt{D}W_i(t) \quad (\text{D.21})$$

in which  $W_i$  is independently, identically Normally distributed with zero mean and covariance one.

Some researchers argue that the stochastic description is the true representation of chemical systems [34]. Deterministic models and solution methods are well established and are quite efficient if the number of particles in a system is large. However, for deterministic agglomeration models such as

$$\begin{aligned} \frac{\partial f}{\partial t} = & \frac{1}{2} \int_0^L f(L', t) f(L - L', t) \beta(L', L - L') dL' \\ & - \int_0^\infty f(L, t) f(L', t) \beta(L, L') dL' \end{aligned} \quad (\text{D.22})$$

discretization is usually required at the expense of the accuracy of the solution.  $\beta(L, L')dt$  (or  $\beta(v, v')dt$ ) is the probability that a given pair of particles with lengths  $L, L'$  (or volumes  $v, v'$ ) will agglomerate in the next infinitesimal time interval  $dt$ . Reconstructing the particle size density from a finite number of discretization size intervals created from discretization is difficult, especially as the number of particles approaches the number of size intervals. If the population of growing and agglomerating particles is small, then the random nature of the system is significant and is simulated in the stochastic model.

To illustrate the simplicity of a stochastic simulation, consider a constant volume batch crystallizer with only 1000 particles of a chosen particle size density. Assume that these particles randomly move in the crystallizer and only grow by agglomerating in biparticle collisions. During the agglomeration event, the new particle volume is the sum of the volumes of the parent particles.

In the case when the frequency of collisions and probability of agglomeration does not depend on the size of the particles, the probability of agglomeration is assumed proportional to

$$N(N - 1)$$

in which  $N$  is the number of particles. The rate of agglomeration is given by

$$r = k_{Agg} N(N - 1) \quad (\text{D.23})$$

The analogous rate equation for the deterministic PBE for size-independent agglomeration in terms of the zero moments is

$$\frac{d\mu_0}{dt} = -\frac{1}{2}\beta_0\mu_0^2 \quad (\text{D.24})$$

in which  $\beta_0 = \beta(L, L')$  is the rate constant for size-independent agglomeration.

Gillespie [33] states an algorithm for simulating coalescence in a batch system.

1. Initialize the event counter to zero. Set  $t = 0$ . Specify  $N$  initial values for the particle volumes  $v_1, v_2, \dots, v_N$ . Calculate the corresponding  $N(N-1)/2$  elements of the matrix  $\{\beta_{kl}\} = \beta(k, l)$ , the agglomeration kernel.  $v_i = F^{-1}(RND_i)$  in which  $F^{-1}$  is the inverse of the distribution function corresponding to a given density function and  $RND_i$  is a random number distributed as  $\mathcal{U}(0, 1)$ .

2. Calculate the quantities  $\beta_i$  and  $\beta_{tot}$

$$\begin{aligned} \beta_i &= \sum_{j=i+1}^N \beta_{ij}, \quad i = 1, \dots, N-1 \\ \beta_{tot} &= \sum_{i=1}^{N-1} \sum_{j=i+1}^N \beta_{ij} \end{aligned}$$

Generate three random numbers  $p_1, p_2$  and  $p_3$  from  $\mathcal{U}(0, 1)$  and generate the random triplet  $(\tau, i, j)$  according to

$$\begin{aligned} \tau &= -\ln(p_1)/\beta_{tot} \\ \sum_{i'=1}^{i-1} \beta_{i'} &< p_2 \beta_{tot} \leq \sum_{i'=1}^i \beta_{i'} \\ \sum_{j'=i+1}^{j-1} \beta_{ij'} &< p_3 \beta_i \leq \sum_{j'=i+1}^j \beta_{ij'} \end{aligned}$$

3. Let  $t = t + \tau$ . Remove particles  $v_i$  and  $v_j$  and replace with a new particle of volume  $v_i + v_j$ .
4. Let  $N = N - 1$ . Update the elements of the matrix  $\{\beta_{kl}\}$  according to the volume of the new particle. Increment the event counter and go to step 2.

If the initial particle size density is

$$f(v, t=0) = \frac{N_0}{v_0} \exp\left(-\frac{v}{v_0}\right) \quad (\text{D.25})$$

then the PBE for size-independent agglomeration has the analytical solution [30]

$$f(v, t) = \frac{4N_0}{v_0 (N_0 \beta_0 t + 2)^2} \exp\left(-\frac{2v}{v_0 (N_0 \beta_0 t + 2)}\right) \quad (\text{D.26})$$

Figure D.5 shows the results when starting with 1000 particles and finishing with 500 particles. The simulation results show the rough appearance of the number of particles at any time unlike the smooth behavior of the deterministic solution. As the number of particles increases and the size of the particle bins for calculating the height of the bars on the histogram decreases, the stochastic solution approaches the deterministic solution. Gooch and Hounslow [35] compute the time increments,  $\tau$ , for each agglomeration event by integrating the zeroth moment equation (Equation D.24) and solving for  $\Delta t (= \tau)$  in which  $\Delta\mu_0 = 1$ . The authors obtain results that agree with the analytical for the same problem in Figure D.5. Stochastic modeling, however, implies that agglomeration events, or any other growth, birth or death mechanism event are considered a Markov process. A Markov process is Markov if and only if the waiting times between events are exponentially distributed. Hence  $\tau = -\ln(p)/\beta_{\text{tot}}$ .

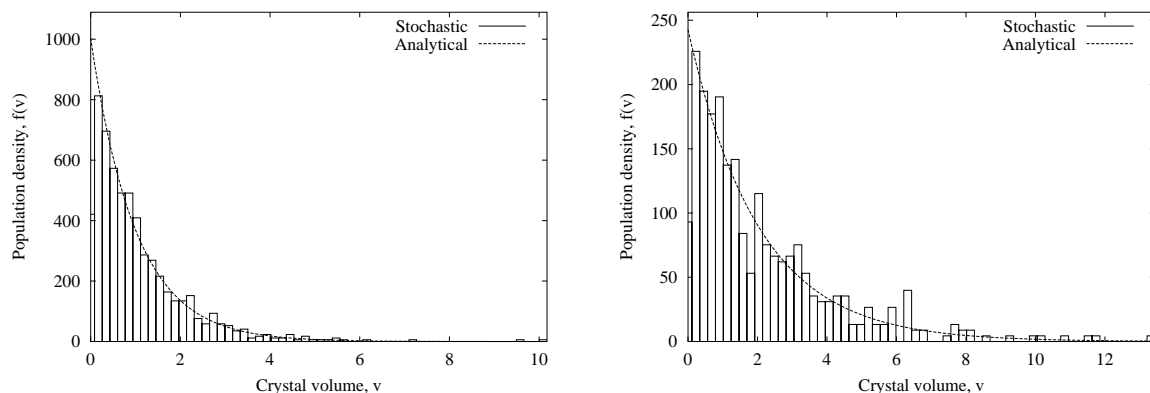
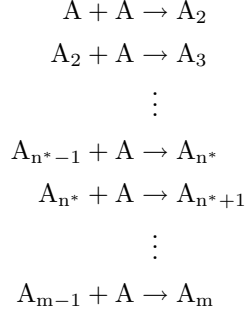


Figure D.5: Crystal size density given by Equation D.25 for 1000 particles at the start of the simulation.  $N_o = 1000$ ,  $v_o = 1$  and after 500 agglomeration events starting with 1000 particles. The analytical solution is given by Equation D.26.  $N_o = 1000$ ,  $v_o = 1$ ,  $\beta_0 = 0.01$ .

In the stochastic approach for modeling nucleation and growth in a large-scale batch crystallizer, the nucleation and growth events are considered as a sequence of bimolecular chemical reactions. In particular, solubilized ions or molecules (units) sequentially add to other units or to an assembly of any number of units. Kashchiev [57] describes this sequence of reactions as the Szilard model (see Chapter C, Section C.1.1) and the chemical reactions

are



The probability of a reaction occurring is assumed proportional to

$$r_1 \propto N_A(N_A - 1) \quad (\text{D.27})$$

for the first reaction and proportional to

$$r_i \propto N_A N_{A_i} \quad (\text{D.28})$$

for the remaining reactions  $i = 2, 3, \dots$ . The kinetic equations that describe the time evolution of the concentrations of the species,  $A, A_2, A_3, \dots$  are

$$\frac{dN_A}{dt} = -k_B N_A(N_A - 1) \quad (\text{D.29})$$

$$\frac{dN_i}{dt} = -k_{G_i} N_A N_i \quad i = A_2, A_3, \dots \quad (\text{D.30})$$

The method for solving the stochastic model given by the Equations D.29 and D.30 is the Gillespie algorithm [34] for chemical kinetics (similar to the coalescence algorithm [33]), which is an exact simulation of one trajectory of this random process. The expected behavior of the system can then be evaluated by averaging over many trajectory simulations.

1. Initialize the event counter to zero. Set  $t = 0$ . Specify  $N$  initial values of the number of species  $A, A_2, \dots, A_N$ .
2. Calculate the quantity  $r_{tot}$

$$r_{tot} = \sum_{i=1}^N r_i$$

Generate two random numbers  $p_1$  and  $p_2$  from  $\mathcal{U}(0, 1)$  and calculate  $\tau$  according to

$$\tau = -\ln(p_1)/r_{tot}$$

and choose a chemical reaction to occur in which the inequality

$$\sum_{i'=1}^{i-1} r_{i'} < p_2 r_{tot} \leq \sum_{i'=1}^i r_{i'}$$

is satisfied

3. Let  $t = t + \tau$ .
4. Adjust the number of species according to the stoichiometry of the chosen reaction.  
Increment the event counter and go to step 2.

The stochastic solution to the chemical reaction scheme described by Equations D.29 and D.30 has the following rate equation for reaction  $i$

$$\frac{dN_i}{dt} = \frac{-GN_i}{L_{i+1} - L_i} + \frac{GN_{i-1}}{L_i - L_{i-1}} \quad (\text{D.31})$$

in which  $G = k_G N_A$ . Letting

$$\Delta L = L_i - L_{i-1} \quad \forall i \in \{1, 2, 3, \dots\}$$

and taking the limit as  $\Delta L \rightarrow 0$

$$\lim_{\Delta L \rightarrow 0} \frac{dN_i}{dt} = -G \lim_{\Delta L \rightarrow 0} \frac{N_i - N_{i-1}}{\Delta L} \quad (\text{D.32})$$

results in

$$\frac{dN_1}{dt} = \frac{B}{\Delta L} - Gf_1 \quad (\text{D.33})$$

for the first reaction and the remaining reactions

$$\frac{dN_i}{dt} = -G(f_i - f_{i-1}) \quad (\text{D.34})$$

Dividing both sides of Equations D.33 and D.34 by  $\Delta L$  and taking the limit as  $\Delta L \rightarrow 0$ , so

$$\lim_{\Delta L \rightarrow 0} \frac{1}{\Delta L} \frac{dN_i}{dt} = -G \lim_{\Delta L \rightarrow 0} \frac{f_i - f_{i-1}}{\Delta L} \quad (\text{D.35})$$

results in

$$\frac{\partial f}{\partial t} = B\delta(L) - G\frac{\partial f}{\partial L} \quad (\text{D.36})$$

which is the PBE given by Equation 4.1.

For non-isothermal systems, Vlachos [140] uses a discretized energy balance to track the temperature. For crystallization in a batch system, the difference is

$$\Delta T = -\frac{UA}{\rho\hat{C}_p V}(T - T_j)\Delta t - \frac{\Delta\bar{H}_{crys}\rho_c k_v}{\rho\hat{C}_p} \left( \frac{\sum_i L_i^2 N_i}{\sum_i N_i} \right) \Delta t \quad (\text{D.37})$$

and a solubility equation of the form of Equation B.3 can be used to predict the number of available monomer units,  $N_A$  for nucleation and growth. Examples of solutions to this framework are given by Haseltine et al. [39].

# Bibliography

- [1] N. L. Abbott. New horizons for surfactant science in chemical engineering. *AICHE Journal*, 47(12):2634–2639, 2001.
- [2] C. F. Abegg, J. D. Stevens, and M. A. Larson. Crystal size distributions in continuous crystallizers when growth rate is size dependent. *AICHE Journal*, 14(1):118–122, January 1968.
- [3] M. B. Ajinkya and W. H. Ray. On the optimal operation of crystallization processes. *Chemical Engineering Communications*, 1:181–186, 1974.
- [4] G. F. Arkenbout. *Melt Crystallization Technology*. Technomic, Basel, 1995.
- [5] R. Bandyopadhyaya, R. Kumar, K. S. Gandhi, and D. Ramkrishna. Modeling of precipitation in reverse micellar systems. *Langmuir*, 13:3610–3620, 1997.
- [6] Y. Bard. *Nonlinear Parameter Estimation*. Academic Press, New York, 1974.
- [7] P. Barrett and B. Glennon. The use of FBRM for in-line monitoring of batch crystallization operations. In *Proceedings of Lasentec users' conference, Barcelona, Spain*, 2001.
- [8] J. R. Beckman and A. D. Randolph. Crystal size distribution dynamics in a classified crystallizer: Part II. Simulated control of crystal size distribution. *AICHE Journal*, 23(4):510–520, July 1977.
- [9] W. Beckmann. Seeding the desired polymorph: Background, possibilities, limitations and case studies. *Organic Process Research & Development*, 4:372–383, 2000.
- [10] K. A. Berglund and M. A. Larson. Modeling of growth rate dispersion of citric acid monohydrate in continuous crystallizers. *AICHE Journal*, 30:280–287, 1984.
- [11] B. Bernard-Michel, S. Rohani, M.-N. Pons, H. Vivier, and H. Hundal. Classification of crystal shape using fourier descriptors and mathematical morphology. *Particle and Particle Systems Characterization*, 14:193–200, 1997.
- [12] M. H. Bharati and J. F. MacGregor. Multivariate image analysis for real-time process monitoring and control. *Industrial and Engineering Chemistry Research*, 37:4715–4724, 1998.

- [13] H. L. Bhat, J. N. Sherwood, and T. Shripathi. The influence of stress, strain and fracture of crystals on the crystal growth process. *Chemical Engineering Science*, 42(4):609–618, 1987.
- [14] R. B. Bird, W. E. Stewart, and E. N. Lightfoot. *Transport Phenomena*. John Wiley & Sons, New York, 2nd edition, 2001.
- [15] M. Bohlin and Å. C. Rasmuson. Application of controlled cooling and seeding in batch crystallization. *The Canadian Journal of Chemical Engineering*, 70:120–126, 1992.
- [16] G. E. P. Box and G. C. Tiao. *Bayesian Inference in Statistical Analysis*. Addison-Wesley Publishing Company, Reading, Massachusetts, 1st edition, 1973.
- [17] R. D. Braatz and S. Hasebe. Particle size and shape control in crystallization processes. In *Chemical Process Control—CPC 6*, Tucson, Arizona, January 2001.
- [18] W. K. Burton, N. Cabrera, and F. C. Frank. The growth of crystals and the equilibrium structure of their surfaces. *Philosophical Transactions of the Royal Society of London*, 243:299–358, June 1951.
- [19] W. J. Cannella. Xylenes and ethylbenzene. In *Encyclopedia of Chemical Technology*. Wiley, 1998.
- [20] T. Chiu and P. D. Christofides. Nonlinear control of particulate processes. *AICHE Journal*, 45(6):1279–1297, 1999.
- [21] S. H. Chung, D. L. Ma, and R. D. Braatz. Optimal seeding in batch crystallization. *The Canadian Journal of Chemical Engineering*, 77:590–596, 1999.
- [22] R. de Goede. *Crystallization of Paraxylene with Scrapped Surface Heat Exchangers*. PhD thesis, TU Delft, 1988.
- [23] J. A. Dirksen and T. A. Ring. Fundamentals of crystallization: Kinetic effects on particle size distributions and morphology. *Chemical Engineering Science*, 46(10):2389–2427, 1991.
- [24] R. A. Eek, H. A. A. Pouw, and O. H. Bosgra. Design and experimental evaluation of stabilizing feedback controllers for continuous crystallizers. *Powder Technology*, 82(1):21–35, 1995.
- [25] N. M. Faqir and M. M. Attarakih. Optimal temperature policy for immobilized enzyme packed bed reactor performing reversible Michaelis-Menten kinetics using the disjoint policy. *Biotechnology and Bioengineering*, 77:163–173, 2002.
- [26] R. J. Farrell and Y. Tsai. Nonlinear controller for batch crystallization: Development and experimental demonstration. *AICHE Journal*, 41:2318–2321, 1995.

- [27] B. A. Finlayson and L. E. Scriven. The method of weighted residuals—a review. *Applied Mechanics Reviews*, 19:735–748, 1966.
- [28] C. E. García and A. M. Morshedi. Quadratic programming solution of dynamic matrix control (QDMC). *Chemical Engineering Communications*, 46:73–87, 1986.
- [29] C. W. Gardiner. *Handbook of Stochastic Methods for Physics, Chemistry, and the Natural Sciences*. Springer-Verlag, Berlin, Germany, 2nd edition, 1990.
- [30] F. Gelbard and J. H. Seinfeld. Numerical solution of the dynamic equation for particulate systems. *Journal of Computational Physics*, 28:357–375, 1978.
- [31] C. Gentric, F. Pla, M. A. Latifi, and J. P. Corriou. Optimization and non-linear control of a batch emulsion polymerization reactor. *The Chemical Engineering Journal*, 75:31–46, 1999.
- [32] P. E. Gill, W. Murray, M. A. Saunders, and M. H. Wright. User's guide for SOL/NPSOL (Version 4.0): A Fortran package for nonlinear programming, technical report SOL 86-2. Technical report, Systems Optimization Laboratory, Department of Operations Research, Stanford University, 1986.
- [33] D. T. Gillespie. An exact method for numerically simulating the stochastic coalescence process in a cloud. *Journal of the Atmospheric Sciences*, 32:1977–1989, 1975.
- [34] D. T. Gillespie. Exact stochastic simulation of coupled chemical reactions. *Journal of Physical Chemistry*, 81:2340–2361, 1977.
- [35] J. R. Gooch and M. J. Hounslow. Monte Carlo simulation of size-enlargement mechanisms in crystallization. *AICHE Journal*, 42(7):1864–1874, 1996.
- [36] H. Groen and K. J. Roberts. Nucleation, growth, and pseudo-polymorphic behavior of citric acid as monitored in situ by attenuated total reflection fourier transform infrared spectroscopy. *Journal of Physical Chemistry B*, 105:10723–10730, 2001.
- [37] W. F. Haddon and J. F. Johnson. Solubility data for p-xylene. *Journal of Chemical and Engineering Data*, 9(1):158–159, 1964.
- [38] R. W. Hartel. Crystallization in foods. In A. S. Myerson, editor, *Handbook of industrial crystallization*, pages 287–304. Butterworth-Heinemann, 2nd edition, 2002.
- [39] E. L. Haseltine, D. B. Patience, and J. B. Rawlings. On the stochastic simulation of particulate systems. In preparation for *ChE. Sci.*, 2001.
- [40] C. M. G. Heffels, D. Heitzmann, E. D. Hirleman, and B. Scarlett. The use of azimuthal intensity variations in diffraction patterns for particle shape characterization. *Particle and Particle Systems Characterization*, 11:194–199, 1994.

- [41] C. M. G. Heffels, D. Heitzmann, E. D. Hirleman, and B. Scarlett. Forward light scattering for arbitrary sharp-edged convex crystals in Fraunhofer and anomalous diffraction approximations. *Applied Optics*, 34(26):6552–6560, 1995.
- [42] C. M. G. Heffels, P. J. T. Verheijen, D. Heitzmann, and B. Scarlett. Correction for the effect of particle shape on the size distribution with a laser diffraction instrument. *Particle and Particle Systems Characterization*, 13:271–279, 1996.
- [43] C. M. G. Heffels, A. Willemse, and B. Scarlett. Possibilities of near backward light scattering for characterizing dense particle systems. *Powder Technology*, 86:127–135, 1996.
- [44] J. M. Herri, F. Gruy, J. S. Pic, M. Cournil, B. Cingotti, and A. Sinquin. Interest of in-situ turbidimetry for the characterization of methane hydrate crystallization: application to the study of kinetic inhibitors. *Chemical Engineering Science*, 54:1849–1858, 1999.
- [45] J. Hildebrand, J. Prausnitz, and R. Scott. *Regular and Related Solutions*. van Noststrand Reinhold Company, New York, 1970.
- [46] A. K. Hipp, B. Walker, M. Mazzotti, and M. Morbidelli. In-situ monitoring of batch crystallization by ultrasound spectroscopy. *Industrial and Engineering Chemistry Research*, 39:783–789, 2000.
- [47] P. G. Hoel, S. C. Port, and C. J. Stone. *Introduction to Stochastic Processes*. Waveland Press, Incorporated, Prospect Heights, IL, 1st edition, 1972.
- [48] M. C. Hoff. *U.S. Patents 2,777,888*. to Standard Oil Company, 1957.
- [49] J. Hsu and L. Fan. Transient analysis of crystallization: Effect of the size dependent growth rate. *Chemical Engineering Communications*, 56:19–40, 1987.
- [50] J. P. Hsu, L. T. Fan, and S. T. Chou. Transient analysis of crystallization: Effect of the initial size distribution. *Chemical Engineering Communications*, 69:95–114, 1988.
- [51] H. M. Hulbert and S. Katz. Some problems in particle technology: A statistical mechanical formulation. *Chemical Engineering Science*, 19:555–574, 1964.
- [52] J. Jager, H. J. M. Kramer, E. J. de Jong, S. de Wolf, O. H. Bosgra, A. Boxman, H. G. Merkus, and B. Scarlett. Control of industrial crystallizers. *Powder Technology*, 69(1):11–20, January 1992.
- [53] A. G. Jones. Optimal operation of a batch cooling crystallizer. *Chemical Engineering Science*, 29:1075–1087, 1974.
- [54] A. G. Jones and J. W. Mullin. Programmed cooling crystallization of potassium sulphate solutions. *Chemical Engineering Science*, 29:105–118, 1974.

- [55] C. M. Jones and M. A. Larson. Characterizing growth-rate dispersion of NaNO<sub>3</sub> secondary nuclei. *AICHE Journal*, 45(10):2128–2135, 1999.
- [56] J. Karlsson, A. Eroglu, T. Toth, E. Cravalho, and M. Toner. Rational design and theoretical optimization of a cryopreservation protocol. In *Advances in heat and mass transfer in biotechnology. American society of mechanical engineers. HTD-Vol. 322/BED-Vol. 32*, pages 85–89, 1995.
- [57] D. Kashchiev. *Nucleation*. Butterworth-Heinemann, Oxford, England, 1st edition, 2000.
- [58] D. G. Kendall. Stochastic processes and population growth. *Journal of the Royal Statistical Society: Series B*, 11:230–264, 1949.
- [59] S. Kumar and D. Ramkrishna. On the solution of population balance equations by discretization–III: Nucleation, growth and aggregation of particles. *Chemical Engineering Science*, 52(24):4659–4679, 1997.
- [60] R. Lacmann and U. Tanneberger. Growth rate dispersion of single potassium alum crystals. *Journal of Crystal Growth*, 147:194–199, 1995.
- [61] G. C. Lammers. *U.S. Patent 3,177,265*. to Standard Oil Company, 1965.
- [62] Y. Lang, A. M. Cervantes, and L. T. Biegler. Dynamic optimization of a batch cooling crystallization process. *Industrial and Engineering Chemistry Research*, 38:1469–1477, 1999.
- [63] I. J. Laurenzi and S. L. Diamond. Monte Carlo simulation of the heterotypic aggregation kinetics of platelets and neutrophils. *Biophysical Journal*, 77:1733–1746, 1999.
- [64] F. Lewiner, J. P. Klein, F. Puel, and G. Févotte. On-line ATR FTIR measurement of supersaturation during solution crystallization processes. Calibration and applications on three solute/solvent systems. *Chemical Engineering Science*, 56:2069–2084, 2001.
- [65] D. L. Ma, S. H. Chung, and R. D. Braatz. Worst-case performance analysis of optimal batch control trajectories. *AICHE Journal*, 45(7):1469–1476, 1999.
- [66] G. Madras and B. J. McCoy. Distribution kinetics theory of Ostwald ripening. *Journal of Chemical Physics*, 115(14):6699–6706, 2001.
- [67] S. Manjunath, K. S. Gandhi, R. Kumar, and D. Ramkrishna. Precipitation in small systems–I. Stochastic analysis. *Chemical Engineering Science*, 49(9):1451–1463, 1994.
- [68] H. B. Matthews. *Model Identification and Control of Batch Crystallization for an Industrial Chemical System*. PhD thesis, University of Wisconsin–Madison, 1997.

- [69] H. B. Matthews, S. M. Miller, and J. B. Rawlings. Model identification for crystallization: Theory and experimental verification. *Powder Technology*, 88:227–235, 1996.
- [70] H. B. Matthews and J. B. Rawlings. Batch crystallization of a photochemical: Modeling, control and filtration. *AICHE Journal*, 44:1119–1127, 1998.
- [71] D. Q. Mayne, J. B. Rawlings, C. V. Rao, and P. O. M. Scokaert. Constrained model predictive control: Stability and optimality. *Automatica*, 36(6):789–814, 2000.
- [72] B. J. McCoy. A new population balance model for crystal size distributions: reversible, size-dependent growth and dissolution. *Journal of Colloid and Interface Science*, 240(1):139–149, 2001.
- [73] D. McKay, G. H. Dale, and D. C. Tabler. Para-xylene via fractional crystallization. *Chemical Engineering Progress*, 62(11):104–112, 1966.
- [74] S. A. Middlebrooks. *Modelling and Control of Silicon and Germanium Thin Film Chemical Vapor Deposition*. PhD thesis, University of Wisconsin–Madison, 2001.
- [75] S. M. Miller. *Modelling and Quality Control Strategies for Batch Cooling Crystallizers*. PhD thesis, The University of Texas at Austin, 1993.
- [76] S. M. Miller and J. B. Rawlings. Model identification and control strategies for batch cooling crystallizers. *AICHE Journal*, 40(8):1312–1327, August 1994.
- [77] O. Monnier, G. Fevotte, C. Hoff, and J. P. Klein. Model identification of batch cooling crystallizations through calorimetry and image analysis. *Chemical Engineering Science*, 52(7):1125–1139, 1997.
- [78] M. Morari. Some comments on the optimal operation of batch crystallizers. *Chemical Engineering Communications*, 4:167–171, 1980.
- [79] P. Mougin, D. Wilkinson, K. J. Roberts, and R. Tweedie. Characterization of particle size and its distribution during the crystallization of organic fine chemical products as measured in situ using ultrasonic attenuation spectroscopy. *Journal of the Acoustical Society of America*, 109:274–282, 2001.
- [80] J. W. Mullin. *Crystallization*. Butterworth & Co (Publishers) Ltd, London, England, 3rd edition, 1993.
- [81] J. W. Mullin and J. Nývlt. Programmed cooling of batch crystallizers. *Chemical Engineering Science*, 26:369–377, 1971.
- [82] J. W. Mullin and O. Söhnel. Expressions of supersaturation in crystallization studies. *Chemical Engineering Science*, 32(7):683–686, 1977.

- [83] H. Offermann and J. Ulrich. On the growth behaviour of hurt and unhurt crystals of different sizes. In S. J. Jančić and E. J. de Jong, editors, *Industrial Crystallization 84*, pages 31–36, The Hague, The Netherlands, 1984. Elsevier.
- [84] P. Ossipov. Optimization of heat-mass transfer at continuous solid layer crystallization on a belt. *Applied Mathematical Modelling*, 23:419–436, 1999.
- [85] M. R. Owen, C. Luscombe, L. W. Lai, S. Godbert, D. L. Crookes, and D. Emiabata-Smith. Efficiency by design: Optimisation in process research. *Organic Process Research & Development*, 5:308–323, 2001.
- [86] D. B. Patience, P. C. Dell'Orco, and J. B. Rawlings. Optimal operation of a seeded pharmaceutical crystallization with growth-dependent dispersion. Submitted to *Organic Process Research & Development*, 2002.
- [87] D. B. Patience, R. W. Hartel, and D. Illingworth. Crystallization and pressure filtration of anhydrous milk fat: mixing effects. *Journal of the American Oil Chemists' Society*, 76(5):585–594, 1999.
- [88] D. B. Patience, E. L. Haseltine, P. C. Dell'Orco, and J. B. Rawlings. Modeling pharmaceutical crystallization with apparent growth-rate dispersion. Submitted to *Journal of Crystal Growth*, 2002.
- [89] D. B. Patience, H. A. Mohameed, and J. B. Rawlings. Crystallization of para-xylene in scraped-surface crystallizers. *AICHE Journal*, 47(11):2441–2451, 2001.
- [90] D. B. Patience and J. B. Rawlings. Particle-shape monitoring and control in crystallization processes. *AICHE Journal*, 47(9):2125–2130, 2001.
- [91] R. H. Perry, D. W. Green, and J. O. Maloney, editors. *Perry's Chemical Engineer's Handbook*. McGraw-Hill Book Company, New York, 6th edition, 1984.
- [92] F. C. Phillips. *An Introduction to Crystallography*. Longmans, Green and Co., London, 4th edition, 1971.
- [93] C. Plummer and H. Kausch. Real-time image analysis and numerical simulation of isothermal spherulite nucleation and growth in polyoxymethylene. *Colloid and Polymer Science*, 273:719–732, 1995.
- [94] F. Podczeck. A shape factor to assess the shape of particles using image analysis. *Powder Technology*, 93:47–53, 1997.
- [95] F. Podczeck. The shape of powder particles and its influence on powder handling. In *Proceedings of the International Fine Particle Research Institute Conference*, Den Haag, The Netherlands, July 2000.

- [96] M.-N. Pons and H. Vivier. Crystallization monitoring by quantitative image analysis. *Analytica Chimica Acta*, 238:243–249, 1990.
- [97] R. S. Porter and J. F. Johnson. Extended xylene solubility studies. *Journal of Chemical and Engineering Data*, 12(3):392–394, 1967.
- [98] F. Puel, P. Marchal, and J. Klein. Habit transient analysis in industrial crystallization using two dimensional crystal sizing technique. *Chemical Engineering Research and Design*, 75(A2):193–205, 1997.
- [99] Y. Qiu and Å. C. Rasmussen. Estimation of crystallization kinetics from batch cooling experiments. *AICHE Journal*, 40(5):799–812, 1994.
- [100] D. Ramkrishna. The status of population balances. *Reviews in Chemical Engineering*, 3(1):49–95, 1985.
- [101] D. Ramkrishna. *Population Balances*. Academic Press, San Deigo, 2000.
- [102] D. Ramkrishna and J. D. Borwanker. A puristic analysis of population balance—I. *Chemical Engineering Science*, 28:1423–1435, 1973.
- [103] D. Ramkrishna and J. D. Borwanker. A puristic analysis of population balance—II. *Chemical Engineering Science*, 29:1711–1721, 1974.
- [104] A. D. Randolph, L. Chen, and A. Tavana. Feedback control of CSD in a KCl crystallizer with a fines dissolver. *AICHE Journal*, 33:583–591, 1987.
- [105] A. D. Randolph and M. A. Larson. Transient and steady-state size distributions in continuous mixed suspension crystallizers. *AICHE Journal*, 8(5):639–645, 1962.
- [106] A. D. Randolph and M. A. Larson. *Theory of Particulate Processes*. Academic Press, San Diego, second edition, 1988.
- [107] A. D. Randolph and E. T. White. Modeling size dispersion in the prediction of crystal-size distribution. *Chemical Engineering Science*, 32:1067–1076, 1977.
- [108] D. L. Ransley. Xylenes and ethylbenzene. In *Encyclopedia of Chemical Technology*. Wiley, 1984.
- [109] J. B. Rawlings, E. S. Meadows, and K. R. Muske. Nonlinear model predictive control: a tutorial and survey. In *ADCHEM '94 Proceedings, Kyoto, Japan*, pages 185–197, 1994.
- [110] J. B. Rawlings, S. M. Miller, and W. R. Witkowski. Model identification and control of solution crystallization processes: A review. *Industrial and Engineering Chemistry Research*, 32(7):1275–1296, July 1993.

- [111] J. B. Rawlings, W. R. Witkowski, and J. W. Eaton. Modelling and control of crystallizers. *Powder Technology*, 69:3–9, 1992.
- [112] T. P. Redman, S. Rohani, and G. Strathdee. On-line control of supersaturation in a continuous cooling KCl crystallizer. *The Canadian Journal of Chemical Engineering*, 73:725–733, 1995.
- [113] H.-K. Rhee, R. Aris, and N. Amundson. *First Order Partial Differential Equations: Volume II Theory and Application of Hyperbolic Systems of Quasilinear Equations*. Prentice-Hall, Englewood Cliffs, N.J., 1986.
- [114] R. Ristić, B. Y. Shekunov, and J. N. Sherwood. Growth of the tetrahedral faces of sodium chlorate crystals in the presence of dithionite impurity. *Journal of Crystal Growth*, 139(3-4):336–343, 1994.
- [115] R. Ristić, J. N. Sherwood, and K. Wojciechowski. Morphology and growth kinetics of large sodium chlorate crystals grown in the presence and absence of sodium dithionite impurity. *Journal of Physical Chemistry*, 97(41):10774–10782, 1993.
- [116] S. Rohani, N. S. Tavare, and J. Garside. Control of crystal size distribution in a batch cooling crystallizer. *The Canadian Journal of Chemical Engineering*, 68:260–267, April 1990.
- [117] Z. H. Rojkowski. Crystal growth rate models and similarity of population balances for size-dependent growth rate and for constant growth rate dispersion. *Chemical Engineering Science*, 48(8):1475–1485, 1993.
- [118] D. F. Rudd. A generalization of the residence time concept. *The Canadian Journal of Chemical Engineering*, pages 197–202, 1962.
- [119] A. Ruf, J. Worlitschek, and M. Mazzotti. Modeling and experimental analysis of PSD measurements through FBRM. *Particle and Particle Systems Characterization*, 17:167–179, 2000.
- [120] E. Sevick-Muraca, J. Pierce, H. Jiang, and J. Kao. Photon–migration measurement of latex size distribution in concentrated suspensions. *AICHE Journal*, 43(3):655–664, 1997.
- [121] B. H. Shah, D. Ramkrishna, and J. D. Borwanker. Simulation of particulate systems using the concept of the interval of quiescence. *AICHE Journal*, 23(6):897–904, 1977.
- [122] J. N. Sherwood and R. I. Ristić. The influence of mechanical stress on the growth and dissolution of crystals. *Chemical Engineering Science*, 56:2267–2280, 2001.
- [123] D. J. Smit, M. J. Hounslow, and W. R. Paterson. Aggregation and gelation—I. Analytical solutions for CST and batch operation. *Chemical Engineering Science*, 49(7):1025–1035, 1994.

- [124] E. Smith, R. Hammond, M. Jones, K. Roberts, J. Mitchell, S. Price, R. Harris, D. Ap- perley, J. Cherryman, and R. Docherty. The determination of the crystal structure of anhydrous theophylline by x-ray powder diffraction with a systematic search algorithm, lattice energy calculations, and  $^{13}\text{C}$  and  $^{15}\text{N}$  solid-state nmr: A question of polymorphism in a given unit cell. *Journal of Physical Chemistry B*, 105:5818–5826, 2001.
- [125] L. A. Smith, K. J. Roberts, D. Machin, and G. McLeod. An examination of the solution phase and nucleation properties of sodium, potassium and rubidium dodecyl sulphates. *Journal of Crystal Growth*, 226:158–167, 2001.
- [126] M. K. Smith. Thermal convection during the directional solidification of a pure liquid with variable viscosity. *Journal of Fluid Mechanics*, 188:547–570, 1988.
- [127] C. A. Spiller. U.S. Patents 2,866,833. to Standard Oil Company, 1958.
- [128] R. Spruijtenburg. Examples of the selective preparation of a desired crystal modification by an appropriate choice of operating parameters. *Organic Process Research & Development*, 4:403–406, 2000.
- [129] W. E. Stewart, M. Caracotsios, and J. P. Sørensen. Parameter estimation from multiresponse data. *AICHE Journal*, 38(5):641–650, 1992.
- [130] W. E. Stewart, Y. Shon, and G. E. P. Box. Discrimination and goodness of fit of multiresponse mechanistic models. *AICHE Journal*, 44(6):1404–1412, 1998.
- [131] Z. Sun and E. Sevick-Muraca. Inversion algorithms for particle sizing with photon migration measurement. *AICHE Journal*, 47(7):1487–1498, 2001.
- [132] N. S. Tavare. Batch crystallizers: A review. *Chemical Engineering Communications*, 61:259–318, 1987.
- [133] N. S. Tavare. Batch crystallizers. *Reviews in Chemical Engineering*, 7(3):211–355, 1991.
- [134] N. S. Tavare. *Industrial Crystallization: Process Simulation Analysis and Design*. Plenum Press, New York, 1995.
- [135] T. Togkalidou, R. D. Braatz, B. K. Johnson, O. Davidson, and A. Andrews. Experimental design and inferential modeling in pharmaceutical crystallization. *AICHE Journal*, 47(1):160–168, 2001.
- [136] T. Togkalidou, M. Fujiwara, S. Patel, and R. D. Braatz. Solute concentration prediction using chemometrics and ATR-FTIR spectroscopy. *Journal of Crystal Growth*, 231:534–543, 2001.

- [137] H. van de Hulst. *Light Scattering by Small Particles*. Dover Publications, New York, 1981.
- [138] J. Villadsen and M. L. Michelsen. *Solution of Differential Equation Models by Polynomial Approximation*. Prentice-Hall, Englewood Cliffs New Jersey, 1978.
- [139] J. V. Villadsen and W. E. Stewart. Solution of boundary-value problems by orthogonal collocation. *Chemical Engineering Science*, 22:1483–1501, 1967.
- [140] D. G. Vlachos. Instabilities in homogeneous nonisothermal reactors: Comparison of deterministic and Monte Carlo simulations. *Journal of Chemical Physics*, 102(4):1781–1790, 1995.
- [141] U. Vollmer and J. Raisch.  $H_\infty$ -control of a continuous crystallizer. Submitted for publication in ADCHEM, 2000.
- [142] U. Vollmer and J. Raisch.  $H$ -infinity-control of a continuous crystallizer. *Control Engineering Practice*, 9(8):837–845, 2001.
- [143] J. S. Wey. Analysis of batch crystallization processes. *Chemical Engineering Communications*, 35:231–252, 1985.
- [144] J. Wiencek. Crystallization of proteins. In A. S. Myerson, editor, *Handbook of industrial crystallization*, pages 267–285. Butterworth-Heinemann, 2nd edition, 2002.
- [145] D. Winn and M. F. Doherty. Modeling crystal shapes of organic materials grown from solution. *AICHE Journal*, 46(7):1348–1367, 2000.
- [146] W. R. Witkowski. *Model Identification and Parameter Estimation of Crystallization Processes*. PhD thesis, The University of Texas at Austin, 1990.
- [147] W. R. Witkowski, S. M. Miller, and J. B. Rawlings. Light scattering measurements to estimate kinetic parameters of crystallization. In A. S. Myerson and K. Toyokura, editors, *Crystallization as a Separations Process*, pages 102–114, Washington, DC, 1990. American Chemical Society.
- [148] K. Wood-Kaczmar. A new look at the control of particle size in the batch crystallization of pharmaceutical products by the application of statistical DOE analysis to FBRM data. In *Proceedings of Lasentec users' conference, Barcelona, Spain*, 2001.
- [149] R. Zauner and A. G. Jones. Scale-up of continuous and semi-batch precipitation processes. *Industrial and Engineering Chemistry Research*, 39:2392–2403, 2000.

200

# Vita

Daniel Bruce Patience is the son of Ian Charles Patience and Helen Marie Patience. He was born in Turangi, New Zealand on November 28, 1971. At the age of 2, his family moved to Tauranga and then at 6 the family moved to Wellington. He graduated at Scots College in 1989 and started his Engineering intermediate year in January 1990 at Victoria University in Wellington. In January 1991, he moved to the University of Canterbury in Christchurch and graduated in December 1993 with a B.E. degree in Chemical and Process Engineering with First Class Honours (degree awarded May 4, 1994). In January 1994, he moved to Madison, Wisconsin to complete an M.S. degree in Food Science under the supervision of Dr. Richard W. Hartel (degree awarded August 25, 1996). In the Fall of 1996, he joined the Rawlings research group in the Department of Chemical Engineering at the University of Wisconsin-Madison.

Permanent Address: 248/5 Oriental Parade  
Wellington 6001  
NEW ZEALAND

This dissertation was prepared with L<sup>A</sup>T<sub>E</sub>X 2 <sub>$\varepsilon$</sub> <sup>2</sup> by the author.

---

<sup>2</sup>This particular University of Wisconsin compliant style was carved from The University of Texas at Austin styles as written by Dinesh Das (L<sup>A</sup>T<sub>E</sub>X 2 <sub>$\varepsilon$</sub> ), Khe-Sing The (L<sup>A</sup>T<sub>E</sub>X), and John Eaton (E<sup>A</sup>T<sub>E</sub>X). Knives and chisels wielded by John Campbell and Rock Matthews.